

Scientific Opportunities with the Long Baseline Neutrino Experiment

July 15, 2013

DRAFT

DRAFT

Abstract

In this document, we describe the science opportunities and capabilities of LBNE, the Long-Baseline Neutrino Experiment. LBNE has been developed to provide a unique and compelling program for the exploration of key questions at the forefront of particle physics. Chief among the discovery opportunities it will enable are observation of CP symmetry violation in neutrino mixing, determination of the neutrino mass hierarchy, determination of maximal or near-maximal mixing in neutrinos, searches for nucleon decay signatures, and detailed studies of neutrino bursts from galactic supernovae. To fulfill these and other goals as a world-class facility, LBNE is conceived around four central components: (1) a new, intense wide-band neutrino source at Fermilab, (2) a fine-grained ‘near’ neutrino detector just downstream of the source, (3) the Sanford Underground Research Facility (SURF) in Lead, South Dakota at an optimal distance (~ 1300 km) from the neutrino source, and (4) a massive liquid argon time-projection chamber (LArTPC) deployed there as a ‘far’ detector. Uniquely among initiatives with such a broad spectrum of ambitious science goals, the advanced state of engineering development, project planning and financial support for LBNE have established a compelling path toward its realization.

This document is being submitted as a white paper to the 2013 DPF Community Summer Study program.

Contents

Contents	ii
List of Figures	v
List of Tables	xi
1 Introduction and Executive Summary	1
1.1 Development of a World-Class Experiment	3
1.2 Summary of Key LBNE Physics Sensitivities	6
1.2.1 Long-Baseline/Oscillation Physics	6
1.2.2 Searches for Baryon Number Violation	8
1.2.3 Physics and Astrophysics with Supernova Neutrinos	8
1.2.4 Physics with a Fine-grained Near Detector.	9
1.3 Concluding Remarks	9
References	11
2 Overview of the LBNE Science Program	14
2.1 Primary and Secondary Science Objectives	14
2.2 Neutrino Oscillations, CP Violation and the Three-Flavor Model	16
2.2.1 Probing the Mass Hierarchy, CP Violation, and Three-Flavor Mixing with the $\nu_\mu \rightarrow \nu_e$ Oscillation Mode in a ν_μ Beam Experiment	16
2.2.1.1 Characterization of Three-Flavor Mixing	16
2.2.1.2 Leptonic CP Violation	19
2.2.1.3 CP-Violating Effects in Long-Baseline Experiments	20
2.2.1.4 Matter Effects and the Mass Hierarchy	21
2.2.1.5 Disentangling Leptonic CPV and the Matter Effect	24
2.2.1.6 Optimization of Baseline	27
2.2.2 Disappearance of ν_μ and Determination of θ_{23}	27
2.2.3 Oscillation Physics with Atmospheric Neutrinos	29
2.3 Grand Unified Theories and Baryon Number Violation Processes	31
2.4 Physics and Astrophysics From Core-Collapse Supernova Neutrinos	34
3 Overview of the LBNE Project and Design	38
3.1 LBNE and the U.S. Neutrino-Physics Program	38

3.2	Sanford Underground Research Facility (SURF)	39
3.3	Fermi National Accelerator Laboratory	44
3.4	The LBNE Beamline	48
3.5	The Near Detector Complex	53
3.6	The LBNE Far Detector	55
3.6.1	Surface Detector for LBNE Phase-I	55
3.6.2	Large Underground LArTPC Modules	59
4	Long-Baseline Neutrino Oscillation Physics	63
4.1	LBNE Detector Simulation and Reconstruction	66
4.1.1	Far Detector Simulation	66
4.1.2	Far Detector Reconstruction	70
4.1.3	Fast Monte Carlo	71
4.1.4	Detector Simulation using the GLoBeS Package	78
4.2	Measurements of Mass Hierarchy and the CP-Violating Phase	83
4.3	Measurement of θ_{23} and Determination of the Octant	89
4.4	Precision Measurements of the Oscillation Parameters in the 3-Flavor Model	93
4.5	Atmospheric Neutrinos	99
4.6	Searches for Physics Beyond ν SM in Long-baseline Oscillations	107
4.6.1	Search for Non-Standard Interactions	107
4.6.2	Long Range Interactions	107
4.6.3	Search for Active-sterile Neutrino Mixing	109
4.6.4	Sensitivity to Large Extra Dimensions	110
5	Physics Opportunities with a High Resolution Near Detector	111
5.1	Precision Physics with Long Baseline Oscillations	112
5.2	Electroweak Precision Measurement: Weak Mixing Angle	119
5.3	Strangeness Content of the Nucleon	124
5.4	Isospin Physics and Sum-Rules	127
5.5	Nucleon Structure, Parton Distribution Functions, and QCD Studies	129
5.6	Neutrino-Nuclear Interactions and Nuclear Effects	131
5.7	Search for Heavy Neutrinos	132
5.8	Search for Non-Standard Interactions: High Δm^2 Neutrino Oscillations	134
5.9	Light (sub-GeV) Dark Matter Searches in the Neutrino Beam at LBNE	136
6	Searches for Baryon Number Non-conservation	139
6.1	Sensitivity to Nucleon Decay	139
6.1.1	LBNE and the Current Experimental Context	139
6.1.2	Signatures for Nucleon Decay in LBNE	140
6.1.2.1	Signatures for $p \rightarrow K^+ \bar{\nu}$	140
6.1.3	Background Levels and Rejection	141
6.1.4	Expected Sensitivity	142
7	Core-Collapse Supernova Neutrinos	144

7.1	Physics and Astrophysics From Core-Collapse Neutrinos	144
7.2	Expected Signal and Detection in Liquid Argon	146
7.3	Low-Energy Backgrounds	148
7.3.1	Intrinsic Backgrounds	149
7.3.1.1	Cleanliness Database	152
7.3.2	Cosmogenic Backgrounds	152
8	Other Physics Opportunities with the LBNE Far Detector	154
8.1	Solar Neutrinos	154
8.2	Geoneutrinos	155
8.3	Indirect Searches for WIMP Dark Matter	156
9	Conclusion	158
	References	161

DRAFT

List of Figures

1-1	The expected 1σ resolution for δ_{cp} as a function of exposure for 700 kW proton beam power.	7
1-2	Sensitivity to the decay $p \rightarrow K^+\bar{\nu}$ with LAr detectors.	8
2-1	Neutrino oscillations vs energy, baseline and as a function of different values of δ_{CP} . The oscillograms on the left show the $\nu_\mu \rightarrow \nu_e$ oscillation probabilities as a function of baseline and energy for neutrinos (top left) and anti-neutrinos (bottom left) with $\delta_{CP} = 0$ and a normal hierarchy . The figures on the right show the projection of the oscillation probability on the neutrino energy axis at a baseline of 1300km for $\delta_{CP} = 0$ (red), $\delta_{CP} = +\pi/2$ (green), and $\delta_{CP} = -\pi/2$ (blue) for neutrinos (top right) and anti-neutrinos (bottom right). The yellow curve is the ν_e appearance solely from the “solar term” due to 1-2 mixing as given by Equation 2.9.	22
2-2	Neutrino oscillations vs energy, baseline and as a function of different values of δ_{CP} . The oscillograms on the left show the $\nu_\mu \rightarrow \nu_e$ oscillation probabilities as a function of baseline and energy for neutrinos (top left) and anti-neutrinos (bottom left) with $\delta_{CP} = 0$ and an inverted hierarchy . The figures on the right show the projection of the oscillation probability on the neutrino energy axis at a baseline of 1300km for $\delta_{CP} = 0$ (red), $\delta_{CP} = +\pi/2$ (green), and $\delta_{CP} = -\pi/2$ (blue) for neutrinos (top right) and anti-neutrinos (bottom right). The yellow curve is the ν_e appearance solely from the “solar term” due to 1-2 mixing as given by Eqn. 2.9.	23
2-3	The CP asymmetry as a function of baseline. The top two figures are for the asymmetry induced by the matter effect only for normal (top left) and inverted (top right) hierarchies. The bottom figures are for the asymmetry induced through the CP violating phase δ_{CP} in vacuum, for $\delta_{CP} = +\pi/2$ (bottom left) and $\delta_{CP} = -\pi/2$ (bottom right)	25
2-4	$\nu/\bar{\nu}$ oscillation asymmetries vs δ_{CP} at the first 2 oscillation nodes. Clockwise from top left: 290km, 810km, 2300km, 1300km.	26
2-5	Fraction of 3σ δ_{cp} values for CP violation and mass hierarchy vs baseline	28
2-6	Atmospheric neutrino flux and spectrum	29
2-7	The probabilities of atmospheric $\nu_\mu \rightarrow \nu_e$ (left) and $\bar{\nu}_\mu \rightarrow \bar{\nu}_e$ (right) oscillations for normal (top) and inverted (bottom) hierarchies as a function of zenith angle.	30

2-8	Proton decay lifetime limits compared to lifetime ranges predicted by Grand Unified Theories. The upper section is for $p \rightarrow e^+\pi^0$, most commonly caused by gauge mediation. The lower section is for SUSY motivated models, which commonly predict decay modes with kaons in the final state. The marker symbols indicate published limits by experiments, as indicated by the sequence and colors on top of the figure.	33
2-9	Number of supernova neutrino interactions in an LAr detector vs distance . . .	36
3-1	General Homestake Mine Development	40
3-2	Predicted cosmic ray flux at Homestake Mine	41
3-3	Photos from Sanford Lab	42
3-4	Experiment timeline at SURF	43
3-5	Fermilabs accelerator chain	44
3-6	NuMI beamline performance	45
3-7	Fermilab proton plan for intensity frontier	45
3-8	Project X accelerator schematics	46
3-9	LBNE Overall Project Layout at Fermilab	48
3-10	Primary beamline elevation view	49
3-11	Cartoon of the LBNE neutrino beamline components	50
3-12	The unoscillated ratio of helium to air flux at the far detector with the beamline, excluding the decay pipe material, set to the configuration as described in the text. The horn currents were set to select ν_μ events. The are approximately 25000k protons on target for both the helium and air configurations.	52
3-13	System of tertiary muon detectors, which will monitor the LBNE neutrino beam in Phase-I of the project.	53
3-14	Two candidate near detectors: a magnetized LAr TPC (left) and a magnetized straw-tube tracker with embedded high-pressure Ar gas targets (right)	54
3-15	View of the Far Detector showing the building, overburden and access regions (left). 3D view of the detector showing the two modules and the orientaiton with the neutrino beam(right).	56
3-16	TPC modular construction concept	57
3-17	Layout of the 34 kT LAr detector hall at the 4850 foot level of Homestake Mine (yellow). A possible layout for an additional 34 kT LAr module is shown next to the LBNE module.	60
3-18	Schematic of the 34 kT LAr-TPC design.	61
3-19	Conceptual 4850 LBNE exploration program	62
4-1	The unoscillated spectrum of ν_μ events from the LBNE beam (black histogram) overlaid with the oscillation probabilities for different values of δ_{cp} as colored curves.	65
4-2	Event displays of beam interactions in an LArTPC	68

4-3	PANDORA's two-dimensional clusterings of hits created by the particles in two charged-current neutrino interactions in liquid argon. Panel (a) shows a 4 GeV ν_e interaction, and panel (b) shows an 18 GeV ν_μ interaction. The colors indicate the clusters into which PANDORA has divided the hits, and the particle labels have been added by hand.	72
4-4	Distributions of the residuals between the reconstructed and the Monte Carlo true locations of primary vertices in neutrino interactions in the MicroBooNE geometry using the LBNE beam spectrum. The x axis is oriented along the drift field, the y axis is parallel to the collection-plane wires, and the z axis points along the beam direction.	73
4-5	Distribution of ν_τ transverse momentum.	76
4-6	Selection of ν_e appearance candidates in a LArTPC	77
4-7	Selection of ν_μ appearance candidates in a LArTPC	77
4-8	Selection efficiency for ν_e appearance in a LArTPC	78
4-9	Selection efficiency for ν_μ appearance in a LArTPC	79
4-10	Disappearance spectra in an LArTPC	81
4-11	Event spectra of neutrino interactions in an LArTPC	82
4-12	Sensitivity to MH and CP-violation in a 10 kiloton LArTPC	85
4-13	Mass hierarchy and CP-violation in LBNE with increased exposure in mass, beam power and time	87
4-14	CP-violation in LBNE with increased exposure in mass, beam power and time - Project X phasing	88
4-15	Measurement of the mixing parameters from Fogli et. al.	89
4-16	Measurement of θ_{23} and Δm_{31}^2 with LBNE 10	90
4-17	Sensitivity of LBNE to the determination of the θ_{23} octant.	91
4-18	Sensitivity of LBNE to the determination of the θ_{23} octant with later phases and Project X upgrades.	92
4-19	Measurement of δ_{cp} and θ_{13} in LBNE with different exposures.	94
4-20	The expected 1σ resolution on different 3-flavor oscillation parameters as a function of exposure in a 700kW beam. The red curve is the precision that could be obtained from LBNE alone, and the blue curve represents the combined precision from LBNE and the T2K and NO ν A experiments. The plots are clockwise from top left: δ_{cp} , $\sin^2 2\theta_{13}$, $ \Delta m_{31}^2 $, and $\sin^2 \theta_{23}$. The width of the bands represents the range of performance with the beam improvements under consideration.	95
4-21	Resolution on δ_{cp} in LBNE and other experiments	97
4-22	Reconstructed L/E Distribution of 'High Resolution' μ -like atmospheric neutrino events in a 350 kt-yr exposure with and without oscillations (top), and the ratio of the two (bottom), with the shaded band indicating the size of the statistical uncertainty.	101
4-23	Reconstructed zenith angle distributions in several ranges of energy for the FC e-like, FC μ -like, and PC μ -like samples. The small contributions from NC backgrounds and tau appearance are also shown.	102

4-24	Reconstructed zenith angle distributions for 6-10 GeV events in the FC e-like, FC μ -like, and PC μ -like samples. Top plots show the expected distributions for no oscillations (black), oscillations with normal mass hierarchy (blue), and inverted hierarchy (red). The ratio of the normal and inverted hierarchy expectations to no oscillations are shown for each category in the bottom plots.	102
4-25	Sensitivity of 350 kt-yr of atmospheric neutrino data to the mass hierarchy as a function of δ_{CP} for true and inverted hierarchy and different values of \sin^2_{23}	104
4-26	Sensitivity to mass hierarchy using atmospheric neutrinos	104
4-27	Sensitivity to octant and CPV using atmospheric neutrinos.	105
4-28	Sensitivity to mass hierarchy using atmospheric neutrinos combined with beam neutrinos	106
4-29	Sensitivity to octant and CPV using atmospheric neutrinos combined with beam neutrinos.	106
4-30	Sensitivity to non-standard interactions	108
4-31	Long-range Interactions in LBNE	109
5-1	The mass hierarchy (top) and CP violation (bottom) sensitivities as a function of exposure in kton-years. The band represents the range of signal and background normalization errors.	113
5-2	The mass hierarchy (top) and CP violation (bottom) sensitivities from shape, rate, and shape+rate. The sensitivity is for a 10 kton detector, 700kW beam, $5+5 \nu + n\bar{u}$ years.	114
5-3	Feynman diagrams for the three main Neutral Current processes	120
5-4	Expected sensitivity to $\sin^2 \theta_W$ from the LBNE ND for a 700 kW beam	124
5-5	Sensitivity of NC/CC to strange contribution to spin of nucleon	126
5-6	Feynman diagrams pertaining to sterile neutrinos	134
5-7	Production mechanisms for dark matter at neutrino beam experiments.	137
5-8	Expected number of neutral current-like events from DM scattering	138
6-1	Isolated Kaon observed during the ICARUS test run at Pavia	141
6-2	Proton decay lifetime limit for $p \rightarrow K^+ \bar{\nu}$ as a function of time	143
7-3	Supernova neutrino event rates in 17 kton of argon for a core collapse at 10 kpc, for the GKVM model [1] (events per 0.5 MeV), showing three relevant interaction channels. Left: interaction rates as function of true neutrino energy. Right: "smeared" rates as a function of detected energy, assuming resolution from reference [2].	147
7-4	Comparison of total event rates for normal and inverted hierarchy, for a specific flux example, for a water Cherenkov detector (left) and for a 17 kt LAr (right) configuration, in events per 0.5 MeV. There are distinctive features in LAr for different neutrino mass hierarchies for this supernova model.	148

7-5	Observed ν_e spectra in 34 kton of LAr for a 10 kpc core collapse, representing about one second of integration time each at one second intervals during the supernova cooling phase. The solid line represents the best fit to a parameterized pinched-thermal spectrum. Clear “non-thermal” features in the spectrum that change with time are visible, on the left at around 20 MeV and on the right at around 35 MeV. Error bars are statistical. These features are present <i>only</i> for normal mass hierarchy. – <i>checking with AF, JJC, HD whether OK to use this plot in the document</i>	149
7-6	Average ν_e energy from fit to SNOwGLoBES-smeared pinched-thermal spectrum as a function of time, for a flux model based on [3] and including collective oscillations, for two different hierarchy assumptions (34 kton at 10 kpc). The bands represent 1σ error bars from the fit. The solid red line is the truth $\langle E_\nu \rangle$ for the unoscillated spectrum. This plot shows that there is meaningful information to be obtained by tracking ν_e spectra as a function of time. – <i>checking with AF, JJC, HD</i>	150
7-7	Left: raw event display of a typical 20-MeV event in the LBNE 10-kton geometry; the top panel shows the collection plane, and the lower two panels show the induction planes (with multiple images due to wire wrapping). Right: zoom of collection plane image.	151
8-1	Measurements of the solar MSW transition	155
8-2	^{40}Cl production rates in a 10 kton detector produced by (n,p) reaction as a function of depth.	156
9-1	Evolution of LBNE CPV sensitivity in one scenario	159

DRAFT

List of Tables

2-1	Best fit values of the neutrino mixing parameters in the PMNS matrix	18
3-1	Principal parameters of LBNE10 as defined at CD-1	39
3-2	The current and future experimental research programs planned for the Fermilab accelerator complex.	47
3-3	Impact of the beam upgrades on the neutrino $\nu_\mu \rightarrow \nu_e$	52
4-1	Raw ν oscillation event rates at the LBNE far site with $E_\nu < 10$ GeV. Assumes 1.7×10^7 seconds/year (Fermilab). Oscillation parameters used are: $\theta_{12} = 0.587$, $\theta_{13} = 0.156$, $\theta_{23} = 0.670$, $\delta m^2 = 7.54 \times 10^{-5} eV^2$, and $\Delta m^2 = 2.47 \times 10^{-3} eV^2$. The NC event rate is for events with visible energy > 0.5 GeV. The rate is given for an exposure of 50 kt.yrs. For comparison, the rates at other neutrino oscillation experiments (current and proposed) are shown for similar exposure in mass and time. Note that for the first 2 stages of the neutrino factory (NF) the beam power requires Project stage 1 and 2 and is higher than that assumed for LBNE. The duty factor for the JPARC beam is $\sim 1/3$ of NuMI/LBNE. There are no detector effects included.	67
4-2	Range of detector efficiencies and background rejection based on handscan studies	80
4-3	Expected number of ν oscillation signal and beam background events at LAr-FD	83
4-4	Summary of achieved systematic error performance in several select prior $\nu_\mu \rightarrow \nu_e$ oscillation experiments. These numbers were extracted from publications to the best of our ability and may not correspond exactly to the description in the text. NBB indicates a narrow band beam and WBB indicates a wide-band beam. No ND indicates there was no near detector, and ND-FD indicates a two detector experiment with extrapolation of the expected background and signal from the near to the far detector.	84
4-5	Summary of 10kton sensitivities	86

4-6	Summary of the oscillation measurements with different configurations given $\theta_{13} = 8.8^\circ, \theta_{23} = 40^\circ, \Delta m_{31}^2 = +2.27 \times 10^{-3} \text{eV}^2$. The fraction of δ_{cp} values for which the mass hierarchy (MH) or CP violation (CPV) are determined with 3σ sensitivity are given in the first 2 columns. For the first 2 columns, all correlations and uncertainties on the known mixing parameters, as well as consideration of the opposite mass hierarchy hypothesis, are included. The measurements assume 5 years of neutrino running and 5 years of anti-neutrino running at a beam power of 708kW with 6×10^{20} protons-on-target accumulated per year with a LAr-TPC. We assume NO ν A will run for a minimum of 3+3 years with the NuMI ME energy beam (NO ν A I). We assume 5×10^{21} protons-on-target total accumulated by T2K (~ 6 yrs) in neutrino only mode. * These measurements are for the combination of neutrino and anti-neutrino running. NOTE: WILL BE UPDATED WITH POST RECONFIG RESULTS	96
4-7	Expected event rates in 100 kton-yr for the Bartol flux and GENIE Argon cross sections (no oscillations).	99
4-8	Detector performance assumptions for the atmospheric neutrino and the combined atmospheric+beam neutrino analyses.	100
4-9	Systematic errors included in the atmospheric and beam+atmospheric neutrino analysis. The beam values assume the existence of a near detector. Atmospheric spectrum ratios include the combined effect of flux and detector uncertainties (e.g. the up/down flux uncertainty as well as the uncertainty on the detector performance for the up/down ratio). The atmospheric spectrum shape uncertainty functions are applied separately for $\nu_\mu, \nu_e, \bar{\nu}_\mu, \bar{\nu}_e$	103
5-1	Estimated ν_μ production rates for argon targets per ton for 1×10^{20} POT at 670 m assuming neutrino cross sections predictions from NUANCE [?] and a 120 GeV proton beam. Processes are defined at the initial neutrino interaction vertex and thus do not include final state effects. These estimates do not include detector efficiencies or acceptance [?,?].	111
5-2	The exposures required to reach 3 and 5σ sensitivity to CP violation for at least 50% of all possible values of δ_{cp} as a function of systematic uncertainties. The resolution on δ_{cp} is also shown.	115
5-3	Precisions achievable from in situ ν_μ and ν_e flux measurements	119
5-4	Uncertainties on the \mathcal{R}^ν measurement, NuTeV vs LBNE	122
5-5	Coefficients entering Equation 5.9 for NC elastic scattering	125
5-6	Expected proton range for the low-density ($\rho \sim 0.1 \text{ g/cm}^3$) tracker	127
7-1	Event rates for different models in 17 kt of LAr for a core-collapse at 10 kpc. Event rates will simply scale by active detector mass.	147

1 Introduction and Executive Summary

In this document, we describe the science opportunities and capabilities of LBNE, the Long-Baseline Neutrino Experiment. LBNE has been developed to provide a unique and compelling program for the exploration of key questions at the forefront of particle physics. Chief among the discovery opportunities it will enable are observation of CP symmetry violation in neutrino mixing, determination of the neutrino mass hierarchy, searches for nucleon decay signatures, and detailed studies of neutrino bursts from galactic supernovae. To fulfill these and other goals as a world-class facility, LBNE is conceived around four central components: (1) a new, intense wide-band neutrino source at Fermilab, (2) a fine-grained ‘near’ neutrino detector just downstream of the source, (3) the Sanford Underground Research Facility (SURF) in Lead, South Dakota at an optimal distance (~ 1300 km) from the neutrino source, and (4) a massive liquid argon time-projection chamber (LArTPC) deployed there as a ‘far’ detector. No other initiative with similar science goals is nearly as advanced in terms of engineering development, project planning and financial support.

Neutrinos are the most abundant known particles with mass in the universe; understanding their nature is an essential goal for particle physics. The observation of CP violation in the lepton sector, while groundbreaking on its own, would provide an experimental underpinning for the basic idea of leptogenesis as an explanation for the baryon asymmetry of the universe. Resolution of the neutrino mass hierarchy would have significant theoretical, cosmological and experimental implications. While strong indications for one hierarchy or the other are possible for favorable values of the CP phase δ_{CP} in the upcoming generation of beam, reactor and atmospheric neutrino experiments, the long baseline of LBNE enables a decisive determination independent of δ_{CP} . LBNE will also extend the precision with which many oscillation parameters (mixing angles and squared-mass differences) are known. Such information, for example, whether the PMNS angle θ_{23} is either distinct from, or very close to maximal, will yield major clues for those aiming to understand the origin of quark and lepton flavor. Taken together, the above suite of measurements will thoroughly test the three neutrino-flavor paradigm that guides our current understanding, and will provide greatly extended sensitivity to signatures for non-standard neutrino interactions in matter. In the arena of non-accelerator physics, the observation of nucleon decay would be a watershed event for the understanding of physics at high energy scales. Neutrinos from supernovae are expected to provide key insights into the physics of gravitational collapse, and may likewise

1 reveal fundamental properties of the neutrino.

2 The LArTPC technology is unmatched among massive detectors for precise spatial and energy
 3 resolution and for reconstruction of complex neutrino interactions with high efficiency over
 4 a broad energy range. It thus provides a compact, scalable approach to achieve sensitivity
 5 to the oscillation physics goals of LBNE. Although large underground water Cherenkov
 6 and/or scintillator-based detectors with specific strengths within non-accelerator physics
 7 may be operating in parallel, the LBNE far detector has unique capabilities here as well.
 8 For example, it is especially well suited for challenging proton decay modes such as the
 9 SUSY-favored $p \rightarrow K^+ \bar{\nu}$ mode, with high detection efficiency and background rejection
 10 sufficient to enable a discovery with single well-reconstructed events. Similarly the LArTPC
 11 technology opens up an avenue to precision studies of oscillation physics with atmospheric
 12 neutrinos. For supernova neutrino detection, liquid argon detectors are primarily sensitive
 13 to ν_e interactions, which is complementary to water and organic scintillator-based detectors
 14 in which $\bar{\nu}_e$ interactions are dominant. The highly-capable near detector envisioned will not
 15 only measure the absolute flux and energy scales of the neutrino species required for the
 16 oscillation parameter measurements, but will enable a broad range of precision neutrino
 17 interaction measurements.

18 The unique combination of exceptional detector resolution, large target mass and deep under-
 19 ground location also opens the possibility of discovery of entirely unanticipated phenomena
 20 – history has repeatedly shown Nature’s ability to reward leading-edge instruments with
 21 unexpected signatures of new physics.

22 LBNE is an ambitious experiment whose execution has substantial impact on the overall
 23 direction of High Energy Physics (HEP) in the US. The US Department of Energy has
 24 endorsed the science goals of LBNE, which it envisions as a phased program, and for which
 25 it has given first stage (CD-1) approval with a cap of \$867M towards the initial phase.
 26 The science scope of this and subsequent phases will depend on the level of investment by
 27 additional national and international partners. This document aims to provide an overview
 28 of the LBNE physics program, and how it may evolve, for the US HEP community as it
 29 pursues long-term planning studies [1]. We summarize the physics reach of this program
 30 under scenarios that are consistent with short, medium and long-term considerations.

31 The general conclusions are twofold: (1) a fully realized LBNE will provide an exciting broad-
 32 based physics program with exceptional capabilities for all of the primary physics goals, and
 33 many secondary ones; and (2) a first phase with a 10-kt LArTPC will substantially ad-
 34 vance the field of neutrino oscillation physics while, uniquely, laying the foundations for an
 35 experiment with the ambitious physics program described above in a later phase. In the
 36 following sections, we provide the context for development of LBNE as a phased program
 37 that maintains flexibility for future enhancements in each of its stages through the contribu-
 38 tions of additional partners and summarize the physics reach of LBNE in the corresponding
 39 configurations.

1.1 Development of a World-Class Experiment

The concept of a high intensity neutrino beam directed toward a distant massive underground detector to simultaneously investigate the nature of the neutrino, proton decay and neutrinos from astrophysical sources has been under serious investigation since the late 1990's. Since that time the both the science goals and concepts for implementation have been the subject of intense study and review by distinguished panels including the National Academies Neutrino Facilities Assessment Committee in 2003 [3], the National Science and Technology Council Committee on Science strategic plan for federal research at the interaction of physics and astronomy in 2004 [4], the National Academies EPP2010 panel in 2006 [5], the HEPAP/NSAC Neutrino Scientific Assessment Group in 2007 [6], the HEPAP Particle Physics Project Prioritization Panel (P5) in 2008 [5], the National Academies ad hoc Committee to Assess the Science Proposed for DUSEL in 2011 [8], and most recently the HEPAP Facilities Subpanel in 2013 [6]. High-level studies performed in Europe and Asia have come to similar conclusions.

Long-Term Vision LBNE as described in this document was developed by a collaboration that was formally established in 2009 and which currently comprises 377 collaborators from 62 institutions in five countries. Fermi National Accelerator Laboratory recognized LBNE as a central part of its long-term future planning and in January 2010 the US Department of Energy (DOE) formally recognized the LBNE science goals with approval of the mission need statement (CD-0) [7], this action establishing LBNE as a DOE project. It should be noted that it has taken more than a decade to reach this stage.

The central role of LBNE within the US particle physics program is also recognized in other documents prepared for the current community planning exercise [1], including the Project X Physics Book [8], and the reports from Intensity Frontier working groups on neutrino physics [9] and baryon number violation [12].

To pursue the transformative physics goals of LBNE in an era of highly constrained funding for basic research in the US, the conceptual design has evolved so as to provide a flexible and cost-effective approach to the science that maintains a world leadership role over the long term. The full scope LBNE detectors are defined as a 50-kt (34-kt fiducial) LArTPC in a new experimental hall to be excavated at the 4850L of the Homestake Mine at SURF (much larger detectors could be accommodated), and a fine-grained near neutrino detector located on the Fermilab site. Simultaneous construction of a new neutrino beam line at Fermilab would permit initial operations with 60 – 120 GeV protons extracted from the Main Injector at 700 kW of beam power. In anticipation of Project X [8], the beam line is designed to be upgradable to accommodate 2.3 MW. The 1300 km baseline is optimized for the neutrino oscillation program, as described in this and other documents. The shielding of cosmic rays provided by the deep underground far detector site enables the non-accelerator portion of the physics program, including nucleon decay searches, sensitive studies of neutrino bursts from galactic supernovae, and precision analyses of atmospheric neutrino samples.

With the choice of far detector technology and underground location, the overall physics reach of LBNE is dominantly limited by detector mass. From the outset, a guiding principle of the far detector design has been scalability. The conceptual design for the LBNE far detector consists of two identical 25-kt (17-kt fiducial) TPC modules housed within separate vessels (cryostats) exploiting technology developed by the liquefied natural gas (LNG) storage and transport industry. The TPC modules themselves consist of arrays of modular anode and cathode plane assemblies (APA's and CPA's) that are suspended from rails affixed to the top of the cryostats. The APA/CPA dimensions are chosen for ease of transportation and installation. Larger detector masses can be achieved by increasing the vessel size and installing additional APA/CPA units, thereby exploiting economies of scale and benefiting from increased volume to surface area ratio. Detector mass may also be increased after completion of the first phase through additional distinct detectors of the same or different technology.

Reconfiguration and CD-1 Approval Since DOE CD-0 approval, the conceptual design for the fully realized LBNE configuration described above has been reviewed several times, most recently at a Fermilab Director's CD-1 Readiness Review in March 2012 [13]. Contemporaneous with this review, however, cost considerations led the DOE to request a plan for implementing LBNE as a phased project, with a cap on the initial configuration cost (now stated as \$867M). An independent panel was established to review reconfiguration options that included consideration of using the existing neutrino beamline along with new massive detectors at the existing Soudan and Ash River sites. The recommendation of this panel [14] led to a Phase-I configuration that we refer to as 'LBNE10'. This configuration maintains the most important aspects of the first phase of the full scope LBNE: the 1300 km baseline to the Sanford Underground Research Facility (SURF) located at the Homestake Mine and the large LArTPC far detector. However, to fit within the first phase DOE investment cap, the far detector was reduced in mass to 10 kt and relocated to a surface site at SURF, and construction of the near neutrino detector was deferred. The conceptual design for this configuration [15] was reviewed in Fall 2012, leading to DOE CD-1 approval [16] in December 2012.

It is important to note that the DOE CD-1 approval document explicitly allows that the LBNE Phase-I scope can be adjusted in advance of CD-2 should additional sources of funding be identified. *Using the CD-1 DOE funding as the foundation, the goal for the first phase of LBNE is an underground far detector of at least 10 kt and a highly capable near detector.* This goal has been endorsed by the collaboration, the project, the Fermilab directorate, and the DOE Office of High Energy Physics. Since a large portion of the LBNE10 project cost is in civil infrastructure (\sim \$500M) incremental funding from partners could have considerable impact on restoring physics scope in the first phase.

Global Partnerships Global conditions are favorable for significant contributions to LBNE. As an example, the 2013 update [17] of the European Strategy for Particle Physics discusses long-baseline neutrino physics among the highest-priority large-scale activities for Europe requiring "significant resources, sizeable collaborations and sustained commitment", with

1 the primary recommendation of exploring “the possibility of major participation in leading
2 long-baseline neutrino projects in the US and Japan.” At present the LBNE Collaboration
3 includes institutions from India, Italy, and the United Kingdom. Discussions with a number
4 of potential international partners are under way, some of these already at an advanced stage.
5 A summary of progress to date in these discussions can be found in the recent presentation
6 of LBNE status to the Fermilab Program Advisory Committee in June 2013 [18].

7 To reflect the physics reach of various phasing scenarios, we present many of the sensitivities
8 for the accelerator neutrino based topics as functions of exposure, defined as the product of
9 detector mass, beam power and run time. However, we explicitly highlight the capabilities
10 of both the surface 10-kt Phase-I configuration and the 34-kt underground detector, both
11 operating at 700 kW. Since the community planning exercise looks beyond the present decade,
12 we also present the long-term physics impact of a fully realized LBNE operating with the
13 beam power anticipated with the full implementation of Project X.

DRAFT

1.2 Summary of Key LBNE Physics Sensitivities

In this section we summarize the reach of LBNE toward its primary physics goals based on our current understanding of (1) the experimental landscape, (2) scenarios for staging LBNE as described above, and (3) the technical capabilities of LBNE at each stage. A detailed description of the physics goals of LBNE is provided in the main text of this document and in the LBNE Project controlled documents database [19]. A comprehensive study of the physics potential of the fully realized LBNE (including both LArTPC and water Cherenkov Detector (WCD) options for the far detector) is documented in a October 2011 collaboration report [20]. Key features of the LBNE10 physics program are documented in the introductory volume (Vol. 1) of the October 2012 LBNE Conceptual Design Report (CDR) [15].

1.2.1 Long-Baseline/Oscillation Physics

Neutrino Mass Hierarchy. A key strength of LBNE is the matter effect due to the 1300 km baseline, which leads to a large discrete asymmetry in the $\nu_\mu \rightarrow \nu_e$ versus $\bar{\nu}_\mu \rightarrow \bar{\nu}_e$ oscillation probability comparison, the sign of which depends on the mass hierarchy. At 1300 km this asymmetry is larger than the CP-violating effect associated with δ_{CP} , meaning that both the mass hierarchy and δ_{CP} can be determined unambiguously within the same experiment, which is not the case for much shorter baselines. For the mass hierarchy, the most recent studies indicate that LBNE on its own can distinguish between normal and inverted hierarchy at 3σ significance or better for all values of δ_{CP} with less than 10 years of operation of an underground 10-kt far detector at 700 kW beam power coupled with concurrent analysis of the corresponding atmospheric neutrino samples.* For half of the range of possible δ_{CP} values (which half depends on the actual hierarchy), the significance is at the level of 5σ or better. For context, we note that even at four times its nominal exposure (of six years of operation at 700 kW), an extended NOvA program [21] would have coverage at the 3σ level or better for only 40% of the δ_{CP} range.

CP Violation and the Measurement of δ_{CP} . The LBNE program has two somewhat distinct goals with regard to CP symmetry violation in the $\nu_\mu \rightarrow \nu_e$ oscillation channel. First, LBNE aims to make a precise determination of the value of δ_{CP} within the context of the standard 3-flavor mixing scenario described by the PMNS matrix. Second, and perhaps more significantly, LBNE aims to observe a signal for leptonic CP violation, independent of the underlying nature of neutrino oscillation phenomenology. Within the standard 3-flavor mixing scenario such a signal will be observable, provided δ_{CP} is not too close to one of the values (0 and π) for which there is no CP violation. Together, the pursuit of these two goals provides a test of the standard 3-flavor picture.

*Exploitation of atmospheric neutrino interactions in a surface detector may also be possible. However, even without this, a 10-kt LArTPC on the surface can reach this level of coverage by incorporating constraints from NOvA and T2K data.

Figure 1-1 shows the expected $1\text{-}\sigma$ resolution for δ_{CP} as a function of exposure for 700 kW proton beam power. We see that 10-kt far detector will be able to measure δ_{CP} to $\pm 20^\circ$ – 30° (depending on its value), independent of other experiments, in a ten-year run on the surface at 700 kW. A fully realized LBNE operating with Project X in a later phase, will achieve a precision of less than $\pm 10^\circ$, comparable to the current precision on the CP phase in the CKM matrix of the quark sector.

For the second goal, a 10-kt LArTPC will, by itself, be able to cover between 40% and 50% of the range of δ_{CP} values at 3σ significance or better in a ten-year run on the surface at 700 kW. To reach 5σ for an appreciable fraction of the range of δ_{CP} , a fully realized LBNE, including a near neutrino detector, will be needed to control systematic errors while accumulating large enough samples in the far detector to reach this level of sensitivity. Note that no experiment can cover at 100%, since CP violation effects vanish as $\delta_{CP} \rightarrow 0$ or π .

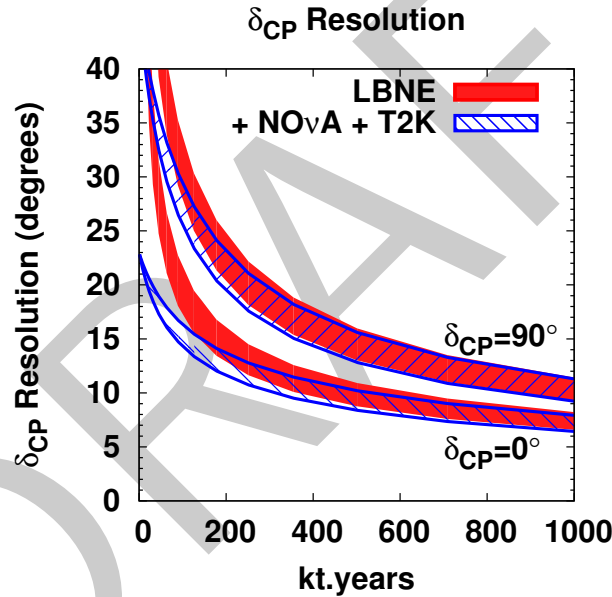


Figure 1-1: The expected $1\text{-}\sigma$ resolution for δ_{CP} as a function of exposure for 700 kW proton beam power. The red curve is the precision that could be obtained from LBNE alone, and the blue curve represents the combined precision from LBNE and the T2K and NO ν A experiments.

Determination of $\sin^2 2\theta_{23}$ and Octant Resolution. In long-baseline experiments with ν_μ beams, the ν_μ disappearance and ν_e appearance signals depend on the mixing angle θ_{23} dominantly in proportion to $\sin^2 2\theta_{23}$ and $\sin^2 \theta_{23}$, respectively, in the standard three-flavor mixing scenario. Current ν_μ disappearance data are consistent with maximal mixing, $\theta_{23} = 45^\circ$. To obtain the best sensitivity to both the magnitude of a deviation of θ_{23} from 45° as well as its sign (θ_{23} octant), a combined analysis of the two channels is needed [27]. As demonstrated in Chapter 4, LBNE10 will be able to resolve the θ_{23} octant at the 3σ level or better for true θ_{23} values less than 40° or greater than 50° , provided δ_{CP} is not too close to zero or π . With a fully realized LBNE, determination of θ_{23} will attain resolution of order

1 1° or less, even for values within a few degrees of 45° .

2 1.2.2 Searches for Baryon Number Violation

3 The LBNE far detector will be competitive for specific nucleon decay modes by virtue of
 4 high detection efficiency and low background rates relative to water Cherenkov detectors.
 5 As an example, LBNE has good capability for the $p \rightarrow K^+ \bar{\nu}$ channel, where predictions
 6 from Supersymmetric Models have lifetimes that extend beyond, but close to, the current
 7 (preliminary) Super-Kamiokande limit of $\tau/B > 5.9 \times 10^{33}$ yr (90% CL) from a 260 kt-
 8 yr exposure [28]. The signature for an isolated semi-monochromatic charged kaon in an
 9 LArTPC is distinctive, with multiple levels of redundancy. A 34-kt LBNE far detector deep
 10 underground will reach a limit of 3×10^{34} yr after 10 years of operation (see Fig. 1-2),
 11 and would see 9 events with a background of 0.3 should τ/B be just around the corner at
 12 1×10^{34} yr. Even a 10-kt detector (placed underground) would have an intriguing signal of
 13 a few events after a 10-year exposure in this scenario.

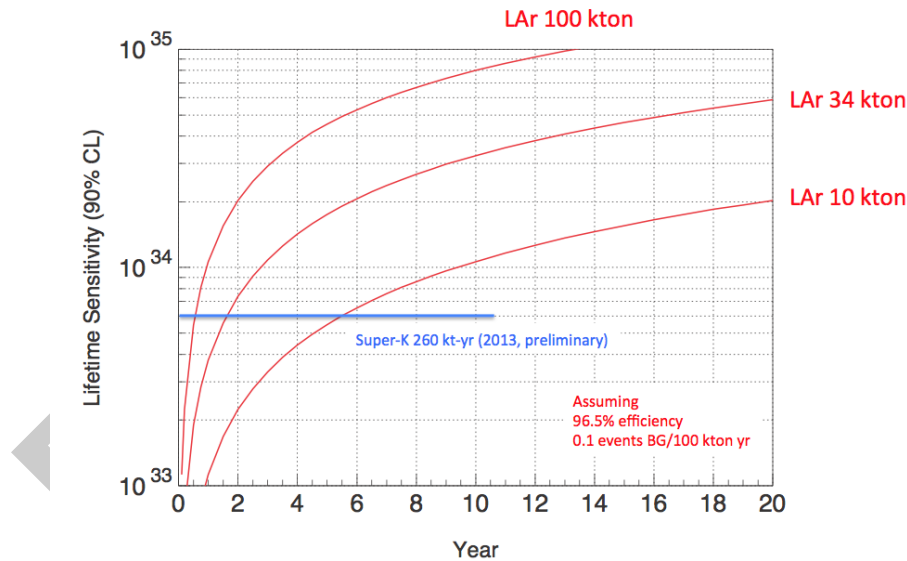


Figure 1-2: Sensitivity to the decay $p \rightarrow K^+ \bar{\nu}$ as a function of time for underground LAr detectors of varying masses

14 1.2.3 Physics and Astrophysics with Supernova Neutrinos

15 The neutrinos from a nearby core-collapse supernova are emitted in a burst of a few tens of
 16 seconds duration, with about half in the first second. Energies are in the few tens of MeV
 17 range, and luminosity is divided roughly equally between flavors. Currently, world-wide sen-
 18 sitivity is primarily to electron anti-neutrinos, via inverse beta decay on free protons, which
 19 dominates the interaction rate in water and liquid-scintillator detectors. LAr has a unique

sensitivity to the *electron neutrino* component of the flux, via the absorption interaction on ^{40}Ar , $\nu_e + ^{40}\text{Ar} \rightarrow e^- + ^{40}\text{K}^*$. In principle, this interaction can be tagged via the de-excitation gamma cascade. About 900 events would be expected in a 10-kton fiducial LAr detector for a supernova at 10 kpc. In the neutrino channel the oscillation features are in general more pronounced, since the initial spectra of ν_e and ν_μ (ν_τ) are always significantly different. A detection of a large neutrino signal in LBNE would help elucidate critical information on key astrophysical phenomena such as 1) the neutronization burst, 2) formation of a black hole 3) shock wave effects 4) shock instability oscillations and 5) turbulence effects.

1.2.4 Physics with a Fine-grained Near Detector.

The near neutrino detector (ND) will provide precision measurements of neutrino interactions which, in the medium to long term, are essential to control the systematic uncertainties in the long-baseline oscillation physics program. The ND, which will include an argon target, will measure the absolute flux and energy-dependent shape of all four neutrino species, ν_μ , $\bar{\nu}_\mu$, ν_e and $\bar{\nu}_e$ to accurately predict for each species the Far/Near flux ratio as a function of energy. It will also measure the 4-vectors of secondary hadrons, such as π^0 , π^+ , π^- , etc., produced in the neutral and charged current interactions that constitute the dominant backgrounds to the oscillation signals.

The near detector will also be the source of data for a rich program of neutrino interaction physics with 100,000 charged-current and 34,000 neutral current interactions per ton, per year, per 10^{20} pot. This corresponds to 10^7 neutrino interactions per year for the range of beam configurations and near detector designs under consideration. Measurement of fluxes, cross sections (to 3%) and particle production over a large energy range of 0.5–50 GeV (which can also help constrain backgrounds to the atmospheric neutrino and nucleon decay) are the key elements of this program. With very high statistics and precision event reconstruction capability, the near detector data can be exploited for sensitive studies of electroweak physics and nucleon structure.

1.3 Concluding Remarks

In this chapter, we have touched only briefly on a portion of the full suite of physics opportunities enabled by LBNE. The following chapters cover these in considerable detail, as well as topics that were omitted here in the interest of brevity and focus. We summarize the key points of this chapter below.

The primary science goals of LBNE are drivers for the advancement HEP in a general sense: questions of broad import – about the origin of flavor and the generation structure of the fermions, what physical mechanism provides the CP violation needed to generate the baryon

1 asymmetry of the universe, and what is the high energy physics that would lead to proton
2 decay. Achieving these goals requires a dedicated, ambitious program. No other proposed
3 long-baseline neutrino oscillation program with the scientific scope and reach of LBNE is
4 as advanced in terms of engineering development and project planning. A phased program
5 with a far detector of even modest size in the initial stage (LBNE10) will enable exciting
6 physics in the intermediate term including definitive mass hierarchy determination and a
7 measurement of the CP phase without ambiguities. If the CP phase is not 0 or π there is
8 good prospect for strong indications ($> 3\sigma$) of leptonic CP violation, while providing the
9 fastest route toward the full LBNE science goals. Global interest is favorable for contributions
10 from international partners to accelerate this program, including enhancements to the LBNE
11 Phase-I scope.

12 Implementing the vision that has brought LBNE to this point will provide a means for
13 continued intellectual leadership for the U.S. within the global HEP community. Finally,
14 although perhaps outside the scope of this document, we also note that the excitement
15 generated by the technical challenges of mounting LBNE as well as the potential physics
16 payoffs is widely felt—including among the young scientists for whom LBNE will provide
17 numerous growth opportunities.

References

- [1] APS Division of Particles and Fields Community Summer Study 2013, <http://www.snowmass2013.org/>.
- [2] DOE Office of Science, Office of High Energy Physics, “Mission Need Statement for a Long Baseline Neutrino Experiment (LBNE) Major System”, LBNE-doc-6259, September 2009, <http://lbne2-docdb.fnal.gov/cgi-bin/ShowDocument?docid=6259>.
- [3] “Neutrinos and Beyond: New Windows on Nature”, The NRC Neutrino Facilities Assessment Committee, The National Academies Press, ISBN 0-309-08716-3, (2003).
- [4] “The Physics of the Universe, a Strategic Plan for Federal Research at the Intersection of Physics and Astronomy”, National Science and Technology Council Committee on Science, February 2004, <http://www.ostp.gov/html/physicsoftheuniverse2.pdf>.
- [5] “Revealing the Hidden Nature of Space and Time: Charting the Course for Elementary Particle Physics”, The National Academies Press, ISBN 0-309-66039-4, (2006).
- [6] “Recommendations to the Department of Energy and the National Science Foundation on a Future U.S. Program in Neutrino Oscillations”, report of the HEPAP/NSAC Neutrino Scientific Assessment Group, July 2007.
- [7] Particle Physics Project Prioritization Panel, “U.S. Particle Physics: Scientific opportunities, a plan for the next ten years”, May 2008, http://www.er.doe.gov/hep/files/pdfs/P5_Report06022008.pdf.
- [8] “An Assessment of the Deep Underground Science and Engineering Laboratory”, The National Academies Press, ISBN 978-0-309-21723-1, (2012).
- [9] “Input to the prioritization of proposed scientific user facilities for the Office of Science”, HEPAP Facilities Subpanel, March 2013.
- [10] A. S. Kronfeld and R. S. Tschirhart, eds., “Project X: Physics Opportunities”, July 2013, <http://projectx-docdb.fnal.gov/cgi-bin/ShowDocument?docid=1199>.

- [11] A. de Gouvea *et al.*, “Neutrinos”, Intensity Frontier Working Group Report, DPF Community Summer Study 2013, posted at <http://www.snowmass2013.org/tiki-index.php?page=Neutrinos>.
- [12] K. S. Babu and E. Kearns, eds., “Baryon Number Violation”, Intensity Frontier Working Group report, DPF Community Summer Study 2013. See <http://www.snowmass2013.org/tiki-index.php?page=Baryon+Number+Violation>.
- [13] Final Report, Director’s Independent Conceptual Design and CD-1 Readiness Review of the LBNE Project, March 2012, <http://lbne2-docdb.fnal.gov:8080/0057/005788/003/FinalReportDirector%27sReviewLBNE2012-03-30.pdf>
- [14] Y.-K. Kim *et al.*, LBNE Reconfiguration Steering Committee Report, August 2012, see http://www.fnal.gov/directorate/lbne_reconfiguration/index.shtml. See also, J. Appel *et al.*, “Physics Working Group Report to the LBNE Reconfiguration Steering Committee”, also posted at the above URL.
- [15] LBNE Conceptual Design Report, October 2012, see <https://sharepoint.fnal.gov/project/lbne/LBNE%20at%20Work/SitePages/Reports%20and%20Documents.aspx>.
- [16] DOE Office of Science, Office of High Energy Physics, “Critical Decision 1: Approve Alternate Selection and Cost Range of the Long Baseline Neutrino Experiment (LBNE) Project at the Fermi National Accelerator Laboratory and Sanford Underground Research Facility”, LBNE-doc-6681, December 2012, <http://lbne2-docdb.fnal.gov/cgi-bin/ShowDocument?docid=6681>.
- [17] The European Strategy for Particle Physics, Update 2013, CERN-Council-S/106, 7 May 2013, <http://council.web.cern.ch/council/en/EuropeanStrategy/ESParticlePhysics.html>.
- [18] R. J. Wilson, “LBNE Collaboration Status”, presentation to the Fermilab Program Advisory Committee, June 2013, http://www.fnal.gov/directorate/program_planning/June2013PACPublic/LBNECollabStatus_PAC_June2013.pdf.
- [19] The LBNE Project, “Physics Research Goals of the LBNE Project”, LBNE-doc-3056v8, January 2013, <http://lbne2-docdb.fnal.gov/cgi-bin/ShowDocument?docid=3056>.
- [20] T. Akiri *et al.* (LBNE Collaboration), “The 2010 Interim Report of the Long-Baseline Neutrino Experiment Collaboration Physics Working Groups”, arXiv:1110.6249 [hep-ex], 2011.
- [21] M. Messier, for the NOvA Collaboration, “Extending the NOvA Physics Program”, Whitepaper submitted to the Neutrino Working Group of the DPF Community Summer Study 2013, January 2013, <http://if-neutrino.fnal.gov/whitepapers/messier-nova.pdf>
- [22] K. Abe *et al.* (T2K Collaboration), Phys. Rev. Lett. **107**, 041801 (2011).

- 1 [23] P. Adamson *et al.* (MINOS Collaboration), Phys. Rev. Lett. **107**, 181802 (2011).
2 [24] Y. Abe *et al.* (Double Chooz Collaboration), Phys. Rev. D **86**, 052008 (2012).
3 [25] F. P. An *et. al* (Daya Bay Collaboration), Phys. Rev. Lett. **108**, 171803 (2012).
4 [26] J. Ahn *et al.* (RENO Collaboration), Phys. Rev. Lett. **108**, 191802 (2012).
5 [27] P. Huber and J. Kopp, JHEP **1103**, 013 (2011).
6 [28] E. Kearns, “Future Experiments for Proton Decay”, presentation at ISOUPS (Inter-
7 national Symposium: Opportunities in Underground Physics for Snowmass), Asilomar,
8 May 2013.

DRAFT

2 Overview of the LBNE Science Program

In this chapter, we describe the science underlying the LBNE research program. We begin by listing the primary and secondary physics objectives adopted by the LBNE Project and Science Collaboration (Sec. 2.1). We then turn to a discussion of the physics underlying the primary objectives to place the role of LBNE in context and to provide motivation for the selection of its key design features. Specifically we cover neutrino oscillation physics in Sec. 2.2, the physics of nucleon decay in Sec. 2.3, and the physics of neutrino emission from core-collapse supernovae in Sec. 2.4. Scientific background on other research areas are described together with the corresponding LBNE sensitivities in later chapters of this document.

2.1 Primary and Secondary Science Objectives

The following discussion of LBNE science objectives is adapted from the LBNE CDR [10]. The LBNE Science Collaboration, working with LBNE Project Management, has developed a prioritized set of research goals for the full implementation of LBNE, which was approved by the then LBNE Project Director, the LBNE Collaboration Co-Spokespersons, the Fermilab Director, and the LBNE Federal Project Director. This set of goals is presented in Version 1.0 of “Physics Research Goals of the LBNE Project” [11].

The goals for the full LBNE program have not changed as a result of a phased implementation of the program. However, not all of the goals of the full program can be achieved in the first phase. Here we present the full set of research goals, specifying which goals will be addressed by the LBNE **Project** in its nominal (LBNE10) initial phase (in normal font), and which ones can only be addressed by subsequent phases of the LBNE *Program* (in italics) absent resources to expand scope in Phase-I. This same information is presented in the current version of the “Physics Research Goals of the LBNE Project” [12].

The **primary objectives** of LBNE, in priority order are the following experiments:

1. precision measurements of, the parameters that govern $\nu_\mu \rightarrow \nu_e$ oscillations; this in-

cludes precision measurement of the third mixing angle θ_{13} , measurement of the CP violating phase δ_{CP} , and determination of the mass ordering (the sign of Δm_{32}^2).

2. precision measurements of θ_{23} and $|\Delta m_{32}^2|$ in the ν_μ -disappearance channel.
3. *search for proton decay, yielding significant improvement in the current limits on the partial lifetime of the proton (τ/BR) in one or more important candidate decay modes, e.g. $p \rightarrow e^+\pi^0$ or $p \rightarrow K^+\nu$.*
4. *detection and measurement of the neutrino flux from a core-collapse supernova within our galaxy, should one occur during the lifetime of LBNE.*

Of these, the first two can be addressed within the present LBNE Phase-I scope, and the configuration of LBNE10 is set to maximize the effectiveness of the facility to achieve them. *The second two require a deep underground location for the Far Detector, and can only be addressed in the initial phase should resources be identified to enable this.*

Secondary objectives, which may be enabled by the facility that is designed to achieve the primary objectives include:

1. other accelerator-based neutrino-oscillation measurements.
2. *measurements of neutrino-oscillation phenomena using atmospheric neutrinos.*
3. *measurement of other astrophysical phenomena using medium-energy neutrinos.*

The first of these can be addressed within the present LBNE Phase-I scope, and will be considered in determining the configuration of LBNE in this phase only if investment to enable these measurements does not compromise the ability to achieve the primary objectives. *Secondary objectives 2 and 3 most likely require a deep underground location for the Far Detector, and would be best addressed in a subsequent phase of LBNE absent resources to enable this in the initial phase.*

Additional secondary objectives, the achievement of which may require upgrades to the facility that is designed to achieve the primary physics objectives, include:

1. *detection and measurement of the diffuse supernova-neutrino flux.*
2. *measurements of neutrino-oscillation phenomena and of solar physics using solar neutrinos.*
3. *measurements of astrophysical and geophysical neutrinos of low energy.*

All of the additional secondary objectives require a deep underground location for the Far Detector, and can only be addressed in a subsequent phase of LBNE absent resources to enable this in the initial phase.

Additionally, research objectives of the near neutrino detector have also been identified. In the interest of maintaining focus here, we defer the discussion of these to Chapter ??.

2.2 Neutrino Oscillations, CP Violation and the Three-Flavor Model

The Standard Model of particle physics presents a remarkably accurate description of the elementary particles and their interactions, but the proliferation of particles, flavors and generations imply that the current model is incomplete and that a more fundamental underlying theory must exist. Results from the last decade, that the three known types of neutrinos have nonzero mass, mix with one another and oscillate between generations, implies physics beyond the Standard Model [13] and the possible presence of mass scales beyond that in the current model.

2.2.1 Probing the Mass Hierarchy, CP Violation, and Three-Flavor Mixing with the $\nu_\mu \rightarrow \nu_e$ Oscillation Mode in a ν_μ Beam Experiment

2.2.1.1 Characterization of Three-Flavor Mixing

The three-flavor-mixing scenario for neutrinos can be described by a rotation between the neutrino weak interaction eigenstate basis (ν_e, ν_μ, ν_τ) and the basis of states of definite mass (ν_1, ν_2, ν_3). In direct correspondance with mixing in the quark sector, the transformations between basis states is expressed in the form of a complex unitary matrix that in full generality depends on just three mixing angles and a CP-odd phase. For neutrino mixing, this matrix is known as the PMNS matrix, and the mixing angles and phase are designated as $(\theta_{12}, \theta_{23}, \theta_{13})$, and δ_{CP} . The frequency of neutrino oscillation also depends on the difference in the squares of the neutrino masses, $\Delta m_{ij}^2 = m_i^2 - m_j^2$; three neutrinos implies two independent mass-squared differences (Δm_{21}^2 and Δm_{32}^2).

The PMNS matrix can be parameterized as the product of three 2-flavor mixing matrices as follows:

$$U_{PMNS} = \underbrace{\begin{pmatrix} 1 & 0 & 0 \\ 0 & c_{23} & s_{23} \\ 0 & -s_{23} & c_{23} \end{pmatrix}}_{\text{I}} \underbrace{\begin{pmatrix} c_{13} & 0 & e^{i\delta_{CP}} s_{13} \\ 0 & 1 & 0 \\ -e^{i\delta_{CP}} s_{13} & 0 & c_{13} \end{pmatrix}}_{\text{II}} \underbrace{\begin{pmatrix} c_{12} & s_{12} & 0 \\ -s_{12} & c_{12} & 0 \\ 0 & 0 & 1 \end{pmatrix}}_{\text{III}} \quad (2.1)$$

1 where $c_{\alpha\beta} = \cos \theta_{\alpha\beta}$ and $s_{\alpha\beta} = \sin \theta_{\alpha\beta}$.

2 The three-flavor-mixing scenario for neutrinos is now well established albeit with a precision
 3 much worse than that of the corresponding mixing in the quark sector, and with several key
 4 parameters undetermined. In addition, several recent anomalous experimental results count
 5 among their possible interpretations phenomena that do not fit in this model. It is clear that
 6 full elucidation of neutrino mass and mixing phenomenology is an imperative for HEP for
 7 the coming years.

8 Specifically, the entire complement of neutrino experiments to date has measured five of the
 9 mixing parameters: three angles, θ_{12} , θ_{23} , and recently θ_{13} , and two mass differences, Δm_{21}^2
 10 and Δm_{32}^2 . The sign of Δm_{21}^2 is known, but not that of Δm_{32}^2 , which (since it is larger in
 11 magnitude) is the origin of the mass hierarchy ambiguity: the case of $\Delta m_{32}^2 > 0$ is known as
 12 the ‘normal hierarchy’, while $\Delta m_{32}^2 < 0$ is referred to as the ‘inverted hierarchy’ case. The
 13 values of θ_{12} and θ_{23} are large, while θ_{13} has been determined to be macroscopic but smaller
 14 than the other two mixing angles [25]. This pattern suggests that mixing is qualitatively
 15 different in the neutrino and quark sectors.

16 Illustrating this difference, the moduli of the entries of the CKM mixing matrix for quarks
 17 can be expressed in approximate form as

$$|V_{\text{CKM}}| \sim \begin{pmatrix} 1 & 0.2 & 0.004 \\ 0.2 & 1 & 0.04 \\ 0.008 & 0.04 & 1 \end{pmatrix}, \quad (2.2)$$

18 while those of the entries of the PMNS matrix are given by

$$|U_{\text{PMNS}}| \sim \begin{pmatrix} 0.8 & 0.5 & 0.2 \\ 0.4 & 0.6 & 0.7 \\ 0.4 & 0.6 & 0.7 \end{pmatrix}. \quad (2.3)$$

19 To quote the discussion in Ref. [9], “while the CKM matrix is almost proportional to the
 20 identity matrix plus hierarchically ordered off-diagonal elements, the PMNS matrix is far
 21 from diagonal and, with the possible exception of the U_{e3} element, all elements are $\mathcal{O}(1)$.”
 22 These data are already proving crucial in the quest for finding a relationship between quarks
 23 and leptons and their seemingly arbitrary generation structure. Any organizing principle
 24 such as a unification model leads to testable predictions such as sum rules between CKM
 25 and PMNS parameters [9]. [13,14].

26 We now display the above comparison in terms of the fundamental parameters, and the
 27 limited precision with which they are determined, in Table 2-1, where a global fit [15] to
 28 existing results from experiments sensitive to neutrino oscillation effects is the source for
 29 the neutrino mixing parameter values. To some degree, the results of global fit highlight the
 30 limited precision of the determination of parameters in the lepton sector.

Table 2–1: Best fit values of the neutrino mixing parameters in the PMNS matrix (assumes normal hierarchy) and comparison to the equivalent values in the CKM matrix from [15,16]. ΔM^2 is defined as $m_3^2 - (m_1^2 + m_2^2)/2$.

Parameter	Value (neutrino PMNS matrix)	Value (quark CKM matrix)
θ_{12}	$34 \pm 1^\circ$	$13.04 \pm 0.05^\circ$
θ_{23}	$38 \pm 1^\circ$	$2.38 \pm 0.06^\circ$
θ_{13}	$8.9 \pm 0.5^\circ$	$0.201 \pm 0.011^\circ$
Δm_{21}^2	$+(7.54 \pm 0.22) \times 10^{-5} \text{ eV}^2$	
$ \Delta M^2 $	$(2.43^{+0.10}_{-0.06}) \times 10^{-3} \text{ eV}^2$	$m_3 \gg m_2$
δ_{CP}	$-170 \pm 54^\circ$	$67 \pm 5^\circ$

Thus, the neutrino mixing parameter values and their ‘1 σ ’ uncertainties shown in the table are valuable from the standpoint of providing broad guidance to the HEP community. However, as an encapsulation of the current knowledge, one must take great care in interpreting both the values and the uncertainties. In some cases (namely, Δm_{21}^2 , ΔM^2 , θ_{12} and θ_{13}), the values are dominated by experimental results that directly probe these parameters (or effects that are roughly linearly related), and the χ^2 surfaces for these parameters are correspondingly parabolic. Thus the interpretation of the global fit results for these parameters is relatively straightforward. On the other hand, the current input into the determination of the values and uncertainties for θ_{23} and δ_{CP} are less direct, and by the nature of what is directly measurable (*i.e.*, $\sin^2(2\theta_{23})$ in long-baseline/atmospheric ν_μ disappearance measurements), χ^2 surfaces are strongly non-parabolic beyond $\pm 1\sigma$.* Furthermore, the issue of combining data from experiments where systematic uncertainties are likely not Gaussian-distributed also complicates such global fits.

The point of the above discussion is that there is a lot of work left to do just to complete the standard three-flavor mixing picture, particularly with regard to θ_{23} (maximal, or not? if not, then $<$, or $> 45^\circ$?), mass hierarchy (normal or inverted?) and δ_{CP} (even taking the global fit at face value, it is completely unconstraining at the 2σ level). Additionally, there is great value in obtaining a set of measurements for multiple parameters **from a single experiment**, where correlations and systematic uncertainties can be handled properly. Such an experiment is also well positioned to **test** the standard picture of three-flavor mixing discussed here. We argue that LBNE is this experiment.

*The authors of Ref. ?? take care to provide the $\pm 2\sigma$ and $\pm 3\sigma$ ranges as well – for θ_{23} and δ_{CP} , these are considerably less constraining than what might be inferred on the basis of the 1σ ranges indicated in the table.

2.2.1.2 Leptonic CP Violation

In the particular decomposition of the PMNS matrix shown in Eqn. 2.1, the central factor, labeled ‘II’, describes the mixing between the ν_1 and ν_3 mass states, and contains the CP-violating phase δ_{CP} . Leptonic CP violation in the three-flavor model thus occurs due to the interference of contributions to an oscillation mode from terms that contain δ_{CP} (*i.e.*, involve the above $\nu_1 - \nu_3$ mixing directly), and terms that do not. The magnitude of the CP violation effect depends most directly on the size of a function of all three mixing angles and the CP phase known the Jarlskog Invariant [17]:

$$J_{CP}^{PMNS} \equiv \frac{1}{8} \sin 2\theta_{12} \sin 2\theta_{13} \sin 2\theta_{23} \cos \theta_{13} \sin \delta_{CP} \quad (2.4)$$

Given the current best fit values of the mixing angles [15], and assuming normal hierarchy, we find

$$J_{CP}^{PMNS} = 0.035 \sin \delta_{CP} \quad (2.5)$$

The large values of the mixing angles in the lepton sector imply that there can potentially be very large leptonic CP violation effects – depending on the value of the unknown phase δ_{CP} . This is in sharp contrast with the very small mixing in the quark sector, which leads to a very small value of the corresponding Jarlskog invariant [18] (despite the large value of δ_{CP}^{CKM}) of

$$J_{CP}^{CKM} \approx 3 \pm 1 \times 10^{-5}. \quad (2.6)$$

The significance of the above comparison is that to date, all observed CP-invariance violating effects have occurred in experiments involving systems of quarks, in particular strange and B -mesons [19]. Furthermore, in spite of several decades of experimental searches, all of these are explained by the CKM paradigm, and all are functions of a unique CP-odd phase parameter. Yet, despite hopes that CP-violation in the quark sector could provide a key ingredient to explain the observed Baryon Asymmetry of the Universe (BAU), the smallness of J_{CP}^{CKM} has rendered such an explanation unlikely.

Neutrino oscillations provide a unique opportunity to probe a new CP-violating sector of Nature. The measurement of CP violation in the neutrino sector is expected to have a deep impact on the issue of the generation of the BAU. Leptogenesis, leading to baryogenesis, has emerged as perhaps the most promising candidate for the origin of the observed BAU. Furthermore, the GUT-based seesaw mechanism has emerged as perhaps the simplest and most natural explanation of the observed superlight neutrino mass scales. The two mechanisms may have a compelling common origin within schemes of grand unification. The goal of establishing an experimental basis for assessing this possibility should rank very high on the list of programmatic priorities within HEP.

2.2.1.3 CP-Violating Effects in Long-Baseline Experiments

If CPT invariance is assumed, then $P(\nu_l \rightarrow \nu_l) = P(\bar{\nu}_l \rightarrow \bar{\nu}_l)$, where $l = e, \mu, \tau$, which is supported by the measurements from the MINOS Experiment of $\nu_\mu \rightarrow \nu_\mu$ and $\bar{\nu}_\mu \rightarrow \bar{\nu}_\mu$ oscillations [20]. This implies that CP-violating effects in neutrino oscillations can only be accessed in appearance experiments. Because of the intrinsic challenges of producing and detecting ν_τ 's, the oscillation modes $\nu_{\mu,e} \rightarrow \nu_{e,\mu}$ provide the most promising experimental signatures of leptonic CPV.

For $\nu_{\mu,e} \rightarrow \nu_{e,\mu}$ oscillations that proceed as the neutrinos propagate through matter as in terrestrial long-baseline experiments, the coherent forward scattering of ν_e 's off of electrons in matter modifies energy and path length dependence of the vacuum oscillation probability in a way that depends on the sign of Δm_{32}^2 . This is essentially the Mikheyev-Smirnov-Wolfenstein (MSW) effect [21,22] that has already been observed in solar neutrino oscillation experiments [?,?]. The oscillation probability of $\nu_{\mu,e} \rightarrow \nu_{e,\mu}$ through matter in a constant density approximation, and keeping terms up to second order in $|\alpha| \equiv |\Delta m_{21}^2|/|\Delta m_{31}^2|$ and $\sin^2 \theta_{13}$, is [23,16]

$$P(\nu_\mu \rightarrow \nu_e) \cong P(\nu_e \rightarrow \nu_\mu) \cong P_0 + \underbrace{P_{\sin \delta}}_{\text{CP violating}} + P_{\cos \delta} + P_3 \quad (2.7)$$

where

$$P_0 = \sin^2 \theta_{23} \frac{\sin^2 2\theta_{13}}{(A-1)^2} \sin^2[(A-1)\Delta], \quad (2.8)$$

$$P_3 = \alpha^2 \cos^2 \theta_{23} \frac{\sin^2 2\theta_{12}}{A^2} \sin^2(A\Delta), \quad (2.9)$$

$$P_{\sin \delta} = \alpha \frac{8J_{cp}}{A(1-A)} \sin \Delta \sin(A\Delta) \sin[(1-A)\Delta], \quad (2.10)$$

$$P_{\cos \delta} = \alpha \frac{8J_{cp} \cot \delta}{A(1-A)} \cos \Delta \sin(A\Delta) \sin[(1-A)\Delta], \quad (2.11)$$

where

$$\alpha = \Delta m_{21}^2 / \Delta m_{31}^2, \quad \Delta = \Delta m_{31}^2 L / 4E, \quad A = \sqrt{3} G_F N_e 2E / \Delta m_{31}^2.$$

In the above, the effect of the CP-odd phase δ_{CP} appears in the expressions for $P_{\sin \delta}$, which switches sign in going from $\nu_\mu \rightarrow \nu_e$ to the $\bar{\nu}_\mu \rightarrow \bar{\nu}_e$ channel, and $P_{\cos \delta}$, which does not. Additionally, the matter effect described above introduces a CP asymmetry as well, the origin of which is simply the presence of electrons and absence of positrons in the matter comprising the earth. The impact of this ‘mundane’ form of CP violation can be seen by noting that the factors that are proportional to Δm_{31}^2 (namely A , Δ and α) change sign in going from normal to inverted neutrino mass hierarchy.

In summary, CP violation can thus be probed using oscillations of muon neutrinos from accelerator neutrino beams produced from pion decays in flight. As shown in Eqn. 2.1, the

CP phase appears in the PMNS matrix through the mixing of the 1-3 states, therefore the physical characteristics of the appearance experiment are determined by the baseline and neutrino energy at which the mixing between the 1-3 state is maximal as follows:

$$\frac{L(\text{km})}{E_\nu(\text{GeV})} = (2n-1) \frac{\pi}{2} \frac{1}{1.27 \times \Delta m_{31}^2 (\text{eV}^2)} \quad (2.12)$$

$$\approx (2n-1) \times 510 \text{ km/GeV} \quad (2.13)$$

where $n = 1, 2, 3, \dots$ denotes the oscillation nodes at which the appearance probability is maximal. For long-baseline experiments where the neutrino beam propagates through the earth, the leptonic CP violation effects must be disentangled from the matter effects. On the other hand, the presence of the matter effect provides a means for determining the currently-unknown mass hierarchy, as described below.

2.2.1.4 Matter Effects and the Mass Hierarchy

The dependence of the matter effect on the mass hierarchy is illustrated in the oscillograms plotted on the left hand side of Figures 2-1 and 2-2, and can be characterized as follows:

- For normal hierarchy $P(\nu_\mu \rightarrow \nu_e)$ is enhanced and $P(\bar{\nu}_\mu \rightarrow \bar{\nu}_e)$ is suppressed. The effect increases with baseline at a fixed L/E .
- For inverted hierarchy $P(\nu_\mu \rightarrow \nu_e)$ is suppressed and $P(\bar{\nu}_\mu \rightarrow \bar{\nu}_e)$ is enhanced. The effect increases with baseline at a fixed L/E .
- The matter effect has the largest impact on the probability amplitude at the 1st oscillation maxima.
- The matter effect introduces a phase shift in the oscillation pattern. The oscillation pattern is shifted to a lower energy for a given baseline when the hierarchy changes from normal to inverted. The shift is ≈ -100 MeV.

In Figures 2-1 and 2-2, the oscillation probabilities given in Eqns. 2.7 to 2.11 for $\nu_\mu \rightarrow \nu_e$ as a function of baseline in km and energy in GeV are shown in the oscillograms for $\delta_{CP} = 0$ for the normal and inverted hierarchy respectively. The oscillograms include the matter effect assuming a constant density of the earth's mantle of 2.8 g/cm^3 . The solid black curves on the oscillograms indicate the location of the first and second oscillation maximum as given by Eqn. 2.13. Equation 2.13 is for vacuum oscillations, matter effects will distort the scale at which the mixing between the 1 and 3 states is maximal. The large impact of the matter effect on the appearance probabilities of ν_e and $\bar{\nu}_e$ at longer baselines implies that appearance measurements over long distances through the earth provide a powerful probe of the neutrino mass hierarchy.

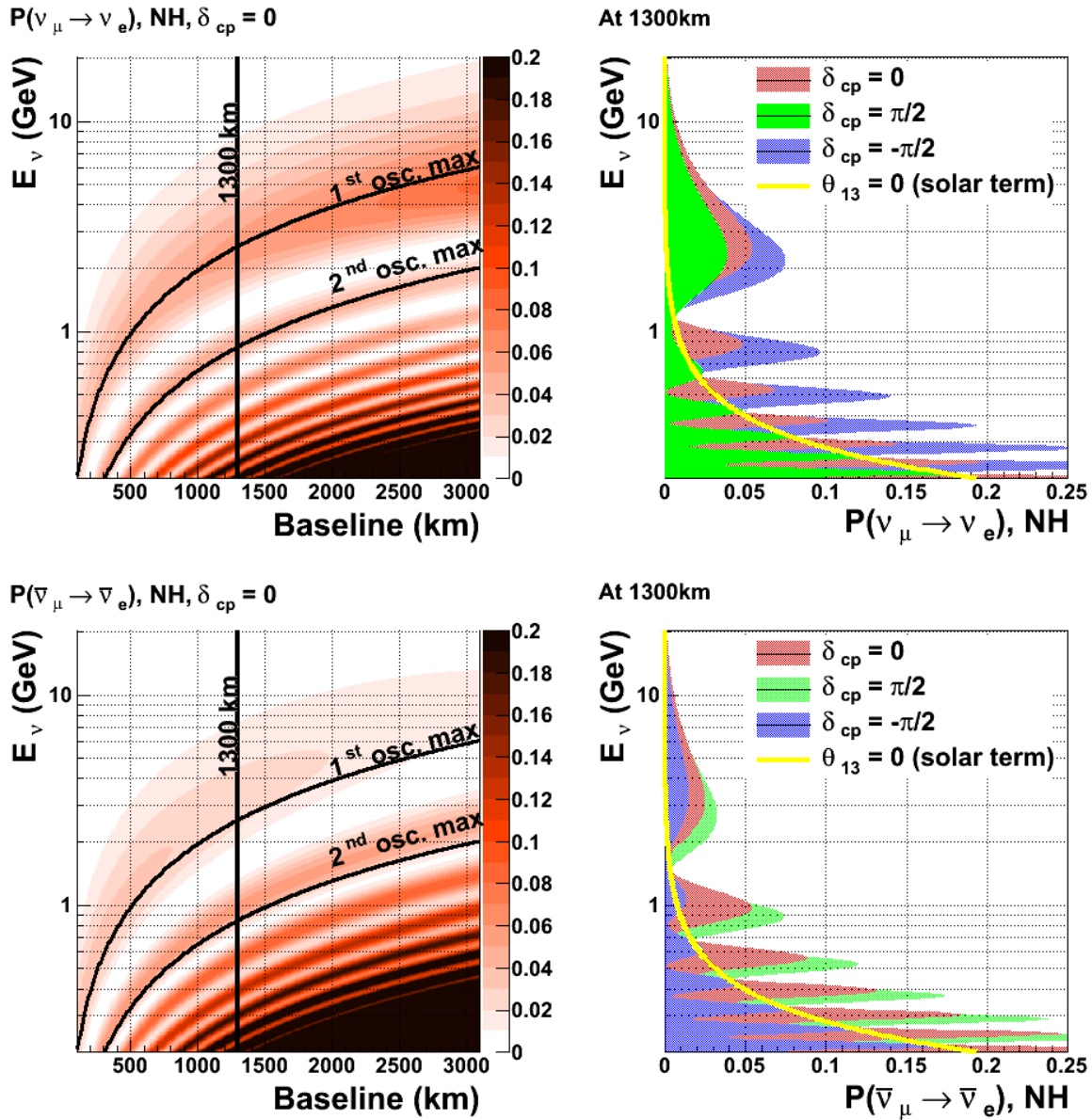


Figure 2-1: Neutrino oscillations vs energy, baseline and as a function of different values of δ_{CP} . The oscillograms on the left show the $\nu_\mu \rightarrow \nu_e$ oscillation probabilities as a function of baseline and energy for **neutrinos** (top left) and **anti-neutrinos** (bottom left) with $\delta_{CP} = 0$ and a **normal hierarchy**. The figures on the right show the projection of the oscillation probability on the neutrino energy axis at a baseline of 1300km for $\delta_{CP} = 0$ (red), $\delta_{CP} = +\pi/2$ (green), and $\delta_{CP} = -\pi/2$ (blue) for neutrinos (top right) and anti-neutrinos (bottom right). The yellow curve is the ν_e appearance solely from the “solar term” due to 1-2 mixing as given by Equation 2.9.

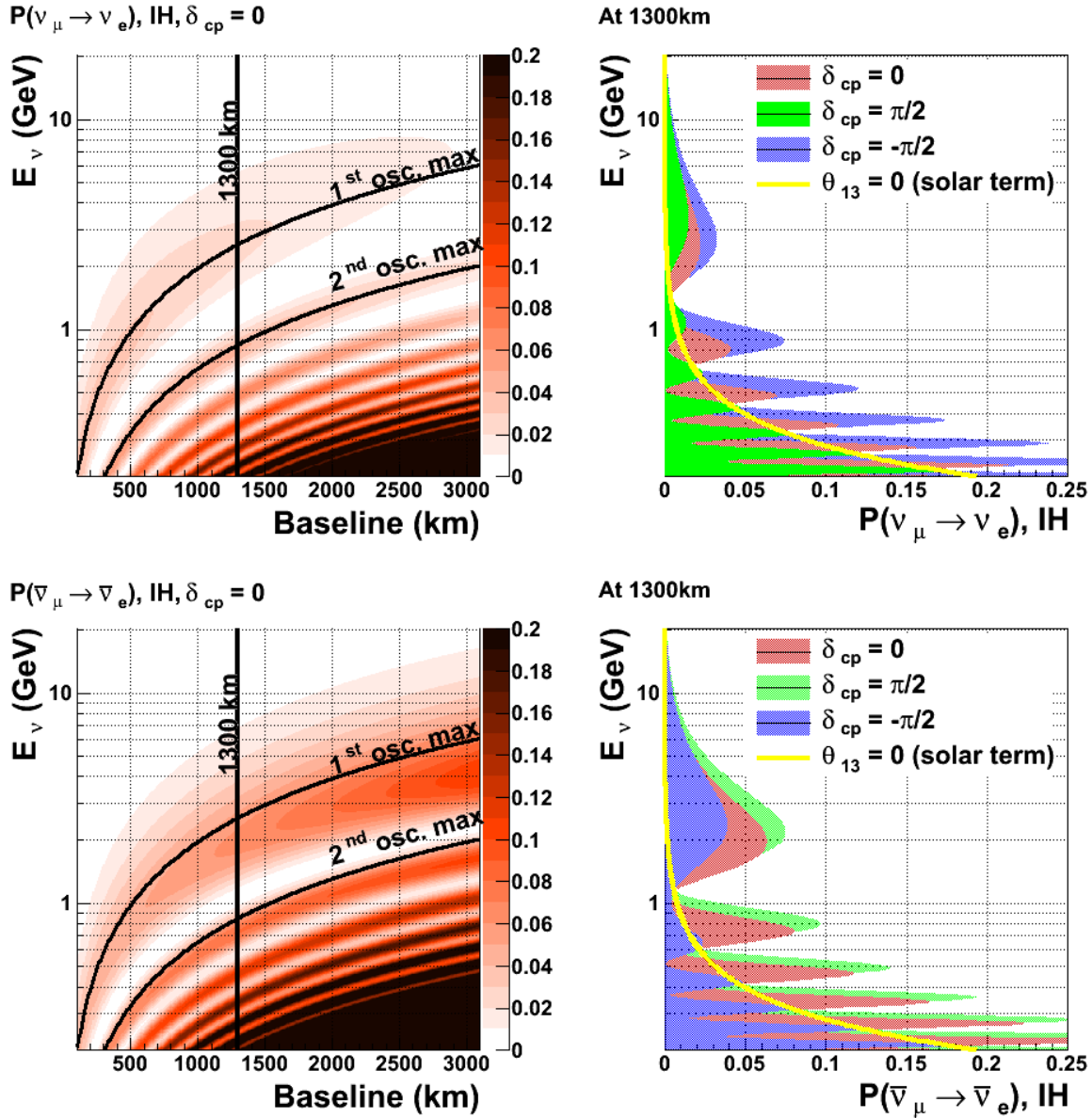


Figure 2-2: Neutrino oscillations vs energy, baseline and as a function of different values of δ_{CP} . The oscillograms on the left show the $\nu_\mu \rightarrow \nu_e$ oscillation probabilities as a function of baseline and energy for **neutrinos** (top left) and **anti-neutrinos** (bottom left) with $\delta_{CP} = 0$ and an **inverted hierarchy**. The figures on the right show the projection of the oscillation probability on the neutrino energy axis at a baseline of 1300km for $\delta_{CP} = 0$ (red), $\delta_{CP} = +\pi/2$ (green), and $\delta_{CP} = -\pi/2$ (blue) for neutrinos (top right) and anti-neutrinos (bottom right). The yellow curve is the ν_e appearance solely from the “solar term” due to 1-2 mixing as given by Eqn. 2.9.

2.2.1.5 Disentangling Leptonic CPV and the Matter Effect

The E_ν dependences of the oscillation probability for a baseline of $L = 1300$ km is plotted at right in Figures 2-1 and 2-2. The different colored curves demonstrate the variation in the ν_e appearance probability as a function of the value of δ_{CP} . The variation in the $\nu_\mu \rightarrow \nu_e$ oscillation probabilities with the value of δ_{CP} indicates that it is experimentally possible to measure the value of δ_{CP} at a fixed baseline using only the observed shape of the $\nu_\mu \rightarrow \nu_e$ OR $\bar{\nu}_\mu \rightarrow \bar{\nu}_e$ appearance signal measured over an energy range that encompasses at least one full oscillation interval. A measurement of the value of $\delta_{CP} \neq 0$ or π implies that CP is violated if neutrino mixing follows the three-flavor model. Regardless of the value obtained for δ_{CP} , evidence for CP violation in the neutrino sector requires the explicit observation of an asymmetry between $P(\nu_l \rightarrow \nu_l')$ and $P(\bar{\nu}_l \rightarrow \bar{\nu}_l')$. The CP asymmetry, \mathcal{A}_{CP} , is defined as

$$\mathcal{A}_{CP} = \frac{P(\nu_\mu \rightarrow \nu_e) - P(\bar{\nu}_\mu \rightarrow \bar{\nu}_e)}{P(\nu_\mu \rightarrow \nu_e) + P(\bar{\nu}_\mu \rightarrow \bar{\nu}_e)} \quad (2.14)$$

In the 3 flavor model the asymmetry can be approximated to leading order in Δm_{21}^2 as [18]:

$$\mathcal{A}_{CP} \sim \frac{\cos \theta_{23} \sin 2\theta_{12} \sin \delta}{\sin \theta_{23} \sin \theta_{13}} \left(\frac{\Delta m_{21}^2 L}{4E_\nu} \right) + \text{matter effects} \quad (2.15)$$

In Figure 2-3, the asymmetries induced by matter and maximal CP violation (at $\delta_{CP} = \pm\pi/2$) are shown separately as a 2-D oscillograms in baseline and neutrino energy. The impact of the matter effect induces an asymmetry in $P(\nu_l \rightarrow \nu_l')$ and $P(\bar{\nu}_l \rightarrow \bar{\nu}_l')$ that is in addition to the CP asymmetry – if any – induced through the CP violating phase, δ_{CP} . At longer baselines ($> 1000\text{km}$), the matter asymmetry in the energy region of the first oscillation node is driven primarily by the change in the ν_e appearance amplitude. At shorter baselines ((100) km) the asymmetry is driven by the phase shift. In general:

$$\mathcal{A}_{cp} \propto L/E, \quad (2.16)$$

$$\mathcal{A}_{matter} \propto L \times E. \quad (2.17)$$

The phenomenology of $\nu_\mu \rightarrow \nu_e$ oscillations described above implies that the experimental sensitivity to CP violation and the mass hierarchy from measurements of the total asymmetry between $P(\nu_l \rightarrow \nu_l')$ and $P(\bar{\nu}_l \rightarrow \bar{\nu}_l')$ necessitates the disambiguation of asymmetries induced by the matter effect and asymmetries induced by CP violation. This is particularly true for experiments using neutrino beams of $\mathcal{O}(1\text{GeV})$ which require baselines of $\mathcal{O}(100\text{km})$ to access the 1-3 mixing scale. At these baselines the matter asymmetries are significant. We note that the magnitude of the matter asymmetry is calculable within an uncertainty of $< 10\%$ using the currently known values of the oscillation parameters. Only the sign of the asymmetry which depends on the sign of Δm_{31}^2 is unknown.

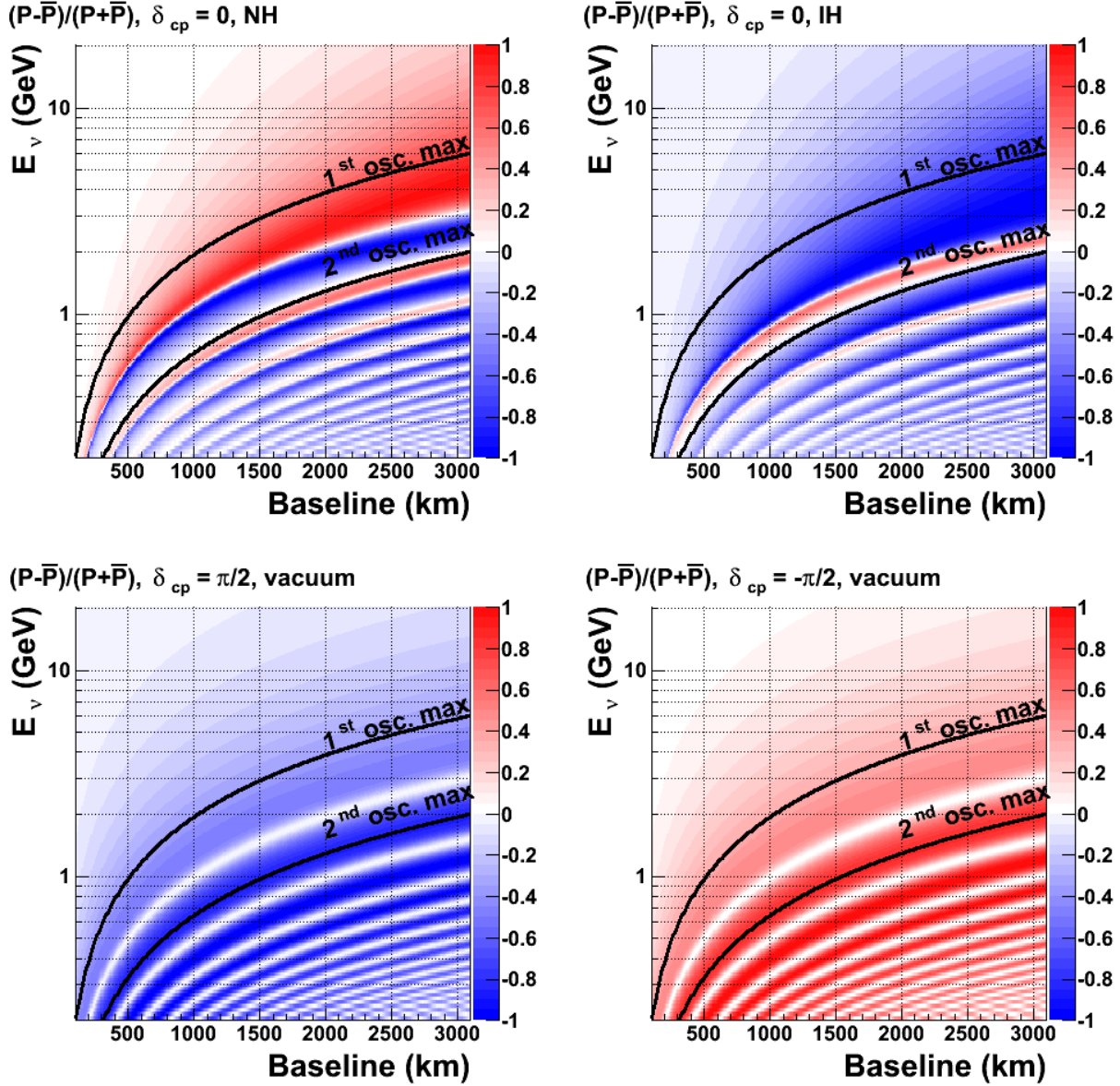


Figure 2-3: The CP asymmetry as a function of baseline. The top two figures are for the asymmetry induced by the matter effect only for normal (top left) and inverted (top right) hierarchies. The bottom figures are for the asymmetry induced through the CP violating phase δ_{CP} in vacuum, for $\delta_{CP} = +\pi/2$ (bottom left) and $\delta_{CP} = -\pi/2$ (bottom right)

1 An example that illustrates the ambiguities that can arise from the interference of the mat-
 2 ter and CP asymmetries is shown in Figure 2-4. The figures show (clockwise from top
 3 left) the total asymmetry as a function of δ_{CP} at baselines of 290 km, 810km, 2300km, and
 4 1300km. The curves in black and red are the asymmetries at the 1st and second oscillation
 5 nodes respectively. The solid lines are for normal hierarchy and dashed lines are for inverted
 6 hierarchy. The figures demonstrate the measurements of the asymmetry at the 1st oscilla-
 7 tion node yield ambiguous results for experiments with short baselines if the hierarchy is
 8 unknown. This occurs in regions of the (L, E, δ_{CP}) phase space where the matter and CP
 9 asymmetries cancel partially or totally. For example the green line in Figure 2-4 indicates
 10 the asymmetry at the first node for maximal CP violation ($\delta_{CP} = \pi/2$) with an inverted
 11 hierarchy. At a baseline of 290 km the measured asymmetry ($\delta_{CP} = \pi/2$, inverted hierarchy)
 12 is degenerate with ($\delta_{CP} \sim 0$, normal hierarchy) at the first node. Measurements of the
 13 asymmetry at different L/E or at different baselines can break the degeneracies (Equa-
 14 tion 2.17). At very long baselines where the matter asymmetry exceeds the maximal CP
 15 asymmetry, there are no degeneracies and the mass hierarchy and CP asymmetries can be
 16 resolved in the same experiment. For the current best fit values of the oscillation parameters
 17 the degeneracies in measurements at the first oscillation maximum are resolved at a baseline
 of ~ 1200 km.

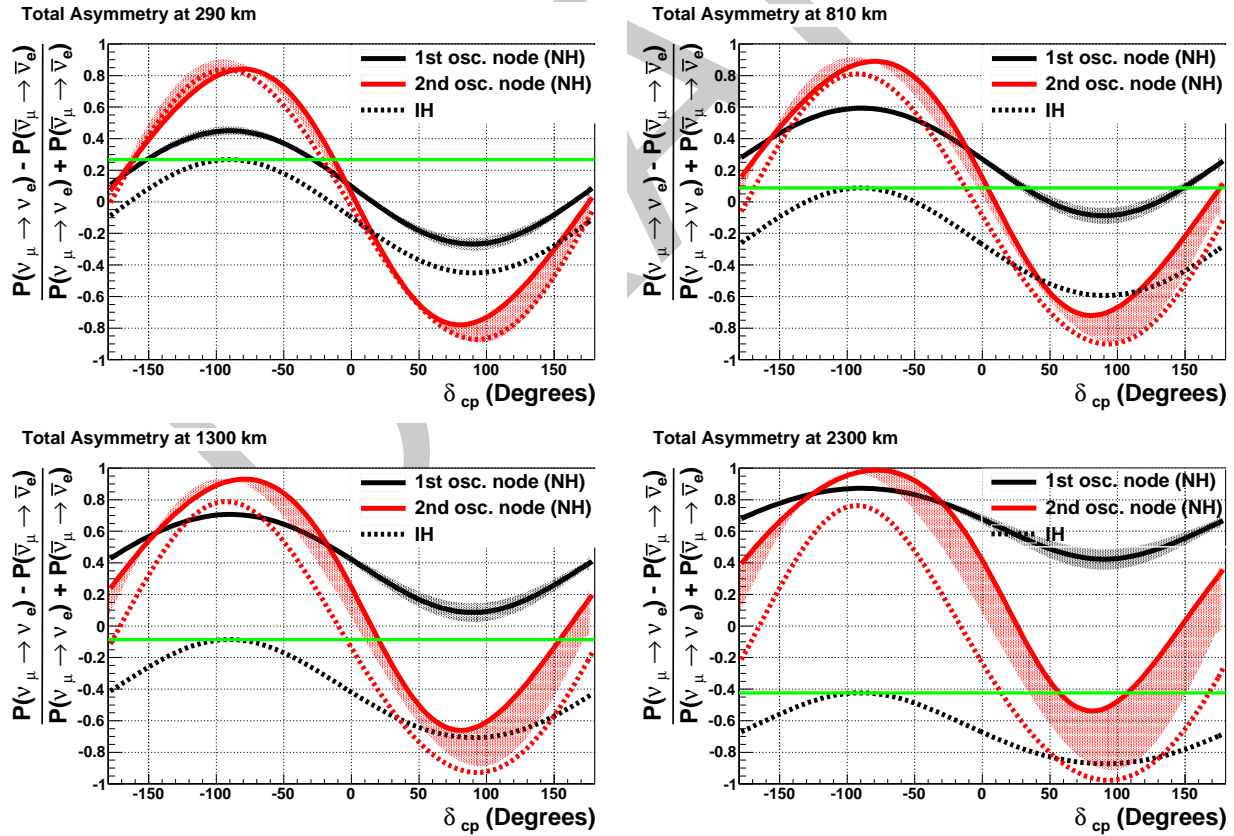


Figure 2-4: $\nu/\bar{\nu}$ oscillation asymmetries vs δ_{CP} at the first 2 oscillation nodes. Clockwise from top left: 290km, 810km, 2300km, 1300km.

2.2.1.6 Optimization of Baseline

To understand the performance of a long-baseline experiment as a function of baseline using more realistic experimental conditions, a study of the sensitivities to CP violation and the mass hierarchy as a function of baseline was carried out using different realistic beam-line designs for each baseline and a 35 kton LArTPC. A large LArTPC was chosen for the far detector since it has a high ν_e identification efficiency that is flat over a large range of energies as presented in Chapter ???. The basic beam-line design was based on the NuMI beamline utilizing the 120 GeV, 700kW beam from the Fermilab Main Injector and was fully simulated using GEANT3. The beam spectrum was changed by varying the distance between the target and the first horn to select a beam spectrum that covers the first and part of the second oscillation node. An evacuated decay pipe of 4m diameter and a length that varied from 280 to 580m was used. For baselines less than 1000km, an off-axis beam was simulated, with the off-axis angle chosen to provide the most coverage of the first oscillation nodes. The results of study are summarized in Figure 2-5. The sensitivity to CP violation assumes that the mass hierarchy is unknown.

The baseline study indicates that with realistic experimental conditions, baselines between 1000-1300km are near optimal for CP violation determination. With baselines > 1500 km the mass hierarchy could be determined with a minimum of 5σ for all values of δ_{cp} with a large LArTPC far detector.

2.2.2 Disappearance of ν_μ and Determination of θ_{23}

The study of the disappearance of ν_μ probes θ_{23} and $|\Delta m_{32}^2|$ with very high precision. Combining the disappearance of ν_μ with the ν_e appearance signal can help determine the θ_{23} octant. Non-standard physics can manifest itself in differences observed in higher-precision measurements of ν_μ and $\bar{\nu}_\mu$ disappearance over long baselines. In addition, experiments at long enough baselines and significant neutrino flux > 3 GeV coupled with high resolution tracking detectors like LBNE can also probe $\nu_\mu \rightarrow \nu_\tau$ appearance using ν_τ charged-current interactions with higher precision than is currently possible. With long enough exposures the combination of $\nu_\mu \rightarrow \nu_\mu$, $\nu_\mu \rightarrow \nu_e$, and $\nu_\mu \rightarrow \nu_\tau$ can over-constrain the 3 flavor model of neutrino oscillations both in neutrino and anti-neutrino modes.

The precision with which the current set of neutrino-oscillation parameters are known ensures that the compelling physics program outlined for LBNE is feasible with the proposed combination of baseline, detector mass and beam.

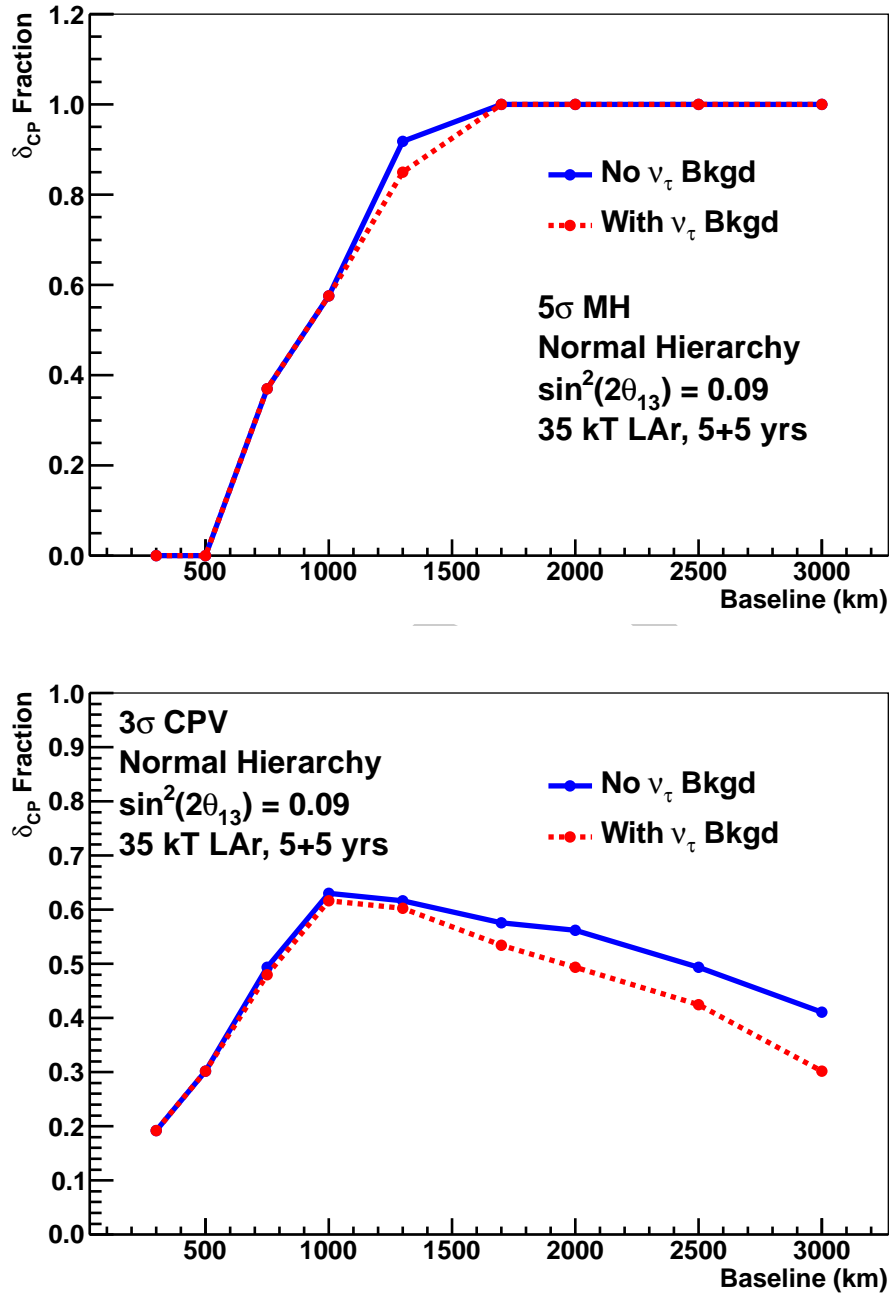


Figure 2-5: The fraction of δ_{cp} values for which the mass hierarchy can be determined at the 5σ level or greater as a function of baseline (top) and the fraction of δ_{cp} values which CP violation can be determined at the 3σ level or greater as a function of baseline (bottom). A NuMI based beam design with a 120 GeV, 708 kW beam was optimized for each baseline. Projections assume $\sin^2 2\theta_{13} = 0.09$ and a 35-kton LArTPC as the Far Detector [24]. An exposure of 5yrs+5yrs neutrino+anti-neutrino running is assumed at each baseline.

2.2.3 Oscillation Physics with Atmospheric Neutrinos

Atmospheric neutrinos are unique among sources used to study oscillations: the flux contains neutrinos and antineutrinos of all flavors, matter effects play a significant role, both Δm^2 values contribute, and the oscillation phenomenology occurs over several decades each in energy (see Figure 2–6) and path length. The probabilities of atmospheric $\nu_\mu \rightarrow \nu_e$ and

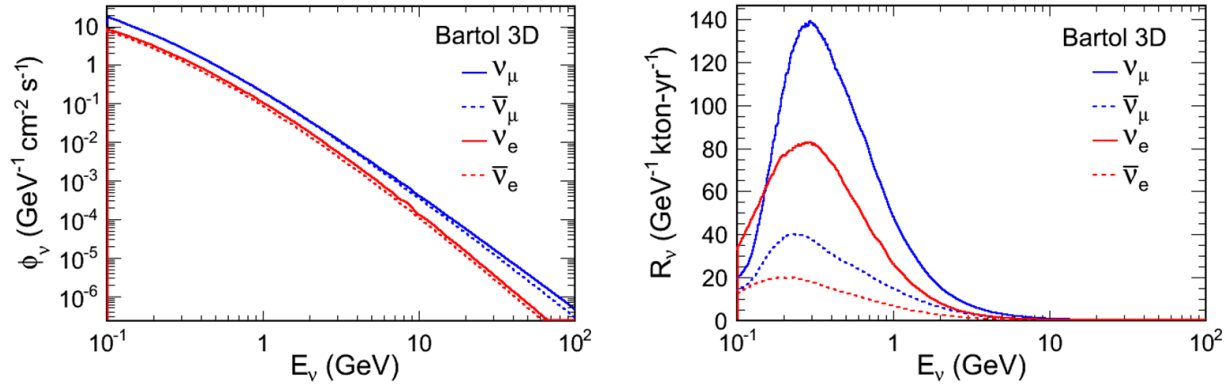


Figure 2–6: The atmospheric neutrino flux in neutrinos per second per steradian as a function of neutrino energy for different flavors is shown at left. The atmospheric neutrino spectrum per GeV per kton per year for the different species is shown on the right.

$\bar{\nu}_\mu \rightarrow \bar{\nu}_e$ oscillations for normal and inverted hierarchies as a function of zenith angle are shown in the oscillograms in Figure 2–7.

These characteristics make it ideal for the study of oscillations (in principle sensitive to all of the remaining unmeasured quantities in the PMNS matrix) and provide a laboratory in which to search for exotic phenomena for which the dependence of the flavor-transition and survival probabilities on energy and path length can be defined.

Even with dedicated long-baseline experiments exploring the large mass splitting for nearly a decade, atmospheric data contributes substantially to our current understanding of the neutrino sector. Broadly speaking it has three roles: demonstrating *complementarity* with beam results, increasing measurement *precision* through global fits, and placing limits on *new physics*. *Complementary* to beam results are 2- and 3- flavor fits and the measurement of a tau appearance signal consistent with expectation. *Precision* improvements come from the sensitivity of atmospheric neutrinos to the mass hierarchy and octant of θ_{23} . *New physics* searches have placed limits on CPT violation, non-standard interactions, mass-varying neutrinos, and Lorentz invariance violation.

Atmospheric neutrinos can continue to play these roles in the LBNE era, if the detector is located underground. In particular, complementarity will be vital in a future where, worldwide, the number of high precision long-baseline beam/detector facilities is small. In Section

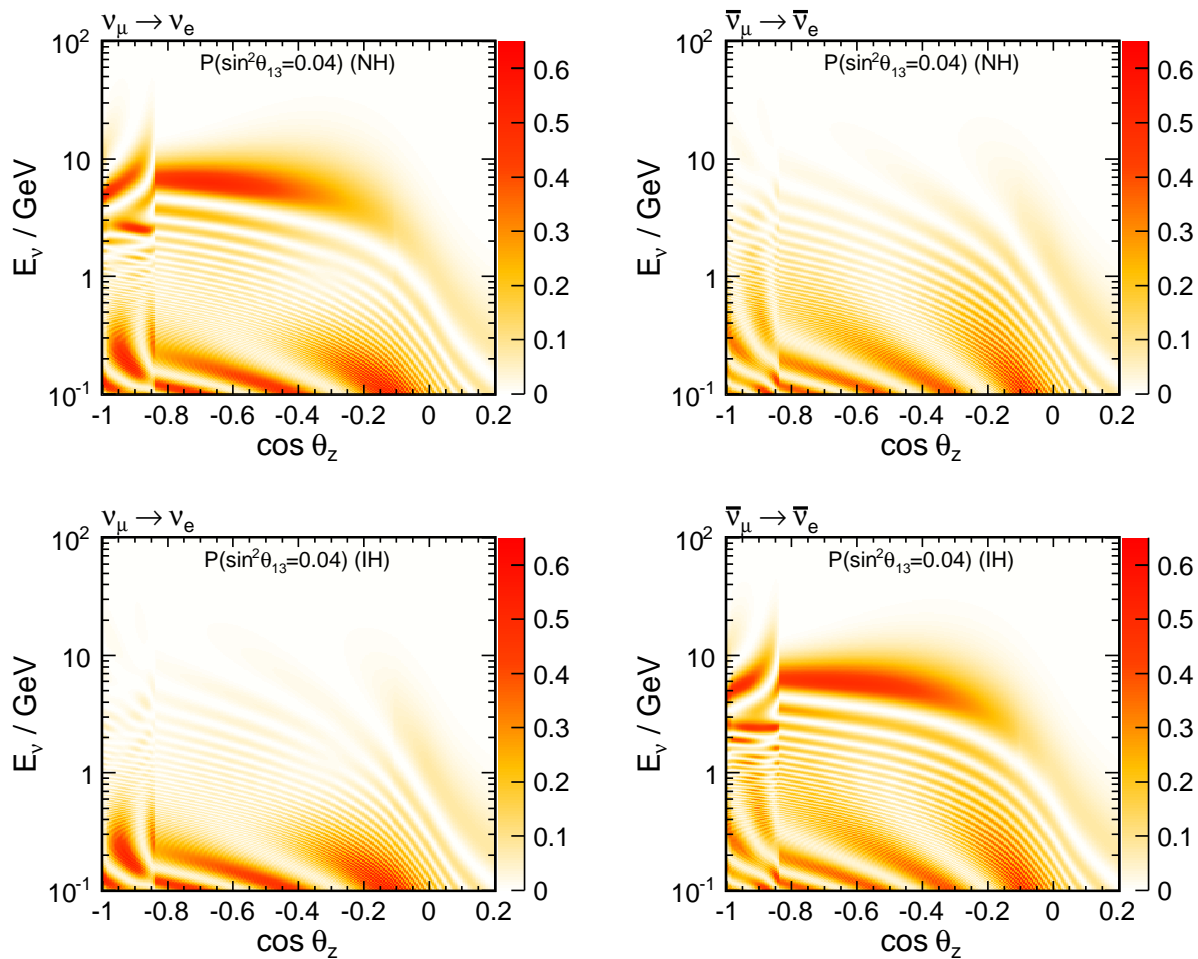


Figure 2-7: The probabilities of atmospheric $\nu_\mu \rightarrow \nu_e$ (left) and $\bar{\nu}_\mu \rightarrow \bar{\nu}_e$ (right) oscillations for normal (top) and inverted (bottom) hierarchies as a function of zenith angle.

4.5 we will explore the physics potential of a large underground liquid argon detector for atmospheric neutrinos.

2.3 Grand Unified Theories and Baryon Number Violation Processes

Proton decay, bound neutron decay, and similar processes such as dinucleon decay and neutron-antineutron oscillation test the apparent but unexplained conservation law of baryon number. These decays are already known to be rare based on decades of prior searches, all of which have been negative. If measurable event rates or even single candidate events are found, one immediately concludes that they must have proceeded via unknown virtual processes based on physics beyond the standard model. The impact of demonstrating the existence of a baryon number violating process would be profound.

The class of theories known as Grand Unified Theories (GUTs) make predictions about baryon number violation and the life of the proton that may be within reach of the LBNE detectors. Early GUTs were the original motivation for putting kiloton-scale detectors underground. The 22.5 kiloton Super-Kamiokande (SK) experiment extended the search for proton decay by more than an order of magnitude. Although there has been no sign of proton decay, the strict limits from these experiments constrain the construction of contemporary GUTs and indeed, a tension between experiment and theory is now commonly discussed. It is very natural to continue the search with 100-kiloton-scale detectors. The grand unified theoretical motivation for the study of proton decay has a long and distinguished history [25,26,27], and has been reviewed many times [28,?,?]. Contemporary reviews [29,30,31] discuss the strict limits already set by SK and the context of proposed multi-100-kiloton scale experiments such as Hyper-Kamiokande and LBNE. Key points related to scientific impact are:

- Conservation of baryon number is unexplained, corresponding to no known long-range force.
- Baryon number non-conservation has cosmological consequences, such as a role in inflation and the baryon asymmetry of the universe.
- Proton decay is predicted by a wide range of GUTs.
- Grand unified theories are also often able to accommodate massive neutrinos with characteristics as discovered over the last decade.
- GUTs incorporate other unexplained features of the standard model such as the relationship of quark and lepton electric charges.

- The unification scale is suggested experimentally and theoretically by the apparent convergence of the running coupling constants of the Standard Model. It is in excess of 10^{15} GeV.
- The unification scale is not accessible by any accelerator experiment, and can only be probed by virtual processes such as a proton decay.
- GUTs usually predict the relative branching fractions of different nucleon decay modes, requiring of course requiring of course a sizeable sample of proton decay events to test.
- The dominant proton decay mode is often sufficient to roughly identify the likely characteristics of the GUT, such as gauge mediation or the involvement of supersymmetry.

In summary, the observation of even a single unambiguous proton decay event would strongly corroborate that the ideas of unification are correct and would give strong guidance as to which ideas are correct. One or two events would also give guidance to the larger size detector needed to explore the physics in more detail. From the body of literature, two decay modes emerge that dominate our experimental design. First, there is the decay mode of $p \rightarrow e^+ \pi^0$ that arises from gauge mediation. This is the most famous proton decay mode, often predicted to have the highest branching fraction, and also demonstrably the most straightforward experimental signature for a water Cherenkov detector. The total mass of the proton is converted into the electromagnetic shower energy of the positron and the two photons from π^0 decay, with a net momentum vector near zero.

The second key mode is $p \rightarrow K^+ \nu$. This mode is dominant in most supersymmetric-GUTs, which also often favor several other modes involving kaons in the final state. The decay mode with a charged kaon is notable because it presents the unique opportunity for a liquid argon TPC to detect it with extremely high efficiency. This is because the momentum of the kaon will result in high ionization density which can be compared to the range of the kaon, not to mention the unique final states of K^+ decay that should be fully reconstructed.

There are a number of other proton decay channels to consider, but they will not influence the design of a next-generation experiment beyond the above decay modes. There are 27 allowed modes of proton or bound neutron into anti-lepton plus meson (conserving $B - L$). The most stringent limits besides $p \rightarrow e^+ \pi^0$ include $p \rightarrow \mu^+ \pi^0$ and $p \rightarrow e^+ \eta$, both of which must have partial lifetimes greater than 4×10^{33} years. Any experiment that will do well for $e^+ \pi^0$ will do well for these decay modes. The decay $p \rightarrow \nu \pi^+$ or $n \rightarrow \nu \pi^0$ may have large theoretically predicted branching fractions but are experimentally difficult due to sizeable backgrounds from atmospheric neutrino interactions. The decay $p \rightarrow \mu^+ K^0$ is detected relatively efficiently by either water Cherenkov or LAr TPC detectors. There are a number of other possibilities such as modes that conserve $B + L$, or violate only baryon number, or that decay into only leptons. These possibilities are less well-motivated theoretically, as they do not appear in a wide range of theories.

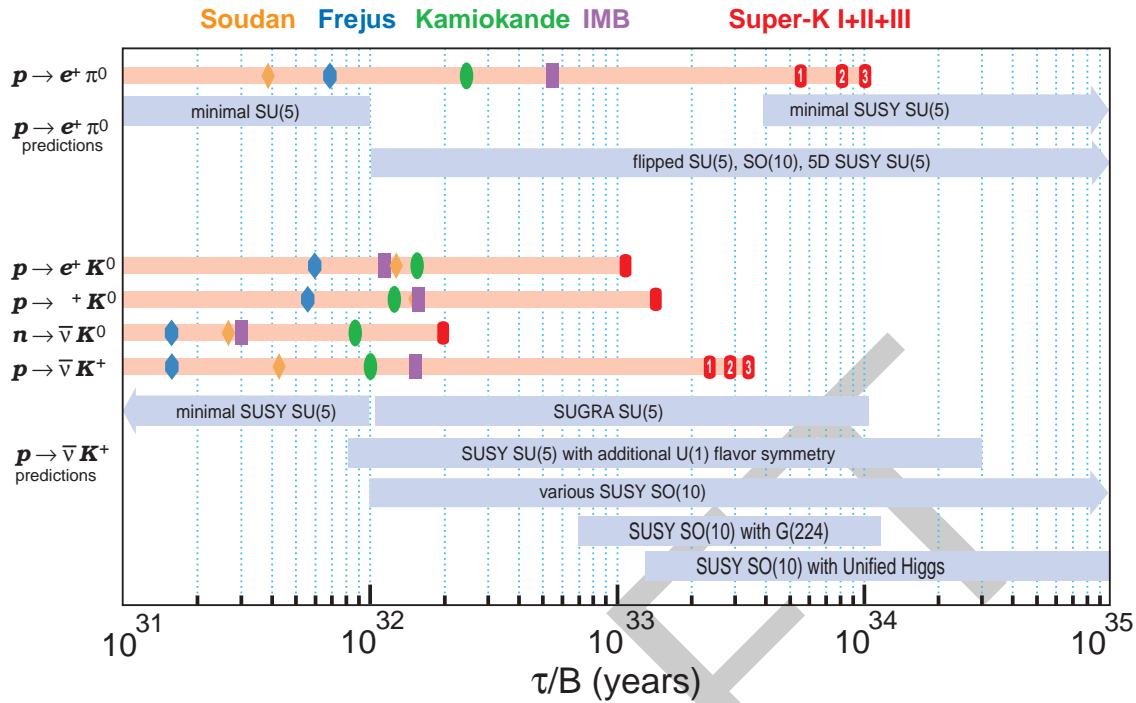


Figure 2-8: Proton decay lifetime limits compared to lifetime ranges predicted by Grand Unified Theories. The upper section is for $p \rightarrow e^+ \pi^0$, most commonly caused by gauge mediation. The lower section is for SUSY motivated models, which commonly predict decay modes with kaons in the final state. The marker symbols indicate published limits by experiments, as indicated by the sequence and colors on top of the figure.

1 Figure 2-8 shows experimental limits, dominated by recent results from Super-Kamiokande,
 2 compared to the ranges of lifetimes predicted by an assortment of GUTs. At this time, the
 3 theory literature does not attempt to precisely predict lifetimes, concentrating instead on
 4 suggesting the dominant decay modes and relative branching fractions. The uncertainty in
 5 the lifetime predictions come from details of the theory, such as unknown heavy particles
 6 masses and coupling constants, as well as poorly known details of matrix elements for quarks
 7 within the nucleon.

8 It is apparent from this figure that a continued search for proton decay is by no means
 9 assured of success. In addition to the lifetime ranges shown, there are models that predict
 10 essentially no proton decay or lifetimes out of reach of likely experiments. With that caveat,
 11 an experiment with sensitivity between 10^{33} and 10^{35} years is searching in the right territory
 12 over a wide range of GUTs and even if no proton decay is detected, the stringent lifetime
 13 limits will restrict efforts to build such theories. Minimal SU(5) was ruled out by the early
 14 work of IMB and Kamiokande; minimal SUSY SU(5) is considered to be ruled out by SK.
 15 In most cases, another order of magnitude in limit will not rule out specific theories, but
 16 will constrain their allowed parameters, perhaps leading to the conclusion that some are
 17 fine-tuned.

In summary, while the detector masses required to qualitatively extend the sensitivity to proton decay are inhibiting, an observation would have tremendous impact. As we will show in Chapter 6, the performance and scalability of the LArTPC technology provides LBNE with a unique opportunity for discovery.

2.4 Physics and Astrophysics From Core-Collapse Supernova Neutrinos

A nearby core-collapse supernova will provide a wealth of information via its neutrino signal (see [32,?] for reviews). The neutrinos are emitted in a burst of a few tens of seconds duration, with about half in the first second. Energies are in the few tens of MeV range, and luminosity is divided roughly equally between flavors. The baseline model of core collapse was confirmed by the observation of 19 neutrino events in two water Cherenkov detectors for SN1987A in the Large Magellanic Cloud, 55 kpc away [33,34]. An observed high-statistics core collapse neutrino signal will shed light on a variety of physics and astrophysics topics.

Core collapses are rare events: the expected rate is 2-3 per century in the Milky Way. As for the Homestake and Super-Kamiokande detectors, the large LBNE detector(s), once constructed, may operate for decades. On this time scale, there is a significant likelihood of a supernova exploding in our galaxy. In a 20-year run of an experiment, the probability of observing a collapse event is about 40%. The detection of the neutrino burst from such an event would dramatically expand the science reach of these detectors: from measuring the neutrino mass hierarchy and θ_{13} mixing angle, to observing the development of the explosion in the core of the star, to probing the equation of state of matter at nuclear densities, to constraining physics beyond the Standard Model. Each of these questions represents an important outstanding problem in modern physics, worthy of a separate, dedicated experiment. The possibility to target them all at once is very attractive, especially since it may come only at incremental cost to the project. The expected harvest of physics is rich enough that is essential to prepare to collect as much information as possible when a burst happens.

In contrast to the SN1987A, for which only 19 neutrinos were observed, the detectors currently on the drawing board would register thousands or tens of thousands of interactions from the burst. The exact type of interactions depends on the detector technology: a water-Cherenkov detector would be primarily sensitive to the electron antineutrinos, while a liquid argon detector has an excellent sensitivity to electron neutrinos. In each case, the high event rates imply that it should be possible to measure not only the time-integrated spectra, but also their second-by-second evolution. This is the key reason behind the impressive physics potential of the planned detectors.

The interest in observationally establishing the supernova explosion mechanism comes from the key role supernova explosions play in the history of the universe. In fact, it would not be

an exaggeration to say that the ancient supernovae have in a very large measure shaped our world. For example, modern simulations of galaxy formation cannot reproduce the structure of our galactic disk without taking the supernova feedback into account. Shock waves from ancient supernovae triggered further rounds of star formation. The iron in our blood was once synthesized inside a massive star and ejected in a supernova explosion.

For over half a century, researchers have been grappling to understand the physics of the explosion. The challenge of reconstructing the explosion mechanism from the light curves and the structure of the remnants is akin to reconstructing the cause of a plane crash from a debris field, without a black box. In fact, the supernova neutrinos are just like a black box: they record the information about the physical processes in the center of the explosion during the first several seconds, as it happens.

The explosion mechanism is thought to have three distinct stages: the collapse of the iron core, with the formation of the shock and its breakout through the neutrinosphere; the accretion phase, in which the shock temporarily stalls at the radius of about 200 km, while the material keeps raining in; and the cooling stage, in which the hot proto-neutron star loses its energy and trapped lepton number, while the re-energized shock expands to push out the rest of the star. All these stages are predicted to have distinct signatures in the neutrino signal. Thus, it should be possible to directly observe, for example, how long the shock is stalled. More exotic features of the collapse may be observable in the neutrino flux as well, such as possible transitions to quark matter or to a black hole. (An observation in conjunction with a gravitational wave detection would be especially interesting.) To correctly interpret the neutrino signal, one needs to take into account neutrino flavor oscillations. Over the last decades, the oscillations have been firmly established in solar neutrinos and a variety of terrestrial sources, which means that including them in the supernova case is no longer optional. As it turns out, however, the physics of the oscillations in the supernova environment is much richer than in any of the cases measured to date. Neutrinos travel through the changing profile of the explosion, with stochastic density fluctuations behind the expanding shock. Their flavor states are also coupled due to their coherent scattering off each other. The net result is a problem that requires supercomputers, as well as state-of-the-art analytical models, to understand.

The effort to understand this complicated evolution has its reward: the oscillation patterns come out very different for the normal and inverted mass hierarchies. There are also several smoking gun signatures one can look for: for example, the expanding shock and turbulence leave a unique imprint in the neutrino signal. The supernova signal also has a very high sensitivity to values of θ_{13} , down to the levels inaccessible in any laboratory experiment. Additional information on oscillation parameters, free of supernova model-dependence, will be available if Earth matter effects can be observed in detectors at different locations around the Earth [35,36]. The observation of this potentially copious source of neutrinos will also allow limits on coupling to axions, large extra dimensions, and other exotic physics (*e.g.* [?,?]).

Two comments need to be made at this point. First, it would be extremely valuable to

detect both the neutrinos and antineutrinos with high statistics, as the oscillations occur very different in the two channels. In the neutrino channel the oscillation features are in general more pronounced, since the initial spectra of ν_e and ν_μ (ν_τ) are always significantly different. Second, the problem is truly multidisciplinary and the neutrino physics and astrophysics go hand-in-hand. One needs to model both, and the payout one gets is simultaneous for both fields. For instance, one learns the sign of the neutrino hierarchy, the speed at which the shock expands, and the density profile of the star, “all in one package”. The better one understands the astrophysics, the better the quality of information about neutrino physics, and vice versa. Hence it is essential to gather as much high-quality information as possible, and to optimize ability to disentangle the flavor components of the flux. Currently, world-wide sensitivity is primarily to electron anti-neutrinos, via inverse beta decay on free protons, which dominates the interaction rate in water and liquid-scintillator detectors. LAr has a unique sensitivity to the *electron neutrino* component of the flux, via the absorption interaction on ^{40}Ar , $\nu_e + ^{40}\text{Ar} \rightarrow e^- + ^{40}\text{K}^*$. In principle, this interaction can be tagged via the de-excitation gamma cascade. About 900 events would be expected in a 10-kton fiducial LAr detector for a supernova at 10 kpc. The number of signal events scales with mass and the inverse square of distance as shown in Figure 2-9. For a collapse in the Andromeda galaxy, detectors of

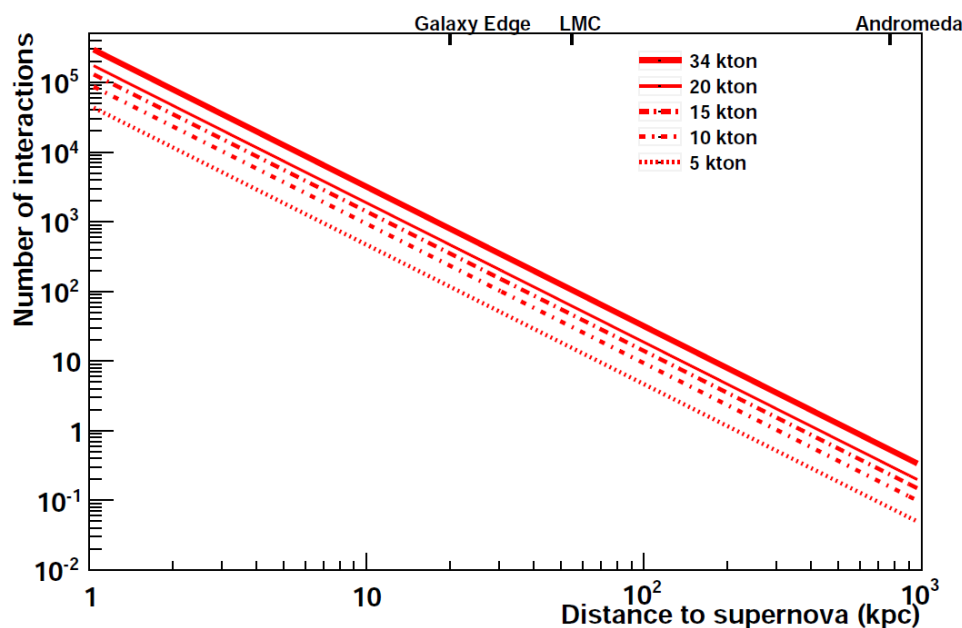


Figure 2-9: Number of supernova neutrino interactions in an LAr detector as a function of distance to the supernova, for different detector masses. Core collapses are expected to occur a few times per century, at a most-likely distance of about 10–15 kpc.

100 ktons of mass would be required to observe a handful of events. However even a small 10-kton detector would gather a unique ν_e signal from supernovas within the Milky Way.

As a final note, because the neutrinos emerge promptly after core collapse, in contrast to the electromagnetic radiation which must beat its way out of the stellar envelope, an observed

1 neutrino signal can provide a prompt supernova alert [37,?]. This will allow astronomers
2 to find the supernova in early light turn-on stages, which may yield information about the
3 progenitor (in turn important for understanding oscillations). The LBNE detector(s) should
4 be designed to allow prompt alert capability.

5 Several other experiments sensitive to supernova neutrinos will be online over the next few
6 decades [32,?]. However one should not consider these to be “competition” for a supernova
7 detection by LBNE: more experiments online during a supernova burst will only enhance
8 the science yield from a supernova, and the ability to measure fluxes at different locations
9 around the Earth will make the whole more than the sum of the parts [35].

DRAFT

3 Overview of the LBNE Project and Design

3.1 LBNE and the U.S. Neutrino-Physics Program

In its 2008 report, the Particle Physics Project Prioritization Panel (P5) recommended a world-class neutrino-physics program as a core component of the U.S. particle-physics program [5]. Included in the report is the long-term vision of a large detector at the formerly proposed Deep Underground Science and Engineering Laboratory (DUSEL, now SURF, the Sanford Underground Research Facility) at the site of the Homestake Mine in Lead, SD, and a high-intensity neutrino source at Fermi National Accelerator Laboratory (Fermilab). The baseline between Fermilab and SURF is 1300km.

On January 8, 2010, the Department of Energy approved the Mission Need [?] for a new long-baseline neutrino experiment that would enable this world-class program and firmly establish the U.S. as the leader in neutrino science. The LBNE Project is designed to meet this Mission Need.

With the facilities provided by the LBNE Project and the unique features of the experiment – in particular the long baseline, the broad-band beam and the high resolution of the detector – the LBNE Science Collaboration proposes to mount a broad attack on the physics of neutrino oscillations with sensitivity to all poorly known parameters in a single experiment. The focus of the program will be the explicit demonstration of leptonic CP violation, if it exists, by precisely measuring the asymmetric oscillations of muon-type neutrinos and antineutrinos into electron-type neutrinos and antineutrinos. The experiment will enable precise measurements of the neutrino-oscillation parameters, in particular, the CP-violating phase in the three-flavor framework, and the search for new physics that would show up as deviations from this model.

It is currently planned to implement LBNE as a phased program, with increased scientific capabilities at each phase. The initial phase project (LBNE10), which received CD-1 approval in December 2012, consists of a new neutrino beamline at Fermilab, tertiary muon detectors to monitor the beam, and a 10-kton liquid argon TPC far detector located at SURF, placed at the surface under several meters of shielding. Table 3-1 summarizes the principal parameters

of LBNE10, as defined at CD-1:

Table 3-1: Principal parameters of LBNE10 as defined at CD-1

Project Element Parameter	Value
Near- to Far-Site Baseline	1,300 km
Primary Proton Beam Power	708 kW, upgradable to 2.3 MW
Protons on Target per Year	6.5×10^{20}
Primary Beam Energy	60 – 120 GeV (tunable)
Neutrino Beam Type	Horn-focused with decay volume
Neutrino Beam Energy Range	0.5 – 5 GeV
Neutrino Beam Decay Pipe Diameter \times Length	4 m \times 200 m
Far Detector Type	LArTPC
Far Detector Active (Fiducial) Mass	13.5 (10) ktons

1

2 Subsequent phases of LBNE will include the construction of a near neutrino detector on the
3 Fermilab site and construction of a larger detector underground at SURF.

4 A configuration of the LBNE facility in which the Far Detector is located deep underground
5 would also provide opportunities for research in other areas of physics, such as nucleon
6 decay and neutrino astrophysics, including studies of neutrino bursts from locally occurring
7 supernovae.

8 3.2 Sanford Underground Research Facility (SURF)

9 The Sanford Underground Research Facility [?] is a laboratory dedicated to underground
10 science located at the former Homestake gold mine in Lead, South Dakota. Underground
11 neutrino experiments at Homestake Mine date back to 1967 when nuclear chemist Ray Davis
12 installed a solar neutrino experiment 4,850 feet underground. Ray Davis earned a share of the
13 Nobel Prize for Physics in 2002 for the Homestake mine solar neutrino experiment which ran
14 until 1993. Homestake mine is the deepest mine in the western hemisphere with extensive
15 drifts both in depth and laterally. A cross-section of the Homestake mine development is
16 shown in Figure 3-1.

17 Homestake mine closed in 2003, but the company donated the property to the state of South
18 Dakota in 2006 for use as an underground laboratory. The South Dakota state legislature
19 created the South Dakota Science and Technology Authority to operate the lab. The state
20 Legislature has committed more than \$40 million in state funds to the project, and South
21 Dakota also obtained a \$10 million Community Development Block Grant to help rehabilitate
22 Homestake. In addition, a \$70 million donation from philanthropist T. Denny Sanford was
23 used to reopen the gold mine for science and to establish a Sanford Center for Science

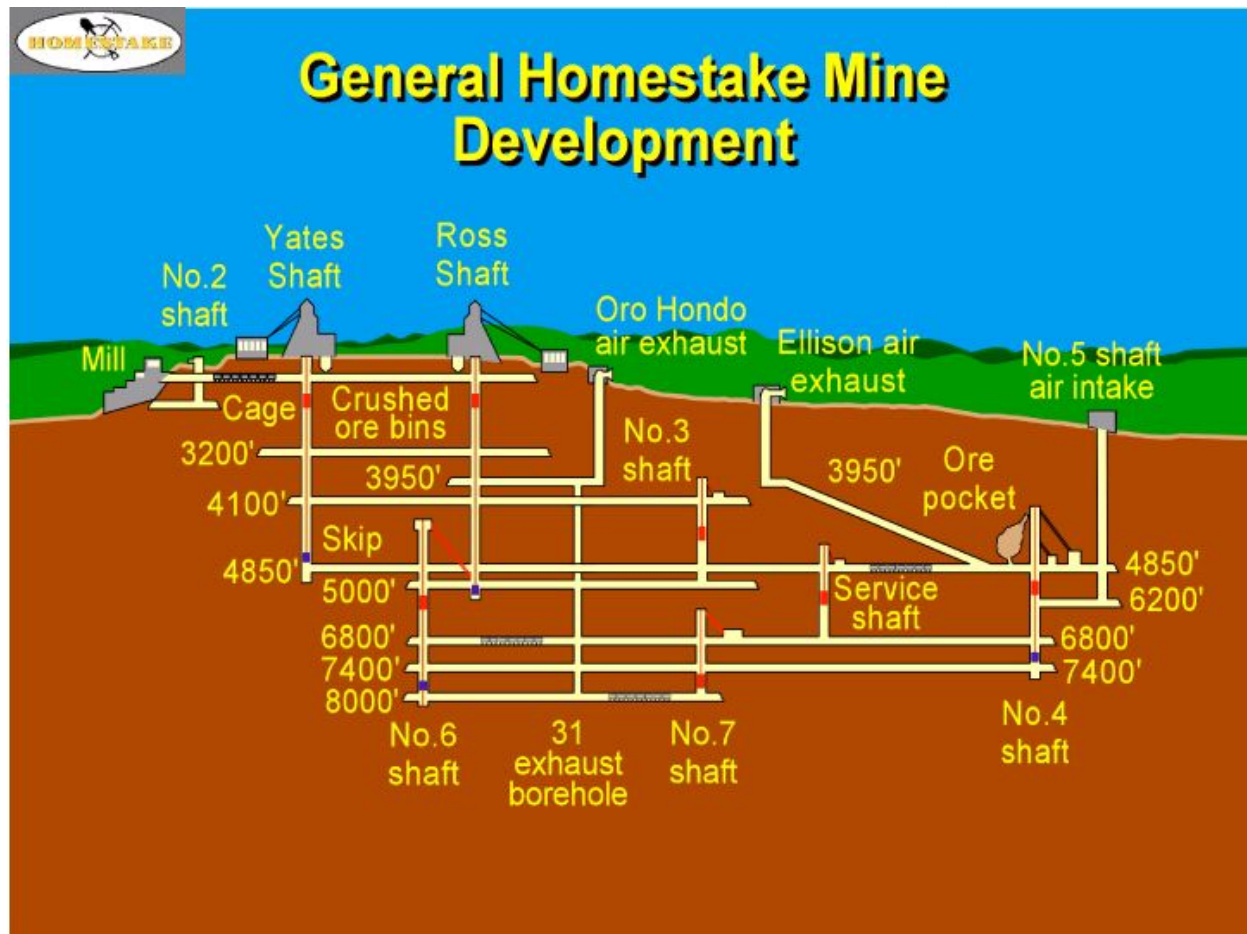


Figure 3-1: Vertical cross-section of the Homestake Mine indicating the areas developed for mining. SURF is currently developing levels down to the 4850' for science applications.

Education. The depth of the areas currently being developed for science at SURF make it an extremely competitive location for a large underground detector like that envisioned for LBNE. The predicted cosmic ray flux at Homestake mine [?] as compared to other underground laboratories world wide is shown in Figure 3-2.

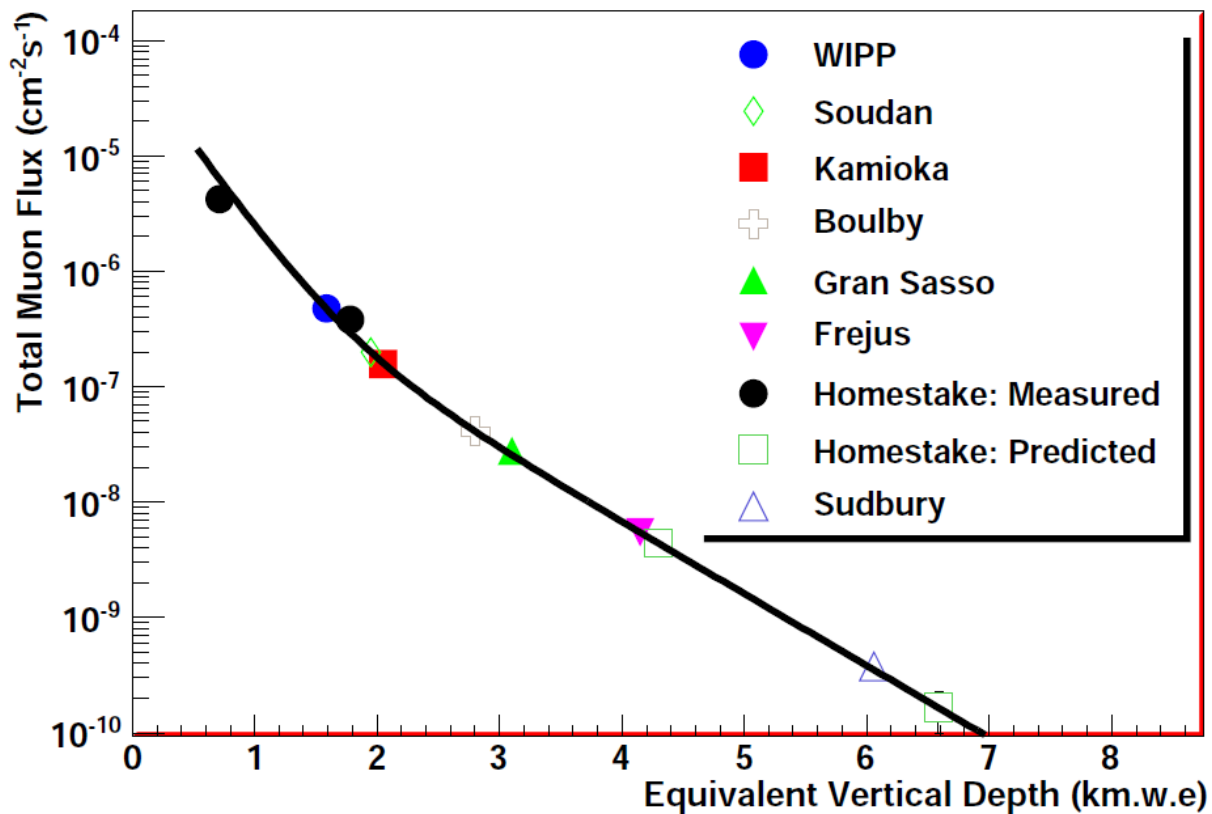


Figure 3-2: The predicted cosmic ray flux at the 4850' and 8000' level at Homestake mine is shown as open green squares. Comparison to other underground laboratories are shown [?].

The first two major physics experiments at the Sanford Lab are being installed 4,850 feet underground in an area called the Davis Campus, named for the late Ray Davis. The Large Underground Xenon (LUX) experiment has been installed in the same cavern excavated for Ray Davis in the 1960s. LUX will be the most sensitive detector yet to search for dark matter. The Majorana Demonstrator experiment, also being installed in 2013, will search for neutrinoless double-beta decay. The Majorana Demonstrator experiment is in a newly excavated space in the Davis Campus, adjacent to the original Davis cavern. Sample images from the LUX and Majorana Demonstrator activities at the 4850 foot level are shown in Figure 3-3. The U.S. Department of Energy is also considering the Sanford Underground Research Facility as the site for proposed longer term experiments in addition to LBNE, including, for example, a project entitled Dual Ion Accelerators for Nuclear Astrophysics (DIANA). Figure 3-4 prepared by Sanford Lab Director Mike Headley and Head of Operations Kevin Lesko demonstrates the long term potential for experiments at SURF.



Figure 3–3: Sanford Underground Research Facility: Administration building and Yates shaft headframe (top left); corridor at 4850 ft (1480m) depth leading to clean rooms and experimental halls (top right); billet of radiopure electroformed copper for the Majorana Demonstrator experiment being placed on a lathe in a clean room at 4850 ft depth (bottom left); LUX experiment at 4850 ft depth (bottom) right.

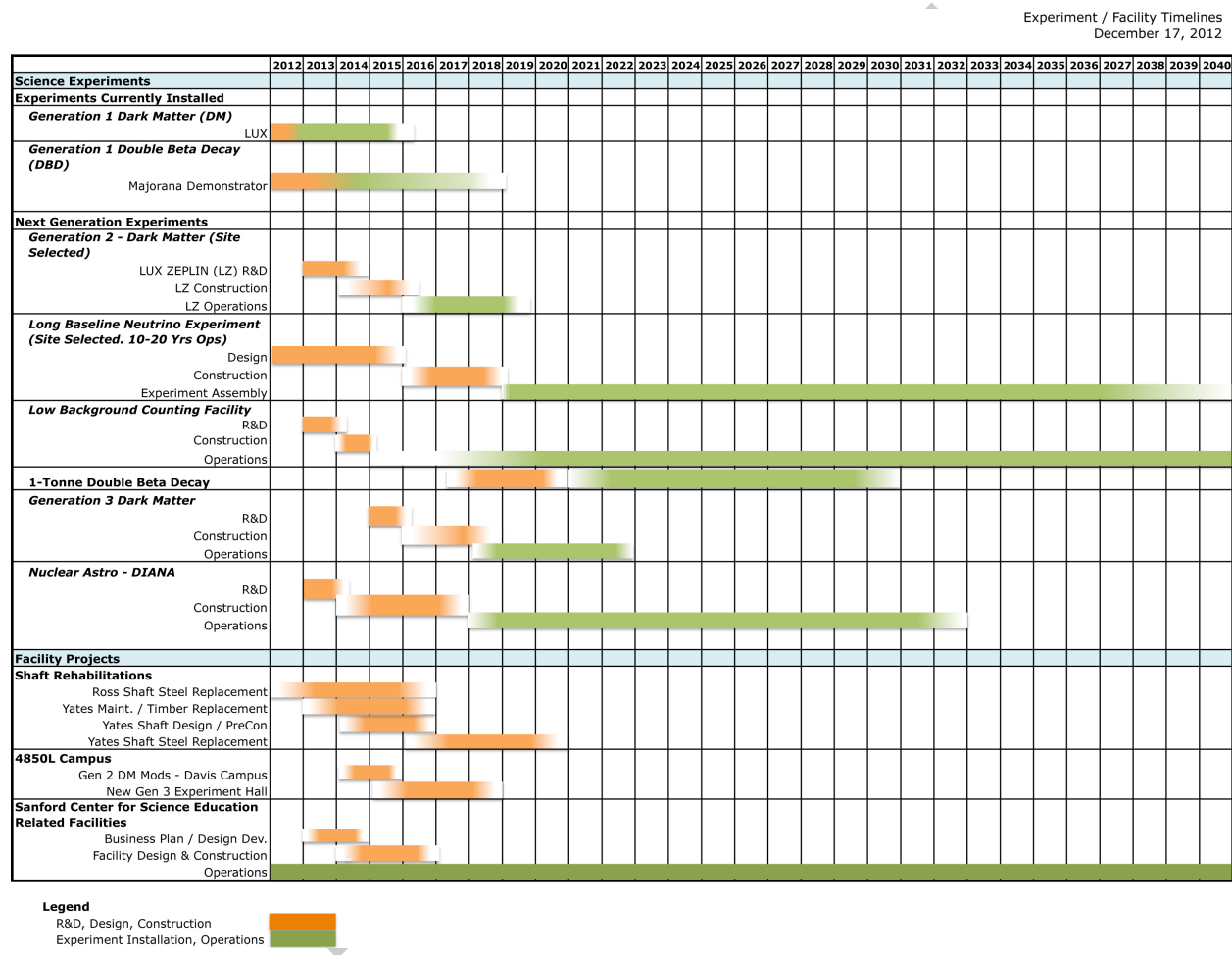


Figure 3-4: Timeline exploring the long term potential of deep science experiments at SURF.

3.3 Fermi National Accelerator Laboratory

Fermi National Accelerator Laboratory, located 40 miles east of Chicago, Illinois produces the worlds most powerful neutrino beams. The neutrino beams come from two of the lab's proton accelerators (see Figure 3-5), the 8 GeV Booster which feeds the Booster Neutrino Beamline (BNB) and the 120 GeV Main Injector which feeds the Neutrinos at the Main Injector beamline (NuMI).

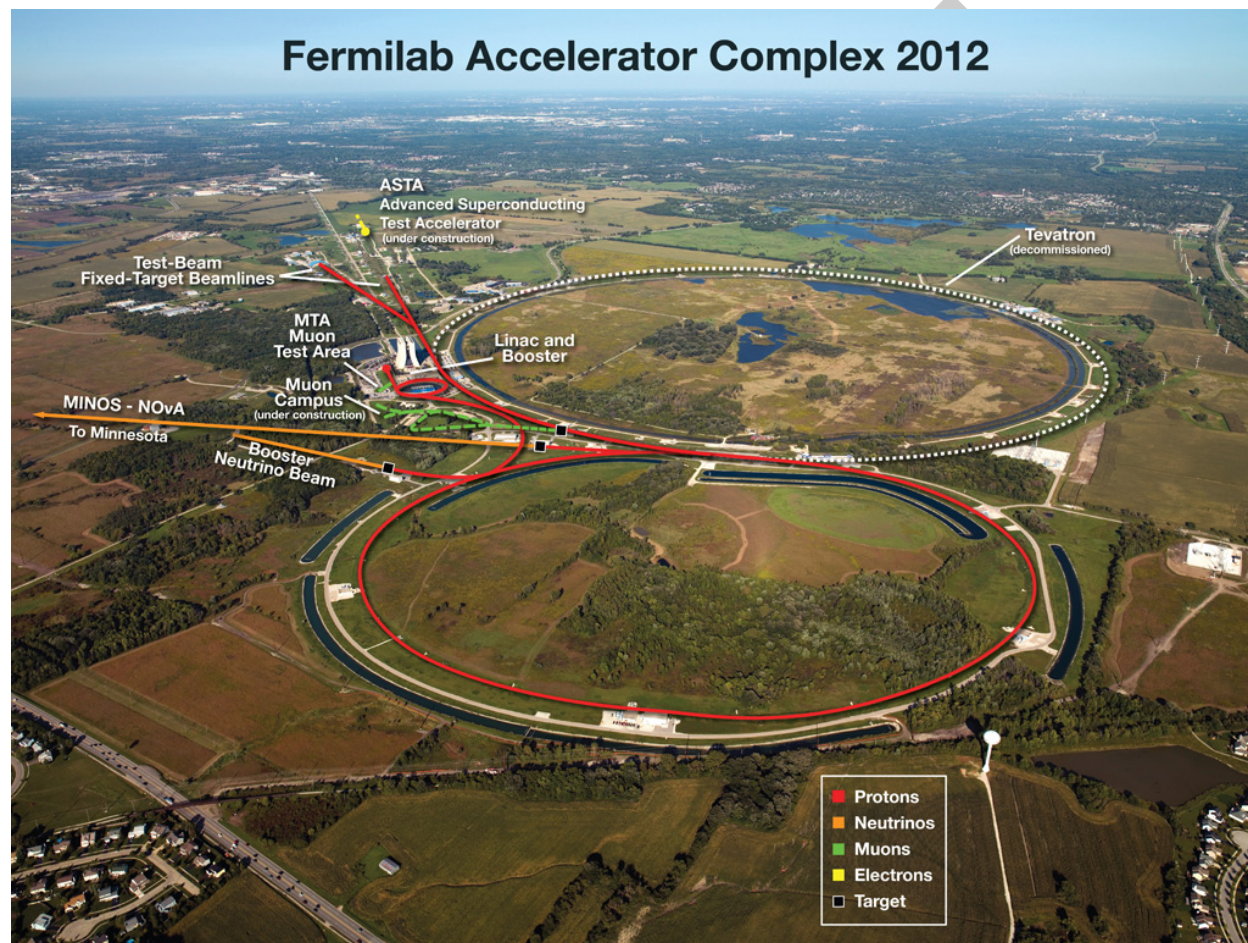


Figure 3-5: The accelerator chain at Fermi National Accelerator Laboratory. A 400 MeV linac feeds into the 15Hz Booster which produces an 8 GeV beam. The Booster beam is used for the Booster Neutrino Beamline experiments. The Booster feeds into the 120 GeV Main Injector which will operate at 708kW beginning in 2013. The Main Injector is the source for the NuMI beamline which supplies a high power high energy neutrino beam to the MINOS/MINOS+ and NOvA experiments.

NuMI is a high energy neutrino beam that has been operating since 2004. NuMI was designed for steady 400 kW operation and achieved that goal by the end of the MINOS experimental

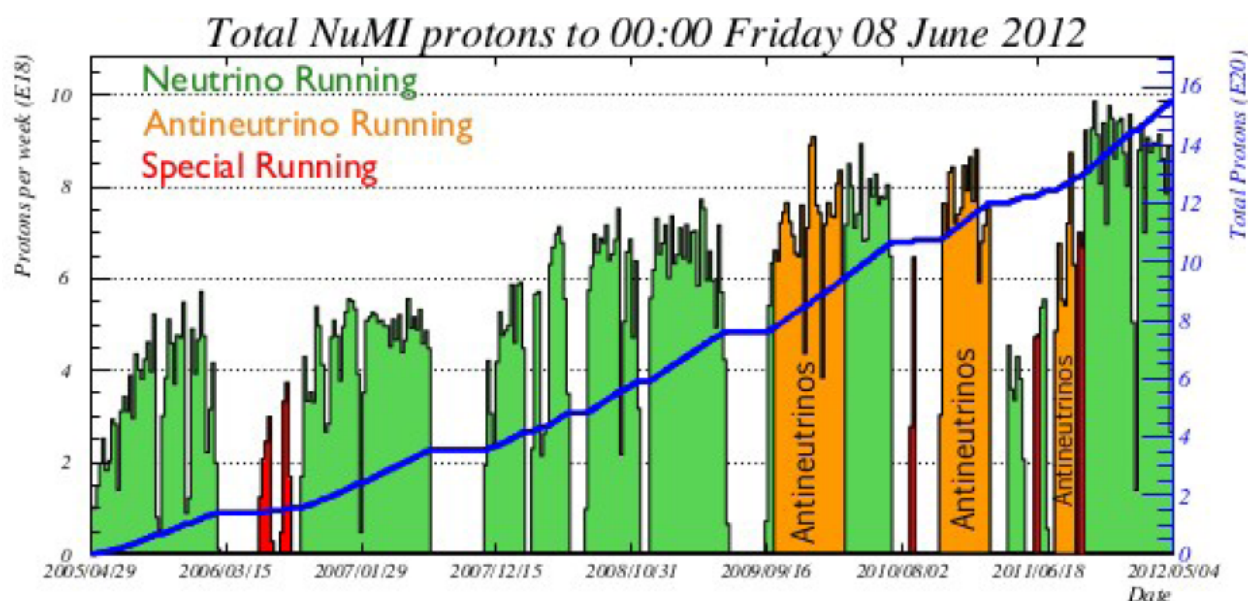


Figure 3-6: The NuMI beamline performance

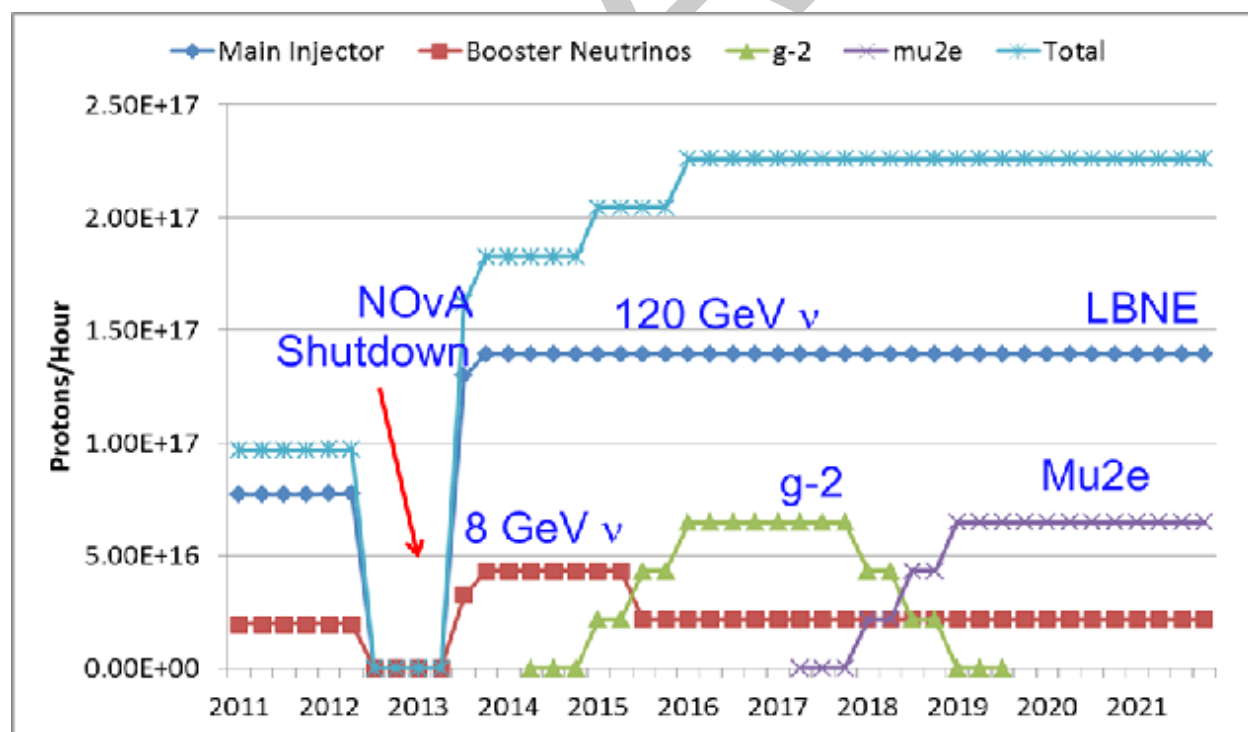


Figure 3-7: Fermilab proton source proton flux ramp up expectations for the Intensity Frontier.

run in 2012. As shown in Figure 3-6, the NuMI beamline was integrating an average of 9×10^{18} protons per week ($\approx 2.7 \times 10^{20}$ protons-on-target per year) in mid 2012.

The Fermilab accelerator complex is currently undergoing an upgrade for the next phase of operations. The proton improvement plan is shown in Figure 3-7. The Main Injector will deliver 708 kW to the neutrino program starting in 2013. ($\approx 6 \times 10^{20}$ protons-on-target per year).

In the decade beyond 2020, Fermilab has proposed a series of upgrades to the current complex known as Project X [8]. The Project X upgrades propose to replace the existing injector complex in stages, first replacing the 400 MeV conventional pulsed linac with a 1 GeV superconducting CW linac, and later replacing the 8 GeV Booster synchrotron with a superconducting pulsed linac, as shown in Figure 3-8

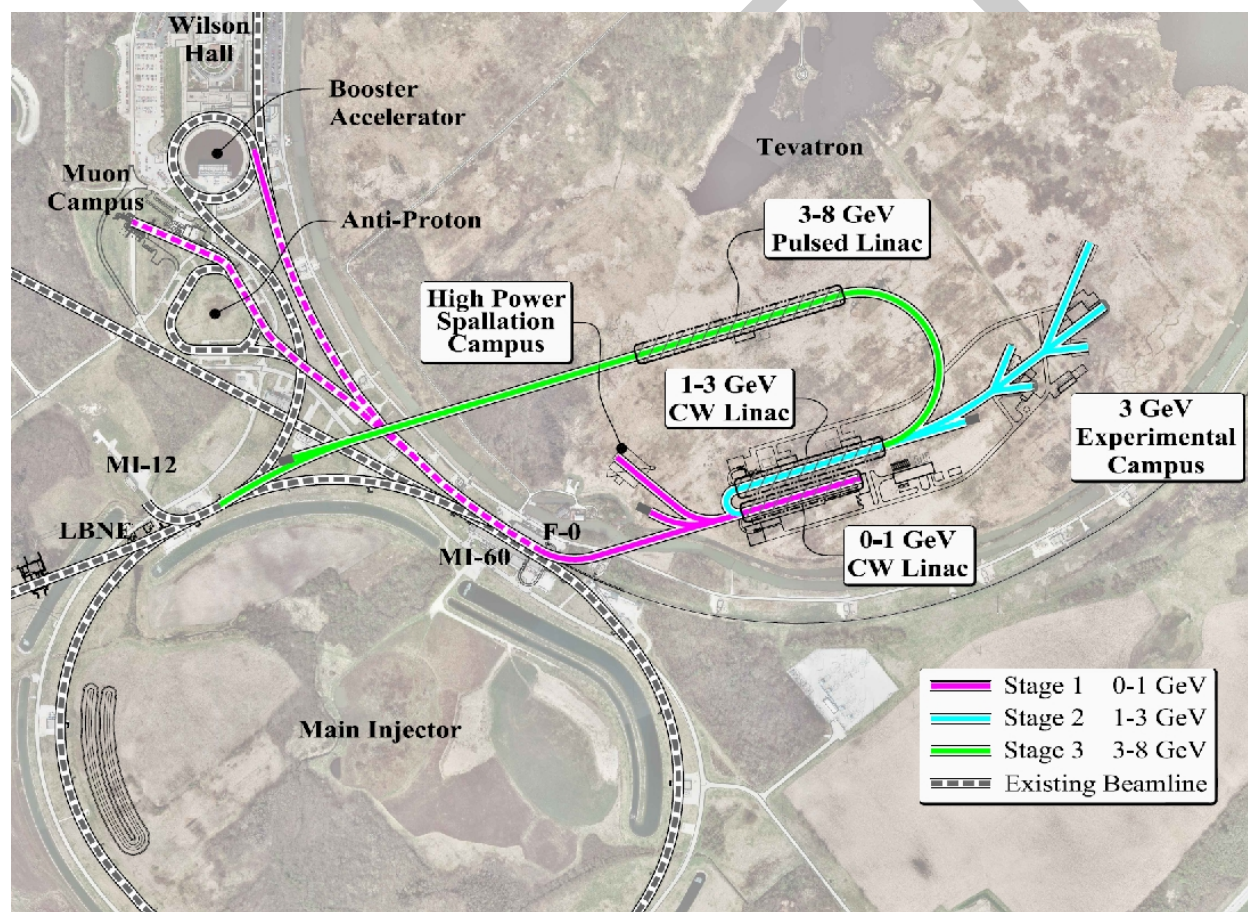


Figure 3-8: Proposed upgrades to the Fermilab accelerator complex under Project X

The planned stages of Project X and the future experimental research programs planned are summarized in Table 3-2.

The LBNE beamline which is described in detail in Section 3.4 will utilize the Main Injector

Table 3–2: The current and future experimental research programs planned for the Fermilab accelerator complex.

Program Description	2013 NO ν A	PROJECT X			
		Stage 1 (2025 ?) 1 GeV CW linac	Stage 2 3 GeV CW linac	Stage 3 RDR	Stage 4 beyond RDR
MI Neutrinos	470-700 kW	515-1200 kW	1200 kW	2450kW	2450-4000 kW
8 GeV neutrinos	15 kW +0-50kW**	0-42kW +0-90 kW**	0-84 kW*	0-172 kW*	3000kW
8 GeV Muons	20 kW	0-20 kW*	0-20 kW*	0-172 kW*	1000 kW
1-3 GeV Muons	—	80 kW	1000 kW	1000 kW	1000 kW
Kaons	0-30 kW** ($< 30\%$ df) (from MI)	0-75 kW** ($< 45\%$ df) (from MI)	1100 kW	1870 kW	1870 kW
Nuclear edm ISOL	none	0-900 kW	0-900 kW	0-1000 kW	0-1000 kW
Ultra-cold neutrons	none	0-900 kW	0-900 kW	0-1000 kW	0-1000 kW
Nuclear technology	none	0-900 kW	0-900 kW	0-1000 kW	0-1000 kW
# Programs	4	8	8	8	8
Total max power	735 kW	2222 kW	4284 kW	6492 kW	11870kW

* Operating point in range depends on Main Injector (MI) energy for neutrinos.

** Operating point in range depends on MI inject or slow-spill duty factor (df) for kaon program.

- 1 120 GeV beam and is heavily modeled on the highly succesful NuMI beamline. LBNE is
- 2 planned to initially use the same targeting and focusing technology as NuMI.

3.4 The LBNE Beamline

LBNE will utilize a Beamline facility located at Fermilab to carry out a compelling research program in neutrino physics. The facility will aim a beam of neutrinos with a net 5.8° downward vertical bent toward a detector placed at the Sanford Underground Research Facility (SURF) in South Dakota, about 1,300 km away. The main elements of the facility, which is expected to be fully contained within Fermilab property, are a primary proton beamline, a neutrino beamline, and conventional facilities to support the technical components of the proton and neutrino beamlines. More detailed information can be found in the Conceptual Design Report [10].

The primary proton beam, in the energy range of 60-120 GeV, will be extracted from the MI-10 straight section of Fermilab's Main Injector using single-turn extraction. The beam is then transported to the target area with very low losses within a beam enclosure embedded in an earthen, engineered filled embankment (hill) whose dimensions are commensurate with the bending strength of the required dipole magnets (see Figures 3-9 and 3-10).



Figure 3-9: Plan view of the overall Near Site Project layout showing the LBNE Beamline extraction point from the Main Injector, the primary beamline, target hall, decay pipe and absorber.

For 120 GeV operation and with the Main Injector upgrades implemented for the NOvA experiment [38], the fast, single turn extraction will deliver all the protons (4.9×10^{13}) in one machine cycle (1.33 sec) to the LBNE target in $10 \mu\text{s}$. The initial operation of the facility is expected to be at a beam power of 700 kW, with the capability to support an upgrade to 2.3 MW with the planned Project X [39], which includes the replacement of the existing proton

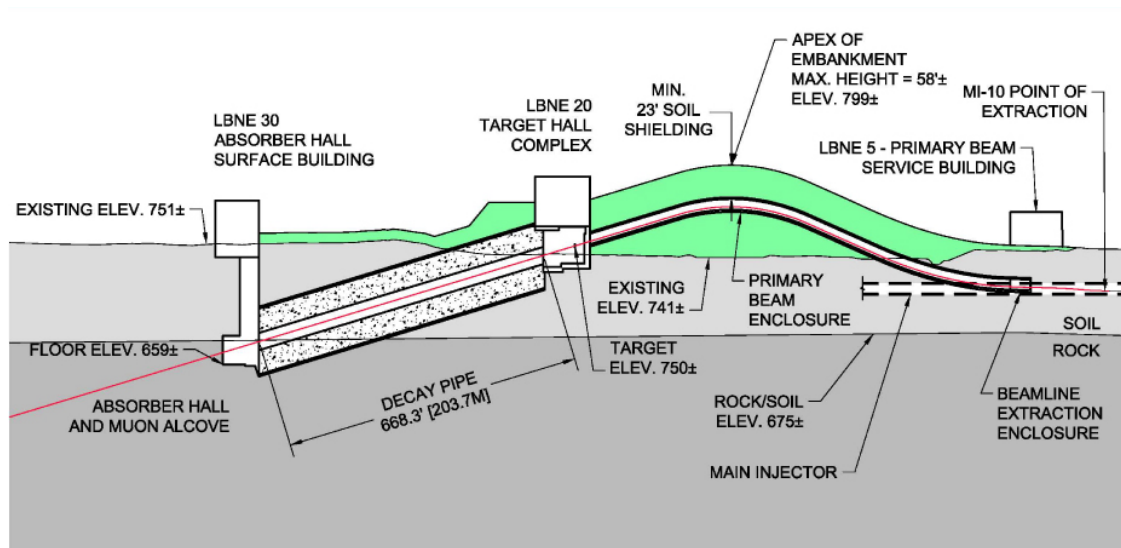


Figure 3-10: Longitudinal section of the LBNE Beam Line facility. The beam comes from the right, the protons being extracted from the MI-10 extraction point at the Main Injector.

source that feeds the Main Injector. The accelerator complex and the primary beamline are planned to deliver 6.5×10^{20} primary protons to the neutrino target per year for 700 kW operation. Neutrinos are produced after protons from the Main Injector hit a solid target where approximately 85% of the protons interact producing pions and kaons which are subsequently focused by a set of magnetic horns into a decay pipe where they decay into muons and neutrinos (Figure 3-11). A wide-band sign-selected neutrino beam is needed to cover the first and second neutrino oscillation maxima, which for a 1,300 km baseline are at approximately 2.5 and 0.8 GeV respectively. The beam therefore must provide neutrino flux in the energy range 0.5 to 5 GeV covering both oscillation peaks.

The reference target design for LBNE is an upgraded version of the NuMI-LE (Low Energy) target that was used for 7 years to deliver beam to the MINOS experiment. The target consists of 47 segments, each 2 cm long, of POCO graphite ZXF-5Q. Focusing of charged particles is achieved by two magnetic horns in series, the first of which partially surrounds the target. They are both NuMI/NOvA design horns with double paraboloid inner conductor profiles and currents of up to 200 kA. The decay volume in the LBNE reference design is an air-filled, air-cooled pipe of circular cross section with its diameter (4m) and length (204m) optimized such that decays of the pions and kaons result in neutrinos in the energy range useful for the experiment. At the end of the decay region, the absorber, a water cooled structure of aluminum and steel, is needed to remove the residual particles remaining at the end of the decay pipe. This complex device, which must absorb a large fraction of the incident beam power of up to 2.3 MW, is also instrumented to measure the transverse distribution of the resultant hadronic showers to monitor the beam on a pulse-by-pulse basis. An array of muon detectors in a small muon alcove immediately downstream of the absorber provide information on the direction, profile and flux of the neutrino beam.

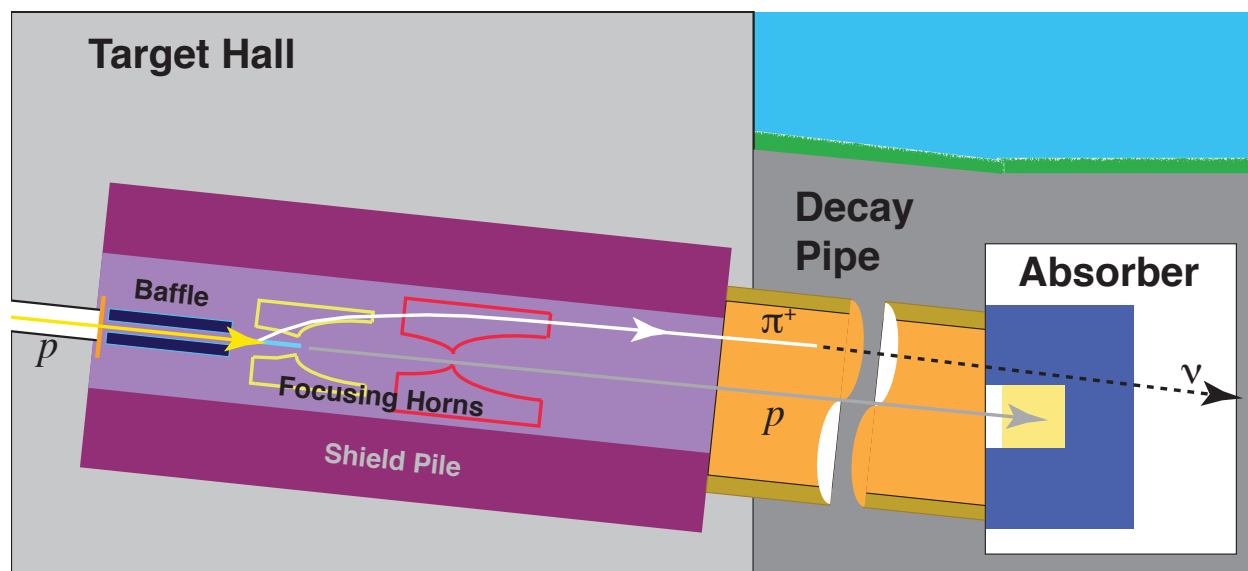


Figure 3–11: A cartoon of the LBNE neutrino beamline showing the major components of the neutrino beam. From left to right (the direction of the beam): the beam window, horn-protection baffle, target, the two toroidal focusing horns, decay pipe and absorber.

1 The Fermilab Conventional Facilities include the civil construction required to house the
 2 Beamline components and their layout is shown in Figs. 3–9 and 3–10. Following the beam
 3 from southeast to northwest, or from right to left in the figure, is the underground Extrac-
 4 tion Enclosure, the Primary Beam Enclosure inside the embankment and its accompanying
 5 surface-based Service Building (LBNE 5), the Target Complex (LBNE 20) located in the
 6 embankment, the Decay Pipe, the underground Absorber Hall with the muon alcove, and its
 7 surface-based Service Building (LBNE 30). The embankment will need to be approximately
 8 290m long and 18 m high above grade at its peak. The planned near neutrino detector facility
 9 is located as near as is feasible to the west site boundary of Fermilab, along the line-of-sight
 10 indicated in red in Fig. 3–9.

11 The parameters of the Beamline facility were determined taking into account several factors
 12 including the physics goals, the Monte Carlo modeling of the facility, spatial and radiologi-
 13 cal constraints and the experience gained by operating the NuMI facility at Fermilab. The
 14 relevant radiological concerns, prompt dose, residual dose, air activation and tritium produc-
 15 tion have been extensively modeled and the results implemented in the system design. The
 16 Beamline facility design described above minimizes expensive underground construction and
 17 significantly enhances capability for ground-water radiological protection. In general, com-
 18 ponents of the LBNE beamline system which cannot be replaced or easily modified after
 19 substantial irradiation at 700 kW operation are being designed for 2.3 MW. Examples of
 20 such components are the shielding of the target chase and decay pipe and the absorber with
 21 its associated shielding.

22 In order to increase the neutrino event rates, we are considering the following design im-

1 improvements before baselining the experiment:

- 2 • Increasing the length of the decay pipe up to 250 m (the maximum length allowed by
3 the existing Fermilab site boundaries), and possibly the diameter of the decay pipe up
4 to 6m.
- 5 • Filling the decay pipe with helium instead of air, which is expected to both increase
6 the neutrino event rates by about 10% as well as reduce the systematics of neutrino
7 flux predictions. The increase of flux with helium in the decay pipe with respect to air
8 is show in figure 3-12 and table 3-3. Fig 3-12 shows the unoscillated ratio of helium to
9 air flux at the far detector with the the beamline, excuding the decay pipe material, set
10 to the configuration as described above. The horn currents were set to select ν_μ events.
11 Table 3-3 shows the integrated values of the ratio over the indicated energy regions. In
12 the region of the first oscillation maximum, for example, there is approximately a 11%
13 increase of the helium flux compared to the air flux. In addition, there is a decrease
14 in $\bar{\nu}$ contamination. Introducing He in the decay pipe would require the design and
15 construction of a decay pipe window. A decay pipe window design and different options
16 for cooling a He filled decay pipe are under study.
- 17 • Increasing the horn current of the NuMI design horns by a modest amount (from 200kA
18 to 230 kA) is expected to increase the neutrino event rates by about 10-12% at the
19 first oscillation maximum [?] and we are in the process of evaluating this option by
20 performing a Finite Element Analysis simulation and cooling test of the horns.
- 21 • Using materials for the target alternate to the POCO graphite (e.g., Be) to increase
22 the target longevity. This would involve additional R&D effort and design work. A Be
23 target could be shorter potentially improving the horn focusing.
- 24 • Developing more advanced horn designs, which could boost the low-energy flux in the
25 region of the second oscillation maximum. It should be noted that the target and horn
26 system can be modified or replaced even after operations have begun, if improved
27 designs are developed that will enable higher instantaneous or integrated beam flux.

28 Table 3-3 summarizes the impact of the beam design changes currently under consideration
29 by the LBNE beam project team. The impact of all the changes is an increase of $\sim 50\%$
30 in the ν_e appearance signal rate at the far detector. Increases to the decay pipe (DP) size
31 would require additional cost of the order several 10's \$M.

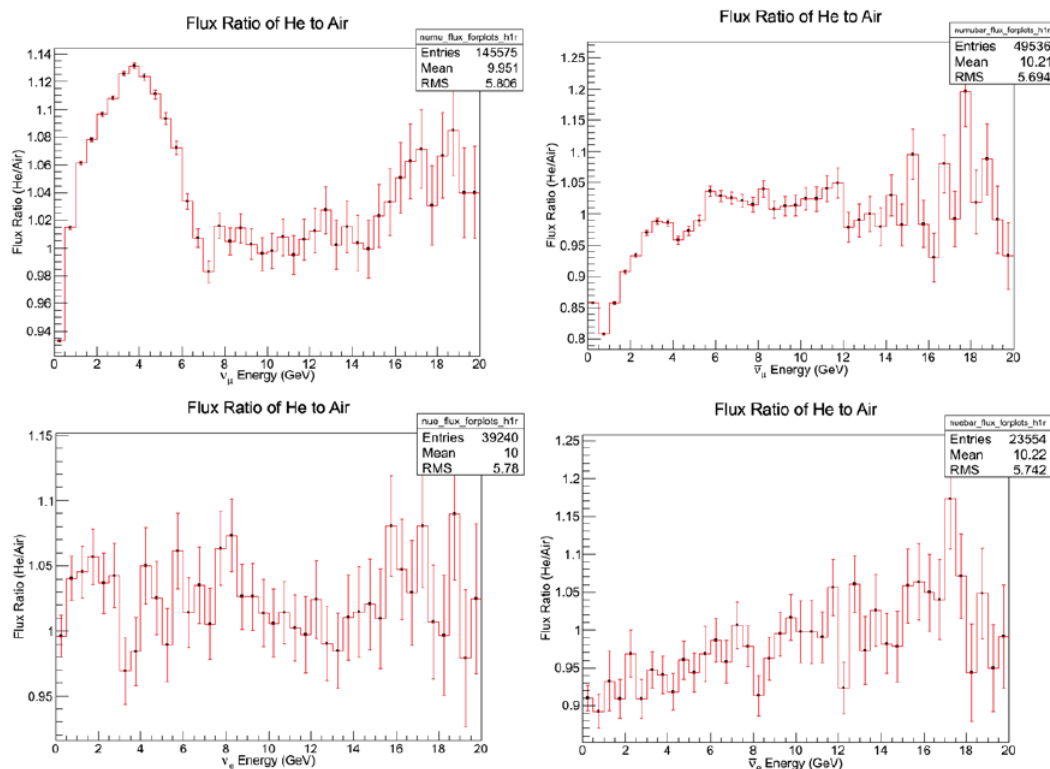


Figure 3-12: The unoscillated ratio of helium to air flux at the far detector with the beamline, excluding the decay pipe material, set to the configuration as described in the text. The horn currents were set to select ν_μ events. There are approximately 25000k protons on target for both the helium and air configurations.

Table 3-3: Impact of the beam upgrades on the neutrino $\nu_\mu \rightarrow \nu_e$ CC appearance rates at the far detector in the range of the first and second oscillation maxima. The numbers are the ratio of appearance rates to the CDR beam design.

Changes	0.5-2GeV	2-5GeV
DP Air \rightarrow He	1.07	1.11
DP length 200m \rightarrow 250m	1.04	1.12
Horn current 200kA \rightarrow 230kA	1.00	1.12
Proton beam 120 \rightarrow 80GeV, 700kW	1.14	1.05
Target graphite \rightarrow Be	1.10	1.00
DP diameter 4m \rightarrow 6m	1.06	1.02
Total	1.48	1.50

3.5 The Near Detector Complex

According to the current plan for LBNE Phase-I, the neutrino beam will be monitored with a sophisticated array of muon detectors placed just downstream of the absorber, as shown in Figure 3-13. The ionization chamber array will provide pulse-by-pulse monitoring of the beam profile and direction. The variable-threshold gas Cherenkov detectors will map the energy spectrum of the muons exiting the absorber on an on-going basis. The stopped muon detectors will sample the lowest energy muons. The muons measured by this system correlate fully with the neutrino flux above 3 GeV. Thus, they sample the equivalent of about half the neutrino flux near the first oscillation maximum, and sample a decreasing fraction at lower energy. Preliminary studies show that this system, augmented by the existing level of understanding of the similar NuMI beam as well as the incorporation of several other strategies, will be adequate for the initial period of LBNE running. We note that with its excellent particle identification capabilities, the choice of an LArTPC far detector results in less reliance on the near detector systems for calibration and neutrino interaction response studies.

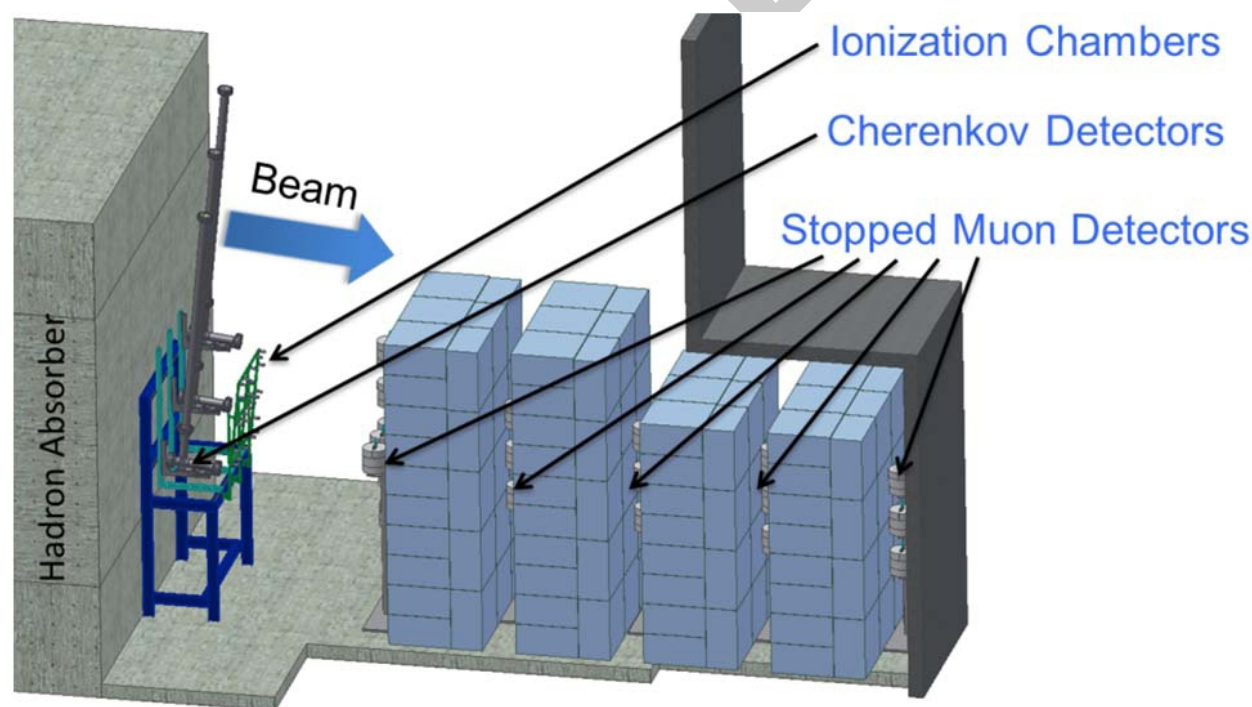


Figure 3-13: System of tertiary muon detectors, which will monitor the LBNE neutrino beam in Phase-I of the project.

Nevertheless, a full near neutrino detector coupled with the tertiary muon measurements is highly desirable in the long term, and is needed to achieve the full scientific agenda of LBNE. We are working with potential international partners who could help build a highly-capable

near neutrino detector in the initial phase or soon after the operation of LBNE.

The neutrino near detector needs to measure the unoscillated flux spectrum for all species in the beam: ν_μ , ν_e , $\bar{\nu}_\mu$, and $\bar{\nu}_e$. This requires a magnetized detector with good efficiency for identifying and measuring electrons and muons. If, in addition, we require the detector to distinguish e^+ from e^- , a low-density detector with a long physical radiation length would be required. The near detector should also make measurements using the same argon target nucleus as the far detector, and ideally should use the same detection technique as the far detector to allow cancellation of systematic errors. The last requirement suggests the use of a magnetized LArTPC.

However the multiple requirements are somewhat at odds, and as a consequence LBNE has considered two candidate neutrino near detector designs: a magnetized LAr TPC and a magnetized straw-tube tracker with embedded high-pressure Ar gas targets (see Figure 3-14). Both are placed inside a 0.4 T dipole magnet, with muon detectors in the yoke steel and downstream steel absorbers. The lower-density straw-tube detector is also surrounded by an electromagnetic calorimeter inside the dipole coil. A full description of these two candidate

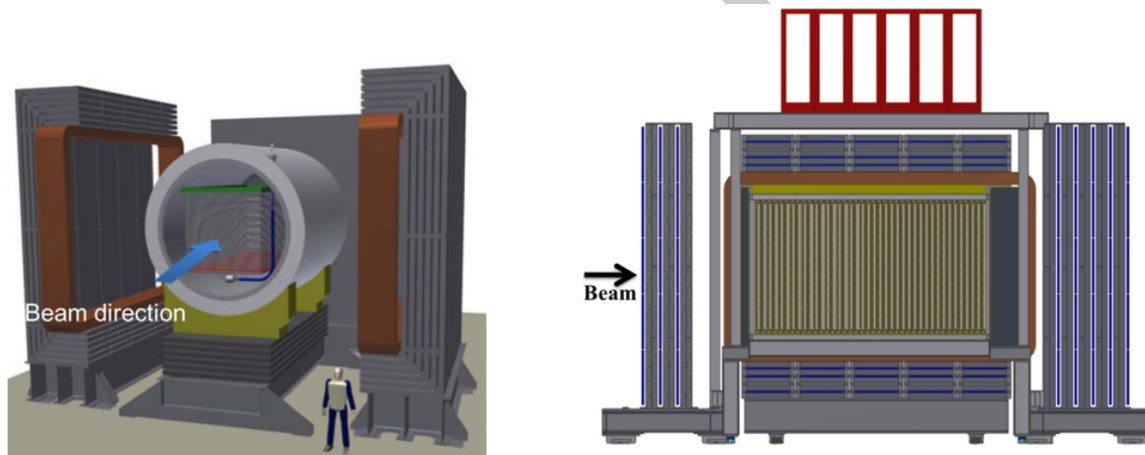


Figure 3-14: Two candidate near detectors: a magnetized LAr TPC (left) and a magnetized straw-tube tracker with embedded high-pressure Ar gas targets (right)

detectors can be found in the March 2012 LBNE CDR (see Volume 3 of Ref. [?]). A more complete description of the straw-tube tracker design, including extensive discussion of its physics capabilities, can be found in Ref. [?].

The addition of a high resolution neutrino near detector to LBNE coupled with the precision absolute flux measurements from the tertiary muon detectors will enable a diverse range of physics measurements as discussed in Chapter 4.

3.6 The LBNE Far Detector

In this section we summarize the key features of the LBNE far detector. As mentioned earlier, the central design consideration throughout the LBNE development process has been the importance of scalability, and the flexibility that it enables. This has been of critical importance for the project as it has evolved since its inception in 2009. Thus, we start with a description of the surface 10-kt LArTPC far detector configuration that has been selected for the initial phase of LBNE and presented at CD-1. We also discuss the significant differences associated with other configurations that could be accomplished in the initial phase with the identification of additional resources, or at a later stage (*i.e.*, the fully realized LBNE configuration). Because of the emphasis on scalability, these differences are modest and easily implemented.

Aside from scalability, general considerations for the construction of a large LArTPC include: (1) cryogenic safety and the elimination of hazards associated with large cryogenic liquid volumes, (2) attainment of stringent argon purity requirements (< 0.2 ppb O_2 concentration, for example) with respect to electronegative contaminants, (3) ease of transport and assembly of TPC mechanical systems, and (4) efficient deployment of high sensitivity/low-noise electronics for readout of the ionization signal.

3.6.1 Surface Detector for LBNE Phase-I

The far detector option presented at CD-1 for the LBNE Phase-I project (LBNE10) consists of two 9.4 kt liquid argon vessels, each designed to hold a 5-kt fiducial mass Liquid Argon Time Projection Chamber (LArTPC) as shown in Figure 3-15 (see Ref. [?]). The detectors will be constructed and operated in a detector hall on the surface of the SURF site, above the former Homestake mine. Construction of the detector hall requires excavation of a pit of depth 17.6m, width 37.4m, and length 30m such that the vessels will be below grade. The building in which this hall will be located is designed to support three meters of overburden to shield the detector against hadronic and electromagnetic showers from cosmic ray interactions.

The choice of outfitting the far site detector complex with two separately-instrumented detector vessels has several benefits. First, this design enables each cryostat and TPC to be filled and commissioned while the other cryostat is available for liquid storage. Thus this setup allows for repairs to be made after the start of commissioning should that be necessary. This two-vessel configuration also allows TPCs of different designs to be deployed. For example, international partners with the resources to construct a TPC of alternate design would be able to make a significant impact with such a contribution.

The detector vessels will be constructed using technology standard in the liquid natural gas

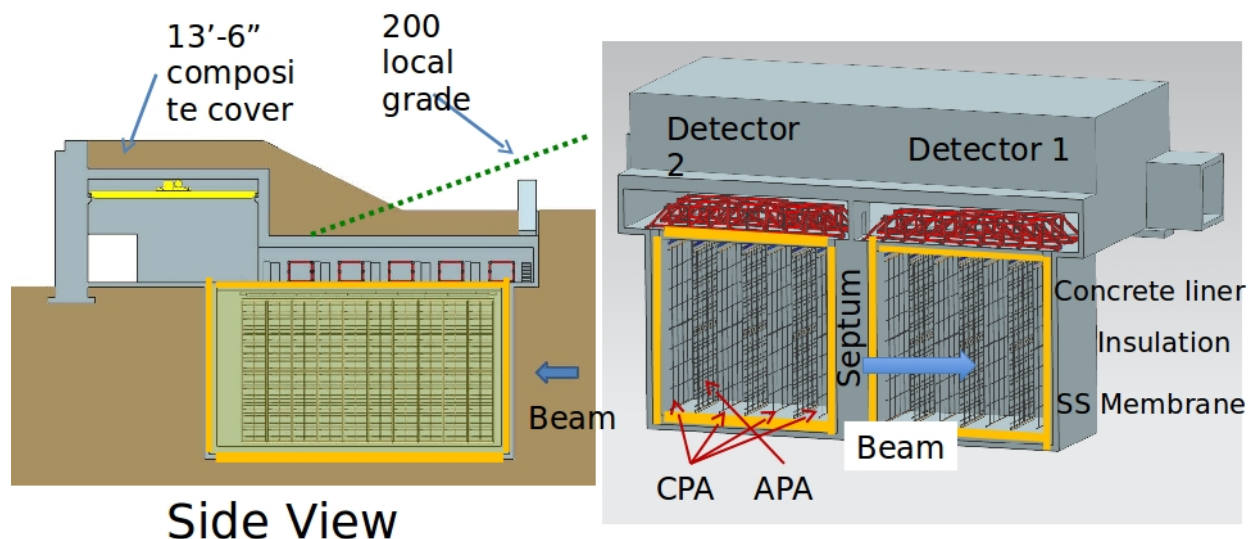


Figure 3-15: View of the Far Detector showing the building, overburden and access regions (left). 3D view of the detector showing the two modules and the orientation with the neutrino beam(right).

(LNG) industry. With similar requirements and geometries, adaptation of industrial LNG cryostat design provides a high-performance, extensively tested approach to the challenge of the construction of large vessels for the containment of liquid argon for LBNE. The cryostats in large LNG tanker ships are constructed using thick foam insulation and a thin (1–2mm) stainless steel inner membrane, supported by the hull. This construction gives a completely passive cryostat with only stainless steel as the wetted surface, making it ideal for liquid argon detectors where high purity is essential.

The cryogenics systems consist of three 55kW liquid nitrogen liquefaction plants, a liquid argon receiving station, a liquid argon circulation system with liquid purifiers, and a liquid argon re-condensing system with gas purifiers. All the cryogenics systems are similar to large-scale systems found in industry applications.

The LBNE TPC (see Figure 3-16) consists of 4 rows of cathode plane assemblies (CPA's) interspersed with three rows of anode plane assemblies (APA's) with readout electronics mounted directly on the APA frames. These elements run the length of a cryostat module, save for space at one end allocated for cryogenics systems. A field cage to shape the electric field covers the top, bottom, and ends of the detector. For the surface detector, the CPA-APA spacing is 2.3 meters, and the cathode planes will be operated at -114 kV , establishing a drift field of 500 V/cm and a corresponding maximum drift time of 1.4 ms .

The APA's and CPA's are designed in a modular fashion as illustrated in Figure 3-16. Each APA/CPA is constructed with a channel frame 2.5 m long and 7 m high; these dimensions are chosen for ease of transportation to the detector site and installation within the cryostat.

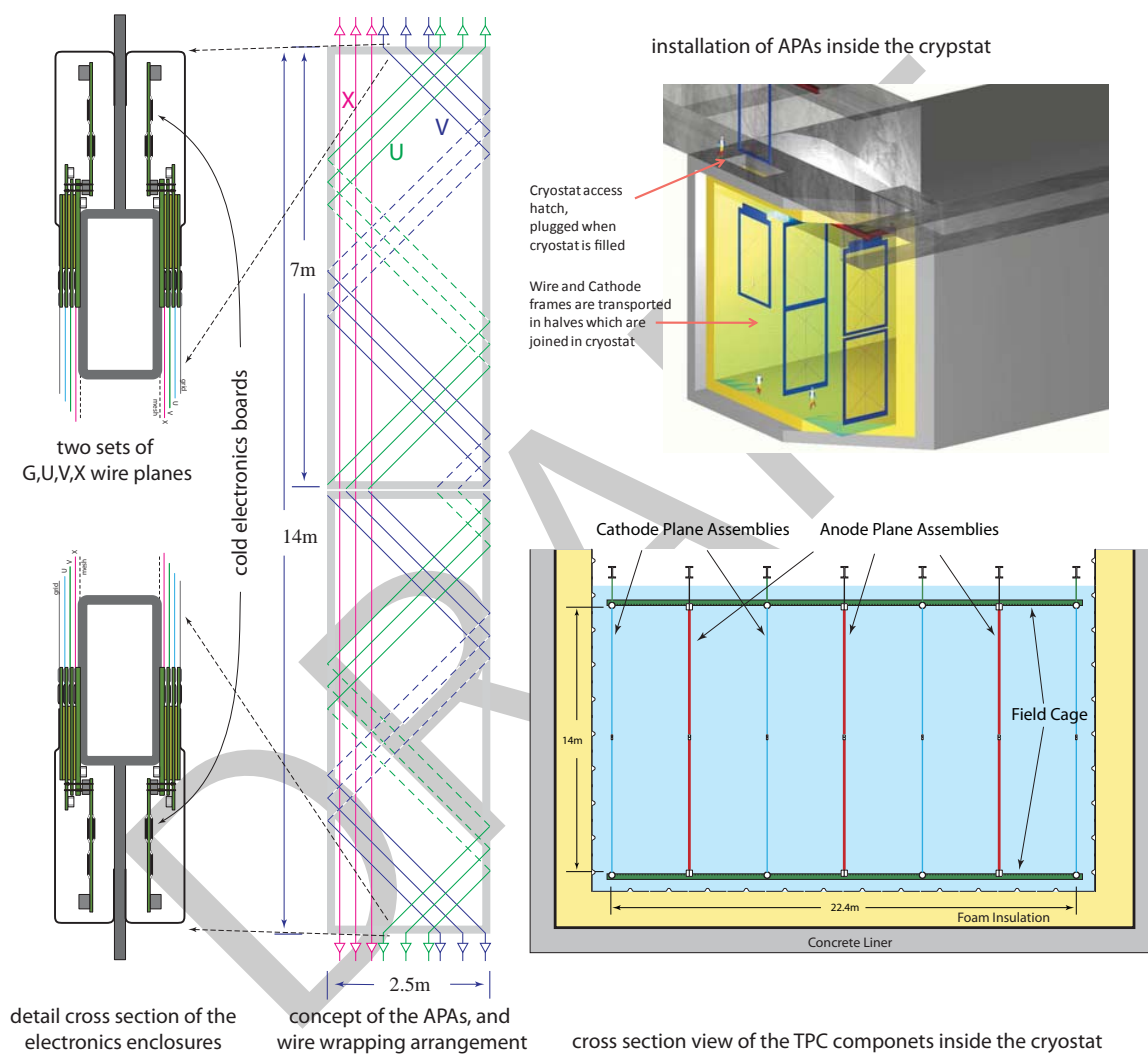


Figure 3-16: TPC modular construction concept

During installation two APAs are connected end-to-end to form a 14m tall 2.5m long unit, which is transported to its final position in the detector and suspended there using a rail system at the top of the detector. Pairs of CPA's are installed in a similar fashion. This system of 2.5m long detector elements enables easy scalability to any desired detector size. A total of 60 APAs and 80 CPAs per cryostat are needed for the present LBNE10 detector design.

Three sense wire planes with wire pitches around 5mm are mounted on each side of an APA frame, for sensitivity to ionization signals originating within the TPC cell on either side. These planes are oriented vertically (collection plane) and at $\pm 45^\circ$ (induction planes). The wires on the induction planes are wrapped around the APA frame, thereby viewing charge arriving from different sides of the APA, depending on where the charge arrives along the length of the wires. This configuration allows placement of readout electronics at the top and bottom of the two-APA unit. (Cables from the bottom APA are routed up through the channel frame, thereby eliminating any obstruction they would otherwise cause.) In this way, adjacent APA-pairs can be abutted so as to minimize the uninstrumented region in the gaps between them along the length of the detector.

Low-noise, low-power CMOS preamplifier and ADC ASICS have been developed for deployment on circuit boards mounted directly on the APA frames as indicated above. This scheme ensures good signal-to-noise performance, even allowing for some attenuation of long-drift ionization signals due to residual impurities in the argon. It also offers the possibility of digital signal processing, including multiplexing and zero suppression, at the front end, thereby limiting the cable plant within the cryostat and the number of penetrations required, while also easing requirements on the downstream readout/DAQ systems located outside the cryostat. The ASICS have been laid out following design rules developed explicitly for long-term operation at cryogenic temperatures.

In order to operate on the surface it is necessary to accurately determine the event time relative to the neutrino beam crossing window. If the event time is understood at the microsecond level then out-of-time cosmic ray backgrounds can be rejected to the level of 10^{-5} (the beam spill duty factor), which is necessary to reduce the background rates to an acceptable level. The slow ionization electron drift velocity gives the TPC its 3-D imaging capability, but an independent fast signal is required to localize events in time and in space along the drift direction. For this we capitalize on the excellent scintillation properties of liquid argon ($\mathcal{O}(10^4)$ photons per MeV of energy deposition). A photon detection system is planned to detect the 128nm scintillation light and thereby determine the event timing. Several detector designs are under study at present with the most advanced design being made of cast acrylic bars coated with wavelength shifter and read out at the ends with SiPM's. These bars would be assembled into paddles of dimensions 10cm by 2m, and would be able to be mounted on the APA frames, fitting within the 5cm gap between the sets of wire planes located on the two sides of the frames. Initial studies indicate a light yield of 0.1 - 0.5 photoelectrons per MeV is expected.

3.6.2 Large Underground LArTPC Modules

The physics for a surface experiment is likely to be limited to the neutrino beam program, as all other physics channels are compromised by cosmic ray backgrounds. If the detector can be moved underground, then sensitivity to supernova core collapse neutrinos, detection of nucleon decay and precision studies of atmospheric neutrinos all become viable. These additional physics programs would greatly broaden the scientific impact of LBNE.

Thus our goal remains to place the detector underground, and LBNE has a complete design for a 34-kt fiducial mass detector at the 4850-foot level of SURF (Figure 3-17). The project is well positioned to do this at any stage should the enabling funding be identified. The possibility of expanding the scope of the initial phase of LBNE is open, and would be enabled by resources brought in by international partners.

Given the modular design of the detector and the use of industrial technologies in the cryogenics system there is a great deal of flexibility in possible contributions from new international partners that could expand the size of the detector, and/or free up U.S funds for the additional cost of moving the detector underground. The details of any scope change would depend on the interests, capabilities and resources of the new partners.

The underground detector option was studied in detail during the conceptual design phase of LBNE. A proposed location of the experimental hall at the 4850-foot level of SURF is shown in Figure 3-17. The layout of a 34-kt (fiducial) detector located there is shown in Figure 3-18. For this configuration the detector modules are end to end instead of side by side as on the surface. Information about the rock quality is available and simulations of the rock stress and resulting ground support have been performed. The LBNE far detector project team is embarking on an underground geotech exploration program that will map out in detail the location of the 34 kton module at the 4840ft level of SURF and an additional cavern for a 70 kton module as shown in Figure 3-19. Significant effort has been invested to minimize the cost of the conventional facilities, but the underground option was eventually deferred due to financial constraints as described in Chapter 1. The underground detector design is very similar to that for the surface detector. It is constructed of modules of the same design as the surface detector. However, as a means of saving costs by reducing channel counts, the drift distance is increased to 3.5 m as allowed by the lower cosmic ray rate at depth. Similar photon detectors are needed underground to provide triggers for non-beam related events. The differential cost between a 10kt surface detector and a 10kt underground detector is estimated to be \$140M (U.S. accounting), mainly due to the underground excavation and infrastructure costs. Thus, constructing a dedicated detector elsewhere capable of performing the non-beam measurements listed above would cost much more than the incremental cost of taking the LBNE far detector underground.

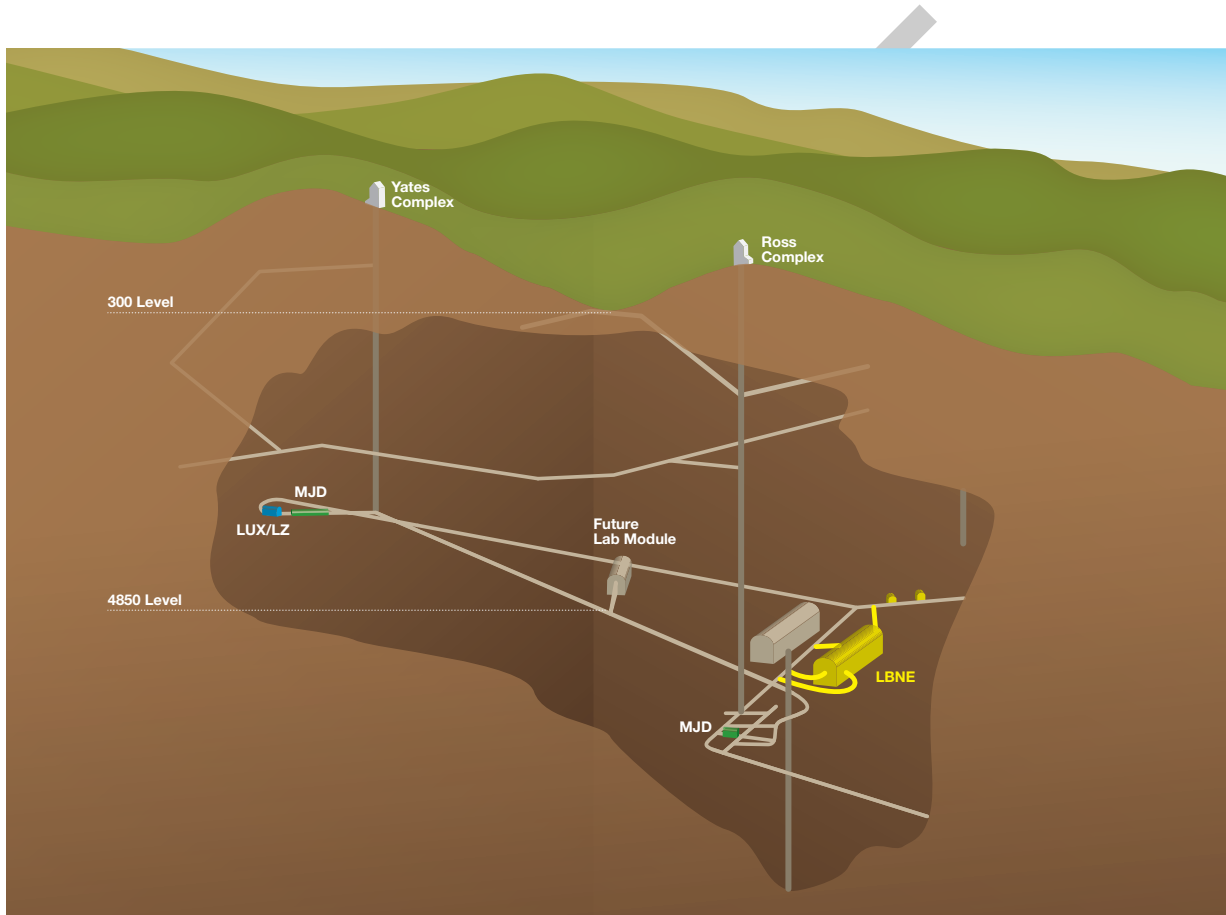


Figure 3-17: Layout of the 34 kT LAr detector hall at the 4850 foot level of Homestake Mine (yellow). A possible layout for an additional 34 kT LAr module is shown next to the LBNE module.

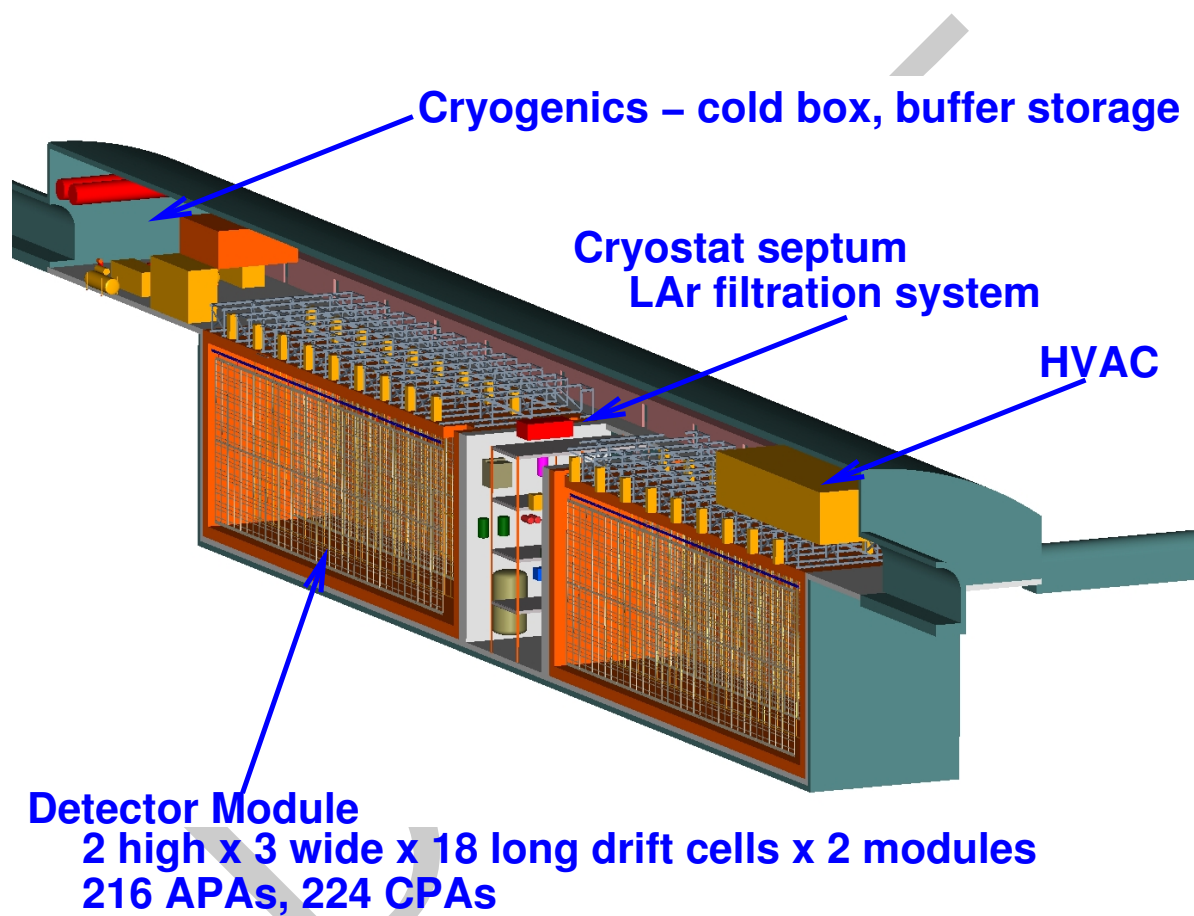


Figure 3-18: Schematic of the 34 kT LAr-TPC design.

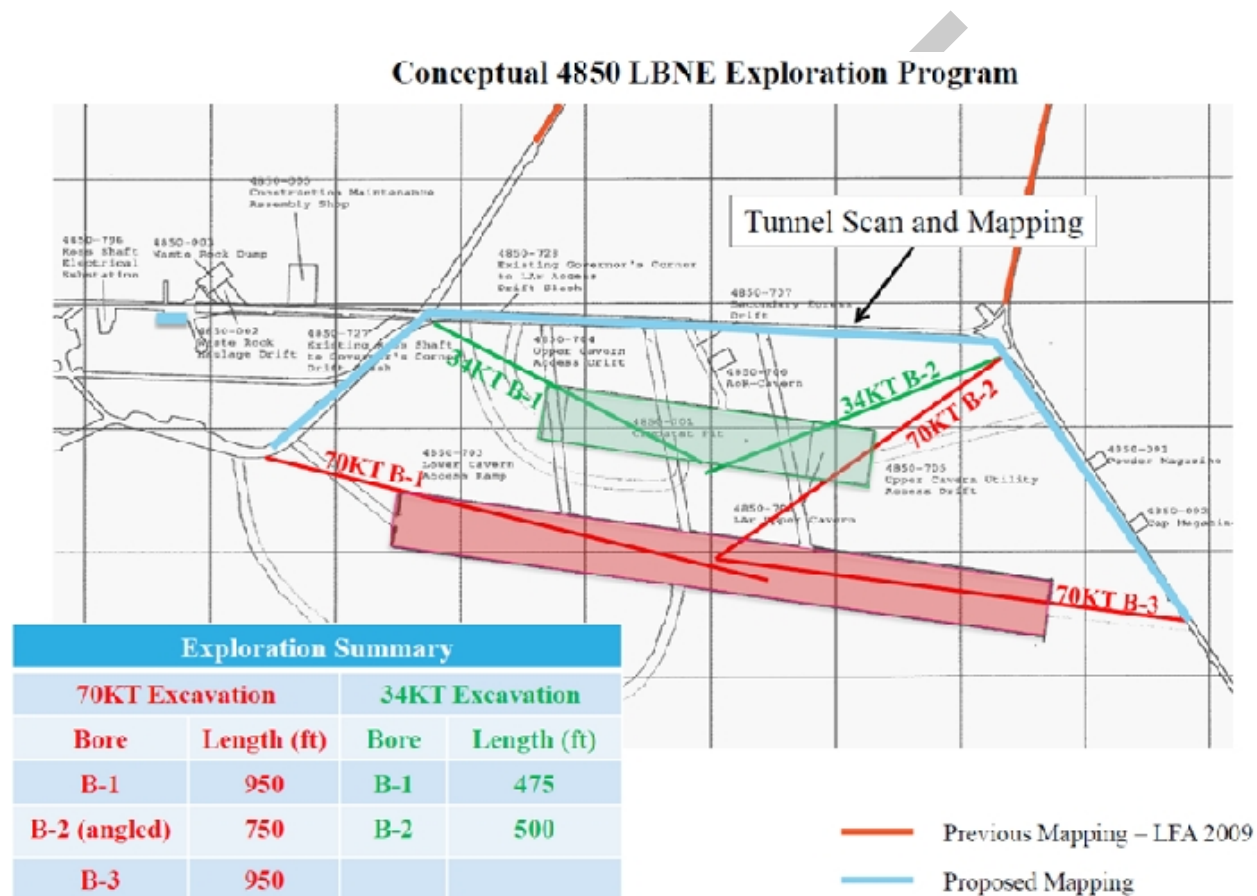


Figure 3–19: Possible layout and proposed geotech exploration for a 70+34 kton LAr detector modules.

4 Long-Baseline Neutrino Oscillation Physics

The LBNE Science Collaboration proposes to mount a broad attack on the science of neutrino oscillations with sensitivity to all known parameters in a single experiment in particular,

1. precision measurements of, the parameters that govern $\nu_\mu \rightarrow \nu_e$ oscillations; this includes precision measurement of the third mixing angle, measurement of the CP violating phase δ_{CP} , and determination of the mass ordering (the sign of Δm_{32}^2).
2. precision measurements of θ_{23} and $|\Delta m_{32}^2|$ in the ν_μ -disappearance channel.
3. search for non-standard physics that can manifest itself in differences observed in higher-precision measurements of ν_μ and $\bar{\nu}_\mu$ disappearance over long baselines.

The general experimental parameters for designing a successful neutrino oscillation experiment to address neutrino CP violation and the mass hierarchy can be extrapolated from the phenomenology summarized in Chapter 2 as follows:

1. *Phenomenology: An appearance experiment is necessary to extract the CP violating effects.*

Experimental requirements:

- The experiment probes oscillations of $\nu_{\mu,e} \rightarrow \nu_{e,\mu}$
- The flavor of the neutrino at production and after flavor transformations must be tagged or known, therefore the experiment needs to identify ν_e and ν_μ with high efficiency and purity.
- Flavor tagging of muon neutrinos using the lepton flavor produced in a charged-current interaction such that $\nu_\mu + N \rightarrow \mu N' X$ requires $E_\nu > 100$ MeV.

Phenomenology: In the 3 flavor mixing model, the CP violating Jarlskog invariant arises in the interference term $P_{\sin \delta}$ as given by Equation 2.10, the oscillation scale where the interference term is maximal is that determined by the mixing between the 1-3 states.

Experimental requirements:

- 1 • The experimental baseline and corresponding neutrino energy is chosen according
2 to Equation 2.13 such that $L/E = 510 \text{ km/GeV}$ to maximize sensitivity to the
3 CP violating term in the neutrino flavor mixing.
- 4 • Flavor tagging of muon neutrinos which can be produced either as the source or
5 after flavor mixing requires $E_\nu > 100 \text{ MeV}$, therefore, the experimental baselines
6 over which to measure neutrino oscillations are $L > 50 \text{ km}$. *
- 7 2. *Phenomenology: In the 3-flavor model $\nu_{\mu,e} \rightarrow \nu_{e,\mu}$ oscillations depend on all parameters in*
8 *the neutrino mixing matrix as well as the mass differences as shown in Equations 2.7 to*
9 **2.10. Experimental requirements:**
 - 10 • The precision with which δ_{cp} can be determined - and the sensitivity to small
11 CP violating effects or CP violation outside the 3-flavor model - requires preci-
12 sion determination of all the other mixing parameters - preferably in the same
13 experiment.
- 14 3. *Phenomenology: Evidence for CP violation necessitates the explicit observation of an asym-*
15 *metry between $P(\nu_l \rightarrow \nu_{l'})$ and $P(\bar{\nu}_l \rightarrow \bar{\nu}_{l'})$. Experimental requirements:*
 - 16 • The experiment must probe the oscillations of both neutrinos and anti-neutrinos
17 in an unambiguous way.
 - 18 • Charge tagging in addition to flavor tagging is required. Charge tagging can be
19 achieved at detection using the lepton charge and/or at production by selecting
20 beams of pure neutrinos or anti-neutrinos.
 - 21 • The mass hierarchy is as yet undetermined. The experiment must be designed
22 to resolve degeneracies between the matter and potential CP asymmetries. This
23 can be achieved by using a baseline of $> 1200 \text{ km}$ or with measurements probing
24 oscillations over different L/E .
- 25 4. *Phenomenology: CP asymmetries are maximal at the secondary oscillation nodes. Experi-*
26 **mental requirements:**
 - 27 • Coverage of the L/E scale of the secondary oscillation nodes improves experimen-
28 tal sensitivity to small values of δ_{cp} by enabling measurements of the asymmetry
29 at the secondary nodes where the CP asymmetries are much larger and where
30 there are no degeneracies with the matter asymmetries.
 - 31 • The secondary oscillation nodes are located at scales set by Equation 2.13 where
32 $n > 1$. The second oscillation maxima is located at scales given by $L/E \sim$
33 1500 km/GeV . If muon flavor tagging at production and/or detection, the ex-
34 perimental baseline is required to be $> 150 \text{ km}$.

*Neutrino experiments using beams from pion decay-at-rest experiments such as DAEδUS are an exception since the $\bar{\nu}_\mu$ production spectrum is well known and only the $\bar{\nu}_e$ flavor after oscillations is tagged through inverse beta decay. The neutrino energies are $\sim 50 \text{ MeV}$ below the CC muon production threshold.

Based on the experimental requirements dictated by the neutrino oscillation phenomenology detailed above, pursuit of the primary science objectives for LBNE dictates the need for very large mass (10-100 kiloton-scale) neutrino detectors located at a distance of > 1000 km from the neutrino source. A large mass coupled with a powerful wide-band beam and long exposures is required to accumulate enough neutrino interactions – $\mathcal{O}(1000)$ events – to make precision measurements of the parameters that govern the sub-dominant $\nu_\mu \rightarrow \nu_e$ oscillations. At 1300km, the baseline chosen for LBNE, both the first and second oscillation node are at neutrino energies > 0.5 GeV as shown in Figure 7-1. This places both neutrino oscillation nodes in a region which is well matched to the energy spectrum of the high power conventional neutrino beams that can be obtained using the 60-120 GeV Main Injector (MI) proton accelerator at Fermilab. The LBNE unoscillated ν_μ spectrum (flux \times cross-section) at 1300km obtained from the LBNE beamline using 80 GeV protons from the MI is shown as the black histogram in Figure 7-1. In addition, at this baseline, there are no matter and CP degeneracies at the first node where the Fermilab neutrino beam spectrum peaks. These degeneracies limit the sensitivities of experiments with baselines < 1000 km. The wide coverage of the oscillation patterns also enables the search for physics beyond the 3 flavor model that interferes with the standard oscillations and induces a distortion in the oscillation patterns. The LBNE reconfiguration study [40] determined that the Far Detector

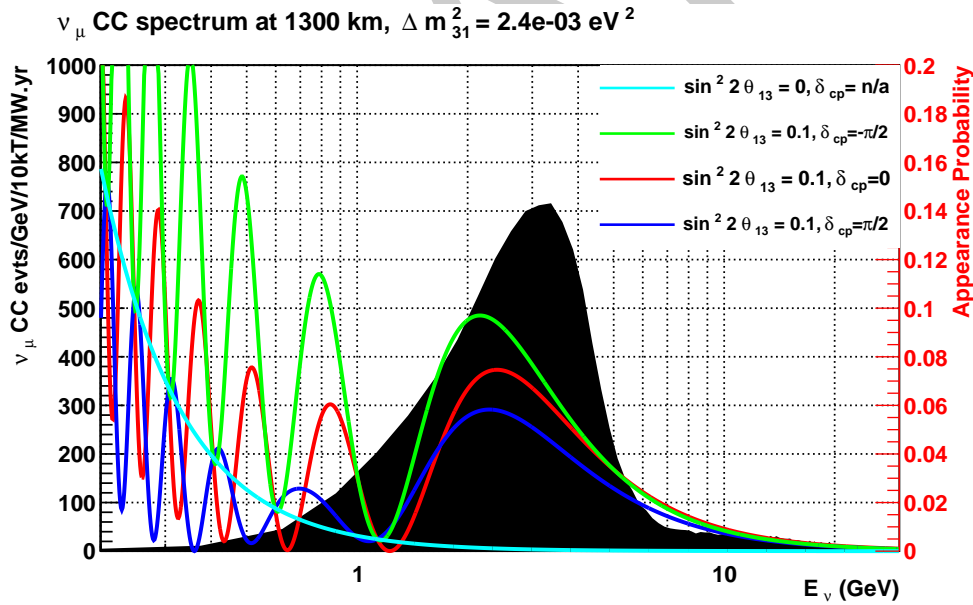


Figure 4-1: The unoscillated spectrum of ν_μ events from the LBNE beam (black histogram) overlaid with the oscillation probabilities for different values of δ_{cp} as colored curves.

location at SURF provides an optimal baseline (1,300 km) for precision measurement of neutrino oscillations using a conventional neutrino beam from Fermilab. The 1300km baseline produces the best sensitivity to CP violation and is long enough to resolve the mass hierarchy with a high level of confidence, as shown in Figure 2-5.

Table 4-1 lists the beam neutrino-interaction rates for all three known species of neutrinos as expected at the LBNE Far Detector site. A tunable beam spectrum, obtained by varying the distance between the target and the first focusing horn (Horn 1), is assumed. The higher energy tunes are chosen to enhance the ν_τ appearance signal, and improve the oscillation fits to the 3 flavor paradigm. For comparison, the rates at other neutrino oscillation experiments such as T2K, MINOS, NO ν A are shown for similar exposure in mass and time. Note that for the first 2 stages of the neutrino factory (NF) the beam power requires Project stage 1 and 2 and is higher than that assumed for LBNE. Table 4-1 shows only the raw interaction rates. No detector effects are included. It is clear that the LBNE beam design and baseline produce high rates of ν_e appearance coupled with larger rate asymmetries when CP violating effects are included. LBNE has higher appearance rates with a 700 kW beam even when compared to Stage 1 of a neutrino factory (NF) with a 1 MW beam.

A 10 kton-scale LArTPC Far Detector, the LAr-FD, fulfills the high-mass requirement for LBNE and provides excellent particle identification with high signal selection efficiency ($\geq 80\%$) over a wide range of energies as described in the LBNE Conceptual Design Report Volume 1 [10]. This is the chosen technology for the LBNE far detector.

4.1 LBNE Detector Simulation and Reconstruction

4.1.1 Far Detector Simulation

Interactions of events in the FD are simulated with GEANT4 [41] using the LArSoft [42] package, which is built on the ART software framework [43]. ART is developed and supported by Fermilab's Scientific Computing division, and it is used by several intensity frontier experiments, including NO ν A, MU2E, MicroBooNE, and ArgoNeuT. The latter two experiments are based on liquid argon TPC's, and thus share many of the same challenges involved in simulating events. It is for this reason that LArSoft is a shared code base. This sharing of code has the further advantage that studies performed with ArgoNeuT data, and MicroBooNE data in the future can be used to tune and validate the simulation software for LBNE. LArSoft is also managed by Fermilab's Scientific Computing Division. Examples of neutrino beam interactions in a LArTPC obtained from the LArSoft package using the MicroBooNE detector geometry are shown in Figure 4-2.

The LBNE far detector (LArFD) design is summarized in Section 3.6. The LBNE FD detector geometries that are available in LArSoft currently are the 10 kT surface detector and the 34 kT underground detector. The 35 Ton prototype geometry is also included. Following the MicroBooNE example, the LBNE FD geometries are specified in GDML files, which are created using Perl scripts. These scripts are easily customizable in order to modify detector design parameters, such as the wire spacing and angles, drift distances, and materials. The photon detectors are included as acrylic bars coated with wavelength-shifting TPB, and are

Table 4-1: Raw ν oscillation event rates at the LBNE far site with $E_\nu < 10$ GeV. Assumes 1.7×10^7 seconds/year (Fermilab). Oscillation parameters used are: $\theta_{12} = 0.587$, $\theta_{13} = 0.156$, $\theta_{23} = 0.670$, $\delta m^2 = 7.54 \times 10^{-5} eV^2$, and $\Delta m^2 = 2.47 \times 10^{-3} eV^2$. The NC event rate is for events with visible energy > 0.5 GeV. The rate is given for an exposure of 50 kt.yrs. For comparison, the rates at other neutrino oscillation experiments (current and proposed) are shown for similar exposure in mass and time. Note that for the first 2 stages of the neutrino factory (NF) the beam power requires Project stage 1 and 2 and is higher than that assumed for LBNE. The duty factor for the JPARC beam is $\sim 1/3$ of NuMI/LBNE. There are no detector effects included.

Beam	ν_μ unosc. CC	ν_μ osc. CC	ν_e beam CC	ν_μ NC	$\nu_\mu \rightarrow \nu_\tau$ CC	$\nu_\mu \rightarrow \nu_e$ CC $\delta_{CP} = -\pi/2, 0, \pi/2$
LBNE low energy beam 80 GeV, 700 kW 9×10^{20} POT/year						
50 kt-years ν	7421	2531	63	1953	91	353 280 204
50 kt-years $\bar{\nu}$	2478	812	20	876	28	30 50 62
LBNE medium energy beam 120 GeV, 700 kW 6×10^{20} POT/year						
50 kt-years ν	11441	7185	42	3388	400	254 233 171
T2K: 295 km 30 GeV, 750 kW 9×10^{20} POT/year						
50 kt-years ν	2100	898	41	360	< 1	73 58 39
MINOS: 735 km 120 GeV, 700 kW 6×10^{20} POT/year LE Beam						
50 kt-years ν	17574	11223	178	4806	115	345 326 232
50 kt-years $\bar{\nu}$	5607	3350	56	2017	32	58 85 88
NOvA: 810 km 120 GeV, 700 kW 6×10^{20} POT/year						
50 kt-years ν	4676	1460	74	1188	10	196 168 116
50 kt-years $\bar{\nu}$	1388	428	19	485	2	22 35 41
LBNO: 2300 km 50 GeV, 485 kW 1×10^{21} POT/year						
50 kt-years ν	2851	824	16	818	190	178 142 112
50 kt-years $\bar{\nu}$	1022	276	4	380	85	8 15 18
Neutrino Factory	ν_μ unosc. CC	ν_μ osc. CC		ν_μ NC	$\nu_\mu \rightarrow \nu_\tau$ CC	$\nu_e \rightarrow \nu_\mu$ CC $\delta_{CP} = -\pi/2, 0, \pi/2$
NF Stage 1 3 GeV, 1MW, no cooling 0.94×10^{20} μ decays/year						
50 kt-years μ^+	1039	339		484	28	71 97 117
50 kt-years μ^-	2743	904		945	89	24 19 12
NF Stage 2 3 GeV, 3MW 5.6×10^{20} μ decays/year						
50 kt-years μ^+	6197	2018		2787	300	420 580 700
50 kt-years μ^-	16349	5390		5635	534	139 115 85

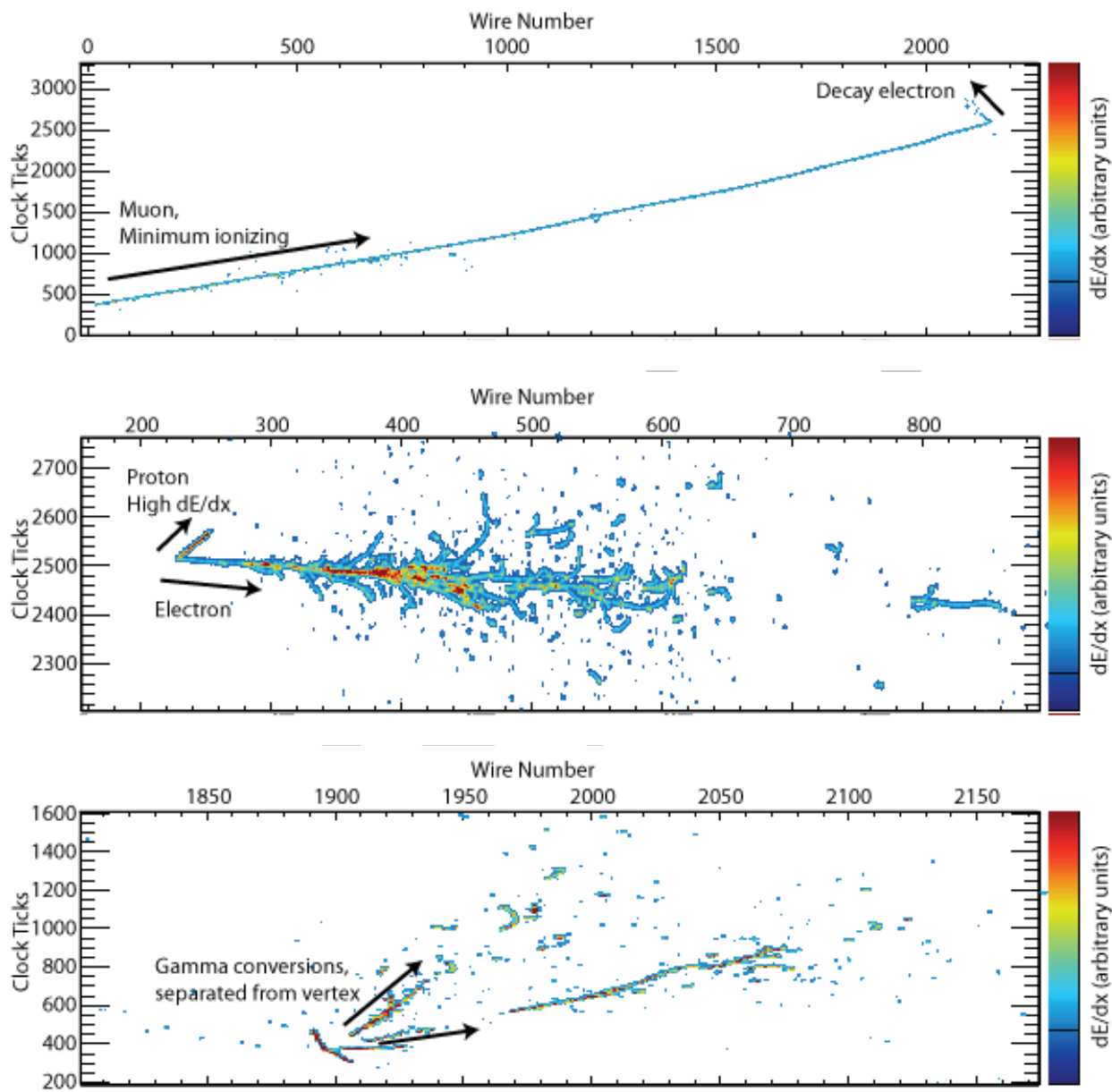


Figure 4-2: Examples of neutrino beam interactions in an LArTPC obtained from a GEANT4 simulation [42]. A CC ν_μ interaction with a stopped μ followed by a decay Michel electron (top), a CCQE ν_e interaction with a single electron and a proton (middle), an NC interaction which produced a π^0 that then decayed into two γ 's with separate conversion vertices (bottom)

read out with SiPM's. GEANT4 is used to model particles traveling through the active and inactive detector volumes and the surrounding materials such as the cryostat and rock. The simulation of photons and electrons produced by the ionized argon however is parameterized as there are tens of thousands of these quanta per MeV of energy deposited. The drifting electrons are parameterized by many small clouds of charge that diffuse as they travel towards the collection wires. These electrons are recorded as functions of drift time. The response of the channels to the drifting electrons is modeled parametrically with a separate response function for collection and induction wires. The signals on the induction plane wires are measurements of the induced currents as functions of time and are thus bipolar as charge drifts past the wires. The signals on the collection plane wires are unipolar. The response functions include the expected response of the electronics. For the 10 kT FD, a 1.5 ms readout of the TPC signals 2 MHz gives a data volume of just under 2 GB per event. More will be required if the readout is extended before and after the drift time including the beam window, which will be required in order to collect charge deposited by cosmic rays which would otherwise be partially contained.

Noise is simulated with a realistic spectrum measured in the ArgoNeuT detector. The decays of ^{39}Ar are included, but some work is required to make them more realistic. In order to reduce the data volume and speed calculation, long strings of consecutive ADC counts below a specifiable threshold are suppressed in the readout. Huffman coding of the remaining data is also included in the digitization.

The photon system likewise requires a full simulation of the particle steps but a parameterized response of VUV photons propagating and being detected or absorbed. We have fully simulated, using GEANT4, photons propagating from the TPC to the acrylic bars, and compute their probabilities of striking each bar as functions of the emission location and the position along the bar at which the photon strikes. Smooth parameterizations of these functions are currently used in the simulation to compute the average numbers of photons expected to strike a bar as a function of position along the bar. Given the current design of the optical detectors, approximately 2-3% of VUV photons produced uniformly in the fiducial detector volume strike the bars. This low number is largely due to the small fraction of the total area in contact with the argon that is represented by the bars, and the low reflectivity of the stainless steel cathode planes, field cage, and CuBe wires. A second function is used to parameterize the attenuation of light within the bar as a function of position along the bar. The expected number of photons surviving propagation, downconversion, attenuation in the bar and the detection efficiency of the SiPM is then used as the mean of a Poisson distribution for simulating individual photons. We use the measured waveforms for cold SiPM's in simulating the digitized response. Measurements in prototype dewars will be used to normalize the yield for signals on the SiPM's as a function of the incident location of the VUV photon on the bar. We are working to incorporate the NEST [?] model which describes the conversion of ionization energy into both electrons and photons in an anticorrelated manner. The modeling of NEST has been shown to model a great range of data from noble liquid detectors.

A variety of different event generators is available for use in simulating events. Neutrino hard scattering interactions and subsequent nuclear breakup are simulated using GENIE [?], though other generators are possible. Cosmic rays are simulated with CRY [?]. Single particles can be generated one at a time, and general text-file interfaces are available allowing arbitrary generators to be used without linking them in with LArSoft.

Currently, samples of single electrons, muons, charged and neutral pions, protons, and tau leptons have been generated and simulated using the 10 kT surface geometry and the 35 Ton geometry, though without photon detector simulation. These samples are being used to develop reconstruction algorithms.

Future directions include interfacing the simulation to a calibration database, updating the response functions with measured responses from MicroBooNE which uses electronics which are very similar to LBNE's design, including the effects of space charge buildup in the drift volume, and more detailed maps of the drift in the gaps between the APA's and for charge that is deposited between the wire planes.

4.1.2 Far Detector Reconstruction

The first stage of reconstruction of TPC data is unpacking and deconvoluting the electronics and field response of the wire planes. The deconvolution function includes a noise filter which must be tuned for the eventual noise observed in the detector but is parameterized with ArgoNeuT's noise for the moment. The deconvolution makes sharp, unipolar pulses from the bipolar induction-plane signals and also sharpens the response to collection-plane signals. Hits are then identified in the deconvoluted signals by fitting Gaussian functions, allowing for sums of several overlapping hits in each cluster. The challenges specific to LBNE at this stage largely arise from the large numbers of channels in the FD, and requires rearrangement of the processing in order to be efficient in CPU and memory.

Reconstruction in ArgoNeuT and MicroBooNE then proceeds with Hough line-finding and clustering in 2D using an algorithm called "fuzzy clustering." [?]. This clustering is performed in each view separately. Three-dimensional track-fitting is performed using a Kalman filter [?], and dedicated algorithms have been developed to optimize electromagnetic shower reconstruction and energy resolution.

LBNE poses unique challenges for reconstruction due to the fact that the APA frames are located within the fiducial volume, and because the induction-plane wires wrap around the edges of the APA frames. Since the hit data on LAr TPC's is inherently two-dimensional – wire number vs. arrival time of the charge, the location of the initial ionization point has a two-dimensional ambiguity (if the deposition time is unknown). For beam events, the t_0 is known, and thus only a one-dimensional ambiguity remains. This ambiguity is broken by angling the induction plane wires relative to the collection plane wires, in order to measure

the y location of the hits for which t (thus x) and z are known. The photon system provides t_0 for cosmic-ray signals which arrive uniformly in time.

The wrapping of the induction plane wires however introduces discrete ambiguities that are not present in other LAr TPC designs. A hit on a collection-plane wire identifies uniquely which side of the APA from which it came, while this is not known for a hit on an induction-plane wire. The angles between the U and V plane wires are slightly different from 45° and from each other in order to assist breaking the ambiguities. A combinatoric issue arises, however, if many hits arrive on different wires at nearly the same time. This occurs if a track, or even a track segment, propagates in a plane parallel to the wire planes (constant drift distance). Showers will also contain many hits on different wires that arrive at similar times. Hits that arrive at different times can be uniquely associated in the Z , U , and V views, while hits that arrive at similar times must be associated using a topological pattern recognition technique. We are developing a version of the fuzzy clustering tool that is to be used as a pattern recognition step in order to associate Z , U , and V hits together, which is a step needed in order to assign which of the discrete choices of wire segment an induction hit falls on. This process is called “disambiguation” of the induction hits, and is needed to assign the correct y position to a track segment or portion of a cluster. Once the induction hits have been disambiguated, standard track, vertex, and cluster reconstruction algorithms are applied. Misassignment of the y locations for pieces of tracks and clusters can affect particle ID performance and reconstructed energy resolution. Fully-contained tracks may appear partially contained and vice versa.

A promising suite of algorithms for event reconstruction is provided by the PANDORA toolkit [?], which provides a framework for reconstruction algorithms and visualization tools. Currently it is being used to develop pattern recognition algorithms, and also to reconstruct the primary vertex. PANDORA’s pattern recognition merges hits based on proximity and pointing to form 2D clusters. Vertices are identified from the clusters that best connects the event, and clusters that correspond to particles emitted from the primary vertex are identified in 2D. These particle candidates are then used to seed 3D reconstructed particles, and a 3D primary vertex is identified. Examples of PANDORA’s 2D clustering are shown in Fig. 4-3 for two simulated charged-current neutrino scattering events. Fig. 4-4 shows the primary vertex spatial resolution in 3D using well-contained simulated beam neutrino events using the nominal LBNE spectrum and MicroBooNE geometry.

4.1.3 Fast Monte Carlo

A parameterized detector response was developed and has been combined with flux simulations and the GENIE event generator to produce a fast MC simulation (Fast MC). The detector response is informed by GEANT4 simulations of particle trajectories in LAr, studies of detector response simulation in MicroBooNE, results reported by the ICARUS collaboration, and the geometry of a detector design. The output of the Fast MC simulations are a set

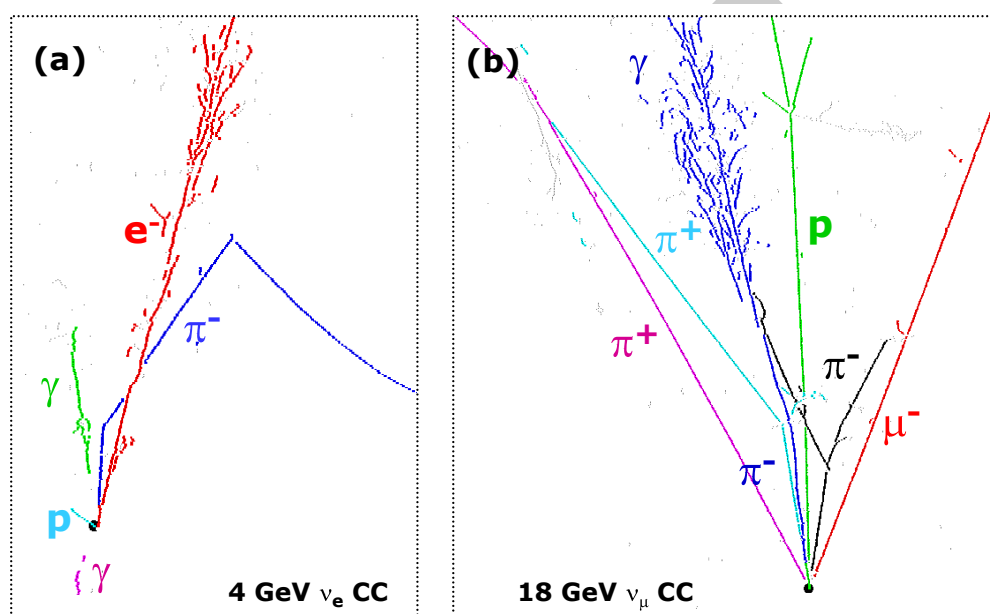


Figure 4-3: PANDORA's two-dimensional clusterings of hits created by the particles in two charged-current neutrino interactions in liquid argon. Panel (a) shows a 4 GeV ν_e interaction, and panel (b) shows an 18 GeV ν_μ interaction. The colors indicate the clusters into which PANDORA has divided the hits, and the particle labels have been added by hand.

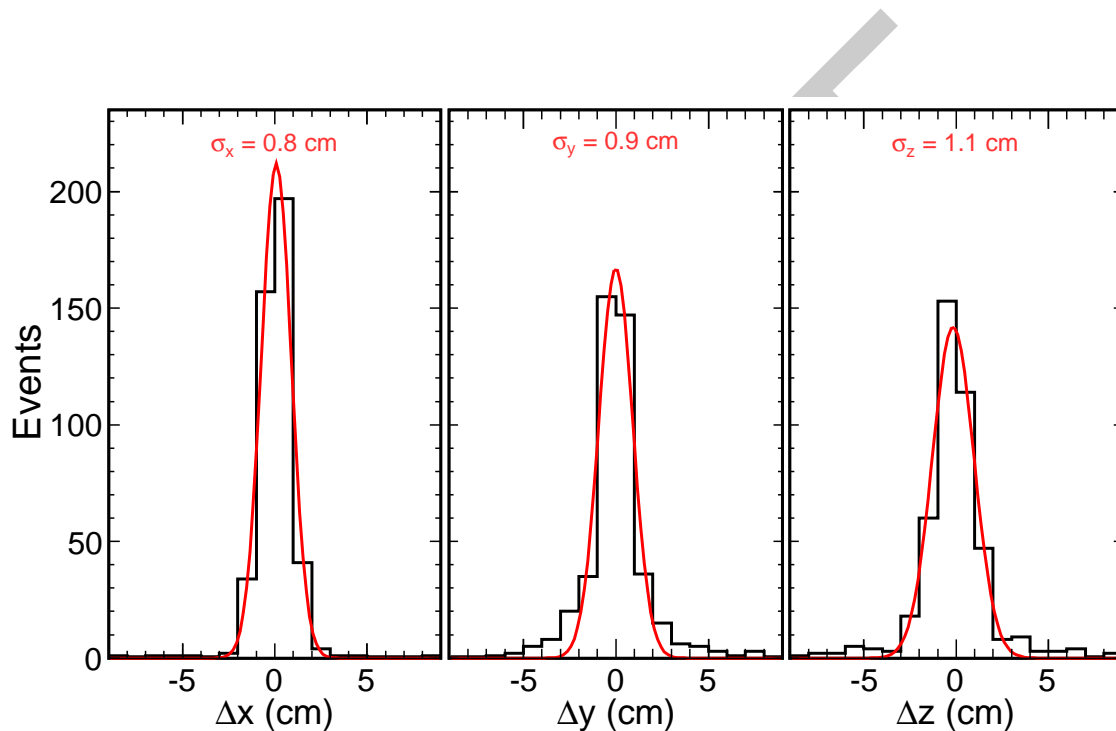


Figure 4-4: Distributions of the residuals between the reconstructed and the Monte Carlo true locations of primary vertices in neutrino interactions in the MicroBooNE geometry using the LBNE beam spectrum. The x axis is oriented along the drift field, the y axis is parallel to the collection-plane wires, and the z axis points along the beam direction.

of analysis-level ‘reconstructed’ quantities that mimic the output of a full MC simulation, and physics analysis sample classification. These Fast MC files can be used to construct the inputs required for GLoBES simulations on an event-by-event basis. This functionality allows for the propagation realistic flux, cross section, and detector response systematic uncertainties to sensitivity studies. In total the Fast MC allows for a full implementation of the LBNE analysis chain starting from the beam flux and propagating detector acceptance, smearing and uncertainties through to the oscillation parameter sensitivities.

The flux simulations are generated from a full GEANT4 simulation of the LBNE beamline described in Section 3.4. The GENIE neutrino monte carlo generator is used to simulate interactions of neutrinos produced in the flux simulations on Ar40 nuclei. For each interaction a record of the interaction process, event kinematics, and a list of final-state particle and their associated four-vectors is produced. The parameterized detector response applies spatial, and energy/momentum smearing to each of the final-state particles based on the particle properties and encoded detector response parameters. Detection thresholds are applied to determine if a final state particle will deposit energy in the detector, and if that energy deposition pattern will allow for particle identification. Response for neutrons and charged pions include a variety of interactions with the detector depending on the ways in which they deposit energy in the detector. These interaction categories are referred to as ‘fates’. Neutral pions are decayed into two photons. The vertex positions of the resulting EM showers are selected randomly from an exponential with a characteristic length based on the radiation length in LAr. Tau leptons are also decayed. The spatial extent of tracks and showers are simulated and energy deposition patterns with respect to detector boundaries are taken into account when assigning associated energy resolutions.

The kinematics of the event (E_ν, Q^2, x, y, etc) are reconstructed based on the smeared four-vectors of particles above detection threshold. Next, interaction final-states particle lists are searched for lepton candidates which are used in an event classification algorithm. The resulting classifications are used to isolate analysis samples for ν_e appearance and ν_μ disappearance which are used to build energy spectra on an event-by-event basis. The GLoBES [?] oscillation analysis package is used for the final oscillation fits. The output of the Fast MC is used to generate matrices which relate the true energy to the reconstructed energy which are used as input to GLoBeS to convert oscillated true energy spectra to reconstructed energy spectra. Furthermore alternate cross section models, flux simulations, and detector response assumptions are incorporated into the Fast MC as event weights and can be used to generate covariance matrices for propagation of systematic uncertainties. Specialized GLoBES functions can read in the covariance matrices generated by the Fast MC and apply realistic simulations of systematic uncertainties to sensitivity studies.

The event classification algorithm uses the following criteria to identify lepton candidates:

- An event with a μ candidate is assumed to be a CC ν_μ interaction. A track passing the following criteria is selected as a muon candidate:

- The longest MIP-like track is evaluated for consistency with a μ hypothesis.
- The track must be at least 2.0 m long.
- If the track is produced by a charged pion its fate must produce a topology consistent with a μ . These include:
 - * Tracks exiting the detector.
 - * Pions that range out. (The 2.0 m cut represents the track length above which the probability for a charged lepton to exhibit ranging behavior becomes minimal.)
 - * Pions that are absorbed (assumed to be 15% of non-ranging pions).
- To account for the expected reduction in selection efficiency for low energy muon candidates in high multiplicity events, an additional selection probability of the form $P(E_{track}) = (E_{track} - m) / (E_{track} - m * n)$, where m is a tunable parameter set to 0.8 GeV and n is the μ detection threshold, is applied as a function of MIP-like track energy to the μ candidates. The falling edge of the applied pdf is well below the energy required to generate a 2.0 m track, thus the effect of this additional selection requirement is minimal.
- An event with no muon candidate and an electron candidate is assumed to be a CC ν_e interaction. An EM shower passing the following criteria is selected as a muon candidate:
 - The highest energy EM shower is evaluated for consistency with an $e\pm$ hypothesis.
 - The vertex of the shower must be within 2.0 cm of the event vertex.
 - The shower is paired with each other EM showers in the event above the identification threshold, and the invariant mass is calculated.
 - If the invariant mass is consistent (135 ± 40 MeV) with the π^0 mass, the candidate is rejected and the next highest energy EM shower is considered.
 - To account for proposed e/γ separation algorithms and for the expected reduction in selection efficiency for low energy $e\pm$ candidates in high multiplicity events, additional selection probabilities are applied as a function of EM shower energy to the $e\pm$ candidates.
 - The e/γ separation algorithm is tuned to preserve 95% of the signal ($e\pm$) across all energies, and selection probability of 0.9 is applied to each true $e\pm$ candidate.
 - The e/γ separation algorithm gives the fraction of background (γ) rejected as a function of candidate energy. This fraction is used as the selection probability for each true γ candidate.
 - The current implementation rejects 50% of γ induced EM showers at 0.25 GeV, and 92% of γ induced EM showers above 1.5 GeV (linear interpolation is applied between these points).

○ A selection probability of the form $P(E_{\text{shower}}) = (E_{\text{shower}} - m)/(E_{\text{shower}} - m * n)$, where m is a tunable parameter set to -5.0 GeV and n is the e^\pm detection threshold, is applied as a function of EM shower energy to the e^\pm candidates. The parameter m is tuned to agree with hand scan studies.

- An event with no muon candidate and no electron candidate is assumed to be a NC.
- Currently no attempt is made to identify tau lepton candidates, either to isolate a tau sample, or to reject $\tau \rightarrow \mu + \nu + \nu$ or $\tau \rightarrow e + \nu + \nu$ from their constituent samples.

Algorithms for τ event selection are under development. Efforts focus on using event kinematics and topological variables. Candidates for kinematic discriminants include the transverse momentum imbalance (see Figure 4-5 with respect to the incoming neutrino direction, and

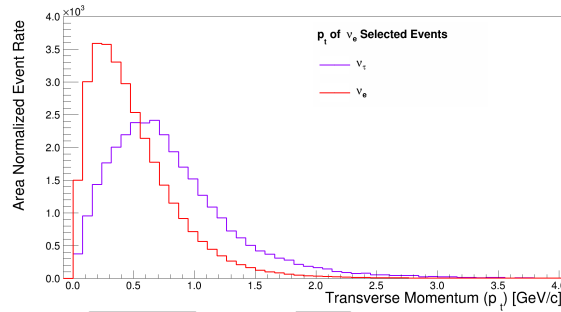


Figure 4-5: Transverse momentum profile - measured with respect to the neutrino beam direction - of ν_e and ν_τ events that pass ν_e selection cuts.

reconstruction of a p mass from hadronic decay products. Topological discriminants will focus on identification of a second hadronic shower vertex at the termination of a MIP-like track originating at the primary vertex. This topology is consistent with the high energy charged pions produced in τ decays.

Figures 4-6 and 4-7 shows the output ν_e and ν_μ appearance spectrum and the backgrounds from the Fast MC respectively. The bottom insert in each plot shows the variation in the spectrum of each component of the spectrum induced by changing the value of CCM_{QE}^A , the effective axial mass for CC interactions in QE cross section model in GENIE. This particular example of the cross-section and nuclear effect systematic studies demonstrates the strong correlation in cross-section systematics in the $\nu_\mu \rightarrow \nu_e$ and $\nu_\mu \rightarrow \nu_\mu$ analyses.

The left-hand side plots of Figures 4-8 and 4-9 show the acceptance (efficiency) of the signal and the background samples for the Fast MC ν_e appearance and ν_μ disappearance selections, respectively. The effects of the low energy selection probabilities induce the observed low energy fall off in the ν_e appearance sample. On the other hand the 2.0 m track length requirement is mainly responsible for the low energy behavior in the ν_μ disappearance sample. The corresponding plots on the right-hand side show the relative fraction (purity) of each

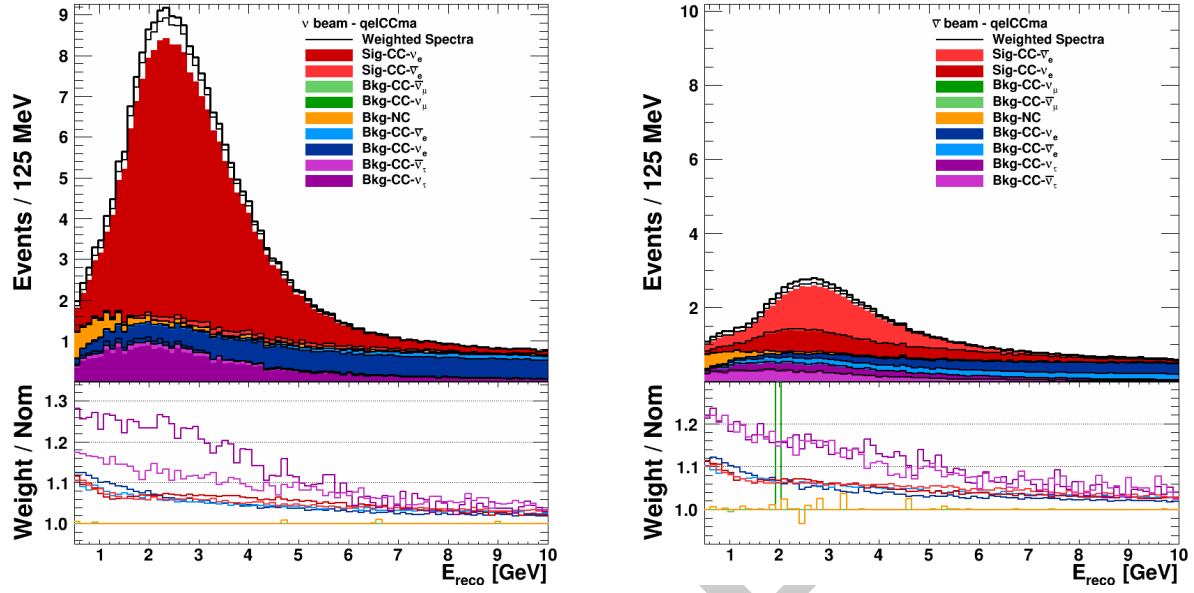


Figure 4-6: The ν_e (left) and $\bar{\nu}_e$ (right) appearance signal produced by the Fast MC simulation package. The bottom insert in each plot shows the variation in the spectrum of each component of the spectrum induced by changing the value of MA_{QE} in the simulation.

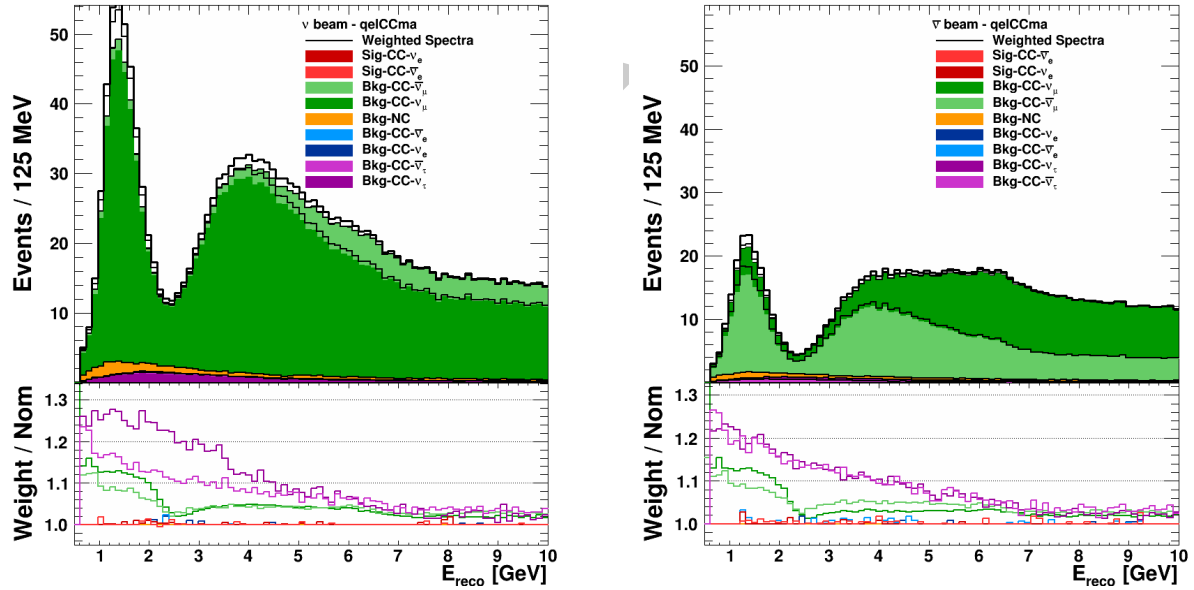


Figure 4-7: The ν_μ (left) and $\bar{\nu}_\mu$ (right) appearance signal produced by the Fast MC simulation package. The bottom insert in each plot shows the variation in the spectrum of each component of the spectrum induced by changing the value of MA_{QE} .

- 1 signal and background sample for the Fast MC ν_e appearance and ν_μ disappearance selections.
 2 The increased wrong-sign contamination is evident in the $\bar{\nu}$ beam samples as compared to
 3 the ν beam samples. No attempt has been made to reduce the tau backgrounds in these
 4 samples.

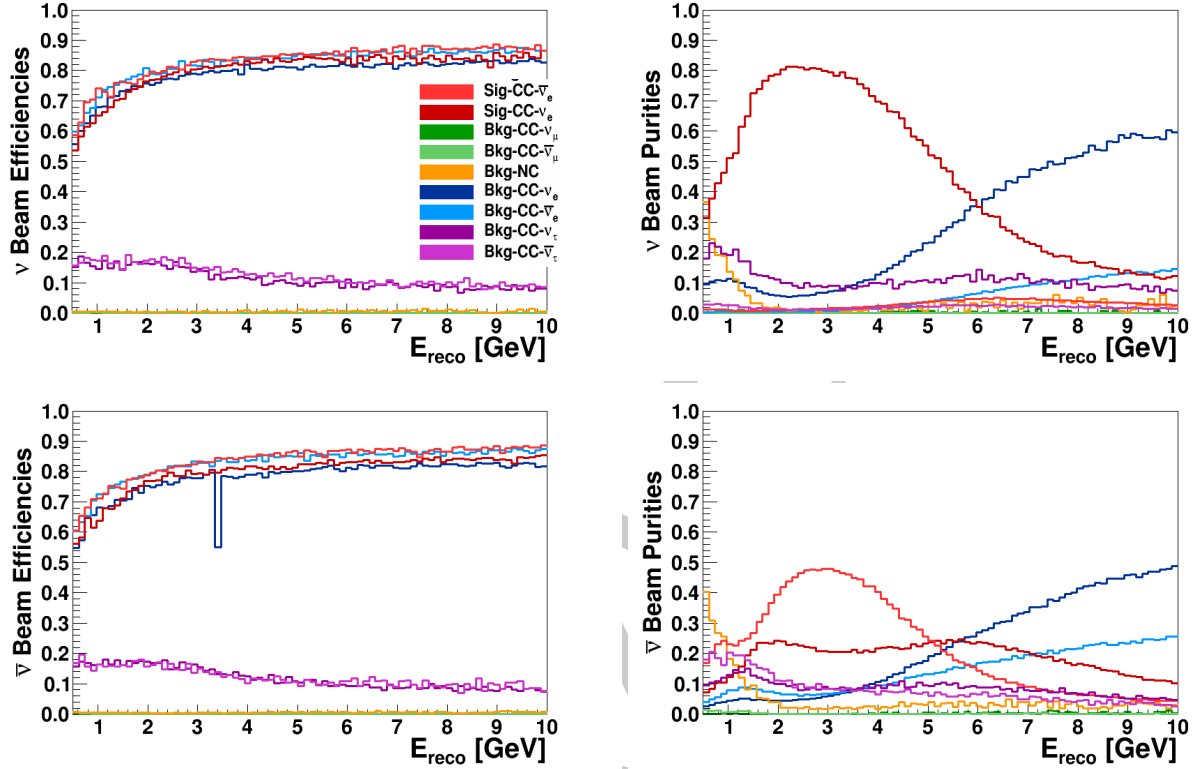


Figure 4-8: The expected efficiencies and purities of selecting ν_e appearance events in a LArTPC obtained from the Fast MC.

5 4.1.4 Detector Simulation using the GLoBeS Package

- 6 For the current set of sensitivity studies, the full implementation of the FastMC had not yet
 7 been developed, and the GLoBeS package was used to simulate the detector response using
 8 much simpler smearing and detector efficiency values based on results from ICARUS and
 9 earlier simulation efforts as documented in [10]. The values used in GLoBeS are shown in
 10 Table 4-2.

- 11 Studies from ICARUS have estimated and measured single-particle energy resolutions in
 12 LAr. Below 50 MeV, the energy resolution of electrons is $11\%/\sqrt{E[\text{MeV}]} + 2\%$. The en-
 13 ergy resolution of an electromagnetic shower with energy in the range (50–5000) MeV is
 14 $33\%/\sqrt{E(\text{MeV})} + 1\%$ [?]. The energy resolution of hadronic showers in an LArTPC is

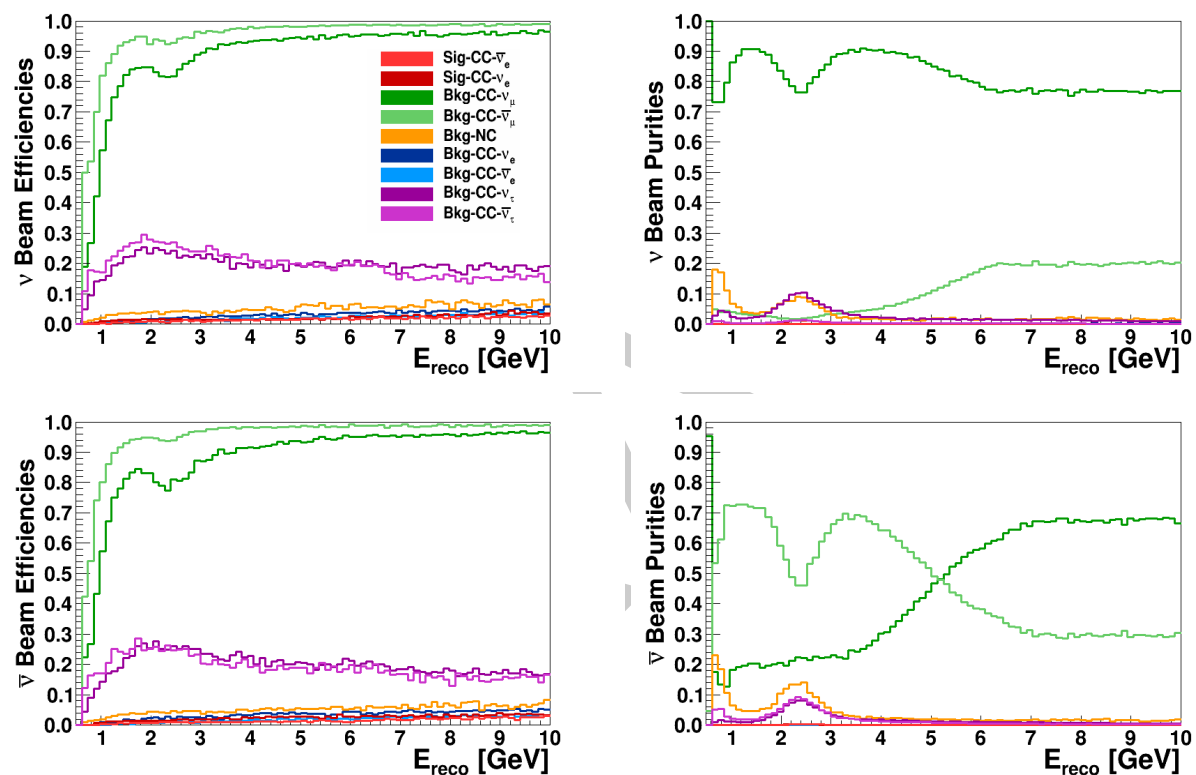


Figure 4-9: The expected efficiencies and purities of selecting ν_μ appearance events in a LArTPC obtained from the Fast MC.

Table 4-2: Estimated range of the LAr-TPC detector performance parameters for the primary oscillation physics. Signal efficiencies, background levels, and resolutions are obtained from the studies described in this chapter (middle column) and the value chosen for the baseline LBNE neutrino-oscillation sensitivity calculations (right column). * For atmospheric neutrinos this is the mis-identification rate for < 2 GeV events, the mis-identification rate is taken to be 0 for > 2 GeV.

Parameter	Range of Values	Value Used for LBNE Sensitivities
For ν_e CC appearance studies		
ν_e CC efficiency	70-95%	80%
ν_μ NC mis-identification rate	0.4-2.0%	1%
ν_μ CC mis-identification rate	0.5-2.0%	1%
Other background	0%	0%
Signal normalization error	1-5%	1-5%
Background normalization error	2-15%	5-15%
For ν_μ CC disappearance studies		
ν_μ CC efficiency	80-95%	85%
ν_μ NC mis-identification rate	0.5-10%	0.5%
Other background	0%	0%
Signal normalization error	1-10%	5-10%
Background normalization error	2-20%	10-20%
For ν NC disappearance studies		
ν NC efficiency	70-95%	90%
ν_μ CC mis-identification rate	2-10%	10% *
ν_e CC mis-identification rate	1-10%	10% *
Other background	0%	0%
Signal normalization error	1-5%	under study
Background normalization error	2-10%	under study
Neutrino energy resolutions		
ν_e CC energy resolution	$15\%/\sqrt{E(\text{GeV})}$	$15\%/\sqrt{E(\text{GeV})}$
ν_μ CC energy resolution	$20\%/\sqrt{E(\text{GeV})}$	$20\%/\sqrt{E(\text{GeV})}$
E_{ν_e} scale uncertainty	under study	under study
E_{ν_μ} scale uncertainty	1-5%	2%

- 1 $\approx 30\%/\sqrt{E(\text{GeV})}$. A significant fraction of the ν_e CC signal in LBNE in the range of 1–
 2 6 GeV is non-quasi-elastic CC interactions with a large component of the visible energy in
 3 the hadronic system. From recent simulations of neutrino interactions in the region of 1–
 4 6 GeV it has been determined that $\langle E_{\text{lepton}}/E_\nu \rangle \approx 0.6$. For this reason, the total electron-
 5 neutrino energy resolution for the neutrino-oscillation sensitivity calculation is chosen to be
 6 $15\%/\sqrt{E(\text{GeV})}$. In a non-magnetized LArTPC the muon momentum can be obtained from
 7 range and multiple scattering. The muon-momentum resolution is found to be in the range
 8 10–15% [?] [?] for muons in the 0.5–3 GeV range. Therefore the total muon-neutrino energy
 9 resolution in LBNE is assumed to be $20\%/\sqrt{E(\text{GeV})}$.
- 10 The predicted spectrum of oscillated ν_μ and $\bar{\nu}_\mu$ CC events in LBNE produced from the
 GLoBeS implementation is shown in Figure 4–10.

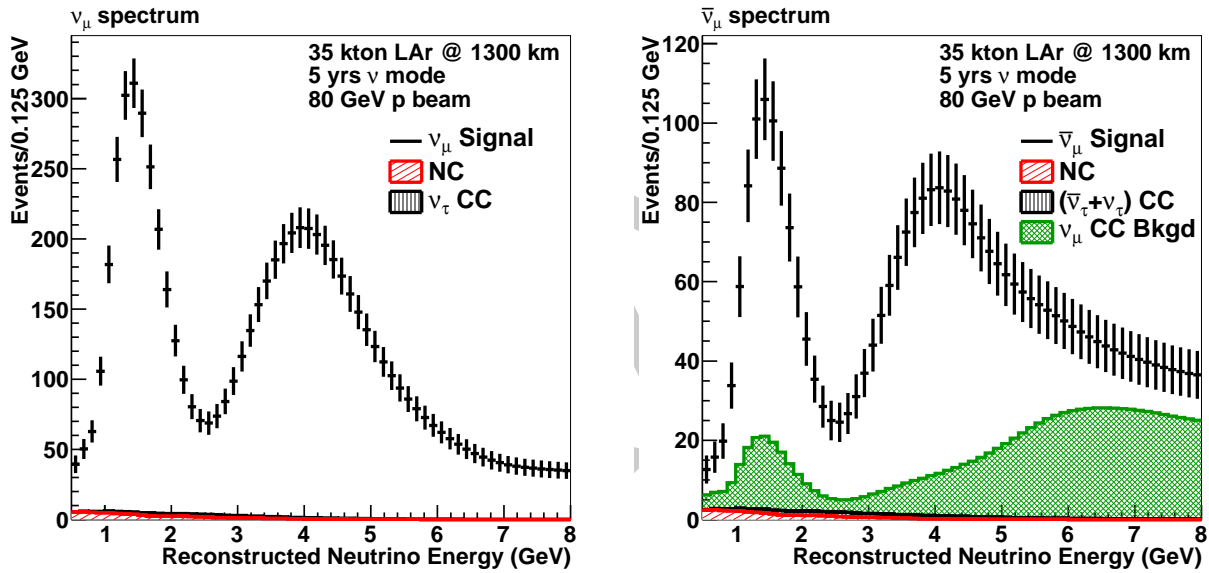


Figure 4–10: The expected spectrum of ν_μ or $\bar{\nu}_\mu$ events in a 34 kton LArTPC for five years of neutrino (left) and anti-neutrino (right) running with a 700 kW beam.

11

- 12 We find that the GLoBeS implementation used in the sensitivity studies is in good agreement
 13 with the more recent results from the FastMC. Updated sensitivity and systematic studies are
 14 currently underway using the FastMC for detector simulation and GLoBeS for the oscillation
 15 fits and propagating of systematics.

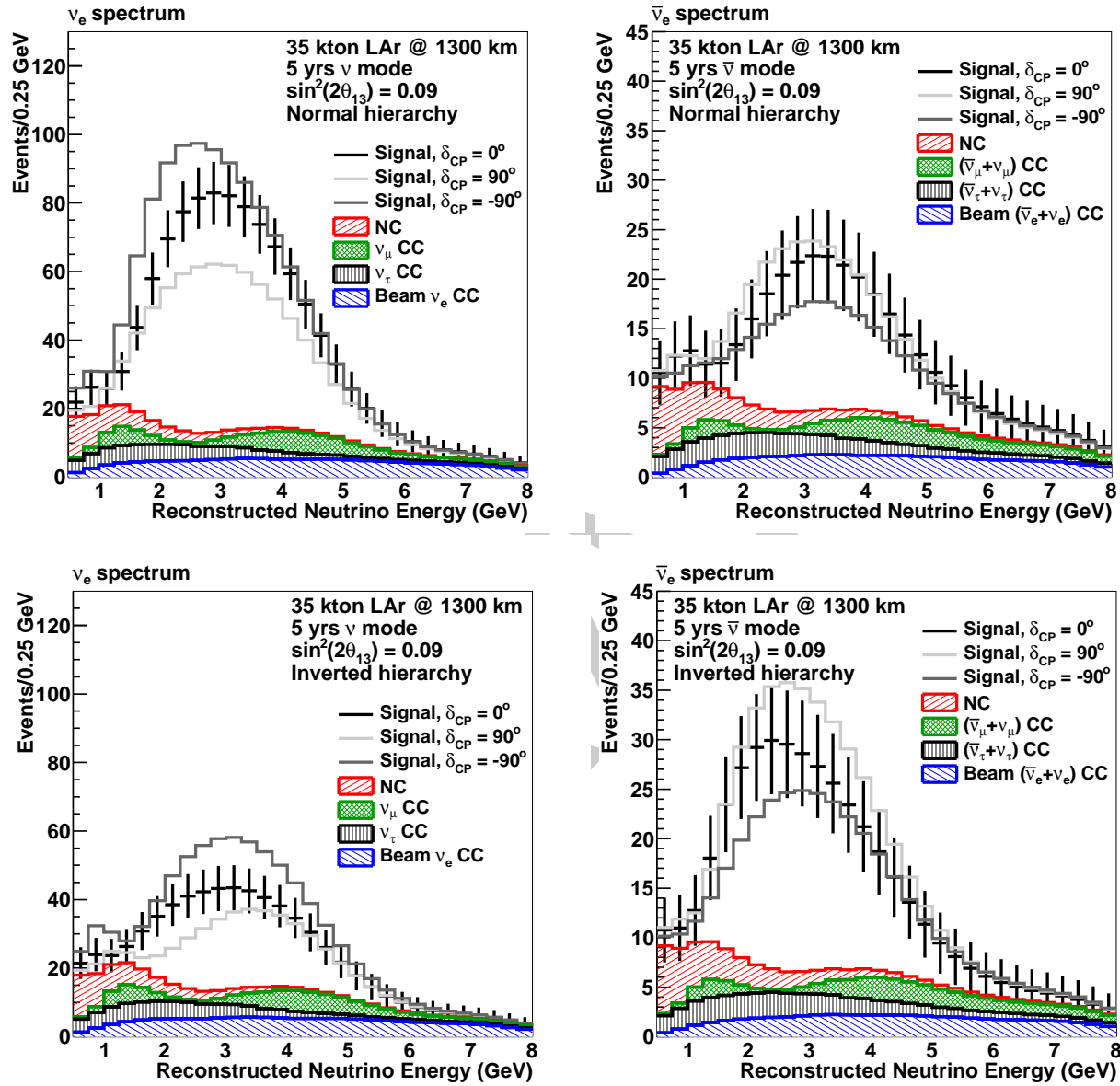


Figure 4-11: The expected spectrum of ν_e or $\bar{\nu}_e$ oscillation events in a 35 kton LArTPC for 5 years of neutrino (left) and anti-neutrino (right) running with a 708 kW 80 GeV beam assuming $\sin^2(2\theta_{13}) = 0.09$. The plots on the top are for normal hierarchy and the plots on the bottom are for inverted hierarchy.

Table 4-3: Expected number of neutrino oscillation signal and background events in the energy range (0.5 – 8.0) GeV at the LAr-FD after detector smearing and event selection. The calculation assumes $\sin^2(2\theta_{13}) = 0.1$ and $\delta_{CP} = 0$. The event rates are given per 10kt LAr-FD and 5 years of running with the upgraded 80 GeV LBNE beam and 9×10^{20} protons-on-target/year.

	Signal Events ν_e	Background Events				Total
		ν_μ NC	ν_μ CC	ν_e Beam	ν_τ CC	
Neutrino Normal Hierarchy	222	19	24	42	14	99
Neutrino Inverted Hierarchy	98	19	23	44	15	100
Anti-neutrino Normal Hierarchy	54	11	11	23	9	54
Anti-neutrino Inverted Hierarchy	80	11	11	23	9	54

4.2 Measurements of Mass Hierarchy and the CP-Violating Phase

The performance of first phase of LBNE which is a 10 kton far detector and a 708 kW beam are detailed in the LBNE Conceptual Design Report Volume 1 [10]. Figure 4-12 summarizes the sensitivities for determining the mass hierarchy and CP violation ($\delta_{cp} \neq 0$ or π) as a function of the true value of δ_{cp} after 10 years of running with a 10kton detector. The sensitivity calculation uses the GLoBeS package with the detector response as summarized in Table 4-2. The sensitivities are obtained by fitting simultaneously both the $\nu_\mu \rightarrow \nu_e$ and $\nu_\mu \rightarrow \nu_\mu$ oscillated spectra (Figures 4-11 and 4-10).

The sensitivity band represents the variation in sensitivity as a function of the beam designs and normalization uncertainties on the signal and background. The solid red curve at the lower end of the red band is the beam design described the LBNE CDR Volume2 [?]. The dashed line above the solid curve represents the sensitivity with the beam design improvements currently under study as described in Section 3.4. In the case where there is no near neutrino detector, we expect the uncertainties on signal and background to be 5% and 10% respectively extrapolating from 1) the performance and detailed knowledge of the NuMI beam on which the LBNE beam is modeled, 2) in-situ measurements of the muon flux at the near site as described in [10], 3) the expectation of improved target hadron production measurements with the NA61 and MIPP experiments, and 4) the experience of previous ν_e appearance experiments as summarized in Table 4-4. In Chapter 5, a detailed discussion of the precision with which the un-oscillated spectrum at the far detector can be predicted using a high resolution tracking near detector is presented. The flux measurement precision expected from the near neutrino detector using different techniques is summarized in Table 5-3. We expect the combination of different techniques in a highly capable near detector to enable a prediction of the far detector ν_e appearance signal with a precision of 1-2%. The background uncertainty in a near-far extrapolation is expected to be at least as good as

Experiment	NC/CC (π^0) Events	Beam- ν_e Events	Syst.Error	Comment
E734	235	418	20%	No ND
E776(89)(NBB)	10	9	20%	No ND
E776 (WBB)	95	40	14%	No ND
MiniBooNE (>450MeV)	140	250	9%	No ND
NOMAD	<300	5500	< 5%	No ND
MINOS [?]	111	12	3.8%	ND-FD

Table 4-4: Summary of achieved systematic error performance in several select prior $\nu_\mu \rightarrow \nu_e$ oscillation experiments. These numbers were extracted from publications to the best of our ability and may not correspond exactly to the description in the text. NBB indicates a narrow band beam and WBB indicates a wide-band beam. No ND indicates there was no near detector, and ND-FD indicates a two detector experiment with extrapolation of the expected background and signal from the near to the far detector.

that achieved by the ν_e appearance search in the MINOS experiment which is $\sim 5\%$ [?]. The known mixing parameters are allowed to float in the fit, but are constrained to be within the uncertainties from the current global fits [15]. The reactor mixing angle, $\sin^2 2\theta_{13}$ is constrained to be $\sin^2 2\theta_{13} = 0.094 \pm 0.003$ which is the expected ultimate precision from the current generation of reactor experiments.

As is obvious from this study, for a 10kton detector, the statistical uncertainties dominate and the impact of the systematic uncertainties on the sensitivity is small. The combination with the expected knowledge from the NO ν A and T2K experiments would allow a 10 kton detector to achieve a $\geq 4\sigma$ sensitivity for at 23% of the allowed values of values of δ_{cp} and a $\geq 3\sigma$ sensitivity for 50% of the allowed values of δ_{cp} . We note that the LBNE 10kton sensitivity is the single most dominant contribution in the combined sensitivities and would represent a significant advance in the search for leptonic CP violation over the existing experiments. The study reported here assumes a normal hierarchy, but similar results were obtained for the case of an inverted hierarchy. The combination with T2K and NO ν A would allow the mass hierarchy to be determined with a precision of $\geq 5\sigma$ over 60% of the allowed values of δ_{cp} and $\geq 3.8\sigma$ for all possible values of δ_{cp} . We note that the combination with NO ν A and T2K only helps the sensitivity in the region of (normal hierarchy, $\delta_{cp} > 0$) or (inverted hierarchy, $\delta_{cp} < 0$) where there are residual degeneracies between matter and CP violating effects due to the low event statistics with the small detector. Alternatively, as will be discussed in Section 4.5, the combination with atmospheric neutrino oscillation studies can also be used to improve the mass hierarchy sensitivity in this region using only the 10kton LAr-FD. Table 4-5 summarizes the mass hierarchy and CP sensitivities that can be reached by the 10kton detector of the Phase I of the LBNE project assuming a running time of 5+5 ($\nu + \bar{\nu}$) years with a 700 kW beam under different scenarios.

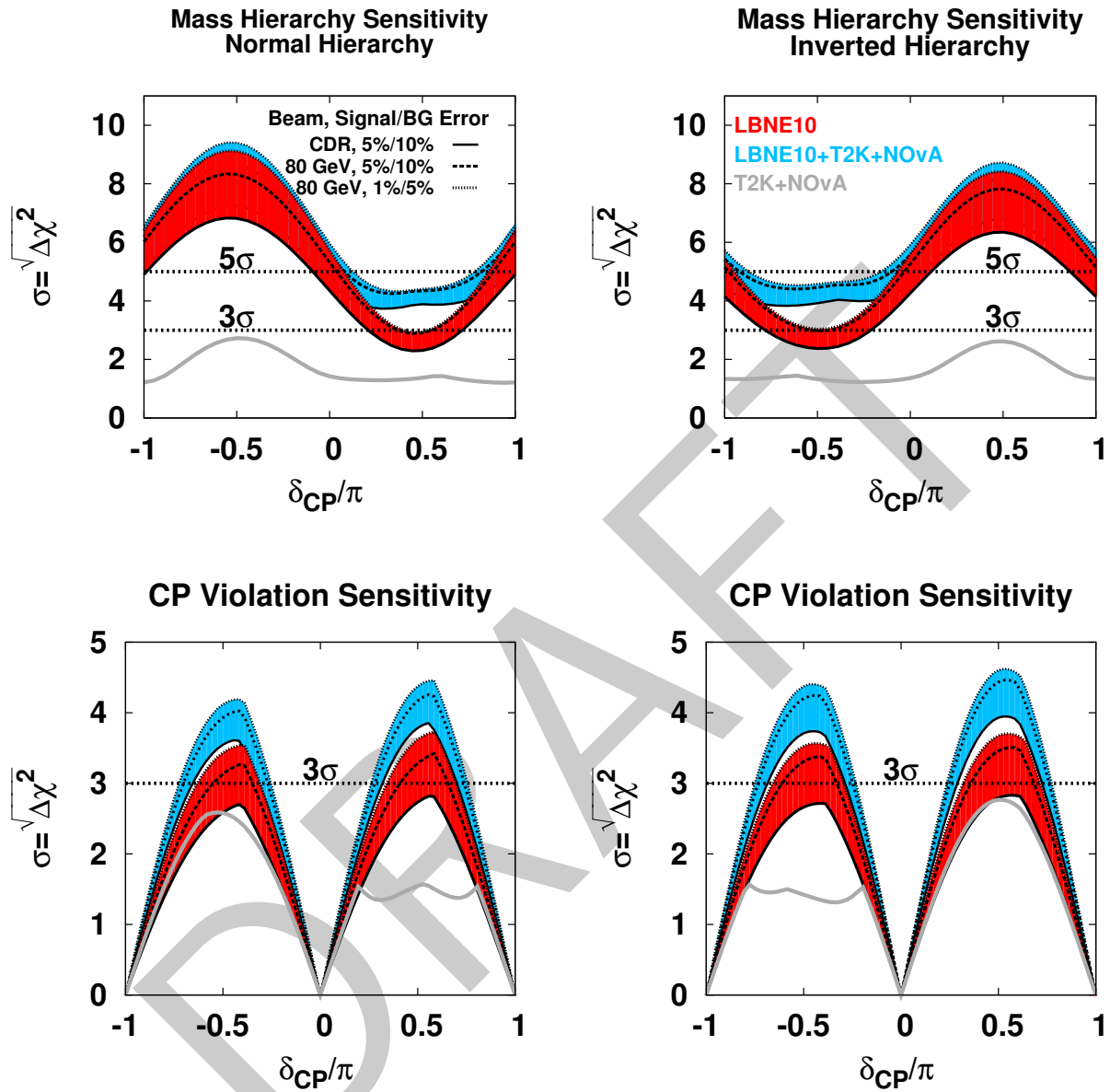


Figure 4-12: The significance with which the mass hierarchy (top) and CP-violation - $\delta_{cp} \neq 0$ or π - (bottom) can be determination as a function of the value of δ_{cp} with a 10-kton fiducial volume LAr-FD. The plots on the right are for normal hierarchy and the plots on the bottom are for inverted hierarchy. The beam exposure assumed is 5+5 yrs ($\nu + \bar{\nu}$) in a 708kW beam. The red band shows the sensitivity that is achieved by LBNE 10 kton alone. The cyan band shows the sensitivity obtained by combining LBNE 10 kton with T2K and NO ν A. The bands indicate the sensitivity range corresponding to different assumptions on background and signal normalization uncertainties and beam design improvements. The gray curves are the expected sensitivities for the combination of NO ν A and T2K. For the CP violation sensitivities, the mass hierarchy is assumed to be unknown.

Table 4-5: The mass hierarchy and CP sensitivities that can be reached by the 10kton detector of the Phase I of the LBNE project with a 700 kW beam and a run time of 5+5 ($\nu + \bar{\nu}$) years under different beam and systematic scenarios.

Scenario	MH sensitivity	CP sensitivity
10kton, CDR beam, no ν ND	$\geq 4/2\sigma$ 50%/all δ_{cp}	$\geq 2\sigma$ 40% δ_{cp}
10kton, beam improvements, no ν ND	$\geq 5/3\sigma$ 50%/all δ_{cp}	$\geq 3/2\sigma$ 23%/55% δ_{cp}
10kton, beam improvements, with ν ND	$\geq 5/3\sigma$ 50%/all δ_{cp}	$\geq 3/2\sigma$ 33%/60% δ_{cp}
+ NO ν A (6 yrs), T2K(6yrs)	$\geq 5/3.8\sigma$ 60%/all δ_{cp}	$\geq 4/3\sigma$ 23%/50% δ_{cp}

Figure 4-13 shows the significance with which the mass hierarchy can be resolved and CP violation determined as a function of increased exposure in LBNE of mass X power X time [†]. For this study the upgraded LBNE beam is used with $E_p = 80$ GeV, and the signal and background systematics are assumed to be 1% and 5% respectively. Both ν_e and ν_μ appearance signals are used in a combined analysis. The determination of the mass hierarchy in LBNE to high precision does not require a large exposure. A 5σ sensitivity for the worst case (NH, $\delta_{cp} = \pi/2$) or (IH, $\delta_{cp} = -\pi/2$) requires an exposure of ~ 200 kton.MW.years, but 5σ sensitivity can be reached for 50% of the allowed values of δ_{cp} with an exposure of less than 100 kton.MW.years. On the other hand, reaching discovery level sensitivities ($\geq 5\sigma$) to leptonic CP violation for at least 50% of the possible values of δ_{cp} will require large exposures of ≈ 450 kton.MW.years. Figure 4-14 demonstrates the sensitivity to CP violation as a function of δ_{cp} and exposure that can be achieved with various stages of Project X (Table 3-2). In this study, Stage 1 and 2 of Project X are assumed to provide 1.1MW at 80 GeV to LBNE, followed by Stage 3 which provides 2.3 MW at 80 GeV. The study demonstrates that it is possible to reach 5σ sensitivity to CP violation over at least 50% of δ_{cp} values with a 34kton LArTPC detector running for a little over 10 years starting with the current MI power and phasing in Project X upgrades. Other possible staging scenarios of detector mass and beam power are discussed in Chapter 3.

[†]Time is denoted in years of running at Fermilab. 1 year of running at Fermilab corresponds to $\approx 1.8 \times 10^7$ seconds.

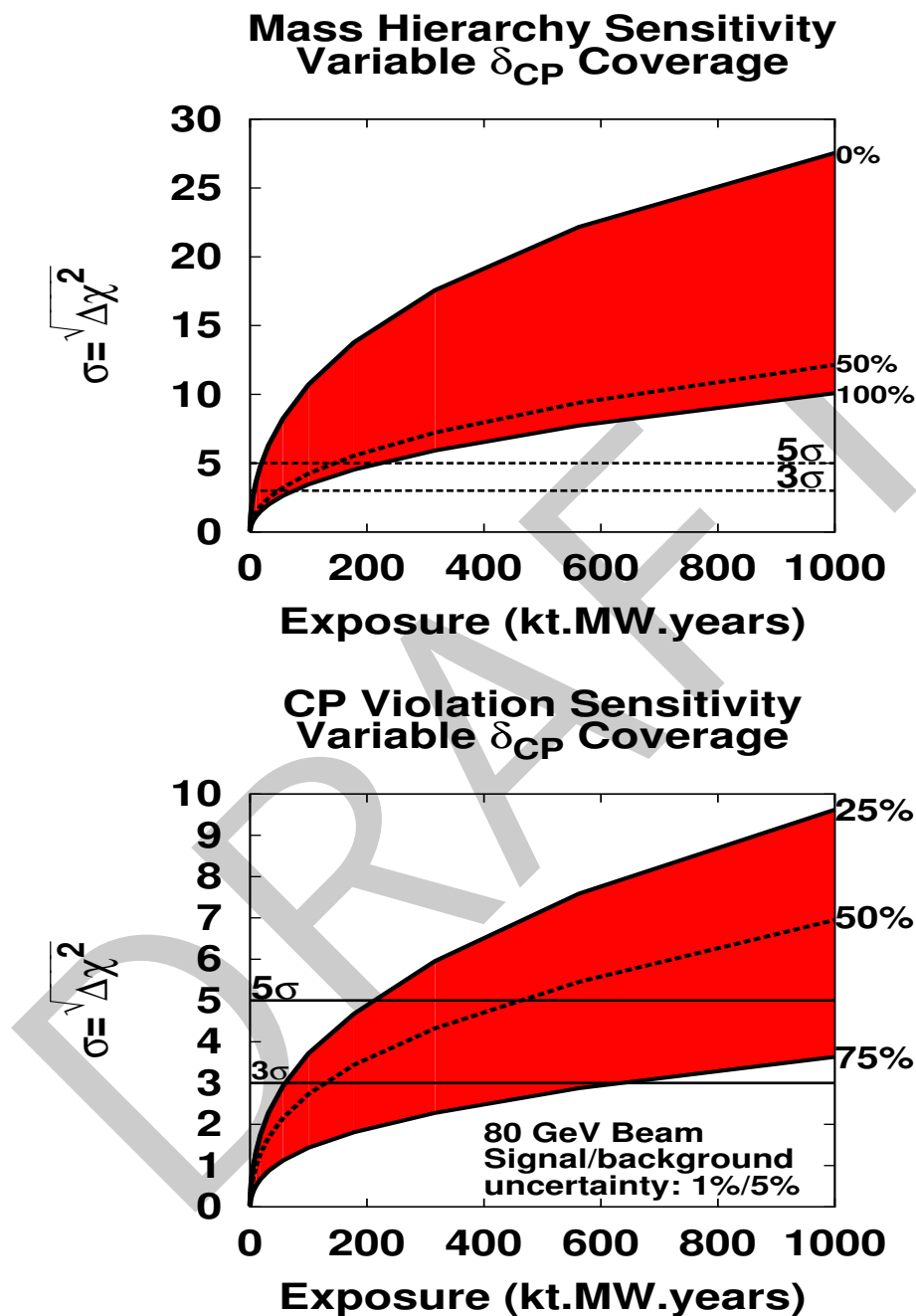


Figure 4-13: The minimum significance with which the mass hierarchy (top) and CP violation (bottom) can be resolved as a function of exposure in detector mass (kton) \times beam power (MW) \times time (years). The red band represents the fraction of δ_{cp} values for which the sensitivity can be achieved with at least the minimal significance on the y-axis. NOTE: THE 50% CURVE FOR MH IS INCORRECT

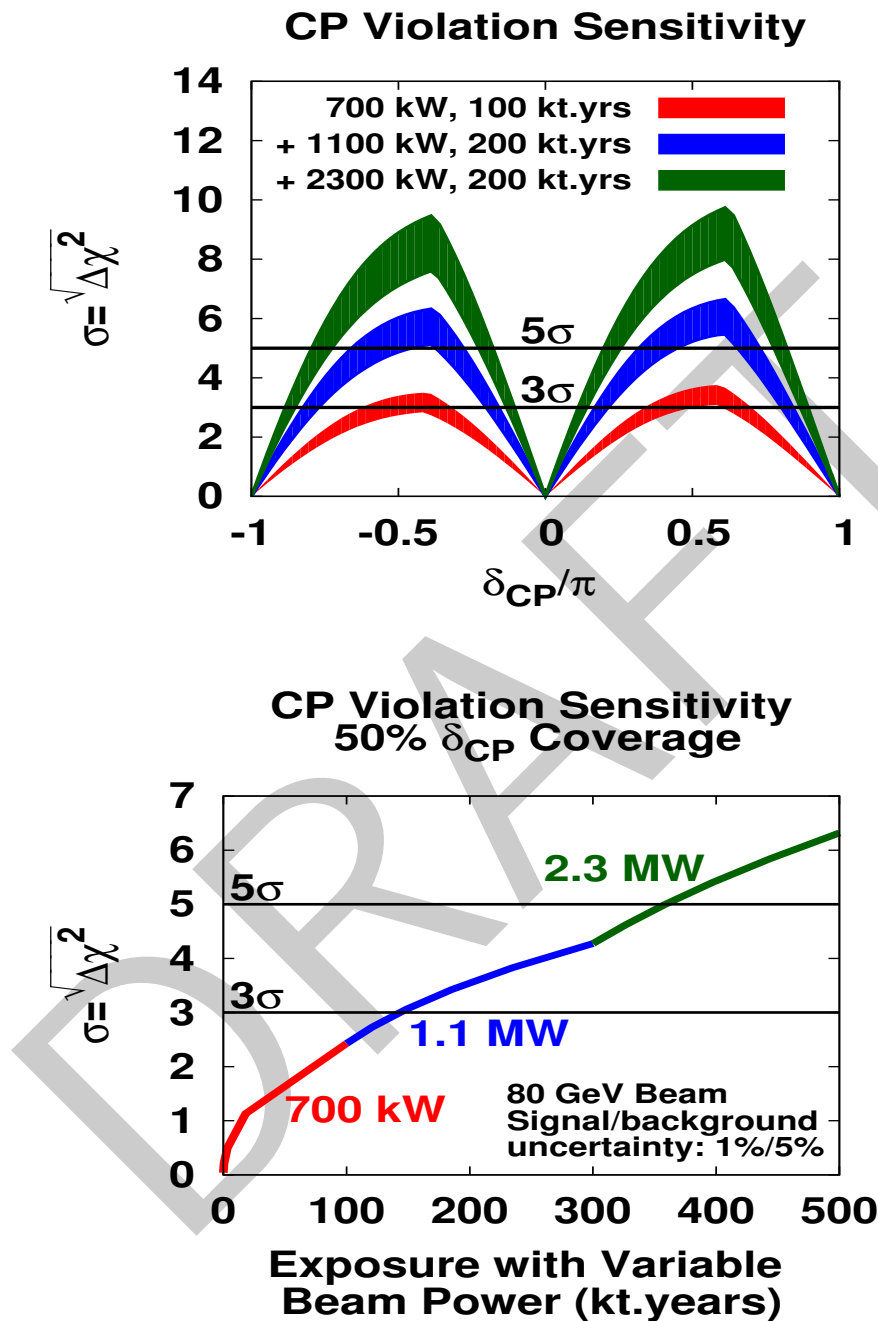


Figure 4-14: The significance with which CP-violation - $\delta_{cp} \neq 0$ or π - can be determined as a function of δ_{cp} (top) and the minimum significance versus exposure for 50% of δ_{cp} values (bottom). The different color curves represent possible exposures from different stages of Project X as follows 700 kW, 100 kton-years (red), + 1.1MW, 200 kton-years (blue) + 2.3MW, 200 kton-years (green). The band on the top figure represents the range of sensitivities obtained from improvements to the CDR beam design.

4.3 Measurement of θ_{23} and Determination of the Octant

The value of the atmospheric mixing angle $\sin^2 \theta_{23}$ from global fits given by [15] is $\sin^2 \theta_{23} = 0.0386^{+0.0024}_{-0.0021}(1\sigma)$ for a normal hierarchy, but as shown in Figure 4–15, the distribution of the χ^2 from the global fit has another local minimum at $\sim \sin^2 \theta_{23} = 0.62$ - particularly if the hierarchy is inverted. As a result a maximal mixing value of $\sin^2 \theta_{23} = 0.5$ is still allowable and the octant is still largely undetermined. The determination of whether there is maximal

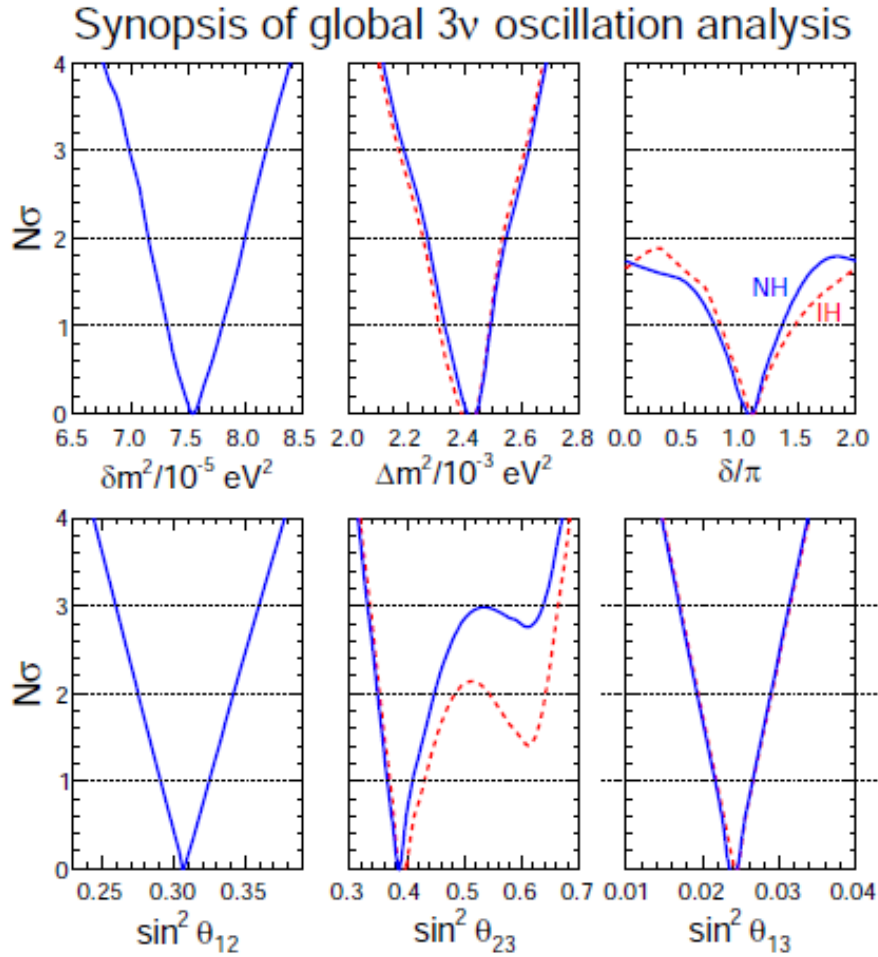


Figure 4–15: Results of the global analysis in terms of $N\sigma$ bounds on the six parameters governing 3 ν oscillations. Blue (solid) and red (dashed) curves refer to NH and IH, respectively. Figure is from ref. [15]

mixing in the lepton sector or a measurement of the size of the deviation from maximal is of great interest theoretically. Models of quark-lepton universality propose that $U^{\text{CKM}} = 1 + (\text{Cabbibo})$ and $U^{\text{PMNS}} = T + (\text{Cabbibo})$ effects where T is determined by Majorana physics [?]. In such models $\theta_{23} \sim \pi/4 + \Delta\theta$, where $\Delta\theta$ is of order the Cabbibo angle, θ_C , and $\theta_{13} \sim \theta_C/\sqrt{2}$. It is therefore important experimentally both to determine the value of $\sin^2 \theta_{23}$ and to

1 determine the octant of θ_{23} . The measurement of $\nu_\mu \rightarrow \nu_\mu$ oscillations is sensitive to $\sin^2 2\theta_{23}$,
 2 whereas the measurement of $\nu_\mu \rightarrow \nu_e$ oscillations is sensitive to $\sin^2 \theta_{23}$. A combination of
 3 both ν_e appearance and ν_μ disappearance measurements can probe both maximal mixing
 4 and the θ_{23} octant. With the large statistics and rich spectral structure in a wide-band long-
 5 baseline experiment like LBNE (see Figure 4-10), precision measurements of $\sin^2 \theta_{23}$ can
 6 be significantly improved compared to existing experiments, particularly for values of θ_{23}
 7 near 45° . Figure 4-16 demonstrates the measurement precision of θ_{23} and Δm_{31}^2 that can
 8 be achieved by LBNE 10kton alone for different allowed values. For the disappearance mode
 9 systematic uncertainties of 5% on signal and 10% on background are assumed - which is
 10 consistent with the assumption of no near neutrino detector. The sub-dominant appearance
 mode in LBNE10 is dominated by statistical uncertainties. The significance with which the

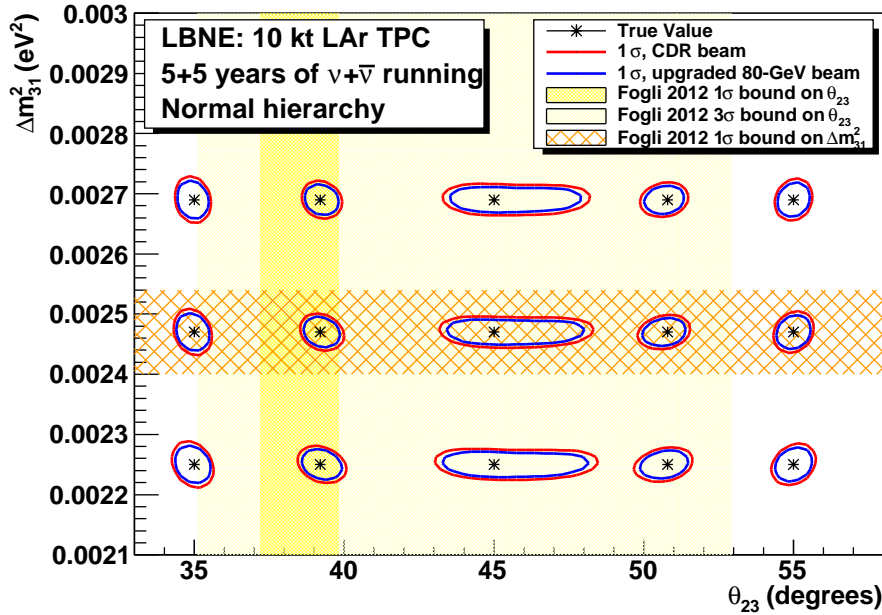


Figure 4-16: The precision with which a simultaneous measurement of θ_{23} and Δm_{31}^2 can be determined in LBNE10. The yellow bands represent the 1σ and 3σ allowed range of θ_{23} from the 2012 global fit.

11 θ_{23} octant can be determined with LBNE10 is shown in Figure 4-17. If θ_{23} is within the
 12 current 1σ bound of the best fit value from the global fits, LBNE10 alone will determine the
 13 octant with $> 3\sigma$ significance for all values of δ_{cp} . Figure 4-18 demonstrates the increasing
 14 sensitivity to the θ_{23} octant for values closer to maximal mixing that can be achieved with
 15 subsequent phases of LBNE coupled with Project X upgrades to the Main Injector power.
 16 With sufficient exposure, LBNE can resolve the θ_{23} octant with $> 3\sigma$ significance even if θ_{23}
 17 is within a few degrees of 45° .
 18

Octant Sensitivity

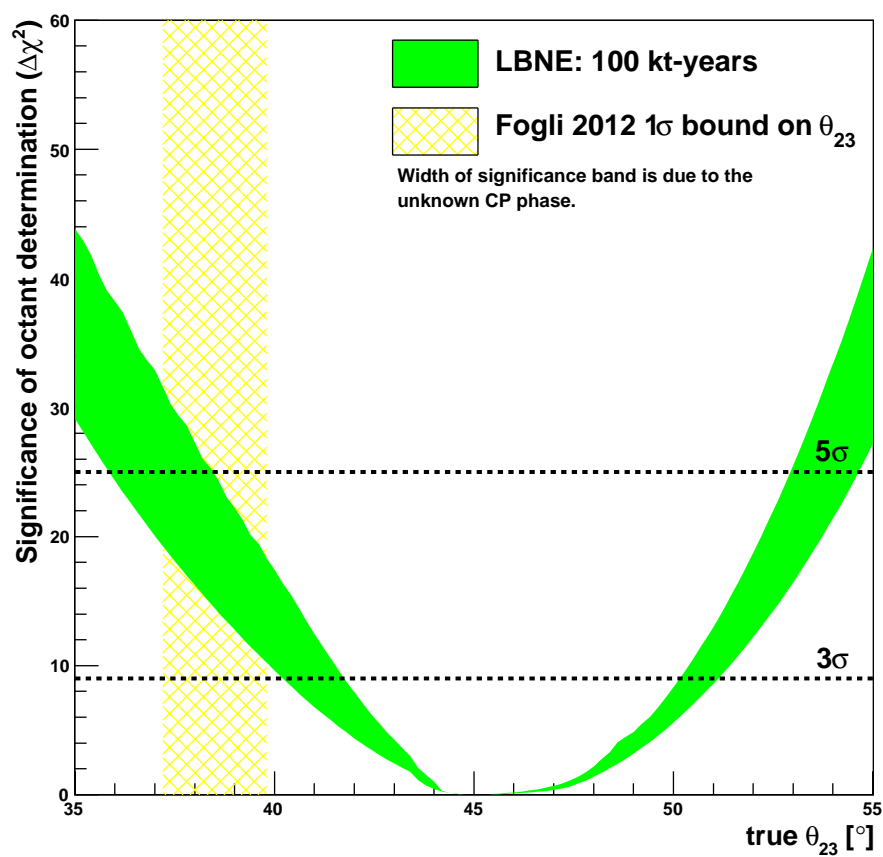


Figure 4-17: Significance with which LBNE can resolve the θ_{23} octant degeneracy for 5+5 years of $\nu+\bar{\nu}$ running at 700 kW and normal mass hierarchy with a 10 kton detector. The width of the green band corresponds to the impact of different true values for δ_{CP} , ranging from a 10% to 90% fraction of δ_{CP} .

Octant Sensitivity

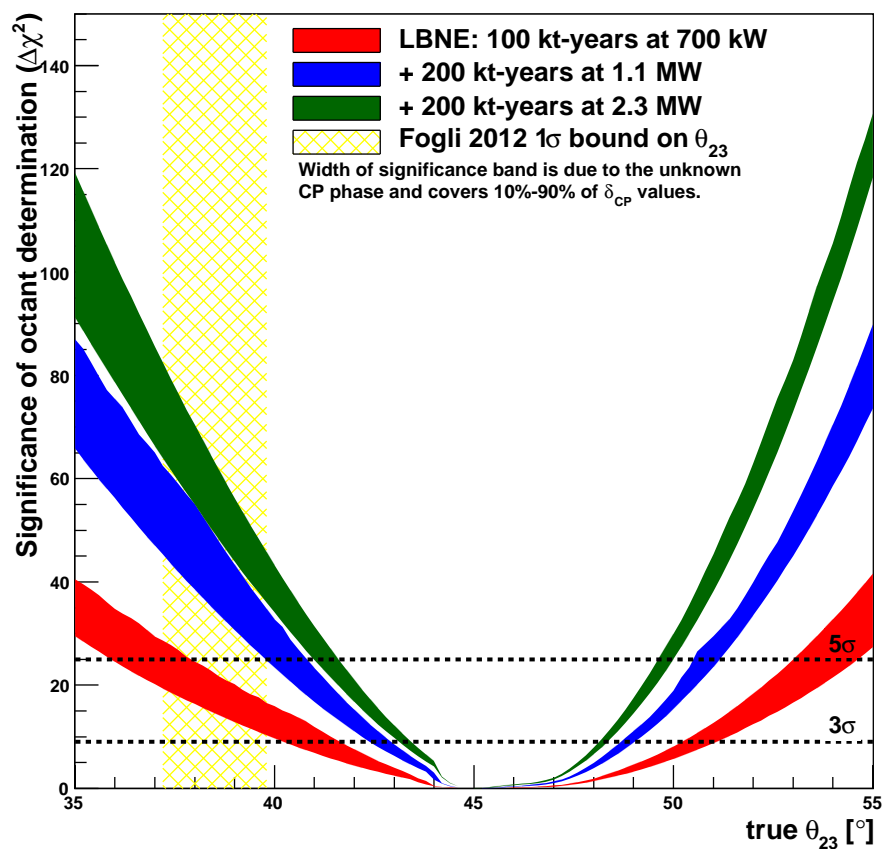


Figure 4-18: Significance with which LBNE can resolve the θ_{23} octant degeneracy for 5+5 years of $\nu+\bar{\nu}$ running with increased exposures as follows 700 kW, 100 kton-years (red), + 1.1MW, 200 kton-years (blue) + 2.3MW, 200 kton-years (green). Normal mass hierarchy is assumed. The width of the bands corresponds to the impact of different true values for δ_{CP} , ranging from a 10% to 90% fraction of δ_{CP} .

4.4 Precision Measurements of the Oscillation Parameters in the 3-Flavor Model

The rich oscillation structure and excellent particle identification of LBNE will enable precision measurement of all the mixing parameters governing the 1-3 and 2-3 mixing in a single experiment. As discussed in Section 4.3, theoretical models probing quark-lepton universality predict specific values of the mixing angles and the relations between them. The reactor mixing angle θ_{13} is expected to be measured accurately in reactor experiments by the end of the decade with a precision that will be limited by systematics. The systematic uncertainty on the value of $\sin^2 2\theta_{23}$ from the Daya Bay reactor neutrino experiment - which has the lowest systematics - is currently 0.005 [44]. While the constraint on θ_{13} from the reactor experiments will be important in the determination of CP violation, measurement of δ_{cp} and the determination of the θ_{23} octant in the early stages of LBNE, eventually LBNE will be able to measure θ_{13} independently with a precision on par with the final precision expected from the reactor experiments. We note that the reactor experiments measure θ_{13} using $\bar{\nu}_e$ disappearance whereas LBNE will measure it through ν_e and $\bar{\nu}_e$ appearance, thus providing an independent constraint on the 3-flavor mixing matrix. Figure 4-19 demonstrates the precision with which LBNE can measure δ_{cp} and θ_{13} simultaneously with no external constraints on θ_{13} as a function of increased exposure starting with the LBNE10 and in subsequent phases with different Project X beams. Both appearance and disappearance modes are included in the fit using the upgraded 80 GeV beam, and with 1%/5% systematic uncertainties assumed on signal/background. Figure 4-20 shows the expected 1σ resolution on different 3-flavor oscillation parameters as a function of exposure in a 700kW beam with LBNE alone, and LBNE in combination with the expected performance from T2K and NO ν A. We note that LBNE alone could reach a precision on $\sin^2 2\theta_{13}$ of 0.005 - on par with the current Daya Bay systematic uncertainty - with an exposure of ~ 300 kton.MW.yrs. LBNE can also significantly improve the resolution on Δm_{23}^2 beyond what the combination of NO ν A and T2K can achieve, reaching a precision of $< 1 \times 10^{-5}$ eV² with an exposure of ~ 300 kton.MW.yrs. The precision on Δm_{23}^2 will ultimately depend on the tight control of the energy scale systematics which is under investigation. Initial studies of the systematics reveal that the measurement of ν_μ disappearance in LBNE over a full oscillation interval with two oscillation peaks and two valleys (Figure 4-10) accessible, reduces the dependency of the Δm_{23}^2 measurement on the energy scale systematics which dominated the measurement precision in MINOS [45]. Table 4-6 summarizes the sensitivities to the mass hierarchy and CP violation and the precision with which the different oscillation parameters can be measured with different far detector masses in LBNE. A 10 year exposure to the 700 kW beam from the current Main Injector complex is assumed.

It is important to note that LBNE alone can potentially reach a precision on δ_{cp} that is $\sim 6 - 10^\circ$ which is close to the 4° CKM precision on δ_{cp}^{CKM} - but an exposure of ~ 700 kton.MW.years is needed. Nevertheless, as shown in Figure 4-21, wide-band long baseline experiments such as LBNE (and LBNO) can achieve close to CKM precision on δ_{cp} with much

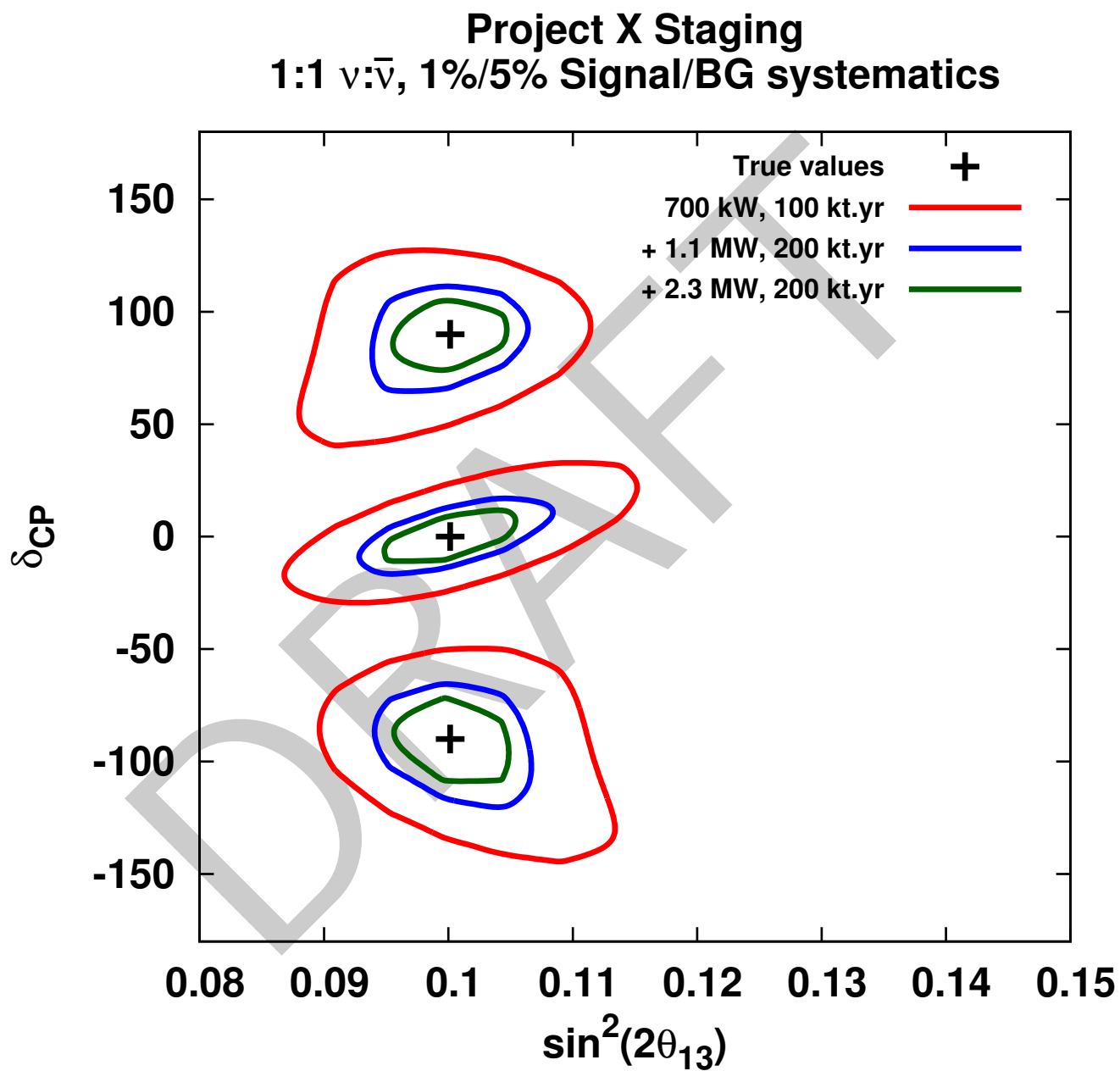


Figure 4–19: Measurement of δ_{cp} and θ_{13} in LBNE with different exposures.

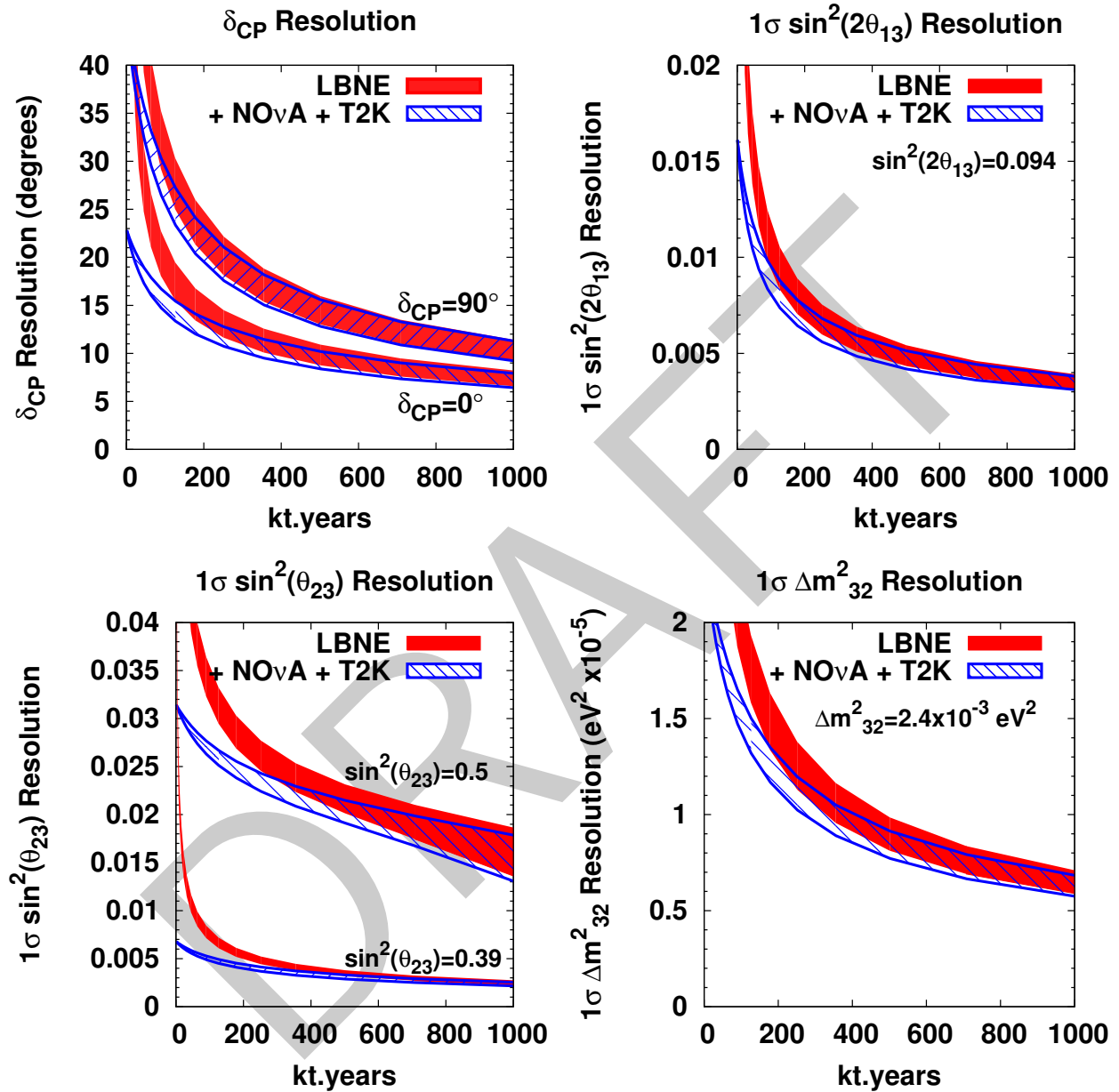


Figure 4–20: The expected 1σ resolution on different 3-flavor oscillation parameters as a function of exposure in a 700kW beam. The red curve is the precision that could be obtained from LBNE alone, and the blue curve represents the combined precision from LBNE and the T2K and NO ν A experiments. The plots are clockwise from top left: δ_{cp} , $\sin^2 2\theta_{13}$, $|\Delta m^2_{31}|$, and $\sin^2 \theta_{23}$. The width of the bands represents the range of performance with the beam improvements under consideration.

Table 4-6: Summary of the oscillation measurements with different configurations given $\theta_{13} = 8.8^\circ$, $\theta_{23} = 40^\circ$, $\Delta m_{31}^2 = +2.27 \times 10^{-3} \text{eV}^2$. The fraction of δ_{cp} values for which the mass hierarchy (MH) or CP violation (CPV) are determined with 3σ sensitivity are given in the first 2 columns. For the first 2 columns, all correlations and uncertainties on the known mixing parameters, as well as consideration of the opposite mass hierarchy hypothesis, are included. The measurements assume 5 years of neutrino running and 5 years of anti-neutrino running at a beam power of 708kW with 6×10^{20} protons-on-target accumulated per year with a LAr-TPC. We assume $\text{NO}\nu\text{A}$ will run for a minimum of 3+3 years with the NuMI ME energy beam ($\text{NO}\nu\text{A}$ I). We assume 5×10^{21} protons-on-target total accumulated by T2K (~ 6 yrs) in neutrino only mode. * These measurements are for the combination of neutrino and anti-neutrino running. NOTE: WILL BE UPDATED WITH POST RECONFIG RESULTS

Configuration	MH* fraction of δ (3σ)	CPV* fraction of δ (3σ)	$\sigma(\delta_{cp})^*$ 0, 90°	$\sigma(\theta_{13})^*$ $\delta = 90^\circ$	$\sigma(\theta_{23})$ ν	$\sigma(\theta_{23})$ $\bar{\nu}$	$\sigma(\Delta m_{31}^2)$ ν (10^{-3}eV^2)	$\sigma(\Delta m_{31}^2)$ $\bar{\nu}$ (10^{-3}eV^2)
$\text{NO}\nu\text{A}$ (6yrs) + T2K (6yrs)	0.0	0.0	22,65°	0.62°				
Homestake 5kt	0.66	0.00	25,41°	0.60°	0.92°	1.4°	0.035	0.055
Homestake 10kt	0.75	0.05	17,30°	0.40°	0.69°	0.97°	0.025	0.040
Homestake 15kt	0.90	0.40	15,25°	0.30°	0.52°	0.80°	0.020	0.030
Homestake 20kt	1.0	0.50	13,21°	0.25°	0.46°	0.63°	0.018	0.026
Homestake 5kt + $\text{NO}\nu\text{A}$ + T2K	1.00	0.33	15,31°					
Homestake 10kt + $\text{NO}\nu\text{A}$ + T2K	1.00	0.45	12,25°					
Homestake 15kt + $\text{NO}\nu\text{A}$ + T2K	1.00	0.53	12,24°					

less exposure when compared to existing experiments such as NO ν A, T2K and proposed experiments short-baseline off-axis experiments such as T2HK. It is important to note that the precision on δ_{cp} in the off-axis experiments shown in Figure 4-21 assumes the mass hierarchy is resolved. If the mass hierarchy is unknown the resolution of T2K, NO ν A and T2HK will be much worse than indicated. LBNE does not require external information on the mass hierarchy to reach the precisions described in this section. Only a neutrino factory can possibly out perform a wide-band long-baseline experiment - but not by much - for equal power, target mass and years of running. We note however, that to achieve this precision LBNE will need to tightly control the systematic uncertainties on the ν_e appearance signal. A high resolution near detector will be needed to reach this level of precision as described in Chapter 5. Future upgrades to the Fermilab accelerator complex, in particular the prospect

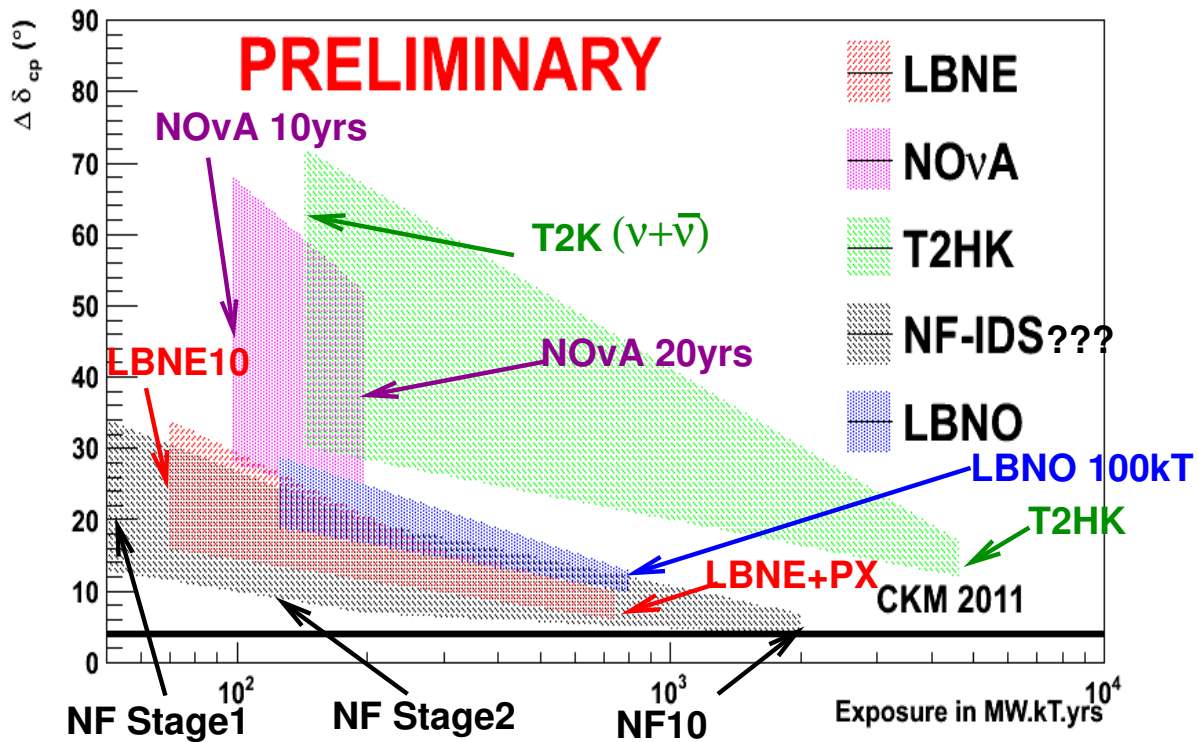


Figure 4-21: The 1σ resolution on δ_{cp} that can be achieved by existing and proposed beam neutrino oscillation experiments as a function of exposure in terms of mass \times beam power \times years of running. The band represents the variation in the resolution as a function of δ_{cp} with the lower edge being the best resolution and the upper edge being the worst. The bands start and stop at particular milestones. For example the LBNE band starts with the resolutions achieved by LBNE10 and ends with the full LBNE running with the first 3 stages of Project X. The black line denotes the 4° resolution point which is the resolution of δ_{cp}^{CKM} from the 2011 global fits.

of high power low energy proton beams such as 3MW at 8 GeV available in Stage 4 of Project X could open up further opportunities to probe CP violation using on-axis low energy

- ¹ beams specifically directed at the 2nd oscillation maximum where CP effects dominate the
- ² asymmetries [?] and even probe 1-2 mixing in very long baseline experiments.

DRAFT

4.5 Atmospheric Neutrinos

Physics sensitivities using information from atmospheric neutrinos were obtained using a Fast MC and a three flavor analysis framework developed for the MINOS experiment [?]. In this section we will briefly describe the Fast MC tools, the assumptions about detector performance, and the three-flavor analysis framework.

Four-vector level events are generated using the GENIE neutrino event generator [?]. For atmospheric neutrinos the Bartol [?] flux calculation for the Soudan, MN site was used, and for beam neutrinos the 700 kW beam designed was used [10]. The expected event rates in 100 kton-yr are shown in Table 4-7. All interactions occur on argon, and are distributed uniformly throughout a toy detector geometry consisting of two modules each 14.0 m high, 23.3 m wide, and 45.4 m long. For this study, events with interaction vertices outside the detector volume, for instance which produce upward-going stopping or throughgoing muons, have not been considered. We have not studied cosmogenic backgrounds in detail, but we expect that since atmospheric neutrinos are somewhat more tolerant of background than proton decay, a depth that is sufficient for a proton decay search should also be suitable for atmospheric neutrinos. For the SURF 4850L depth, a veto should not be necessary, and one can assume full fiducial mass; at depths around 2,700 feet, a one-meter fiducial cut should be adequate.

Table 4-7: Expected event rates in 100 kton-yr for the Bartol flux and GENIE Argon cross sections (no oscillations).

Flavor	CC	NC	Total
ν_μ	10069	4240	14309
$\bar{\nu}_\mu$	2701	1895	4596
ν_e	5754	2098	7852
$\bar{\nu}_e$	1230	782	2012
Total:	19754	9015	28769

A Fast MC then runs on the produced four-vectors, placing events into containment and flavor categories. Containment is evaluated by tracking leptons through the LAr detector box geometry and classifying events as either fully or partially contained. A detection threshold of 50 MeV is assumed for all particles. The flavor determination is based on the primary and secondary particles above detection threshold, and events are placed into e-like or μ -like categories based on the identity of these particles. Electrons and muons are assumed to be correctly identified with 90% and 100% probability, while other electromagnetic particles (π^0, γ) are misidentified as electrons 5% of the time, and charged pions are misidentified as muons 1% of the time. Events that do not have an identified muon or electron as one of the two leading particles are placed into an 'NC-like' category. With these assumptions the purities of the flavor-tagged samples are 97.8% for the FC e-like sample, 99.7% for the FC μ -like sample, and 99.6% for the PC μ -like sample. The NC-like category is not used in this

analysis, but would be useful for tau appearance studies.

The energy and direction of the event are then estimated by separately smearing the energy and direction of the leptonic and hadronic system, where the width of the gaussian resolution functions for each flavor / containment category are given in Table 4-8. Detector performance assumptions are taken from the LBNE CDR and published results from the ICARUS experiment [10,?].

Table 4-8: Detector performance assumptions for the atmospheric neutrino and the combined atmospheric+beam neutrino analyses.

Angular Resolutions	Electron	1°
	Muon	1°
	Hadronic System	10°
Energy Resolutions	Stopping Muon	3%
	Exiting Muon	15%
	Electron	$1\%/\sqrt{E(GeV)} \oplus 1\%$
	Hadronic System	$30\%/\sqrt{E(GeV)}$

Including oscillations, in 100 kt-yrs we expect 4015 events in the FC e-like sample, 5958 events in the FC μ -like sample and 1963 events in the PC μ -like sample. Figure 4-22 shows the expected L/E distribution for ‘High-Resolution’ μ -like events from a 350 kt-yr exposure. ‘High-resolution’ events are defined in a similar way to Super-Kamiokande, by excluding a region of events that are low energy or pointing towards the horizon where the L resolution is poor. The data provides excellent resolution of the first two wavelengths, even taking into account the expected statistical uncertainty. Unless otherwise specified, in this section oscillation parameters are taken to be: $\Delta m^2 = 1/2(\Delta m_{32}^2 + \Delta m_{31}^2) = 2.40 \times 10^{-3} \text{ eV}^2$, $\sin^2 \theta_{23} = 0.40$, $\Delta m_{12}^2 = 7.54 \times 10^{-5} \text{ eV}^2$, $\sin^2 \theta_{12} = 0.307$, $\sin^2 \theta_{13} = 0.0242$, $\delta_{CP} = 0$, and normal hierarchy.

In performing oscillation fits the data in each flavor/containment category are binned in energy and zenith angle. Figure 4-23 shows the zenith angle distributions for several ranges of reconstructed energy, where oscillation features are clearly evident.

The power to resolve the mass hierarchy with atmospheric neutrinos comes primarily from the MSW enhancement of few-GeV neutrinos at large zenith angles. This enhancement occurs for neutrinos in the normal hierarchy and anti-neutrinos in the inverted hierarchy. Figure 4-24 shows zenith angle distributions of events in the relevant energy range for each of the three flavor/containment categories. Small differences are evident in comparing the normal and inverted hierarchy predictions.

Since the resonance peak occurs for neutrinos in normal hierarchy and antineutrinos for inverted hierarchy, the MH sensitivity can be greatly enhanced if neutrino and anti-neutrino

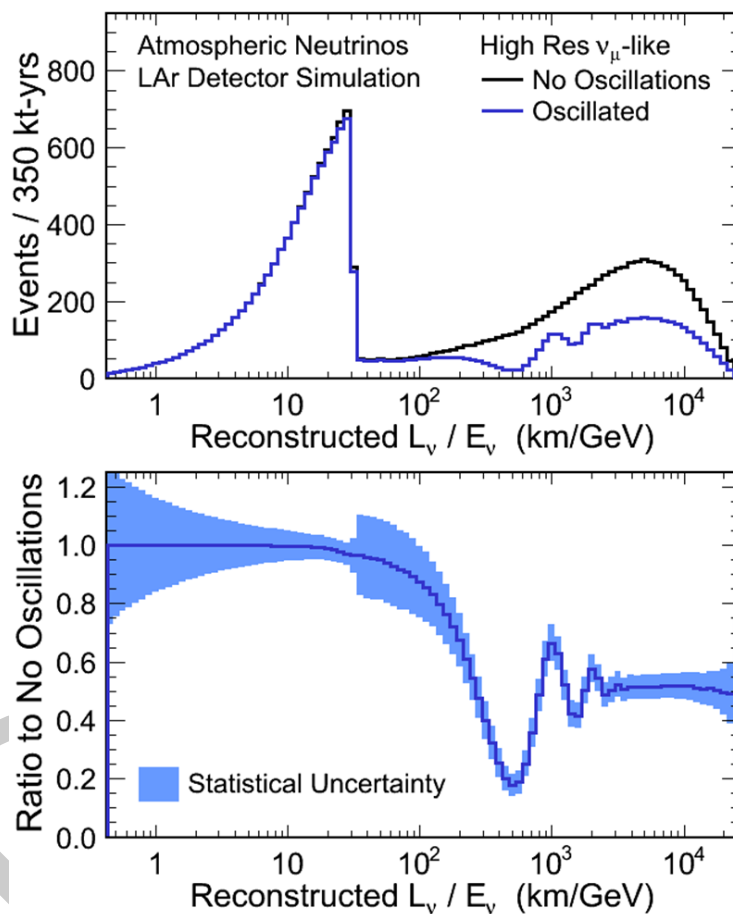


Figure 4-22: Reconstructed L/E Distribution of 'High Resolution' μ -like atmospheric neutrino events in a 350 kt-yr exposure with and without oscillations (top), and the ratio of the two (bottom), with the shaded band indicating the size of the statistical uncertainty.

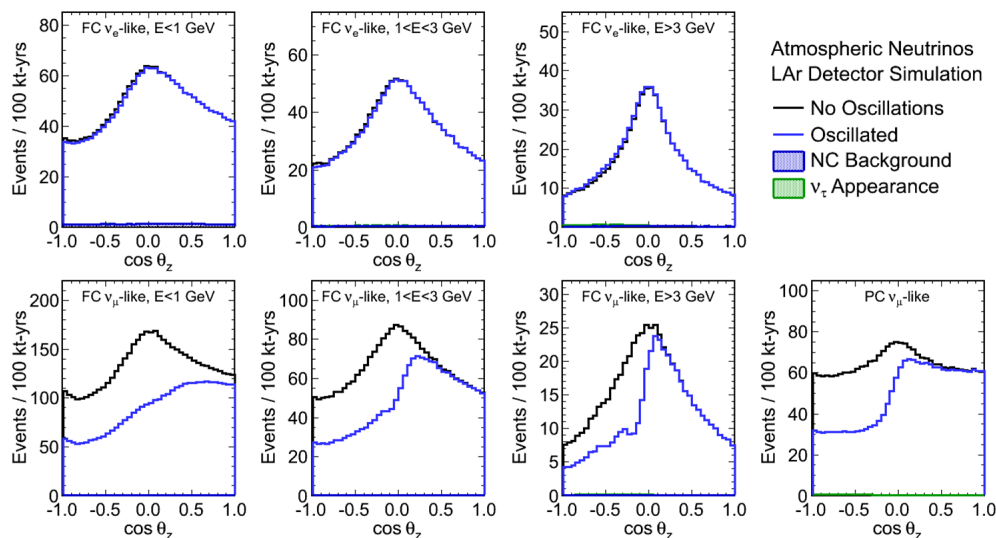


Figure 4-23: Reconstructed zenith angle distributions in several ranges of energy for the FC e-like, FC μ -like, and PC μ -like samples. The small contributions from NC backgrounds and tau appearance are also shown.

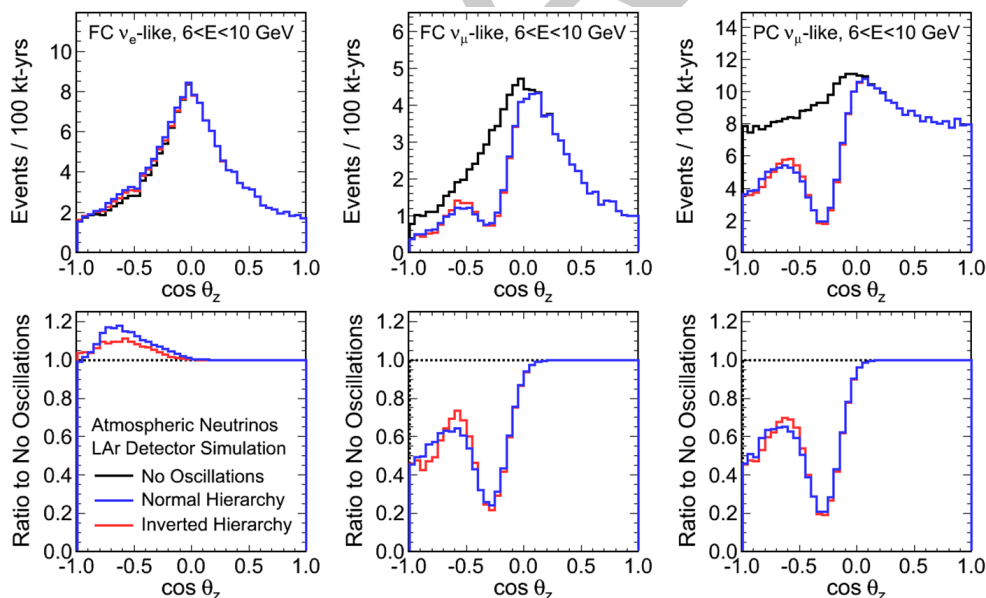


Figure 4-24: Reconstructed zenith angle distributions for 6-10 GeV events in the FC e-like, FC μ -like, and PC μ -like samples. Top plots show the expected distributions for no oscillations (black), oscillations with normal mass hierarchy (blue), and inverted hierarchy (red). The ratio of the normal and inverted hierarchy expectations to no oscillations are shown for each category in the bottom plots.

events can be separated. The LBNE detector will not be magnetized, however the high-resolution imaging does offer some possibilities for tagging features of events that provide statistical discrimination between neutrinos and anti-neutrinos. For the sensitivity calculations that follow, we have included two such tags: a proton tag and a decay-electron tag. Protons are tagged with 100% efficiency if their kinetic energy is greater than 50 MeV; for low-multiplicity events protons occur preferentially in neutrino interactions. Decay electrons are assumed to be 100% identifiable and are assumed to occur 100% of the time for μ^+ and 25% of the time for μ^- .

In the oscillation analysis 18 nuisance parameters are included, with detector performance parameters correlated between beam and atmospheric data. In all cases we take $\sin^2 \theta_{12}$, $\Delta m^2 = 1/2(\Delta m_{32}^2 + \Delta m_{31}^2)$, and Δm_{12}^2 to be fixed at the previously given values. The fits then range over θ_{23} , θ_{13} , δ_{CP} , and the mass hierarchy. A 2% constraint is assumed on the value of θ_{13} . The systematic errors included in this analysis are given in Table 4-9.

Table 4-9: Systematic errors included in the atmospheric and beam+atmospheric neutrino analysis. The beam values assume the existence of a near detector. Atmospheric spectrum ratios include the combined effect of flux and detector uncertainties (e.g. the up/down flux uncertainty as well as the uncertainty on the detector performance for the up/down ratio). The atmospheric spectrum shape uncertainty functions are applied separately for $\nu_\mu, \nu_e, \bar{\nu}_\mu, \bar{\nu}_e$.

	Atmospheric	Beam (Assumes ND)
Normalisations	Overall (15%)	μ -like (1%) e-like (1%)
NC Backgrounds	e-like (10%)	μ -like (10%) e-like (5%)
Spectrum Ratios	up/down (2%) ν_e/ν_μ (2%) $\bar{\nu}_\mu/\nu_\mu$ (5%) $\bar{\nu}_e/\nu_e$ (5%)	
Spectrum Shape	$f(E < E_0) = 1 + \alpha(E - E_0)/E_0$ $f(E > E_0) = 1 + \alpha \log(E/E_0)$ where $\sigma_\alpha = 5\%$	
Energy Scales (Correlated)	Muons (stopping 1%, exiting 5%) Electrons (1%) Hadronic System (5%)	

For the hierarchy determination, the $\Delta\chi^2$ value is calculated between the best fit points in the normal and inverted hierarchies, where at each the nuisance parameters have been marginalized. The sensitivity in the plots that follow is given as $\sigma = \sqrt{\Delta\chi^2}$. Figure 4-25 shows the MH sensitivity from a 350 kt-yr exposure of atmospheric neutrino data alone. For all values of the hierarchy and δ_{CP} , the hierarchy can be determined at $> 3\sigma$. The resolution depends significantly on the true value of θ_{23} , and the sensitivity for three values is shown. The sensitivity depends relatively weakly on the true hierarchy and the true value of δ_{CP} .

- 1 This is in sharp contrast to the MH sensitivity of the beam, which has a strong dependence
 2 on the true value of δ_{CP} . Figure 4-26 shows the MH sensitivity as a function of the fiducial
 3 exposure. Over this range of fiducial exposures the sensitivity goes essentially as the square
 4 root of the exposure, indicating that the measurement is not systematics limited.

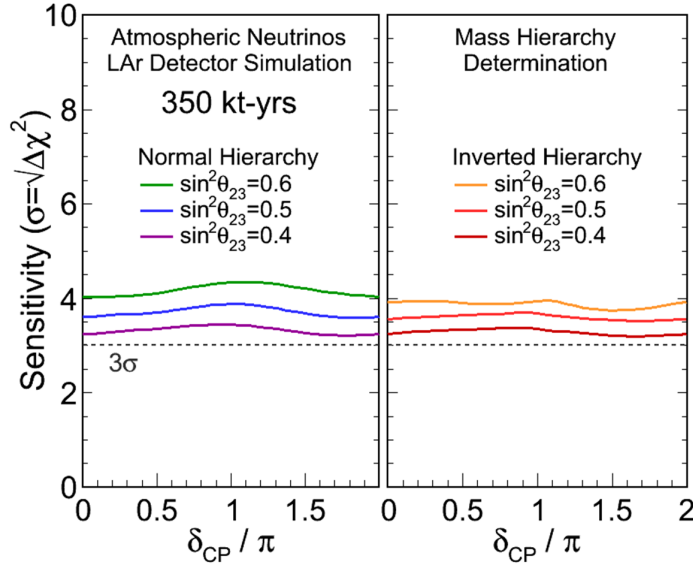


Figure 4-25: Sensitivity of 350 kt-yr of atmospheric neutrino data to the mass hierarchy as a function of δ_{CP} for true and inverted hierarchy and different values of \sin^2_{23} .

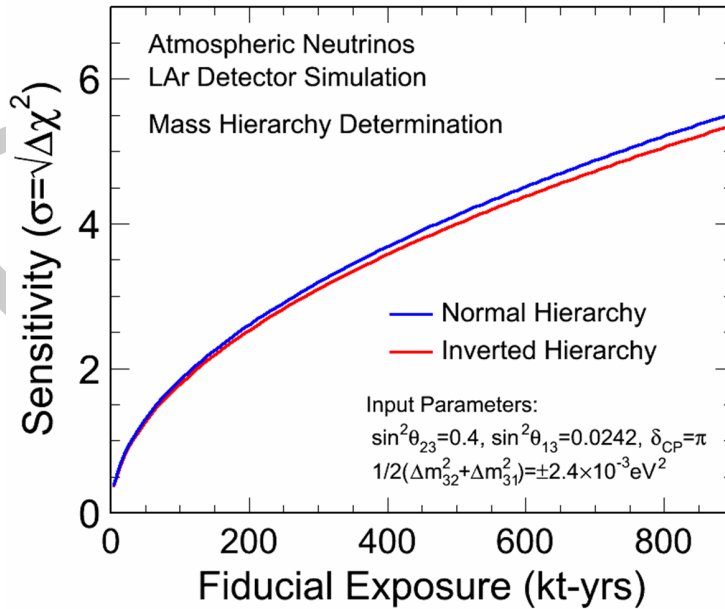


Figure 4-26: Sensitivity to mass hierarchy using atmospheric neutrinos as a function of fiducial exposure in a LAr detector.

- 5 Figure ?? shows the octant and CPV sensitivity from a 350 kt-yr exposure of atmospheric

neutrino data alone. For the determination of the octant of θ_{23} , the $\Delta\chi^2$ value is calculated between the best fit points in the lower ($\theta_{23} < 45^\circ$) and higher ($\theta_{23} > 45^\circ$) octants, where at each the nuisance parameters have been marginalized. The discontinuities in the slopes of the octant sensitivity plot are real features, indicating points at which the best fit moves from one hierarchy to the other. For the detection of CP violation the $\Delta\chi^2$ exclusion is similarly computed for $\delta_{CP} = (0, \pi)$.

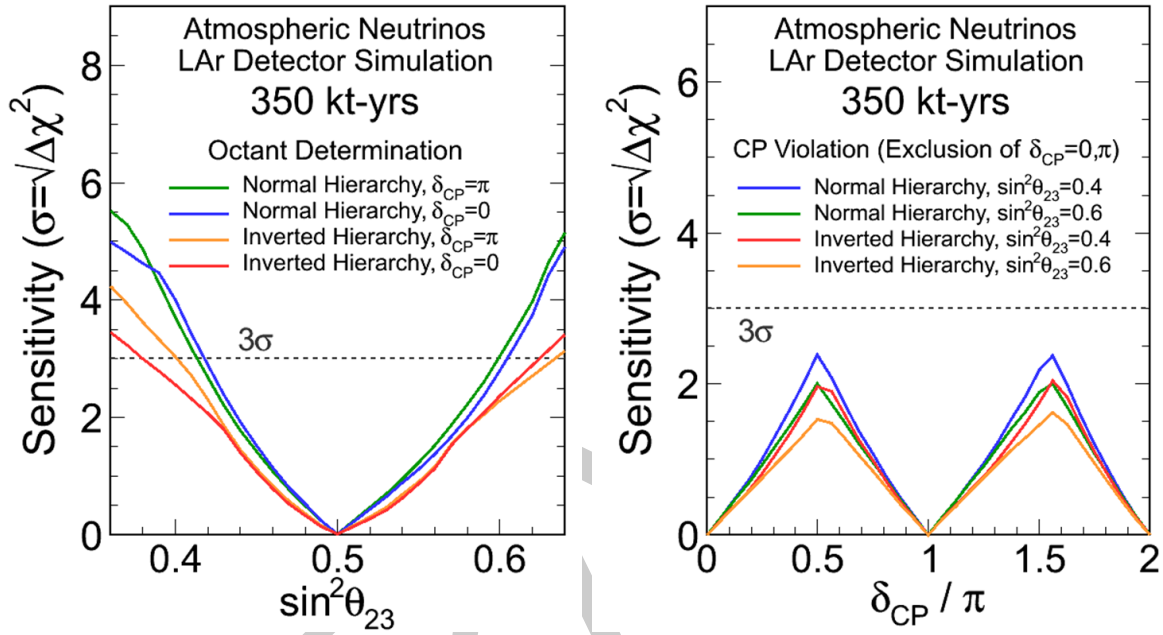


Figure 4-27: Sensitivity to octant (left) and CPV (right) using atmospheric neutrinos.

6

Figure ?? shows the combined sensitivity to beam and atmospheric neutrinos for the mass hierarchy. This assumes a 10 yr run with equal amounts of neutrino and anti-neutrino running. In the region of δ_{CP} where the beam is least sensitive, atmospheric neutrinos offer comparable sensitivity, resulting in a combined sensitivity greater than 5σ for all values of δ_{CP} . The combined sensitivity is also better than the sum of the separate chi-squared values, as the atmospheric data helps to remove degeneracies in the beam data. Figure ?? shows the combined sensitivity to beam and atmospheric neutrinos for the octant determination and CPV. The role played by atmospheric data in resolving beam degeneracies is also clear from considering the combined and beam-only sensitivities in these plots.

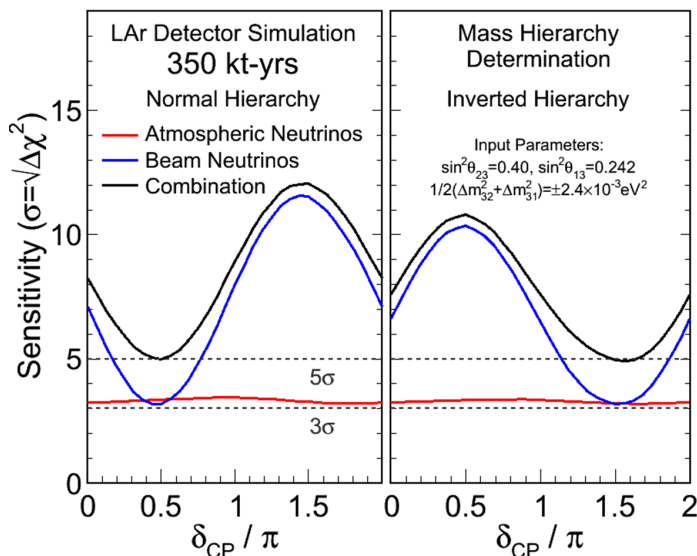


Figure 4-28: Sensitivity to mass hierarchy using atmospheric neutrinos combined with beam neutrinos with an exposure of 350 kt-years in a 700 kW beam.

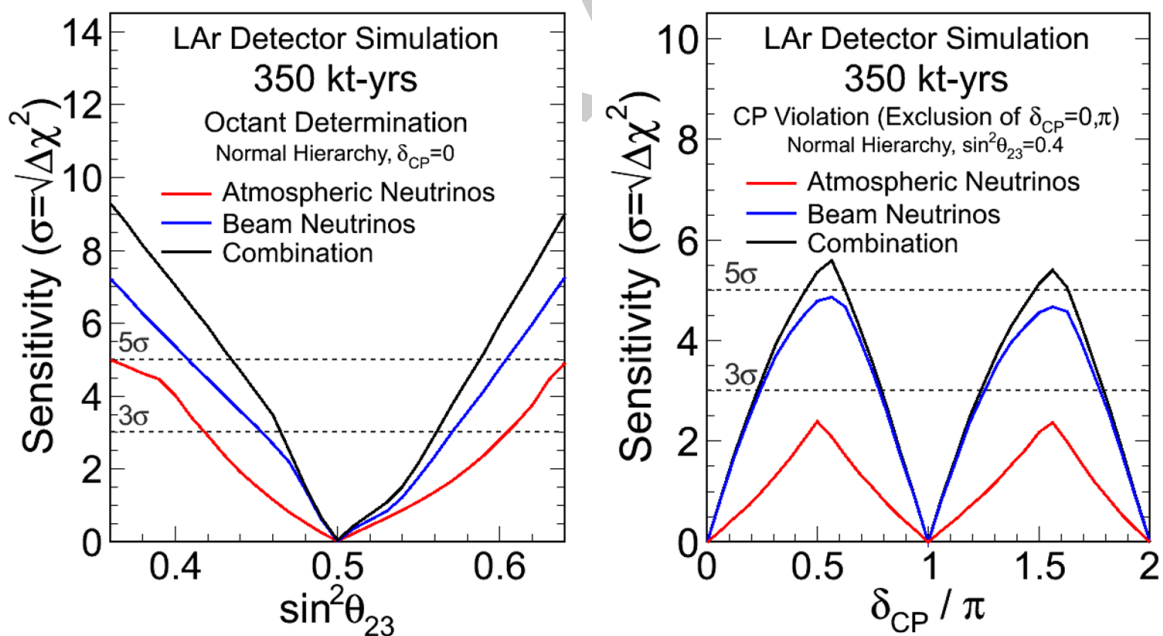


Figure 4-29: Sensitivity to octant (left) and CPV (right) using atmospheric neutrinos combined with beam neutrinos with an exposure of 350 kt-years in a 700 kW beam.

4.6 Searches for Physics Beyond ν SM in Long-baseline Oscillations

In addition to precision measurements of the standard three-flavor neutrino-oscillation parameters, the design of LBNE provides the best potential for discoveries of physics beyond the standard three-flavor oscillation model. This section discusses some examples of new physics that the LBNE design is well suited to pursue. It is to be noted that to fully exploit the sensitivity of the LBNE design to new physics will require higher precision predictions of the unoscillated neutrino flux at the Far Detector and larger exposures (detector mass \times beam power) than currently proposed in the Phase I project.

4.6.1 Search for Non-Standard Interactions

NC non-standard interactions (NSI) can be understood as non-standard matter effects that are visible only in a Far Detector at a sufficiently long baseline. LBNE has a unique advantage in this area compared to other long-baseline experiments (except atmospheric-neutrino experiments, which are, however, limited by systematic effects). NC NSI can be parameterized as new contributions to the MSW matrix in the neutrino-propagation Hamiltonian:

$$H = U \begin{pmatrix} 0 & & \\ & \Delta m_{21}^2/2E & \\ & & \Delta m_{31}^2/2E \end{pmatrix} U^\dagger + \tilde{V}_{\text{MSW}}, \quad (4.1)$$

with

$$\tilde{V}_{\text{MSW}} = \sqrt{2}G_F N_e \begin{pmatrix} 1 + \epsilon_{ee}^m & \epsilon_{e\mu}^m & \epsilon_{e\tau}^m \\ \epsilon_{e\mu}^{m*} & \epsilon_{\mu\mu}^m & \epsilon_{\mu\tau}^m \\ \epsilon_{e\tau}^{m*} & \epsilon_{\mu\tau}^{m*} & \epsilon_{\tau\tau}^m \end{pmatrix} \quad (4.2)$$

Here, U is the leptonic mixing matrix, and the ϵ -parameters give the magnitude of the NSI relative to standard weak interactions. For new physics scales of few $\times 100$ GeV, $|\epsilon| \lesssim 0.01$ is expected.

4.6.2 Long Range Interactions

The small scale of neutrino-mass differences implies that minute differences in the interactions of neutrinos and antineutrinos with background sources can be detected through perturbations to the time evolution of the flavor eigenstates. The longer the experimental baseline, the higher the sensitivity to a new long-distance potential acting on neutrinos. For example, some of the models for such long-range interactions (LRI) as described in [?] (see

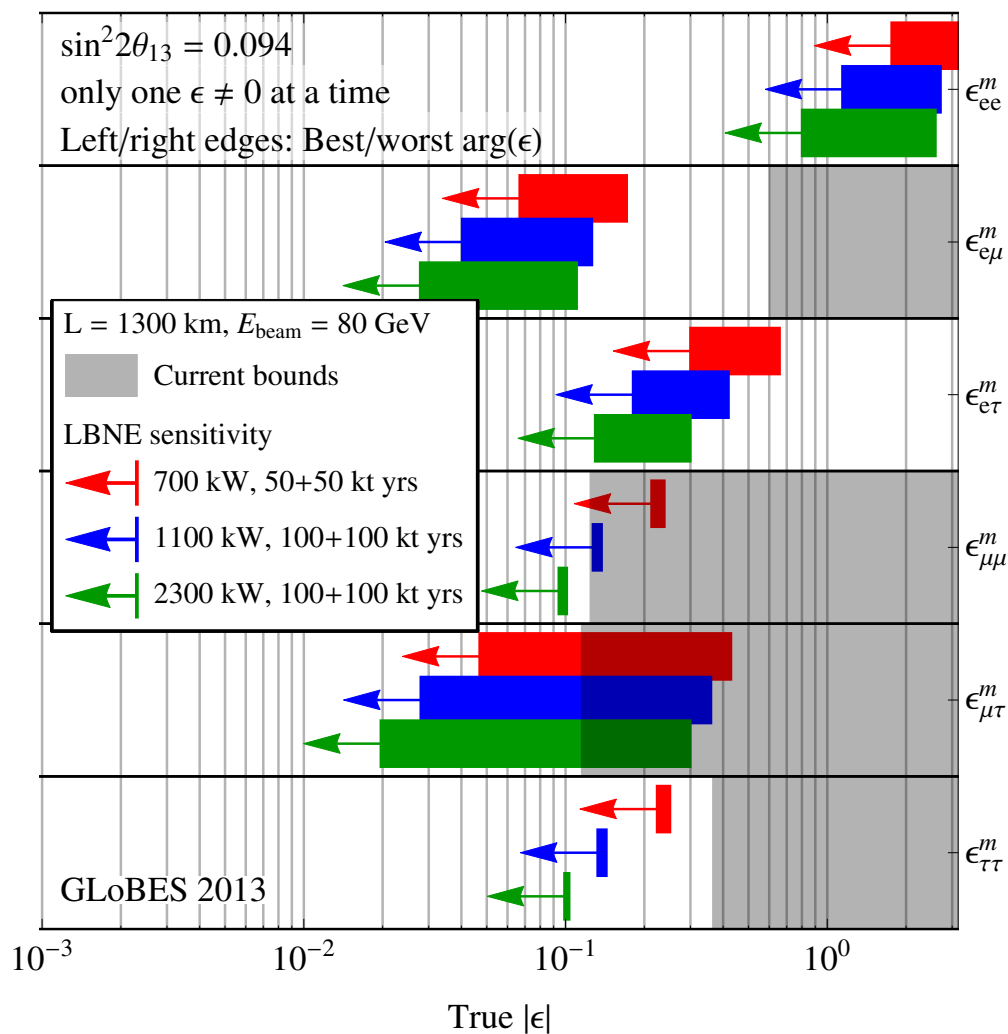
NC NSI discovery reach (3σ C.L.)

Figure 4–30: Non-standard interaction discovery reach in LBNE with increasing exposure: 700 kW 100 kt.years (red) + 1.1MW 200 kt.yrs (blue) + 2.3MW 200 kt.yrs (green). The left and right edges of the error bars correspond to the most favorable and the most unfavorable values for the complex phase of the respective NSI parameters. The gray shaded regions indicate the current model-independent limits on the different parameters at 3σ [?] and [?]. For this study the value of $\sin^2 2\theta_{13}$ was assumed to be 0.09

Figure 4-31) could contain discrete symmetries that stabilize the proton and a dark matter particle and thus provide new connections between neutrino, proton decay and dark matter experiments. The longer baseline of LBNE improves the sensitivity to LRI beyond that possible by the current generation of long-baseline neutrino experiments. The sensitivity will be determined by the amount of $\nu_\mu/\bar{\nu}_\mu$ CC statistics accumulated and the accuracy with which the unoscillated and oscillated ν_μ spectra can be determined.

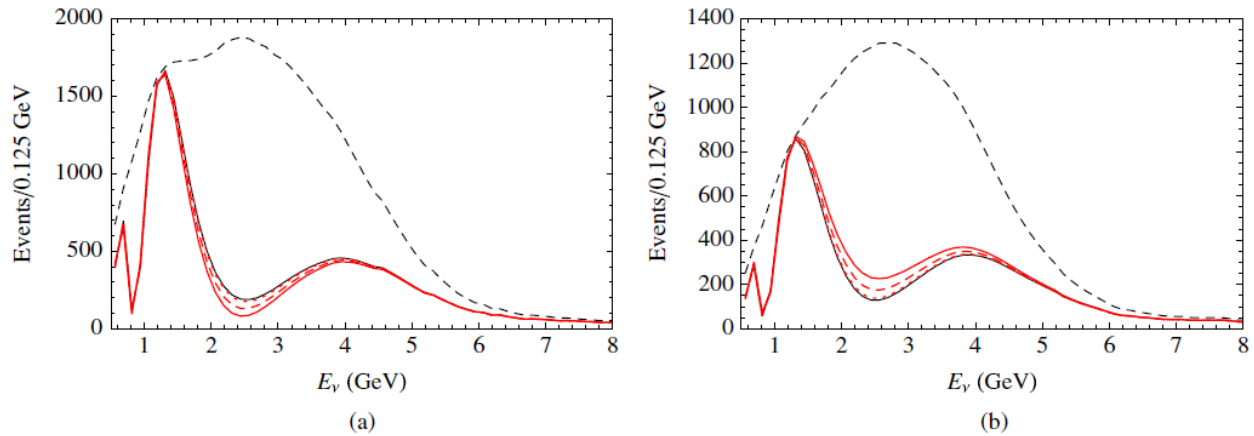


Figure 4-31: Long-range Interactions in LBNE. The number of (a) neutrino and (b) antineutrino events versus E_ν , in a long-baseline experiment with a 1,300-km baseline. The unoscillated case (top black dashed curves) and the case of no new physics (thin black solid curves) are displayed, as well as the cases with $\alpha' = 1.0, 0.5, 0.1 \times 10^{-52}$ corresponding to thick solid, dashed, and dotted curves, respectively. α' is the “fine structure constant” of such interactions which is constrained to be $\alpha' \leq 10^{-47}$ [?].

4.6.3 Search for Active-sterile Neutrino Mixing

Searches for evidence of active-sterile neutrino mixing at LBNE can be conducted by examining the NC event rate at the Far Detector and comparing it to a precision estimate of the expected rate extrapolated from ν_μ flux measurements from the Near Detector Complex and beam and detector simulations. Observed deficits in the NC rate could be evidence for active-sterile neutrino mixing. The latest such search in a long-baseline experiment was conducted by the MINOS experiment [?]. The expected rate of NC interactions in a 10kton detector with visible energy > 0.5 GeV in LBNE is approximately 2,000 events over five years (see Table 4-1) in the LE beam tune and 3,000 events over five years in the ME beam tune. The NC identification efficiency is high, with a low rate of ν_μ CC background misidentification as shown in Table 4-2. LBNE will provide a unique opportunity to revisit this search with higher precision over a large range of neutrino energies and a longer baseline. The high resolution LArTPC will enable a coarse measurement of the incoming neutrino energy in a NC interaction by using the event topology and correcting for the missing energy

1 of the invisible neutrino. This will greatly improve the sensitivity of LBNE to active-sterile
2 mixing as compared to current long baseline experiments such as MINOS+ since both the
3 energy spectrum as well as the rate of NC interactions can be measured at both near and
4 far detectors. Studies are currently underway to determine the LBNE sensitivity.

5 **4.6.4 Sensitivity to Large Extra Dimensions**

6 Several theoretical models propose that right-handed neutrinos propagate in large com-
7 pactified extra dimensions, while the standard left-handed neutrinos are confined to the
8 4-dimensional brane [?]. Mixing between the Kaluza-Klein modes and the standard neu-
9 trinos would change the mixing patterns beyond that predicted by the 3 flavor model. The
10 effects could manifest as distortions in the disappearance spectrum of ν_μ for example. The
11 rich oscillation structure visible in LBNE, measured with a high resolution detector such as
12 the LArTPC using both beam and atmospheric oscillations provides further opportunities
13 to probe for new physics such as compactified extra dimensions. Studies are underway to
14 understand the limits that LBNE can impose in the future compared to current and expected
15 limits from other experiments.

5 Physics Opportunities with a High Resolution Near Detector

The unprecedented large neutrino fluxes available for the LBNE program will allow the collection of $\mathcal{O}(10^8)$ inclusive neutrino charged current (CC) interactions for 10^{22} POT at a near detector location. Table 5-1 lists the expected number of muon neutrino interactions at the LBNE 670-m near detector site per ton of Argon detector.

Production mode	Number of events
CC QE ($\nu_\mu n \rightarrow \mu^- p$)	23,152
NC elastic ($\nu_\mu N \rightarrow \nu_\mu N$)	7,165
CC resonant π^+ ($\nu_\mu N \rightarrow \mu^- N \pi^+$)	24,014
CC resonant π^0 ($\nu_\mu n \rightarrow \mu^- p \pi^0$)	7,696
NC resonant π^0 ($\nu_\mu N \rightarrow \nu_\mu N \pi^0$)	6,198
NC resonant π^+ ($\nu_\mu p \rightarrow \nu_\mu n \pi^+$)	2,182
NC resonant π^- ($\nu_\mu n \rightarrow \nu_\mu p \pi^-$)	2,930
CC DIS ($\nu_\mu N \rightarrow \mu^- X, W > 2$)	31,788
NC DIS ($\nu_\mu N \rightarrow \nu_\mu X, W > 2$)	10,285
CC coherent π^+ ($\nu_\mu A \rightarrow \mu^- A \pi^+$)	1,505
NC coherent π^0 ($\nu_\mu A \rightarrow \nu_\mu A \pi^0$)	790
NC resonant radiative decay ($N^* \rightarrow N \gamma$)	6
Inverse Muon Decay ($\nu_\mu e \rightarrow \mu^- \nu_e$)	11
$\nu_\mu e^- \rightarrow \nu_\mu e^-$	17,193
Other	
Total CC	100,645
Total NC+CC	134,189

Table 5-1: Estimated ν_μ production rates for argon targets per ton for 1×10^{20} POT at 670 m assuming neutrino cross sections predictions from NUANCE [?] and a 120 GeV proton beam. Processes are defined at the initial neutrino interaction vertex and thus do not include final state effects. These estimates do not include detector efficiencies or acceptance [?,?].

The reduction of systematic uncertainties for the neutrino oscillation program of the full LBNE scope requires a highly segmented near detector, thus providing excellent resolution

in the reconstruction of neutrino events. The combination of this substantial flux with a finely segmented near detector offers a unique opportunity to produce a range of neutrino scattering physics measurements in addition to those needed by the long base line oscillation program. The combined statistics and precision expected in the ND will allow precise tests of fundamental interactions and better understanding of the structure of matter.

Since the potential of the neutrino probe is largely unexplored, the substantial step forward offered by the LBNE program also provides the opportunity for unexpected discoveries. Given the broad energy range of the beam, a diverse range of physics measurements is possible in the LBNE ND, complementing the physics programs using proton, electron or ion beams from colliders to the Jefferson Laboratory. This complementarity not only would boost the physics output of LBNE, but it can also attract new collaborators into the LBNE project from different physics communities.

In the following sections we list the main physics topics. To provide a flavor for the outstanding physics potential, we give a short description of the studies which can be performed at LBNE for few selected topics. A more detailed and complete discussion of the near detector physics potential can be found in [?].

5.1 Precision Physics with Long Baseline Oscillations

In order to achieve the goals of the full LBNE scientific program - in particular sensitivity to CP violation and the precision measurement of the 3-flavor oscillation parameters, it is necessary to characterize the expected unoscillated neutrino flux and physics backgrounds to the oscillation signals at the far detector with high precision. In Figure 5-1 the mass hierarchy and CP violation sensitivities as a function of exposure are evaluated using different sets of assumptions on the the signal/background uncertainties: 1% (signal)/ 5% (background) is the goal of the LBNE scientific program, 2% (signal)/ 5% (background) and 5% (signal)/ 10%(background). The latter is a conservative estimate on the uncertainties that can be achieved in LBNE project without unoscillated neutrino beam measurements at the near site, using the detailed muon flux measurements, target hadron production and, the data tuned simulation of the NuMI beamline which shares the same targetry and focusing as LBNE.

The impact of the systematic uncertainties on the signal and background on the mass hierarchy sensitivity is negligible even at high exposures given the large $\nu/\bar{\nu}$ asymmetry at 1300km. For CP violation, the impact is significant at exposures ≥ 100 kton years as large systematic uncertainties start to dominate the statistical uncertainties.

Table 5-2 summarizes the exposures required to reach $3, 5\sigma$ sensitivity to CP violation for at least 50% of all possible values of δ_{cp} . The resolution on δ_{cp} is also shown.

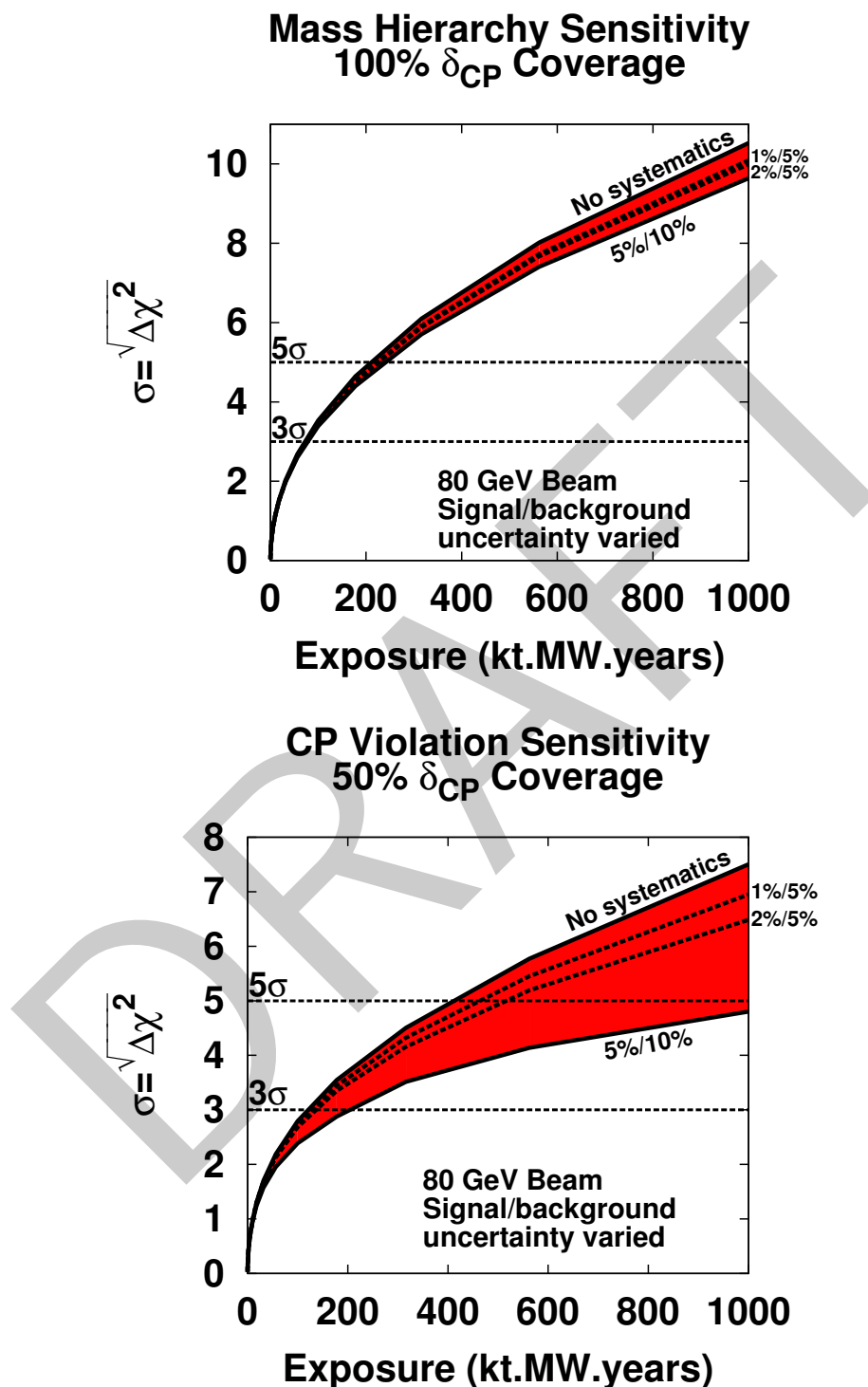


Figure 5–1: The mass hierarchy (top) and CP violation (bottom) sensitivities as a function of exposure in kton-years. The band represents the range of signal and background normalization errors.

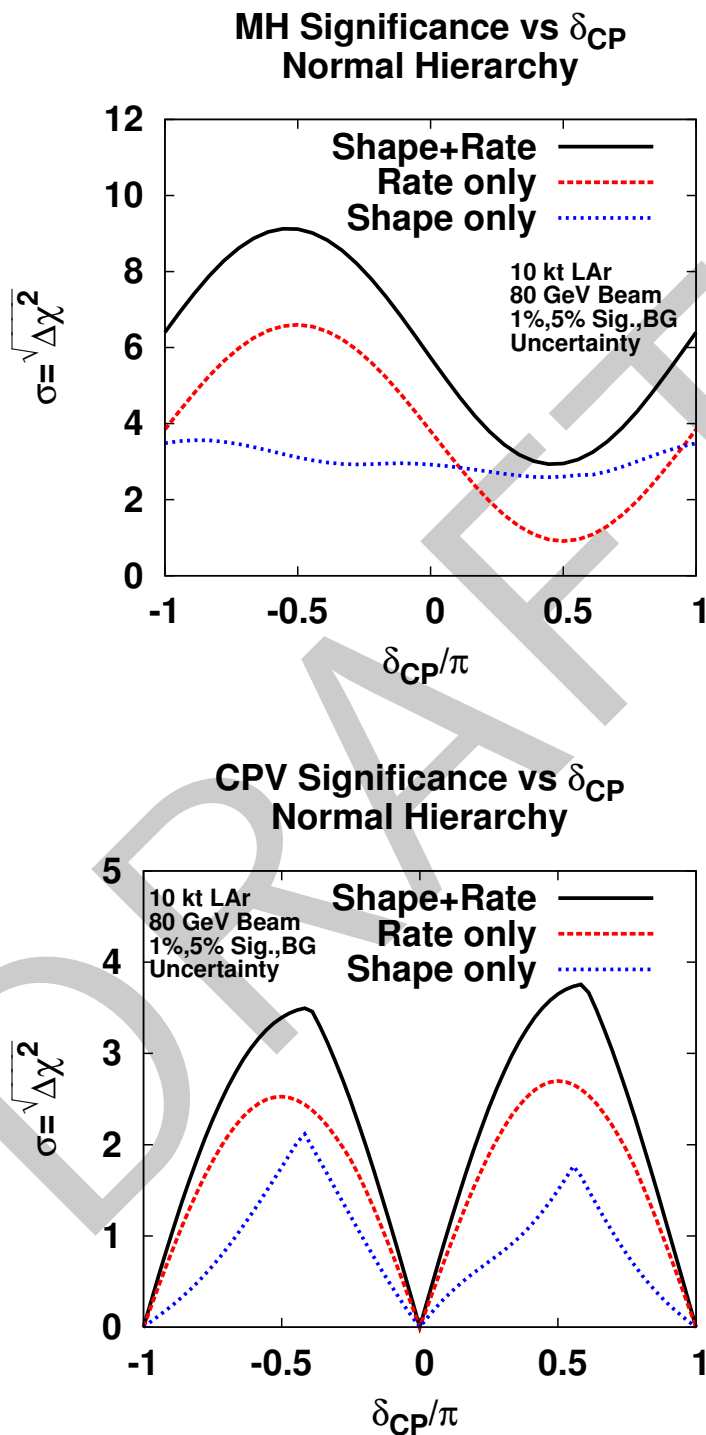


Figure 5–2: The mass hierarchy (top) and CP violation (bottom) sensitivities from shape, rate, and shape+rate. The sensitivity is for a 10 kton detector, 700kW beam, 5+5 $\nu + \bar{\nu}$ years.

Systematic uncertainty	Sensitivity	Required Exposure	$\sigma(\delta_{cp})$
0 (statistical only)	3 σ , 50% δ_{cp}	100 kt.MW.yr	
0 (statistical only)	5 σ , 50% δ_{cp}	400 kt.MW.yr	
1%/5% (Sig/bkgd)	3 σ , 50% δ_{cp}	100 kt.MW.yr	
1%/5% (Sig/bkgd)	5 σ , 50% δ_{cp}	450 kt.MW.yr	8°, 13°
2%/5% (Sig/bkgd)	3 σ , 50% δ_{cp}	120 kt.MW.yr	
2%/5% (Sig/bkgd)	5 σ , 50% δ_{cp}	500 kt.MW.yr	
5%/10% (no near ν det.)	3 σ , 50% δ_{cp}	200 kt.MW.yr	

Table 5–2: The exposures required to reach 3 and 5 σ sensitivity to CP violation for at least 50% of all possible values of δ_{cp} as a function of systematic uncertainties. The resolution on δ_{cp} is also shown.

The uncertainties listed in Table 5–2 and shown in the sensitivity figures are on the ν_e appearance signal and background normalization. In Figure 5–2 the sensitivity obtained from the rate only, shape only and rate+shape of the appearance spectrum is shown. In a broad-band long-baseline experiment such as LBNE, the shape information is as important if not more important than the rate information.

From the studies of uncertainties and the impact of the spectral shape presented earlier, it is evident that to fully realize the physics potential of possible enhancements to the current LBNE program, a near neutrino detector that can both measure the unoscillated neutrino flux shape and normalization with high precision is highly desirable. In addition to the precise determination of the neutrino flux, shape and flavor composition, the characterization of different neutrino interactions and interaction cross-sections on a LAr target is necessary to estimate the physics backgrounds to the oscillation measurements.

A high resolution near tracking detector such as that described in Chapter 5 can measure the unoscillated flux normalization, shape and flavor to a few % using the following systematically independent techniques:

Relative Neutrino and Antineutrino Flux Measurement The most promising method of determining the shape of the ν_μ and $\bar{\nu}_\mu$ flux is by measuring the low-hadronic (low- ν) charged current events: the Low- ν_0 method of relative flux determination [?]. The dynamics of neutrino-nucleon scattering implies that the number of events in a given energy bin with hadronic energy $E_{had} < \nu_0$ is proportional to the neutrino (antineutrino) flux in that energy bin up to corrections $\mathcal{O}(\nu_0/E_\nu)$ and $\mathcal{O}(\nu_0/E_\nu)^2$. The method follows from the general expression of the ν -nucleon differential cross section:

$$\mathcal{N}(\nu < \nu_0) = C\Phi(E_\nu)\nu_0 \left[\mathcal{A} + \left(\frac{\nu_0}{E_\nu}\right) \mathcal{B} + \left(\frac{\nu_0}{E_\nu}\right)^2 \mathcal{C} + \mathcal{O}\left(\frac{\nu_0}{E_\nu}\right)^3 \right], \quad (5.1)$$

where the coefficients $\mathcal{A} = \mathcal{F}_2$, $\mathcal{B} = (\mathcal{F}_2 \pm \mathcal{F}_3)/2$, $\mathcal{C} = (\mathcal{F}_2 \mp \mathcal{F}_3)/6$ and $\mathcal{F}_i = \int_0^1 \int_0^{\nu_0} F_i(x) dx d\nu$ is the integral of structure function $F_i(x)$. The number $\mathcal{N}(\nu < \nu_0)$

is proportional to the flux up to correction factors of the order $\mathcal{O}(\nu_0/E_\nu)$ or smaller, which are not significant for small values of ν_0 at energies $\geq \nu_0$. It should be pointed out that the coefficients $\mathcal{A}, \mathcal{B}, \mathcal{C}$ are determined for each energy bin and neutrino flavor within the ND data themselves. Since our primary interest is the relative flux determination, i.e., neutrino flux in an energy bin relative to another energy bin, variations in the coefficients do not affect the relative flux. The prescription for the relative flux determination is simple: we count the number of ν -CC events below a certain small value of hadronic energy (ν_0). The observed number of events, up to the correction of the order $\mathcal{O}(\nu_0/E_\nu)$ due to the finite ν_0 , in each total visible energy bin is proportional to the relative flux. The smaller the factor ν_0/E_ν , the smaller is the correction. Furthermore, the energy of events passing the low- ν_0 cut is dominated by the corresponding lepton energy. It is apparent from the above discussion that this method of relative flux determination is not very sensitive to nucleon structure, QCD corrections or types of ν -interactions such as scaling or non-scaling. With the excellent granularity and resolution foreseen in the low-density magnetized tracker it will be possible to use a value of $\nu_0 \sim 0.5$ GeV or lower, thus allowing flux predictions down to $E_\nu \sim 0.5$ GeV. In a preliminary analysis with the high resolution tracker we achieved a precision $\leq 2\%$ on the relative ν_μ flux with the low- ν_0 method in the energy region $1 \leq E_\nu \leq 30$ GeV in the fit with $\nu_0 < 0.5$ GeV. Similar uncertainties are expected for the $\bar{\nu}_\mu$ component (the dominant one) in the antineutrino beam mode (negative focusing).

Flavor Content of the Beam: $\nu_\mu, \bar{\nu}_\mu, \nu_e, \bar{\nu}_e$ The empirical parametrization (EP) of the pions and kaons, determined from the low- ν_0 flux at ND, allows one to predict the ν_μ and $\bar{\nu}_\mu$ flux at the FD location. The EP provides a measure of the $\pi^+/K^+/\mu^+$ ($\pi^-/K^-/\mu^-$) content of the beam at the ND. Additionally, with an ND capable of identifying $\bar{\nu}_e$ CC interactions, one can directly extract the elusive K_L^0 content of the beam. Therefore, an accurate measurement of $\nu_\mu, \bar{\nu}_\mu$ and $\bar{\nu}_e$ CC interactions provides an absolute prediction of the ν_e content of the beam, which is an irreducible background for the ν_e appearance search in the FD:

$$\nu_e \equiv \mu^+(\pi^+ \rightarrow \nu_\mu) \oplus K^+(K^+ \rightarrow \nu_\mu) \oplus K_L^0 \quad (5.2)$$

$$\bar{\nu}_e \equiv \mu^-(\pi^- \rightarrow \bar{\nu}_\mu) \oplus K^-(K^- \rightarrow \bar{\nu}_\mu) \oplus K_L^0 \quad (5.3)$$

The μ component is well constrained from $\nu_\mu(\bar{\nu}_\mu)$ CC data at low energy, while the K^\pm component is only partially constrained by the $\nu_\mu(\bar{\nu}_\mu)$ CC data at high energy and requires external hadro-production measurements of K^\pm/π^\pm ratios at low energy from MIPP. Finally, the K_L^0 component can be constrained by the $\bar{\nu}_e$ CC data and by external dedicated measurements at MIPP. The approximate relative contributions to the ν_e spectrum are 85% (55%) from μ^+ , 10% (30%) from K^+ and 3% (15%) from K_L^0 in the energy range $1(5) \leq E_\nu \leq 5(15)$ GeV. Based on the NOMAD experience, we expect to achieve a precision of $\leq 0.1\%$ on the flux ratio ν_e/ν_μ . Taking into account the projected precision of the ν_μ flux discussed in the previous section, this translates into an absolute prediction for the ν_e flux at

the level of 2%. Finally, the fine-grained ND can directly identify ν_e CC interactions from the LBNE beam. The relevance of this measurement is twofold: a) it provides an independent validation for the flux predictions obtained from the low- ν_0 method and b) it can further constrain the uncertainty on the knowledge of the absolute ν_e flux.

Constraining the Unoscillated ν Spectral Shape with the Quasi-Elastic Interaction

In any long-baseline neutrino oscillation program, including LBNE, the quasi-elastic (QE) interactions are special. First, the QE cross section is substantial because the energy is low. Second, a measurement of ν_μ -QE provides, to first order, a direct measurement of flux. Third, because of the simple topology — a μ^- and a proton — the interaction provides, to the first order, a close approximation to the neutrino energy (E_ν). In the context of a fine-grained tracker, precise measurement of QE will impose direct constraints on neutrino interaction associated with Fermi-motion and final state interaction (FSI) dynamics: processes that must be determined empirically since they affect the entire oscillation program. The key to ν_μ -QE is the two-track topology, μ^- and p . A high resolution ND can efficiently identify the proton and measure its momentum vector as well as the ability to measure the dE/dx of the recoil proton. Preliminary studies indicate that in a fine grained tracking detector the efficiency (purity) is 52% (82%). The high purity selection will enable the LBNE ND to empirically constrain nuclear motion and the FSI parameters.

Low-Energy Absolute Flux: Neutrino-Electron Neutral Current Scattering

Neutrino neutral current interaction with the atomic electron in the target, $\nu_\mu e^- \rightarrow \nu_\mu e^-$ (NuElas), provides an elegant measure of the absolute flux. The total cross section for NC elastic scattering off electrons is given by [?]:

$$\sigma(\nu_l e \rightarrow \nu_l e) = \frac{G_\mu^2 m_e E_\nu}{2\pi} \left[1 - 4 \sin^2 \theta_W + \frac{16}{3} \sin^4 \theta_W \right], \quad (5.4)$$

$$\sigma(\bar{\nu}_l e \rightarrow \bar{\nu}_l e) = \frac{G_\mu^2 m_e E_\nu}{2\pi} \left[\frac{1}{3} - \frac{4}{3} \sin^2 \theta_W + \frac{16}{3} \sin^4 \theta_W \right], \quad (5.5)$$

where θ_W is the weak mixing angle (WMA). For $\sin^2 \theta_W \simeq 0.23$ the above cross sections are very small $\sim 10^{-42} (E_\nu/\text{GeV}) \text{ cm}^2$. The NC elastic scattering off electrons can be used to determine the absolute flux normalization since the cross section only depends upon the knowledge of $\sin^2 \theta_W$. Within the SM the value of $\sin^2 \theta_W$ at the average momentum transfer expected at LBNE, $Q \sim 0.07 \text{ GeV}$, can be extrapolated down from the LEP/SLC measurements with a precision of $\leq 1\%$. The $\nu_\mu e^- \rightarrow \nu_\mu e^-$ will produce a single e^- collinear with the ν -beam ($\leq 40 \text{ mrad}$). The background, dominated by the asymmetric conversion of a photon in an ordinary ν -N neutral current event, will produce e^- and e^+ in equal measure with much broader angular distribution. A preliminary analysis of the expected elastic scattering signal in the high resolution tracking near detector shows that the scattering signal can be selected with an efficiency of about 60% with a small background contaminant. The measurement will be dominated by the statistical error. We estimate that the absolute flux of the LBNE neutrinos will

be determined to a $\simeq 2.5\%$ precision for $E_\nu \leq 10$ GeV. The measurement of NC elastic scattering off electrons can only provide the integral of all neutrino flavors.

High-Energy Absolute Flux: Neutrino-Electron Charged Current Scattering The ν_μ - e^- CC interaction, $\nu_\mu + e^- \rightarrow \mu^- + \nu_e$ — the inverse muon decay (IMD) — offers an elegant way to determine the absolute flux. Given the threshold due to the massive-muon, IMD requires a minimum $E_\nu \geq 10.8$ GeV. A high resolution near detector such as that described in Chapter 5 observes ≥ 2000 IMD events in 3 years. The reconstruction efficiency of the single, energetic and forward μ^- will be $\geq 98\%$; the angular resolution of the IMD- μ is ≤ 1 mrad. The background, primarily from the ν_μ -QE, can be precisely constrained using control samples. In particular, the systematic limitations of the CCFR [?] and [?] and those of the CHARM-II [?] IMD measurements can be substantially alleviated with the proposed near detector design. A preliminary analysis indicates that the absolute flux can be determined with an accuracy of $\approx 3\%$ for $E_\nu \geq 11$ GeV (average- $E_\nu \approx 25$ GeV);

Low-Energy Absolute Flux: QE in Water and Heavy-Water Targets . A third independent method to extract the absolute flux is through the Quasi-Elastic (QE) CC scattering $\nu_\mu n(p) \rightarrow \mu^- p(n)$. Neglecting terms in $(m_\mu/M_n)^2$, at $Q^2 = 0$ the QE cross section is independent of neutrino energy for $(2E_\nu M_n)^{1/2} > m_\mu$:

$$\frac{d\sigma}{dQ^2} \big|_{Q^2=0} = \frac{G_\mu^2 \cos^2 \theta_c}{2\pi} [F_1^2(0) + G_A^2(0)] = 2.08 \times 10^{-38} \text{ cm}^2 \text{GeV}^{-2}, \quad (5.6)$$

which is determined by neutron β decay and has a theoretical uncertainty $< 1\%$. The flux can be extracted experimentally by measuring low Q^2 QE interactions ($0 - 0.05$ GeV) and extrapolating the result to the limit of $Q^2 = 0$. The measurement requires a deuterium or hydrogen (for antineutrino) target to minimize the smearing due to Fermi motion and other nuclear effects. This requirement can only be achieved by using both H_2O and D_2O targets embedded in the fine-grained tracker and extracting the events produced in deuterium by statistical subtraction of the larger oxygen component. The experimental resolution on the muon and proton momentum and angle is crucial. Dominant uncertainties of the method are related to the extrapolation to $Q^2 = 0$, to the theoretical cross section on deuterium, the experimental resolution, and to the statistical subtraction. Sensitivity studies and the experimental requirements are under study.

Measurement of Neutral Pions, Photons, and π^\pm in Neutral and Charged Current Events

The principal background to the ν_e and $\bar{\nu}_e$ appearance comes from the NC-events where a photon from the π^0 decay produces a signature identical to that produced by ν_e -induced electron; the second source of background is due to π^0 s from ν_μ -CC where the μ^- evades identification — typically at high- y_{BJ} . Since the energy spectra of NC and CC are different, it is critical for ND to measure π^0 s in NC and CC in the full kinematic phase space.

The proposed ND is designed to measure π^0 s with high accuracy in three topologies: (a) both photons convert in the tracker ($\simeq 25\%$), (b) one photon converts in the tracker and the other in the calorimeter ($\simeq 50\%$), and (c) both photons convert in the calorimeter. The first two topologies afford the best resolution because the tracker provides precise γ -direction measurement.

The π^0 reconstruction in the proposed fine grained tracker is expected to be $\geq 75\%$ if photons that reach the ECAL are included. By contrasting the π^0 mass in the tracker versus in the calorimeter, the relative efficiencies of photon reconstruction will be well constrained.

Finally, the π^\pm will be measured by the tracker including the dE/dx information. An *in situ* determination of the charged pions in the $\nu_\mu/\bar{\nu}_\mu$ -CC — with μ ID and without μ ID — and the ν -NC is crucial to constrain the systematic error associated with the $\nu_\mu(\bar{\nu}_\mu)$ -disappearance, especially at low E_ν .

Table 5–3: Precisions achievable from in situ ν_μ and ν_e flux measurements in the fine-grained high resolution ND with different techniques.

Flavor	Technique	Relative abundance	Absolute normalization	Relative flux $\Phi(E_\nu)$	Detector requirements
ν_μ	$\nu_\mu e^- \rightarrow \nu_\mu e^-$	1.00	2.5%	$\sim 5\%$	e^- ID θ_e Resolution e^-/e^+ Separation
ν_μ	$\nu_\mu e^- \rightarrow \mu^- \nu_e$	1.00	3%		μ^- ID θ_μ Resolution 2-Track ($\mu+X$) Resolution μ energy scale
ν_μ	$\nu_\mu n \rightarrow \mu^- p$ $Q^2 \rightarrow 0$	1.00	3 – 5%	5 – 10%	D target p Angular & Energy resolution Back-Subtraction
$\bar{\nu}_\mu$	$\bar{\nu}_\mu p \rightarrow \mu^+ n$ $Q^2 \rightarrow 0$	0.70	5%	10%	H target Back-Subtraction
ν_μ	Low- ν_0	1.00		2.0%	μ^- vs μ^+ E_μ -Scale Low- E_{Had} Resolution
$\bar{\nu}_\mu$	Low- ν_0	0.70		2.0%	μ^- vs μ^+ E_μ -Scale Low- E_{Had} Resolution
$\nu_e/\bar{\nu}_e$	Low- ν_0	0.01	1-3%	2.0%	e^-/e^+ Separation (K_L^0)

5.2 Electroweak Precision Measurement: Weak Mixing Angle

Neutrinos are a natural probe for the investigation of electroweak physics. Interest in a precise determination of the weak mixing angle ($\sin^2 \theta_W$) at LBNE energies via neutrino scattering

is twofold: (a) it provides a direct measurement of neutrino couplings to the Z boson and (b) it probes a different scale of momentum transfer than LEP by virtue of not being on the Z pole. The weak mixing angle can be extracted experimentally from three main NC physics processes:

1. Deep Inelastic Scattering off quarks inside nucleons: $\nu N \rightarrow \nu X$;
2. Elastic Scattering off electrons: $\nu e^- \rightarrow \nu e^-$;
3. Elastic Scattering off protons: $\nu p \rightarrow \nu p$.

Figure 5-3 shows the corresponding Feynman diagrams for the three processes.

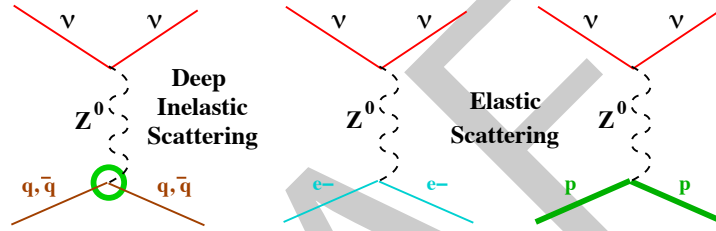


Figure 5-3: Feynman diagrams for the three main Neutral Current processes which can be used to extract $\sin^2 \theta_W$ with the LBNE Near Detector complex.

The most precise measurement of $\sin^2 \theta_W$ in neutrino deep inelastic scattering (DIS) comes from the NuTeV experiment which reported a value that is 3σ from the standard model [?]. The LBNE ND can perform a similar analysis in the DIS channel by measuring the ratio of NC and CC interactions induced by neutrinos:

$$\mathcal{R}^\nu \equiv \frac{\sigma_{\text{NC}}^\nu}{\sigma_{\text{CC}}^\nu} \simeq \rho^2 \left(\frac{1}{2} - \sin^2 \theta_W + \frac{5}{9} (1 + r) \sin^4 \theta_W \right). \quad (5.7)$$

Here ρ is the relative coupling strength of the neutral-to-charged current interactions ($\rho = 1$ at tree-level in the Standard Model) and r is the ratio of antineutrino to neutrino cross section ($r \sim 0.5$). The absolute sensitivity of \mathcal{R}^ν to $\sin^2 \theta_W$ is 0.7, which implies that a measurement of \mathcal{R}^ν of 1% precision would provide $\sin^2 \theta_W$ with a precision of 1.4%. Contrary to the NuTeV experiment, the antineutrino interactions cannot be used for this analysis at LBNE due to the large number of ν_μ DIS interactions in the $\bar{\nu}_\mu$ beam compared to the $\bar{\nu}_\mu$ DIS interactions.

The measurement of $\sin^2 \theta_W$ from DIS interactions can be only performed with the low-density magnetized tracker since an accurate reconstruction of the NC event kinematics and of the ν CC interactions are crucial to keep the systematic uncertainties on the event selection under control. The analysis selects events in the ND after imposing a cut on the visible hadronic energy of $E_{\text{had}} > 3 \text{ GeV}$, as in the NOMAD $\sin^2 \theta_W$ analysis (the CHARM

analysis had $E_{\text{had}} > 4$ GeV). With the reference 700 kW primary beam we expect about 3.3×10^6 CC events and 1.1×10^6 NC events, giving a statistical precision of 0.11% on \mathcal{R}^ν and 0.15% on $\sin^2 \theta_W$ (Table 5-4).

The use of a low-density magnetized tracker can substantially reduce systematic uncertainties compared to a massive calorimeter. Table 5-4 shows a comparison of the different uncertainties on the measured \mathcal{R}^ν between NuTeV and LBNE. The largest experimental systematic uncertainty in NuTeV is related to the subtraction of the ν_e CC contamination from the NC sample. Since the low-density tracker at LBNE can efficiently reconstruct the electron tracks, the ν_e CC interactions can be identified on an event-by-event basis, reducing the corresponding uncertainty to a negligible level. Similarly, uncertainties related to the location of the interaction vertex, noise, counter efficiency and so on are removed by the higher resolution and by changing the analysis selection. The experimental selection at LBNE will be dominated by two uncertainties: the knowledge of the $\bar{\nu}_\mu$ flux and the kinematic selection of NC interactions. The former is relevant due to the larger NC/CC ratio for antineutrinos. The total experimental systematic uncertainty on $\sin^2 \theta_W$ is expected to be about 0.14%.

The measurement of \mathcal{R}^ν will be dominated by model systematic uncertainties on the structure functions of the target nucleons. The estimate of these uncertainties for LBNE is based upon the extensive work performed for the NOMAD analysis and includes a NNLO QCD calculation of structure functions (NLO for charm production) [?, ?, ?], parton distribution functions (PDFs) extracted from dedicated low- Q global fits, high twist contributions [?], electroweak corrections [?] and nuclear corrections [?, ?, ?]. The charm quark production in CC, which has been the dominant source of uncertainty in all past determinations of $\sin^2 \theta_W$ from ν N DIS, is reduced to about 2.5% of the total ν_μ CC DIS with $E_{\text{had}} > 3$ GeV with the low-energy beam spectrum at LBNE. This number translates into a systematic uncertainty of 0.13% on \mathcal{R}^ν (Table 5-4), assuming a knowledge of the charm production cross section to 5%. It is worth noting that the recent measurement of charm dimuon production by the NOMAD experiment allowed a reduction of the uncertainty on the strange sea distribution to $\sim 3\%$ and on the charm quark mass m_c to ~ 60 MeV [?]. The lower neutrino energies available at LBNE reduce the accessible Q^2 values with respect to NuTeV, increasing in turn the effect of non-perturbative contributions (High Twists) and R_L . The corresponding uncertainties are reduced by the recent studies of low- Q structure functions and by improved modeling with respect to the NuTeV analysis (NNLO vs. LO). The total model systematic uncertainty on $\sin^2 \theta_W$ is expected to be about 0.29% with the reference beam configuration. The corresponding total uncertainty on the value of $\sin^2 \theta_W$ extracted from ν N DIS is 0.36% with the 700 kW beam.

Most of the model uncertainties will be constrained by in situ dedicated measurements using the large CC samples and employing improvements in theory that will have evolved over the course of the experiment. In the low-density tracker we shall collect about 80,000 neutrino-induced inclusive charm events with the 700 kW beam. The precise reconstruction of charged tracks will allow measurement of exclusive decay modes of charmed hadrons (e.g. D^{*+}) and measurement of charm fragmentation and production parameters. The average

Table 5-4: Comparison of uncertainties on the \mathcal{R}^ν measurement between NuTeV and LBNE with the reference beam. The corresponding relative uncertainties on $\sin^2 \theta_W$ must be multiplied by a factor of 1.4, giving for LBNE a projected overall precision of 0.36%.

Source of uncertainty	$\delta R^\nu / R^\nu$	
	NuTeV	LBNE
Data statistics	0.00176	0.00110
Monte Carlo statistics	0.00015	
Total Statistics	0.00176	0.00110
$\nu_e, \bar{\nu}_e$ flux ($\sim 1.7\%$)	0.00064	0.00010
Energy measurement	0.00038	0.00040
Shower length model	0.00054	n.a.
Counter efficiency, noise	0.00036	n.a.
Interaction vertex	0.00056	n.a.
$\bar{\nu}_\mu$ flux	n.a.	0.00070
Kinematic selection	n.a.	0.00060
Experimental systematics	0.00112	0.00102
d,s \rightarrow c, s-sea	0.00227	0.00130
Charm sea	0.00013	n.a.
$r = \sigma^{\bar{\nu}} / \sigma^\nu$	0.00018	n.a.
Radiative corrections	0.00013	0.00013
Non-isoscalar target	0.00010	N.A.
Higher twists	0.00031	0.00070
$R_L (F_2, F_T, xF_3)$	0.00115	0.00140
Nuclear correction		0.00020
Model systematics	0.00258	0.00206
TOTAL	0.00332	0.00255

1 semileptonic branching ratio $B_\mu \sim 5\%$ with the low-energy LBNE beam. The most precise
2 sample of 15,400 dimuon events is collected by the NOMAD experiment [?]. Finally, precision
3 measurements of CC structure functions in the fine-grained tracker would further reduce the
4 uncertainties on PDFs and on High Twist contributions.

5 The precision that can be achieved from νN DIS interactions is limited by both the event
6 rates and by the energy spectrum of the reference 700 kW beam configuration. The high-
7 statistics beam exposure combined with a dedicated run with the high-energy beam option
8 would increase the statistics by more than a factor of 20. This major step forward would
9 not only reduce the statistical uncertainty to a negligible level, but would provide large
10 control samples and precision auxiliary measurements to reduce the systematic uncertainties
11 on structure functions. The two dominant systematic uncertainties, charm production in
12 CC interactions and low Q^2 structure functions, are essentially defined by the available
13 data at present. Overall, the use of a high-energy beam with an upgraded intensity can

potentially improve the precision achievable on $\sin^2 \theta_W$ from νN DIS to about 0.2%. It is worth mentioning that the high-energy beam is also required for the determination of the fluxes in case high Δm^2 oscillations are present.

A second independent measurement of $\sin^2 \theta_W$ can be obtained from NC $\nu_\mu e$ elastic scattering. This channel has lower systematic uncertainties since it does not depend upon the knowledge of the structure of nuclei, but has limited statistics due to its very low cross section. The value of $\sin^2 \theta_W$ can be extracted from the ratio of neutrino to antineutrino interactions [?]:

$$\mathcal{R}_{\nu e}(Q^2) \equiv \frac{\sigma(\bar{\nu}_\mu e \rightarrow \bar{\nu}_\mu e)}{\sigma(\nu_\mu e \rightarrow \nu_\mu e)}(Q^2) \simeq \frac{1 - 4 \sin^2 \theta_W + 16 \sin^4 \theta_W}{3 - 12 \sin^2 \theta_W + 16 \sin^4 \theta_W}, \quad (5.8)$$

in which systematic uncertainties related to the selection and electron identification cancel out. The absolute sensitivity of this ratio to $\sin^2 \theta_W$ is 1.79, which implies a measurement of $\mathcal{R}_{\nu e}$ of 1% precision would provide $\sin^2 \theta_W$ with a precision of 0.65%.

The event selection was described earlier since the NC elastic scattering off electrons is also used for the absolute flux normalization. The WMA analysis can be performed only with the low-density magnetized tracker in conjunction with a large LAr detector. In the former case the total statistics available is limited to about a few thousand $\nu(\bar{\nu})$ events. These numbers do not allow a competitive determination of $\sin^2 \theta_W$ by using the magnetized tracker alone. However, if we consider a 100 ton LAr detector in the ND complex, we expect to collect about 20,000 (12,000) $\nu(\bar{\nu})$ events; and a factor of four more with a high-intensity beam.

A combined analysis of both detectors can achieve the optimal sensitivity: the fine-grained tracker is used to reduce systematic uncertainties (measurement of backgrounds and calibration), while the LAr ND provides the statistics required for a competitive measurement. Overall, the use of the massive LAr detector can provide a statistical accuracy on $\sin^2 \theta_W$ of about 0.3%. However, the extraction of the weak mixing angle is dominated by the systematic uncertainty on the $\bar{\nu}_\mu/\nu_\mu$ flux ratio in Equation (5.8). We evaluated this uncertainty with the low- ν_0 method for the flux extraction and we obtained a systematic uncertainty of about 1% on the ratio of the $\bar{\nu}_\mu/\nu_\mu$ flux integrals. Therefore, the overall precision on $\sin^2 \theta_W$ achievable from NC elastic scattering off electrons is limited to about 0.9%.

Together, the DIS and the NC elastic scattering channels involve substantially different scales of momentum transfer, providing a tool to test the running of $\sin^2 \theta_W$ in a single experiment. To this end, the study of NC elastic scattering off protons can provide additional information since it occurs at a momentum scale which is intermediate between the two other processes. Figure 5-4 summarizes the target sensitivity from the LBNE ND, compared with existing measurements as a function of the momentum scale.

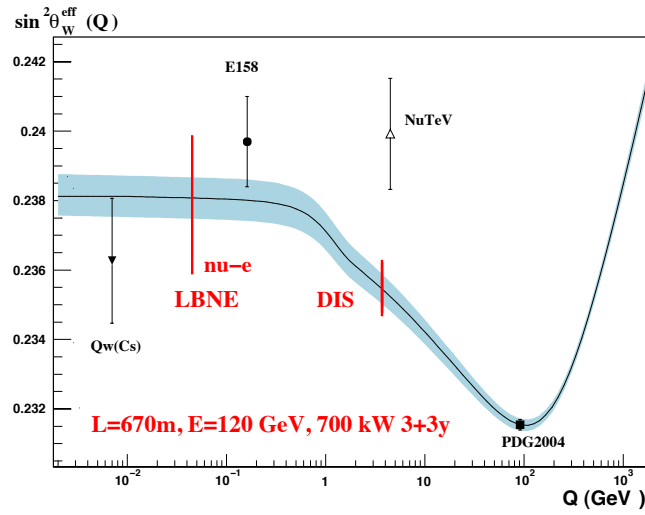


Figure 5-4: Expected sensitivity to the measurement of $\sin^2 \theta_W$ from the LBNE ND with the reference 700 kW beam. The curve shows the Standard Model prediction as a function of the momentum scale [?]. Previous measurements from Atomic Parity Violation [?,?], Moeller scattering (E158 [?]), ν DIS (NuTeV [?]) and the combined Z pole measurements (LEP/SLC) [?] are also shown for comparisons. The use of a high-energy beam can reduce the LBNE uncertainties by almost a factor of two.

5.3 Strangeness Content of the Nucleon

The strange quark content of the proton and its contribution to the proton-spin remain enigmatic. The question is whether the strange quarks contribute substantially to the vector and axial-vector currents of the nucleon. A large observed value of the strange quark contribution to the nucleon spin (axial current), Δs , would change our understanding of the proton structure. The spin structure of the nucleon also affects the couplings of axions and supersymmetric particles to dark matter. The salient topics in this section include:

- Neutral Current Elastic Scattering and Measurement of Δs
- Strange Form Factors
- Charm Production and (anti)strange Parton Distribution Function
- Strange Particle Production in NC and CC

The strange **vector** elastic form factors of the nucleon have been measured to high precision in parity-violating electron scattering (PVES) at Jefferson Lab, Mainz and elsewhere. A recent global analysis [?] of PVES data finds a strange magnetic moment $\mu_s = 0.37 \pm 0.79$ (in

units of the nucleon magneton), so that the strange quark contribution to proton magnetic moment is less than 10%. For the strange electric charge radius parameter ρ_s , defined in terms of the Sachs electric form factor at low Q^2 as $G_E^s = \rho_s Q^2 + \rho_s' Q^4 + \mathcal{O}(Q^6)$, one finds a very small value, $\rho_s = -0.03 \pm 0.63 \text{ GeV}^{-2}$, consistent with zero.

Both results are consistent with theoretical expectations based on lattice QCD and phenomenology. [?]. In contrast, the strange *axial vector* form factors are poorly determined. A global study of PVES data [?] finds $\tilde{G}_A^N(Q^2) = \tilde{g}_A^N (1 + Q^2/M_A^2)^2$, with the effective proton and neutron axial charges $\tilde{g}_A^p = -0.80 \pm 1.68$ and $\tilde{g}_A^n = 1.65 \pm 2.62$.

The strange axial form factor at $Q^2 = 0$ is related to the *spin* carried by strange quarks, Δs . Currently the world data on the spin-dependent g_1 structure function constrain Δs to be ≈ -0.055 at a scale $Q^2 = 1 \text{ GeV}^2$, with a significant fraction coming from the region $x < 0.001$. In addition, the HERMES collaboration [?] extracted the strange quark spin from semi-inclusive DIS data over the range $0.02 \leq x \leq 0.6$, yielding a *negative* central value, $\Delta s = 0.037 \pm 0.019 \pm 0.027$, although still consistent with the above global average.

Table 5-5: Coefficients entering Equation 5.9 for NC elastic scattering and CC QE interactions, with $\tau = Q^2/4M_p$.

A	B	C
$\frac{1}{4} [G_1^2 (1 + \tau) - (F_1^2 - \tau F_2^2) (1 - \tau) + 4\tau F_1 F_2]$	$-\frac{1}{4} G_1 (F_1 + F_2)$	$\frac{1}{16} \frac{M_p^2}{Q^2} (G_1^2 + F_1^2 + \tau F_2^2)$

An independent extraction of Δs , which does not rely on the difficult measurements of the g_1 structure function at very small x values, can be obtained from (anti)neutrino NC elastic scattering off protons, see Figure 5-5. Indeed, this process provides the most direct measurement of Δs . The differential cross section for NC elastic and CC QE scattering of (anti)neutrinos from protons can be written as:

$$\frac{d\sigma}{dQ^2} = \frac{G_\mu^2 Q^2}{2\pi E_\nu^2} (A \pm BW + CW^2); \quad W = 4E_\nu/M_p - Q^2/M_p^2, \quad (5.9)$$

where the positive (negative) sign is for (anti)neutrino scattering and the coefficients A , B , and C contain the vector and axial form factors as listed in Table 5-5.

The axial-vector form factor for NC scattering can be written as the sum of the known axial form factor G_A plus a strange form factor G_A^s :

$$G_1 = \left[-\frac{G_A}{2} + \frac{G_A^s}{2} \right], \quad (5.10)$$

while the NC vector form factors can be written as:

$$F_{1,2} = \left[\left(\frac{1}{2} - \sin^2 \theta_W \right) (F_{1,2}^p - F_{1,2}^n) - \sin^2 \theta_W (F_{1,2}^p + F_{1,2}^n) - \frac{1}{2} F_{1,2}^s \right], \quad (5.11)$$

where $F_1^{p(n)}$ is the Dirac form factor of the proton (neutron), $F_2^{p(n)}$ is the corresponding Pauli form factor, and $F_{1,2}^s$ are the strange vector form factors. These latter are expected to be

small from the PVES measurements summarized above. In the limit $Q^2 \rightarrow 0$, the differential cross section is proportional to the square of the axial-vector form factor $d\sigma/dQ^2 \propto G_1^2$ and $G_A^s \rightarrow \Delta s$. The value of Δs can therefore be extracted experimentally by extrapolating the NC differential cross section to $Q^2 = 0$.

Previous neutrino scattering experiments have been limited by the statistics and by the systematic uncertainties on background subtraction. The only information available comes from the analysis of 951 NC νp and 776 NC $\bar{\nu} p$ collected by the experiment BNL E734. [?, ?, ?]. The LBNE neutrino beam will be sufficiently intense that a measurement of NC elastic scattering on proton in the fine-grained ND can provide a definitive statement on the contribution of the strange sea to either the axial or vector form factor.

Systematic uncertainties can be reduced by measuring the NC/CC ratios for both neutrinos and antineutrinos:

$$\mathcal{R}_{\nu p}(Q^2) \equiv \frac{\sigma(\nu_\mu p \rightarrow \nu_\mu p)}{\sigma(\nu_\mu n \rightarrow \mu^- p)}(Q^2); \quad \mathcal{R}_{\bar{\nu} p}(Q^2) \equiv \frac{\sigma(\bar{\nu}_\mu p \rightarrow \bar{\nu}_\mu p)}{\sigma(\bar{\nu}_\mu p \rightarrow \mu^+ n)}(Q^2), \quad (5.12)$$

as a function of Q^2 . Figure 5-5 shows the absolute sensitivity of both ratios to Δs for different values of Q^2 . The sensitivity for $Q^2 \sim 0.25 \text{ GeV}^2$ is about 1.2 for neutrinos and 1.9 for antineutrinos, which implies that a measurement of $\mathcal{R}_{\nu p}$ and $\mathcal{R}_{\bar{\nu} p}$ of 1% precision would enable the extraction of Δs with an uncertainty of 0.8% and 0.5%, respectively.

MEASUREMENT OF Δs

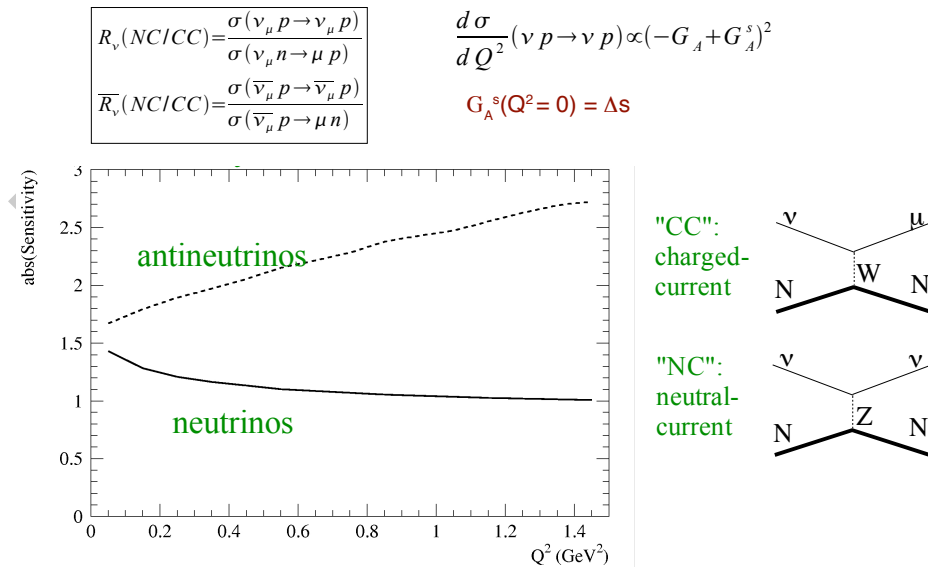


Figure 5-5: Absolute sensitivity of the ratios $\mathcal{R}_{\nu p}$ (solid) and $\mathcal{R}_{\bar{\nu} p}$ (dashed) to the strange contribution to the spin of the nucleon, Δs , as a function of Q^2 .

The design of HIRESMNU includes several different nuclear targets. Therefore, most of the neutrino scattering is from nucleons embedded in a nucleus, requiring nuclear effects to be

taken into account. Fortunately, in the ratio of NC/CC the nuclear corrections are expected to largely cancel out. The Δs analysis requires a good proton reconstruction efficiency as well as high resolution on both the proton angle and energy. To this end, the low-density magnetized tracker at LBNE can increase the range of the protons inside the ND, allowing the reconstruction of proton tracks down to $Q^2 \sim 0.07 \text{ GeV}^2$. This capability will reduce the uncertainties in the extrapolation of the form factors to the limit $Q^2 \rightarrow 0$.

Table 5-6 summarizes the expected proton range for the low-density ($\rho \sim 0.1 \text{ g/cm}^3$) STT. We expect about $1 \times 10^5 \nu p(\bar{\nu} p)$ events after the selection cuts in the low-density tracker, yielding a statistical precision of the order of 0.3%.

Table 5-6: Expected proton range for the low density ($\rho \sim 0.1 \text{ g/cm}^3$) tracker. The first column gives the proton kinetic energy and the last column the proton momentum. The Q^2 value producing T_p is calculated assuming the struck nucleon was initially at rest.

T_p MeV	Q^2 GeV^2/c^2	Range STT cm	P_p GeV/c
20	0.038	4.2	0.195
40	0.075	14.5	0.277
60	0.113	30.3	0.341
80	0.150	50.8	0.395
100	0.188	75.7	0.445

We follow the analysis performed by the FINESS collaboration [?] and in the SciBooNE experiment for the determination of Δs . In particular, based upon the latter, with the scintillator tracker we expect a purity of about 50%, with background contributions of 20% from neutrons produced outside of the detector, 10% νn events and 10% NC pion backgrounds. The dominant systematic uncertainty will be related to the background subtraction. The low-energy beam spectrum at LBNE provides the best sensitivity for this measurement since the external background from neutron-induced proton recoils will be reduced by the strongly suppressed high-energy tail. The low-density magnetized tracker is expected to increase the purity by reducing the neutron background and the NC pion background. We point out that the outside neutron background can be determined using the $n \rightarrow p + \pi^-$ process in the STT. In summary, we believe that we can achieve a precision on Δs of about 0.02 – 0.03. The sensitivity analysis is in progress.

5.4 Isospin Physics and Sum-Rules

One of the most compelling physics topics accessible to the HIRESMNU detector in the LBNE is the isospin physics using neutrino and antineutrino interactions. The salient topics are:

- Adler Sum Rule
- Tests of Isospin (Charge) Symmetry in Nucleons and Nuclei

The Adler sum rule relates the integrated difference of the antineutrino and neutrino F_2 to the isospin of the target:

$$\mathcal{S}_A(Q^2) = \int_0^1 dx \left[F_2^{\bar{\nu}}(x, Q^2) - F_2^{\nu}(x, Q^2) \right] / (2x) = 2 I_z, \quad (5.13)$$

where the integration is performed over the entire kinematic range of the Bjorken variable x and I_z is the projection of the target isospin vector on the quantization axis (z axis). For the proton $\mathcal{S}_A^p = 1$ and for the neutron $\mathcal{S}_A^n = -1$.

In the quark parton model the Adler sum is the difference between the number of valence u and d quarks of the target. The Adler sum rule survives the strong interaction effects because of the conserved vector current (CVC) and provides an exact relation to test the local current commutator algebra of the weak hadronic current. We note that in the derivation of the Adler sum rule the effects of both non-conservation of the axial current and heavy quark production are neglected.

Experimental tests of the Adler sum rule require the use of a hydrogen target to avoid nuclear corrections to the bound nucleons inside nuclei. The structure functions $F_2^{\bar{\nu}}$ and F_2^{ν} have to be determined from the corresponding differential cross sections and must be extrapolated to small x values in order to evaluate the integral. The only test available is limited by the modest statistics and was performed in bubble chambers by the BEBC collaboration using about 9,000 $\bar{\nu}$ and 5,000 ν events collected on hydrogen [?].

The LBNE program can provide the first high precision test of the Adler sum rule. To this end, the use of the high-energy beam configuration, although not essential, would increase the sensitivity allowing us to reach higher Q^2 values. Since the use of a liquid H_2 bubble chamber is excluded in the ND hall due to safety concerns, the (anti)neutrino interactions off a hydrogen target can only be extracted with a subtraction method from the composite materials of the ND targets. Using this technique to determine the position resolution in the location of the primary vertex is crucial to reducing systematic uncertainties. For this reason a precision test of the Adler sum rule can be only performed with the low-density magnetized ND.

Two different targets are used resulting in a fiducial hydrogen mass of about 1 tonne: the polypropylene $(C_3H_6)_n$ foils placed in front of the STT modules and pure carbon foils. The statistical subtraction increases the statistical uncertainty by a factor of four. With the LBNE fluxes from the standard exposure we would collect about 1×10^6 inclusive $\nu(\bar{\nu})$ CC events on the hydrogen target. This level of precision will open up the possibility of making new discoveries in the quark and hadron structure of the proton.

5.5 Nucleon Structure, Parton Distribution Functions, and QCD Studies

Precision measurements of (anti)neutrino structure functions and differential cross sections would directly affect the oscillation measurements by providing accurate simulation of neutrino interaction and offer an estimate of all background processes that are dependent upon the angular distribution of the outgoing particles in the FD. Furthermore, QCD analyses within the framework of global fits to extract parton distribution functions (PDF) by using the differential cross sections measured in ND data provide a crucial step by constraining systematic error in precision electroweak measurements not only in neutrino physics but also in hadron-collider measurements.

Under the rubric of nucleon-structure, the topics include:

- Measurement of Form Factors and Structure Functions
- QCD Analysis of Parton Distribution Functions
- d/u Parton Distribution Functions at Large x
- GLS Sum Rule and α_s
- Non-perturbative Contributions and High Twists
- Quark-hadron Duality
- Generalized Parton Distributions

For quantitative studies of inclusive deep-inelastic lepton-nucleon scattering, it is vital to have precise F_3 structure functions, which can only be measured with neutrino and antineutrino beams, as input into global PDF fits. Because it depends on weak axial quark charges, the F_3 structure function is unique in its ability to differentiate between the quark and antiquark content of the nucleon. On a proton target, for instance, the neutrino and antineutrino F_3 structure functions (at leading order in α_s) are given by

$$xF_3^{\nu p}(x) = 2x(d(x) - \bar{u}(x) + \bar{s}(x) + \cdots), \quad (5.14)$$

$$xF_3^{\bar{\nu} p}(x) = 2x(u(x) - \bar{d}(x) - \bar{s}(x) + \cdots). \quad (5.15)$$

In contrast, electromagnetic probes are sensitive only to a sum of quark and antiquark PDFs. Unfortunately, the neutrino scattering cross sections have considerably larger uncertainties than the electromagnetic inclusive cross sections at present. The proposed HIRESMNU offers a promise to reduce the gap between the uncertainties on the weak and electromagnetic structure functions, and would have a major impact on global PDF analyses.

Recent experiments at JLab have collected high-precision data on the individual F_1 and F_2 (or F_T and F_L) structure functions at large x from Rosenbluth-separated cross sections. This avoids the need for model-dependent assumptions about the ratio $R = \sigma_L/\sigma_T$ of the longitudinal to transverse cross sections in the extraction of the structure functions from the measured cross sections. Similar quality data on the individual F_T and F_L structure functions from neutrino scattering would be available from the ND at Fermilab to maximally complement and facilitate the flavor decomposition of these functions.

In addition to data in the DIS region, there is considerable interest in obtaining data at low Q^2 (down to $Q^2 \sim 1 \text{ GeV}^2$) and low W ($W < 2 \text{ GeV}$), to complement data from JLab. Unpolarized structure functions can be expressed in terms of powers of $1/Q^2$ (power corrections):

$$F_{2,T,3}(x, Q^2) = F_{2,T,3}^{\tau=2}(x, Q^2) + \frac{H_{2,T,3}^{\tau=4}(x)}{Q^2} + \frac{H_{2,T,3}^{\tau=6}(x)}{Q^4} + \dots \quad (5.16)$$

where the first term ($\tau = 2$), expressed in terms of PDFs, represents the Leading Twist (LT), which describes the scattering off a free quark, and is responsible for the scaling of SF via perturbative QCD $\alpha_s(Q^2)$ corrections. The Higher Twist (HT) terms ($\tau = 4, 6$) reflect instead the strength of multi-parton correlations (qq and qg). The ND data at LBNE would allow a good separation of target mass and higher twist corrections, both of which are $1/Q^2$ suppressed at high Q^2 , from leading twist contributions [?], [?].

Global PDF fits show that at large values of x ($x > 0.5 - 0.6$) the d quark distribution (or the d/u ratio) is very poorly determined. The main reason for this is the absence of free neutron targets. Because of the larger electric charge on the u quark than on the d , the electromagnetic proton F_2 structure function data provide strong constraints on the u quark distribution, but are relatively insensitive to the d quark distribution.

To constrain the d quark distribution a precise knowledge of the corresponding neutron F_2^n structure functions is required, which in practice is extracted from inclusive deuterium F_2 data. At large values of x the nuclear corrections in deuterium become large and, more importantly, strongly model-dependent, leading to large uncertainties on the resulting d quark distribution.

Several planned experiments at JLab with the energy upgraded 12 GeV beam will measure the d/u ratio up to $x \sim 0.85$ using several different method to minimize the nuclear corrections. One method will use semi-inclusive DIS from deuterium with a low-momentum ($|\vec{p}| < 100 \text{ MeV}$) spectator proton detected in the backward center-of-mass hemisphere, to ensure scattering on an almost free neutron (the “BoNuS” experiment [?]). Preliminary results have confirmed the feasibility of this method at the current 6 GeV energies, and a proposal for the extension at 12 GeV has been approved.

Perhaps the cleanest and most direct method to determine the d/u ratio at large x is from neutrino and antineutrino DIS on hydrogen. Existing neutrino data on hydrogen have rela-

tively large errors and do not extend beyond $x \sim 0.5$. A new measurement of neutrino and antineutrino DIS from *hydrogen* at LBNE with significantly improved uncertainties would therefore make an important discovery about the d/u behavior as $x \rightarrow 1$. This measurement might be possible with a statistical subtraction of pure-carbon from the hydro-carbon target with negligible systematic errors due to acceptance. To well complement the proposed JLab 12 GeV experiments, the kinematical reach would need to be up to $x \sim 0.85$ and with as large a Q^2 range as possible to control for higher twist and other sub-leading effects in $1/Q^2$.

5.6 Neutrino-Nuclear Interactions and Nuclear Effects

An integral part of the physics program envisioned in this proposal involves detailed measurements of (anti)neutrino interactions in a variety of nuclear targets. The standard target of the proposed ND is hydro-carbon, largely due to the mass of the the STT radiators. Among the additional nuclear targets, the most important is the argon-target which composes the LBNE FD. We propose to have argon gas in pressurized aluminium tubes with sufficient mass to provide $\simeq 5$ times the ν_μ -CC and NC statistics as expected in the LBNE FD. Equally important nuclear targets are iron, which is used in the ICAL of INO, and carbon. Indeed the modularity of the STT provides for successive measurements using thin nuclear targets such as lead, calcium, etc. An arrangement of nuclear targets positioned upstream of the detector, as shown in Figure ?? and Figure ??, provides the desired sample in (anti)neutrino interactions. For example, a single 1-mm-thick Pb sheet, at the upstream end of the detector, will provide about 2×10^5 ν_μ -CC interactions in one year.

The topics in nuclear effects include the following studies:

- Nuclear Modifications of Form Factors
- Nuclear Modifications of Structure Functions
- Mechanisms for Nuclear Effects in Coherent and Incoherent Regimes
- A Dependence of Exclusive and Semi-exclusive Processes
- Effect of Final-State Interactions
- Effect of Short-Range Correlations
- Two-Body Currents

The study of nuclear effects in (anti)neutrino interactions off nuclei is directly relevant for the oscillation studies. The use of argon or iron in the LBNE FD requires a measurement of nuclear cross sections on the same targets in the ND. In addition to the different p/n ratio

in argon or iron or water, nuclear modifications of cross sections can differ from 5% to 15% between oxygen and argon, while the difference in the final state interactions could be larger. Additionally, nuclear modifications can introduce a substantial smearing of the kinematic variables reconstructed from the observed final-state particles. Detailed measurements of the A dependence of different processes are then required in order to understand the absolute energy scale of neutrino events and to reduce the corresponding systematic uncertainties on the oscillation parameters.

Furthermore, an important question in nuclear physics is how the structure of a free nucleon is modified when said nucleon is inside a nuclear medium. Studies of the ratio of structure functions of nuclei to those of free nucleons (or in practice, the deuteron) reveal nontrivial deviations from unity as a function of x and Q^2 . These have been well explored in charged lepton scattering experiments, but little empirical information exist from neutrino scattering. Another reason to investigate the medium modifications of neutrino structure functions is that most neutrino scattering experiments are performed on nuclear targets, from which information on the free nucleon is inferred by performing a correction for the nuclear effects. In practice this often means applying the same nuclear correction as for the electromagnetic structure functions, which introduces an inherent model dependence in the result. In particular, significant differences between photon-induced and weak boson-induced nuclear structure functions are predicted, especially at low Q^2 and low x , which have not been tested. A striking example is offered by the ratio R of the longitudinal-to-transverse structure functions [?]. While the electromagnetic ratio tends to zero in the photoproduction limit, $Q^2 \rightarrow 0$, by current conservation, the ratio for neutrino structure functions is predicted to be *finite* in this limit. Thus significant discovery potential exists in the study of neutrino scattering from nuclei. Finally, the extraction of (anti)neutrino interactions on deuterium from the statistical subtraction of H_2O from D_2O , which is required to measure the fluxes (Section ??), would allow the first direct measurement of nuclear effects in deuterium. This measurement can be achieved since the structure function of a free isoscalar nucleon is given by the average of neutrino and antineutrino structure functions on hydrogen ($F_2^{\nu n} = F_2^{\bar{\nu} p}$). A precise determination of nuclear modifications of structure functions in deuterium would play a crucial role in reducing systematic uncertainties from the global PDF fits.

5.7 Search for Heavy Neutrinos

The most economic way to handle the problems of neutrino masses, dark matter and baryon asymmetry of the Universe in a unified way may be to add to the SM three Majorana singlet fermions with masses roughly on the order of the masses of known quarks and leptons. The appealing feature of this theory (called the νMSM for “Neutrino Minimal SM”) is the fact that there every left-handed fermion has a right-handed counterpart, leading to an equal way of treating quarks and leptons. The lightest of the three new leptons is expected to have a mass from 1 keV to 50 keV and play the role of the dark matter particle. Two other neutral fermions are responsible for giving masses to ordinary neutrinos via the see-

saw mechanism at the *electroweak scale* and for creation of the baryon asymmetry of the Universe (for a review see [?]). The masses of these particles and their coupling to ordinary leptons are constrained by particle physics experiments and cosmology. They should be almost degenerate, thus nearly forming Dirac fermions (this is coming from the requirement of successful baryogenesis). Different considerations indicate that their mass should be in $\mathcal{O}(1)$ GeV region [?].

The ν MSM is described by the most general renormalizable Lagrangian containing all the particles of the SM and three singlet fermions. For the purpose of the present discussion we take away from it the lightest singlet fermion N_1 (the “dark matter sterile neutrino”), which is coupled extremely weakly to the ordinary leptons. In addition, we take N_2 and N_3 degenerate in mass, $M_2 = M_3 = M$. Then the convenient parametrization of the interaction of N 's with the leptons of SM is:

$$L_{\text{singlet}} = \left(\frac{\kappa M m_{\text{atm}}}{v^2} \right)^{\frac{1}{2}} \left[\frac{1}{\sqrt{\epsilon e^{i\eta}}} \bar{L}_2 N_2 + \sqrt{\epsilon e^{i\eta}} \bar{L}_3 N_3 \right] \tilde{H} - M \bar{N}_2^c N_3 + \text{h.c.}, \quad (5.17)$$

where L_2 and L_3 are the combinations of L_e , L_μ and L_τ

$$L_2 = \sum_{\alpha} x_{\alpha} L_{\alpha}, \quad L_3 = \sum_{\alpha} y_{\alpha} L_{\alpha}. \quad (5.18)$$

with $\sum_{\alpha} |x_{\alpha}|^2 = \sum_{\alpha} |y_{\alpha}|^2 = 1$.

In Equation (5.17) $v = 246$ GeV is the vacuum expectation value of the Higgs field H , $\tilde{H}_i = \epsilon_{if} H_j^*$, $m_{\text{atm}} \simeq 0.05$ eV is the atmospheric neutrino mass difference, and $\kappa = 1$ (2) for normal (inverted) hierarchy of neutrino masses. The x_{α} and y_{α} can be expressed through the parameters of the active neutrino-mixing matrix (explicit relations can be found in [?]). The parameter ϵ (by definition, $\epsilon < 1$) and the CP-breaking phase η cannot be fixed by using neutrino masses and mixings.

If the mass of N is fixed, smaller ϵ yields stronger interactions of singlet fermions to the SM leptons. This would have led to equilibration of these particles in the early Universe above the electroweak temperatures, and, therefore, to erasing of the baryon asymmetry. In other words, the mixing angle U^2 between neutral leptons and active neutrinos must be small, explaining why these new particles have not been seen previously. For small ϵ ,

$$U^2 = \frac{\kappa m_{\text{atm}}}{4M\epsilon}. \quad (5.19)$$

The most efficient mechanism of sterile neutrino production is through weak decays of heavy mesons and baryons, as can be seen from the left panel of Figure 5–6, showing some examples of relevant two- and three-body decays. Heavy mesons can be produced by energetic protons scattering off the target material.

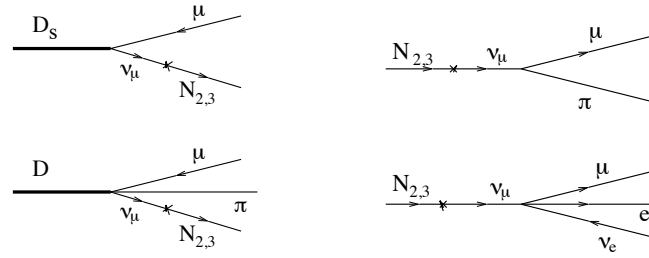


Figure 5-6: Left panel: Feynman diagrams of meson decays producing heavy sterile neutrinos. Right panel: Feynman diagrams of sterile neutrino decays.

Several experiments have conducted searches for heavy neutrinos, for example BEBC [?], CHARM [?], NuTeV [?] and the CERN PS191 experiment [?,?] (see also discussion of different experiments in [?]). In the search for heavy neutrinos, the strength of the proposed high-resolution ND, compared to earlier experiments, lies in reconstructing the exclusive decay modes including electronic, hadronic and muonic. Furthermore, the detector offers a means to constrain and measure the backgrounds using control samples. Preliminary investigations suggest that HIRESMNU will have an order of magnitude higher sensitivity in exclusive channels than previous experiments. We are actively advancing the sensitivity evaluation.

5.8 Search for Non-Standard Interactions: High Δm^2 Neutrino Oscillations

The evidence for neutrino oscillations obtained from atmospheric, long-baseline accelerator, solar and long-baseline reactor data from different experiments consistently indicates two different scales with $\Delta m_{32}^2 \sim 2.4 \times 10^{-3} \text{ eV}^2$ defining the atmospheric oscillations and $\Delta m_{21}^2 \sim 7.9 \times 10^{-5} \text{ eV}^2$ defining the solar oscillations. The only way to accommodate oscillations with relatively high Δm^2 at the eV^2 scale is therefore to add one or more sterile neutrinos to the conventional three light neutrinos.

Recently, the MiniBooNE experiment reported that their antineutrino data might be consistent with the LSND $\bar{\nu}_\mu \rightarrow \bar{\nu}_e$ oscillation with $\Delta m^2 \sim \text{eV}^2$ [?]. Contrary to the antineutrino data, the MiniBooNE neutrino data seem to exclude high Δm^2 oscillations, possibly indicating a different behavior between neutrinos and antineutrinos.

Models with five (3+2) or six (3+3) neutrinos can potentially explain the MiniBooNE results. In addition to the cluster of the three neutrino mass states accounting for “solar” and “atmospheric” mass splitting two (or three) states at the eV scale are added, with a small admixture of ν_e and ν_μ to account for the LSND signal. One distinct prediction from such models is a significant probability for $\bar{\nu}_\mu$ disappearance into sterile neutrinos, of the order of 10%, in addition to the small probability for $\bar{\nu}_e$ appearance.

Since the ND at LBNE is located at a baseline of 460 m and uses the LE beam, it can reach the same value $L/E_\nu \sim 1$ of MiniBooNE and LSND. The large fluxes and the availability of fine-grained detectors make the LBNE program well suited to search for oscillations at the eV^2 scale. Due to the potential differences between neutrinos and antineutrinos four possibilities have to be considered in the analysis: ν_μ disappearance, $\bar{\nu}_\mu$ disappearance, ν_e appearance and $\bar{\nu}_e$ appearance. As discussed in Section ??, the search for high Δm^2 oscillations has to be performed simultaneously with the in situ determination of the fluxes.

To this end, we need to obtain an independent prediction of the ν_e and $\bar{\nu}_e$ fluxes starting from the measured ν_μ and $\bar{\nu}_\mu$ CC distributions since the ν_e and $\bar{\nu}_e$ CC distributions could be distorted by the appearance signal. The low- ν_0 method can provide such predictions if external measurements for the K_L^0 component are available from hadro-production experiments (Section ??).

We will follow an iterative procedure:

1. Extract the fluxes from ν_μ and $\bar{\nu}_\mu$ CC distributions assuming no oscillations are present
2. Comparison with data and determination of oscillation parameters (if any)
3. New flux extraction after subtraction of the oscillation effect
4. Iterate until convergence

The analysis has to be performed separately for neutrinos and antineutrinos due to potential CP or CPT violation according to MiniBooNE/LSND data.

We measure the ratio of electron-to-muon CC events:

$$\mathcal{R}_{e\mu}(L/E) \equiv \frac{\# \text{ of } \nu_e N \rightarrow e^- X}{\# \text{ of } \nu_\mu N \rightarrow \mu^- X}(L/E); \quad \bar{\mathcal{R}}_{e\mu}(L/E) \equiv \frac{\# \text{ of } \bar{\nu}_e N \rightarrow e^+ X}{\# \text{ of } \bar{\nu}_\mu N \rightarrow \mu^+ X}(L/E) \quad (5.20)$$

which is then compared with the predictions obtained from the low- ν_0 method. Deviations of $\mathcal{R}_{e\mu}$ or $\bar{\mathcal{R}}_{e\mu}$ from the expectations as a function of L/E would provide evidence for oscillations. It must be noted that this procedure only provides a relative measurement of $\nu_e(\bar{\nu}_e)$ vs. $\nu_\mu(\bar{\nu}_\mu)$. Actually, since the fluxes are extracted from the observed ν_μ and $\bar{\nu}_\mu$ CC distributions, an analysis of the $\mathcal{R}_{e\mu}(\bar{\mathcal{R}}_{e\mu})$ ratio cannot distinguish between $\nu_\mu(\bar{\nu}_\mu)$ disappearance and $\nu_e(\bar{\nu}_e)$ appearance.

The process of NC elastic scattering off protons (Section 5.3) can provide the complementary measurement needed to disentangle the two hypotheses of $\nu_\mu(\bar{\nu}_\mu)$ disappearance into sterile neutrinos and $\nu_e(\bar{\nu}_e)$ appearance. In order to cancel systematic uncertainties, we will measure the NC/CC ratio with respect to quasi-elastic scattering:

$$\mathcal{R}_{NC}(L/E) \equiv \frac{\# \text{ of } \nu p \rightarrow \nu p}{\# \text{ of } \nu_\mu n \rightarrow \mu^- p}(L/E); \quad \bar{\mathcal{R}}_{NC}(L/E) \equiv \frac{\# \text{ of } \bar{\nu} p \rightarrow \bar{\nu} p}{\# \text{ of } \bar{\nu}_\mu p \rightarrow \mu^+ n}(L/E) \quad (5.21)$$

We can reconstruct the neutrino energy from the proton angle and momentum under the assumption of neglecting the nuclear smearing (the same for the neutrino CC sample). In the oscillation analysis we are only interested in relative distortions of the ratio $\mathcal{R}_{NC}(\bar{\mathcal{R}}_{NC})$ as a function of L/E and not in the absolute values of the ratios. For $Q^2 > 0.2 \text{ GeV}^2$ the relative shape of the total cross sections is not very sensitive to the details of the form factors. To improve the energy resolution we can use events originating from the deuterium inside the D_2O target embedded into the fine-grained tracker.

An improved oscillation analysis is based on a simultaneous fit to both $\mathcal{R}_{e\mu}(\bar{\mathcal{R}}_{e\mu})$ and $\mathcal{R}_{NC}(\bar{\mathcal{R}}_{NC})$. The first ratio provides a measurement of the oscillation parameters while the latter constrains the $\nu_e(\bar{\nu}_e)$ appearance vs. the $\nu_\mu(\bar{\nu}_\mu)$ disappearance. This analysis results in two main requirements for the ND:

- e^+/e^- separation to provide an unambiguous check of the different behavior between neutrinos and antineutrinos suggested by MiniBooNE
- Accurate reconstruction of proton momentum and angle

In order to validate the unfolding of the high Δm^2 oscillations from the in situ extraction of the (anti)neutrino flux, we would also need to change the beam conditions, since the ND cannot be easily moved. To this end, it will be important to have the possibility of a short run with a high energy beam and to change/switch off the beam focusing system.

5.9 Light (sub-GeV) Dark Matter Searches in the Neutrino Beam at LBNE

According to the latest cosmological and astrophysical measurements, nearly eighty percent of the matter in the universe is in the form of cold, non-baryonic dark matter (DM). The search to find evidence of the particle (or particles) that make up DM, however, has so far turned up empty. Direct detection experiments and measurements at the LHC alike, however, are starting to severely constrain the parameter space of Weakly-Interacting Massive Particles (WIMPs), one of the leading candidates for DM. The lack of evidence for WIMPs at these experiments has forced many in the theory community to reconsider the WIMP paradigm. One alternative possibility is that DM has a mass which is much lighter than the electroweak scale (e.g., below the GeV level). In these theories, in order to satisfy constraints on the relic density of DM, the DM particles must be accompanied by light "mediator" particles that allow for efficient DM annihilation in the early universe. The simplest form of these theories is that of an extra $U(1)$ gauge field mixes with the Standard Model (SM) $U(1)$ gauge field with an additional kinetic term. This mixing term provides a "portal" from the dark sector to the charged particles of the SM. In this model, the mediators are called

"dark photons" and are denoted by V . Recently, a great deal of interest has been paid to the possibility of studying these models at low-energy, fixed-target experiments (see Refs. [?] to [?]). High flux neutrino beam experiments, such as LBNE, have been shown to provide coverage of DM+mediator parameter space which cannot be covered by either direct detection or collider experiments. Upon striking the target, the proton beam can produce the dark photons either directly through $pp(pn) \rightarrow V$ as in Figure 5-7 (left) or indirectly through the production of a π^0 or a η meson which then promptly decays into a SM photon and a dark photon as in Figure 5-7 (center). For the case where $m_V > 2m_{DM}$, the dark photons will quickly decay into a pair of DM particles. These relativistic DM particles from the beam

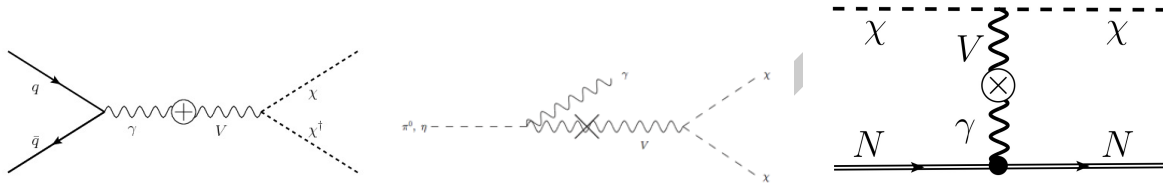


Figure 5-7: On the left is shown the direct production of a dark photon, while, in the center, the dark photon is produced via the decay of a neutral pion or eta meson. In both cases, the dark photon promptly decays into a pair of DM particles. Right: Tree-level scattering of a DM particle off of nuclei. Analogous interactions with electrons in the detector are also possible.

will travel along with the neutrinos to the LBNE near detector. The DM particles can then be detected through neutral-current like interactions either with electrons or nucleons in the detector as shown in Figure 5-7 (right). Since the signature of DM events looks just like those of the neutrinos, the neutrino beam provides the major source of background for the DM signal. Several ways have been proposed to suppress neutrino backgrounds by using the unique characteristics of the DM beam. Since DM will travel much slower than the neutrinos with much higher masses, the timing of the DM events in the near detector. In addition, since the electrons struck by DM will be much more forward direction, the angle of these electrons may be used to reduce backgrounds, taking advantage of fine angular resolution LBNE can provide. Finally, a special run can be devised to turn off the focusing horn to significantly reduce the charged particle flux that will produce neutrinos. Fig. 5-8 shows an example of the number of DM neutral current like events which would have been produced in the MINOS near detector (980t) depending on the mass of the DM particle and the size of the mixing between the SM and dark photons (κ). If LBNE near detector were LAr TPC, since the entire detector volume will be active, the effective number of DM events detected will be much higher with the detector of the same mass. Much more thorough studies must be conducted to obtain reliable sensitivity. This requires an integration of theoretical predictions into a simulation package for the detector.

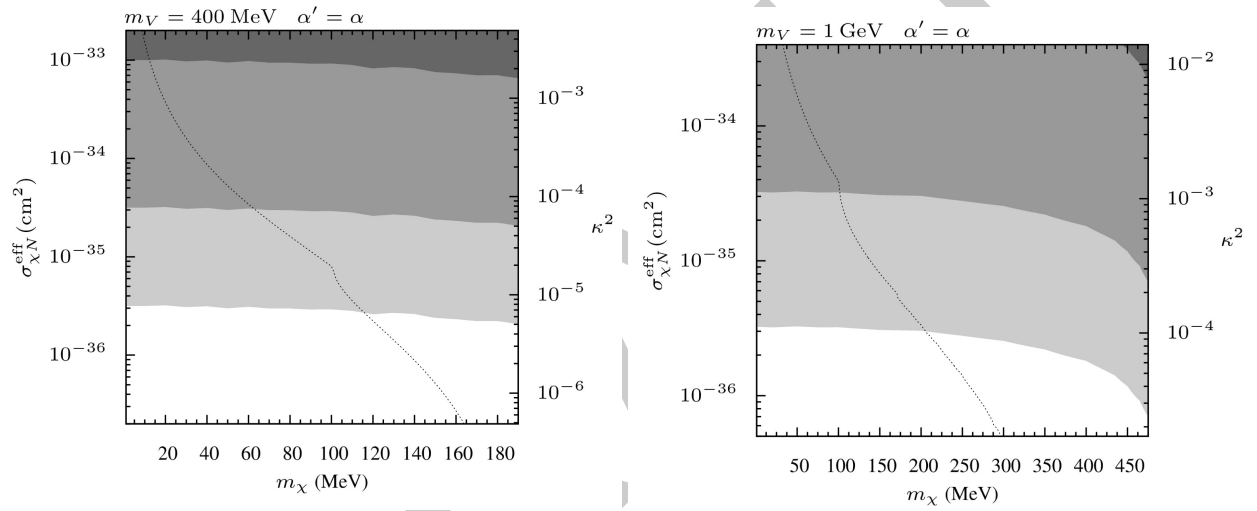


Figure 5-8: Expected number of neutral current-like events from DM scattering. On the left is shown the case where V is directly produced, while the right plot shows the case where V is produced from η decay. The contours show greater than 10 (light), 1000 (medium) and 106 (dark) events. These plots were taken from [?]

6 Searches for Baryon Number Non-conservation

As described in Section 2.3, searches for baryon-number-violating processes probe high-energy scales, being strongly motivated by grand unified theories (GUTs). Predicted rates for nucleon decay and mixing processes from a wide range of modes are directly accessible with large underground detectors. It is essential to push forward the sensitivity to such processes; LBNE provides an excellent opportunity to do just this in a way that is entirely compatible with the neutrino oscillation program as well as other primary physics objectives.

6.1 Sensitivity to Nucleon Decay

6.1.1 LBNE and the Current Experimental Context

Current limits on nucleon decay via numerous channels are dominated by Super-Kamiokande (SK) [?], for which the most recently reported preliminary results are based on an overall exposure of 260 kt-yr. The SK data has yielded order-of-magnitude improvement on the 90% CL limits on the partial lifetimes for modes of particular interest such as $\tau/B(p \rightarrow e^+\pi^0) < 1.3 \times 10^{34}$ yr and $\tau/B(p \rightarrow K^+\bar{\nu}) < 0.59 \times 10^{34}$ yr [?]. While the results for these two modes were obtained in searches that produced no candidates, backgrounds (estimated at ~ 2 and 4 events per Mt-yr, respectively) [?] may be just around the corner. Thus, with more than ten years of operation already, not only will the SK limits improve slowly at this point with the incremental future exposure anticipated, but also the prospect of obtaining a convincing proton decay signal has all but vanished in these modes. Future large-scale proton decay detectors like Hyper-Kamiokande will have to contend with backgrounds that may not be reducible, although it should be noted that promising strategies have been identified (such as Gadolinium-doping to veto atmospheric neutrino backgrounds where neutrons are produced).

This state the field provides an opening for the large underground LBNE far detector. The uniqueness of proton decay signatures in the LArTPC and the potential for reconstructing them with redundant information has been long recognized as a key strength for this technology. As is generally the case for experiments dedicated to the search for a specific rare

process, one wants both a large sample of parent particles (*i.e.*, large fiducial mass and large acceptance/detection efficiency), and a detection technique that can provide convincing evidence for the process of interest from even just one candidate event. With their scalability and detection capability, large LArTPC detectors can meet these design goals.

Because the strengths of the water Cherenkov technology (including ease of obtaining very large masses) are well matched to the $p \rightarrow e^+\pi^0$ final state topology, LArTPC's do not compete well in this mode, despite the strength of the signature (clean identification of the electron and two gammas, reconstruction of the $e^+\pi^0$ invariant mass, and zero net momentum of the system). On the other hand, for the $p \rightarrow K^+\bar{\nu}$ channel, the efficiency for water Cherenkov detectors is low, giving detectors that can cleanly reconstruct kaon and its decay products a substantial advantage in efficiency and background rejection capability. Other modes for which LArTPCs have an edge include $n \rightarrow e^-K^+$ and $p \rightarrow e^+\gamma$. Below, we discuss some of the issues relevant for the search for nucleon decay in the LBNE far detector, focusing on $p \rightarrow K^+\bar{\nu}$ as a prime example.

6.1.2 Signatures for Nucleon Decay in LBNE

6.1.2.1 Signatures for $p \rightarrow K^+\bar{\nu}$

The key signature for $p \rightarrow K^+\bar{\nu}$ is the presence of an isolated monochromatic ($p = 340 \text{ MeV}/c$ for the case of free protons) charged kaon. Unlike the case of $p \rightarrow e^+\pi^0$, where the maximum detection efficiency is limited to 40–45% because of inelastic intranuclear scattering of the π^0 , the kaon in $p \rightarrow K^+\bar{\nu}$ emerges intact (due to strangeness conservation) from the nuclear environment of the decaying proton $\sim 97\%$ of the time. On the other hand, nuclear effects are important: the kaon momentum is smeared by the proton's Fermi motion and shifted downward by rescattering. [?]

In water detectors, the kaon is below Cherenkov threshold, and must be detected after stopping, via its decay products. Not all K decay modes are reconstructable, and even for those that are there is insufficient information to determine the initial K momentum. Still, water detectors enable reconstruction of significant hadronic channels like $K^+ \rightarrow \pi^+\pi^0$ decay, and the 6 MeV gamma from de-excitation of O^{16} provides an added signature to help with the $K^+ \rightarrow \mu^+\nu$ channel, such that the overall detection efficiency is approaching 20% in SK [?].

In the case of LAr detectors, the K^+ can be tracked, its momentum measured by range, and its identity positively resolved via detailed analysis of its energy loss profile. Additionally, all decay modes can be cleanly reconstructed and identified, including those with neutrinos since the decay is at rest. With this level of detail, a single event can provide overwhelming evidence for the appearance of an isolated kaon of the right momentum originating from a point within the fiducial volume. The strength of this signature is clear from single event

- 1 displays of kaons observed by the ICARUS Collaboration in the cosmic ray test run of the
 2 T600 module on the surface at Pavia in 2001. One example is shown below in Fig. ??.

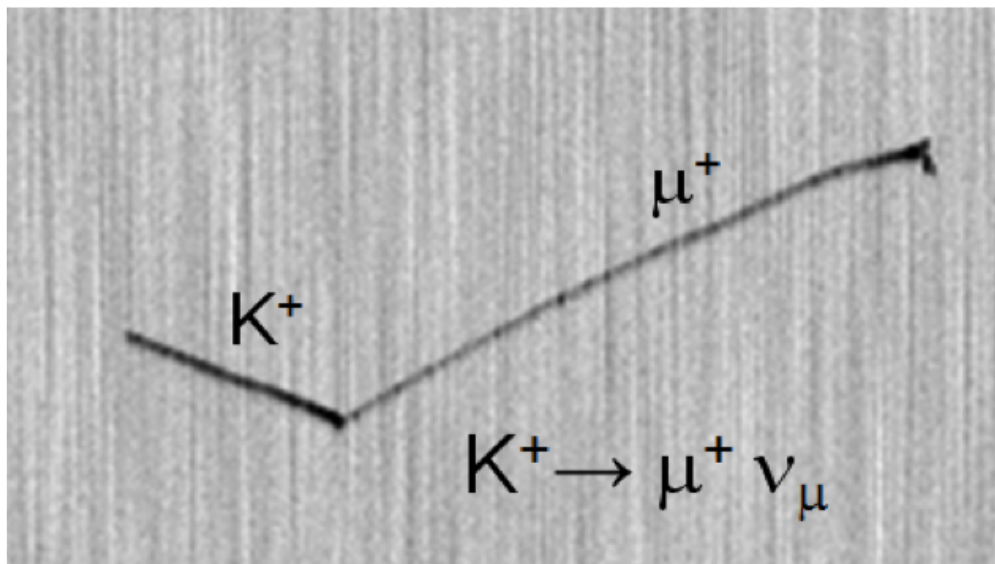


Figure 6-1: Single event display for an isolated charged kaon in the ICARUS T600 detector. In this event, the kaon is observed as a heavily ionizing track that stops and decays to $\mu\nu$, producing a muon track that also stops and decays such that the Michel electron track is also visible in this view.

- 3 Provided that it can be demonstrated that background processes that mimic this signature
 4 can be rejected at the appropriate level, a single $p \rightarrow K^+\bar{\nu}$ candidate can be viewed as
 5 evidence for proton decay. We discuss the background rejection capability of the LBNE far
 6 detector in the section below.

7 6.1.3 Background Levels and Rejection

- 8 In LAr, the most pernicious background for proton decay with kaon final states comes from
 9 cosmic rays that produce entering kaons in photonuclear interactions in the rock near the
 10 detector. Backgrounds as a function of depth have been studied for LAr in references [?, ?, ?].
 11 At 4850 ft level, the vertical rock overburden will be approximately 4 km w. e. and the
 12 muon rate through a 34 kt LArTPC will be about 0.1 s^{-1} . With a maximum of 2 ms drift
 13 time the probability of having a muon passing through the detector during any candidate
 14 event will be 2×10^{-4} . (Here the candidate event is defined as an event to be considered as
 15 a candidate for the proton decay or neutrino.) So any candidate event which coincides in
 16 time with a large energy deposition from a muon or muon-induced cascade, can be rejected
 17 with a loss of 0.02% of % efficiency. Then we can consider only a background from events
 18 associated with cosmic-ray muons when the muon itself does not cross the detector. We have
 19 considered cosmic-ray background for a particular proton decay mode, $p^+ \rightarrow K^+\bar{\nu}$, which is

the most promising to search for in a LArTPC. The main background for this decay mode comes from a neutral particle originated in a muon-induced cascade (most likely long-lived neutral kaon) coming into the detector from outside and producing a positive kaon within the fiducial volume (most likely via charge-exchange reaction). After simulating cosmic-ray muons and their secondaries at a depth of 4 km w. e. we have found the rate of positive kaons produced inside the detector by a neutral particle coming from outside (no muon inside) as about 0.9 events per year before any other cuts are applied. In further studies we considered the following cuts:

1. No muon in the detector
2. K^+ s are produced inside LAr at a distance from the wall greater than 10 cm,
3. energy deposition from K^+ and its descendants (excluding decay products) is less than 150 MeV
4. Energy deposition from K^+ s, their descendants and decay products is less than 1 GeV,
5. energy deposition from other particles in the muon-induced cascade (excluding energy deposition from positive kaons, their descendants and decay products) is less than 100 MeV.

No event survived the cuts giving the rate of background events which can mimic the proton decay mode specified above, as 0.07 per year in a 34 kt LArTPC. The key point here is that, although a large number of K^+ s deposit an energy similar to what is expected from a proton decay, the energy depositions from K^+ s are not the only ones recorded for these events: there are other particles entering the detector and depositing more energy making the rejection of background events simpler than initially thought. These studies show that proton decay searches can be successful at the 4850L at SURF and would not require an external veto system.

6.1.4 Expected Sensitivity

Figure 6-2 shows the expected limit on the proton lifetime as a function of time in LBNE for $p \rightarrow K^+ \bar{\nu}$. According to this plot, at least 10 kton of LAr is required to improve the limits significantly beyond continued Super-Kamiokande running. A 34 kton detector can eventually improve the limits on the $p \rightarrow K^+ \bar{\nu}$ by an order of magnitude compared to Super-Kamiokande.

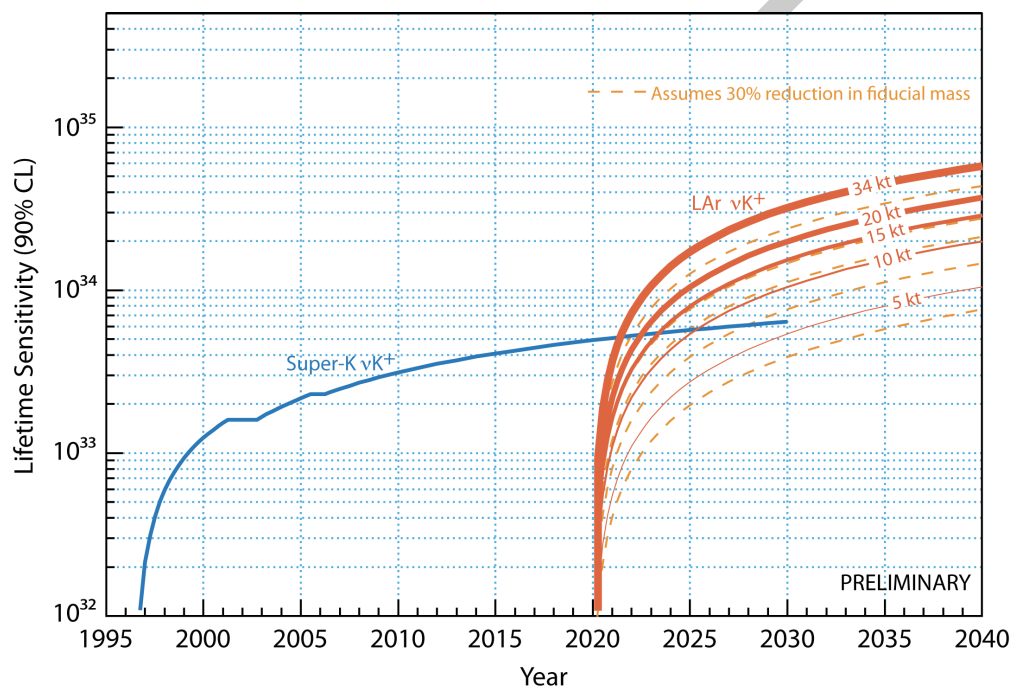


Figure 6-2: Proton decay lifetime limit for $p \rightarrow K^+ \bar{\nu}$ as a function of time for Super-Kamiokande compared to different LAr masses at the 4850 level SURF starting in 2020. The dashed lines show the effect of a 30% reduction of fiducial mass, conservatively assumed for a shallower depth of 2300 feet. The limits are at 90% C.L., calculated for a Poisson process including background assuming that the detected events equal the expected background.

7 Core-Collapse Supernova Neutrinos

7.1 Physics and Astrophysics From Core-Collapse Neutrinos

The information in a supernova neutrino burst is contained in the energy and flavor evolution of the burst as a function of time. This information will shed light both on astrophysics of the collapse, and on neutrino properties. We emphasize here again that liquid argon has unique sensitivity to the ν_e component of the burst. It must also be emphasized that the combination of information from different detectors with different flavor sensitivities will bring highly-enhanced information.

Some fairly generic core-collapse signal features are illustrated in Fig. 7-1 reproduced from reference [46]. The event starts with a short, sharp “neutronization” or “break-out” burst primarily composed ν_e , and is followed by an “accretion” phase lasting some hundreds of milliseconds. The final “cooling” phase over ~ 10 seconds represents the main part of the signal, over which the proto-neutron star sheds its gravitational binding energy. Flavor content and spectrum changes throughout these phases, and the core collapse’s temperature evolution can be followed with the neutrino signal (see Fig. 7-6).

The core-collapse neutrino spectrum at a given moment in time is expected to be well described by a “pinched-thermal” form, with one popular parameterization [47,48] given by:

$$\phi(E_\nu) = \mathcal{N} \left(\frac{E_\nu}{\langle E_\nu \rangle} \right)^\alpha \exp \left[-(\alpha + 1) \frac{E_\nu}{\langle E_\nu \rangle} \right], \quad (7.1)$$

where E_ν is the neutrino energy, $\langle E_\nu \rangle$ is the mean neutrino energy, α is the “pinching parameter”, and \mathcal{N} is a normalization constant. Large α corresponds to a more “pinched” spectrum (suppressed high-energy tail). The different ν_e , $\bar{\nu}_e$ and ν_x flavors are expected to have different average energy and α parameters and to evolve differently in time.

Many phenomena have impact on the flavor-energy time evolution, including neutrino oscillation effects that are determined by the mass hierarchy, and “collective” effects due to

- 1 neutrino-neutrino interactions. See *e.g.* references [49,50,51,52,53,54,55,56,57] as examples;
 2 a voluminous literature exists exploring these phenomena.

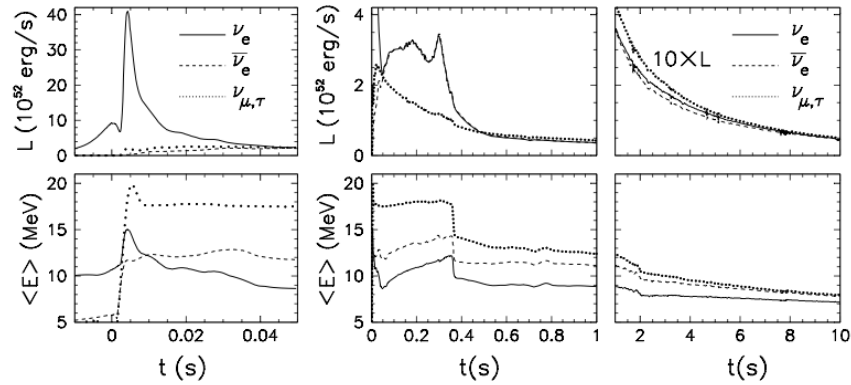


Figure 7-1: Expected core-collapse neutrino signal from the “Basel” model [46] (figure from [58]), for a $10.8 M_{\odot}$ progenitor. The left panel shows the very early signal, including “neutronization burst”; the middle panel shows the “accretion phase”, and the right panel shows the cooling phases. The top plots show luminosities as a function of time and the bottom plots show average energy as a function of time for ν_e , $\bar{\nu}_e$ and $\nu_{\mu,\tau}$ flavor components of the flux (note that fluxes for ν_{μ} , $\bar{\nu}_{\mu}$, ν_{τ} , and $\bar{\nu}_{\tau}$ should be identical).

- 3 The following lists some examples of astrophysical phenomena that should have observable
 4 impact on the signal:

- 5 • The neutronization burst, which will be mainly composed of ν_e .
- 6 • Formation of a black hole, which would cause a sharp signal cutoff (*e.g.* [59])
- 7 • Shock wave effects [60]
- 8 • Standing Accretion Shock Instability (SASI) oscillations [61,62]
- 9 • Turbulence effects [63,64]

10 This list is far from comprehensive. In addition there are possible effects that would give
 11 indications of beyond-the-standard-model physics [65], *e.g.* axions, extra dimensions, anomalous
 12 neutrino magnetic moment (and the non-observation of which would enable constraints
 13 on these phenomena).

14 Signatures of collective effects and signatures depending on the mass hierarchy impact many
 15 of the above signals (see next section for examples).

The supernova neutrino burst is prompt with respect to the electromagnetic signal and therefore provides an early warning to astronomers [37,66]. Some pointing should also be possible with a liquid argon signal [67] (primarily from elastic scattering on electrons).

One can note also that non-observation of a burst, or non-observation of a ν_e component of a burst, in the presence of supernovae (or other astrophysical events) observed in electromagnetic or gravitational wave channels would provide valuable information about the nature of the sources. A long-timescale sensitive search yielding no bursts will also provide limits on the rate of core collapse.

7.2 Expected Signal and Detection in Liquid Argon

The predicted event rate from a supernova burst may be calculated by folding expected neutrino differential energy spectra with cross sections for the relevant channels, and with detector response. We use of SNOwGLOBES software [68]. SNOwGLOBES takes as input fluxes, cross sections (see Fig. 7-2), “smearing matrices” and post-smearing efficiencies. The smearing matrices incorporate both interaction product spectra and detector response.

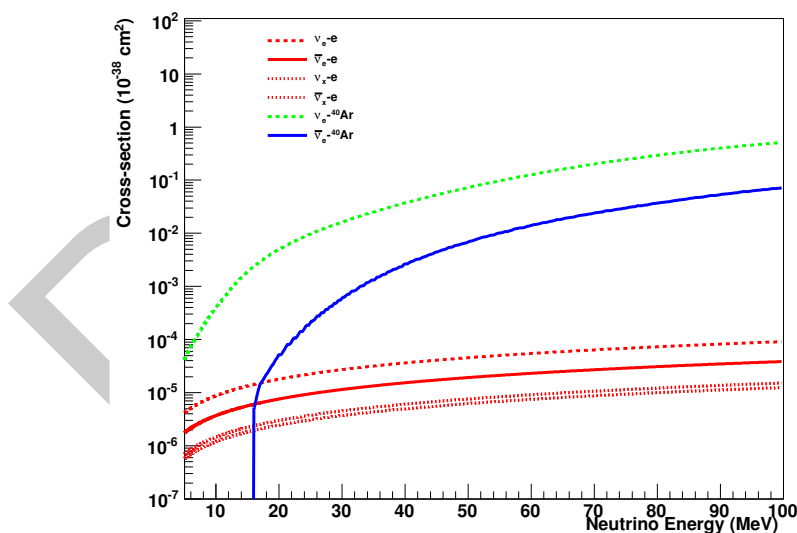


Figure 7-2: Cross-sections for SN-relevant interactions in argon.

Table 7-1 shows calculated rates for the dominant interactions in argon for the “Livermore” model [69], and the “GKVM” model [1]. Figure 7-3 shows the expected observed differential event spectra. Clearly ν_e flavor dominates.

Another example is for “Duan” fluxes [57] for which different oscillation hypotheses have

Channel	Events, “Livermore” model	Events, “GKVM” model
$\nu_e + {}^{40}\text{Ar} \rightarrow e^- + {}^{40}\text{K}^*$	1154	1424
$\bar{\nu}_e + {}^{40}\text{Ar} \rightarrow e^+ + {}^{40}\text{Cl}^*$	97	67
$\nu_x + e^- \rightarrow \nu_x + e^-$	148	89
Total	1397	1580

Table 7–1: Event rates for different models in 17 kt of LAr for a core-collapse at 10 kpc. Event rates will simply scale by active detector mass.

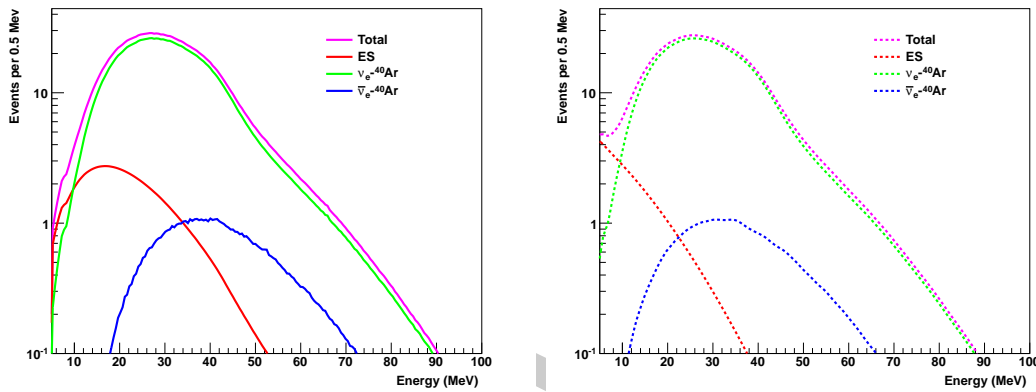


Figure 7–3: Supernova neutrino event rates in 17 kton of argon for a core collapse at 10 kpc, for the GKVM model [1] (events per 0.5 MeV), showing three relevant interaction channels. Left: interaction rates as function of true neutrino energy. Right: “smeared” rates as a function of detected energy, assuming resolution from reference [2].

1 been applied, to illustrate (anecdotally) potential mass hierarchy signatures: see Fig. 7–4. *

2 Another example is shown in in Figure 7–5, for which a clear feature is visible for the normal

3 mass hierarchy case.

4 Figure 7–6 shows another example of a preliminary study showing how one might track

5 supernova temperature as a function of time with the ν_e signal in liquid argon. Here, a fit is

6 made to the pinched-thermal form of 7.1. Not only can one effectively measure the internal

7 temperature of the supernova, but the time evolution is observably different for different

8 hierarchies.

9 Most LBNE supernova physics sensitivity studies so far have been done using parameterized

10 detector responses from [2] in SNOwGLoBES. Work is currently underway using LArSoft

11 to characterize low-energy response for LBNE detector configurations. Figure 7–7 shows an

12 example 20-MeV event. Preliminary results show that energy resolutions for baseline detector

13 parameters will not differ too significantly from those in [2]. Also under study is the potential

14 for tagging CC ν_e absorption events using the cascade of deexcitation γ -rays, which should

*Note that the “Duan” flux represents only a single late time slice of the supernova burst and not the full flux; hierarchy information will be encoded in the time evolution of the signal as well.

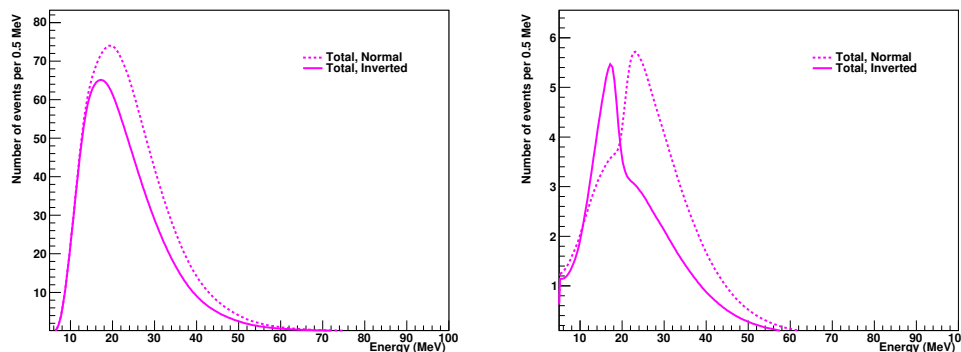


Figure 7-4: Comparison of total event rates for normal and inverted hierarchy, for a specific flux example, for a water Cherenkov detector (left) and for a 17 kt LAr (right) configuration, in events per 0.5 MeV. There are distinctive features in LAr for different neutrino mass hierarchies for this supernova model.

- 1 serve the dual purposes of rejecting background and isolating the CC component of the
- 2 signal.

3 7.3 Low-Energy Backgrounds

4 Due to their low energy, supernova events are subject to background, although the short-
 5 timescale-burst nature of the signal means that the background can be well known and
 6 subtracted. Muons and their associated Michel electrons can in principle be removed. Pre-
 7 liminary studies from reference [70], extended for cosmic-ray rates on the surface, suggest
 8 that the 4850L depth available at the Homestake mine is acceptable.

9 We are in the process of creating a physics driven radioactive background budget and associ-
 10 ated event generator for low-energy background events in the LBNE far detector. Radioactive
 11 decays will have the capacity to directly overlap with the energy spectrum created by super-
 12 nova neutrino events in LBNE (these will mostly be from $\nu_e + {}^{40}\text{Ar} \rightarrow e^- + {}^{40}\text{K}^*$). It is also
 13 possible that an ensemble of radioactive decay events in and around higher energy particle
 14 interactions (e.g. from beam neutrinos) could server to obscure the edges of electromagnetic
 15 showers from highly scattering particles like electrons and pions. This would serve as the
 16 radiological equivalent of dark noise in a digital image, and would have the potential to
 17 introduce a systematic uncertainty in the energy calculated for events even at much higher
 18 energy than the decays themselves. It is therefore very important to calculate the radioactive
 19 decay backgrounds in the LBNE far detector with sufficient accuracy to properly account
 20 for their presence, whether that is as a direct background with the capacity to obscure the
 21 supernova neutrino signal or as a systematic effect in energy calculations.

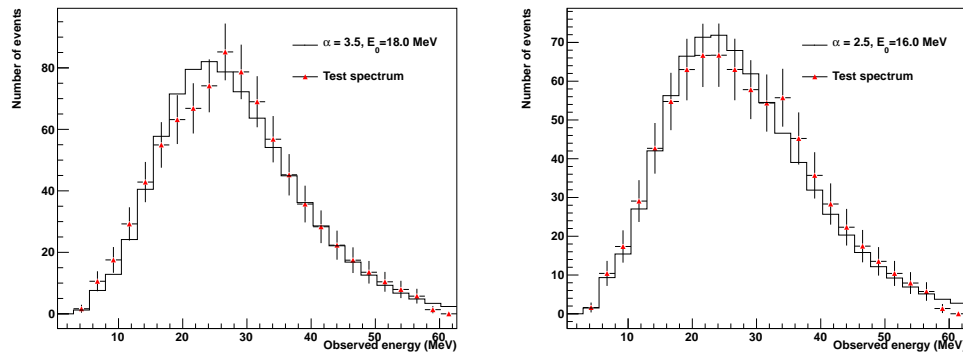


Figure 7–5: Observed ν_e spectra in 34 kton of LAr for a 10 kpc core collapse, representing about one second of integration time each at one second intervals during the supernova cooling phase. The solid line represents the best fit to a parameterized pinched-thermal spectrum. Clear “non-thermal” features in the spectrum that change with time are visible, on the left at around 20 MeV and on the right at around 35 MeV. Error bars are statistical. These features are present *only* for normal mass hierarchy. – checking with AF, JJC, HD whether OK to use this plot in the document

The radioactive background budget will have many components, each of which will fall into one of two categories: intrinsic radioactive contamination in the argon or support materials, and cosmogenic radioactivity produced *in situ* from cosmic ray showers interacting with the argon or the support materials. The former is dependent on the materials comprising the detector itself, and is therefore independent of far detector site depth. The latter is strongly coupled to the cosmic ray flux and spectrum, so any depth dependence to the background model will live here. Both of these background categories are of course in addition to the direct energy depositions from cosmic rays themselves and associated showers. Those have been discussed and well-studied elsewhere, so we will simply refer to their existence here.

7.3.1 Intrinsic Backgrounds

Intrinsic backgrounds in the far detector come from the radioactive material that is ubiquitous in the materials comprising the detector (both active and instrumentation/support materials), the cryostat, cavern walls, and dust. The isotopes of interest will largely be “the usual suspects” in experiments where radioactive backgrounds must be controlled: ^{232}Th and ^{238}U (and their associated decay chains), ^{40}K , and ^{60}Co . In addition to these, there will also be a large component from ^{39}Ar , which is present in natural argon harvested from the atmosphere at the level of approximately 1 Bq/kg. This means that a 10 kT far detector filled with $^{\text{nat.}}\text{Ar}$ will have a rate from ^{39}Ar of approximately 10 MHz across the whole detector. The beta decay spectrum from ^{39}Ar is thankfully quite low in energy ($Q_\beta = 0.565$ MeV), so it will not interfere directly with the supernova signal, but can contribute to the “dark noise” effect

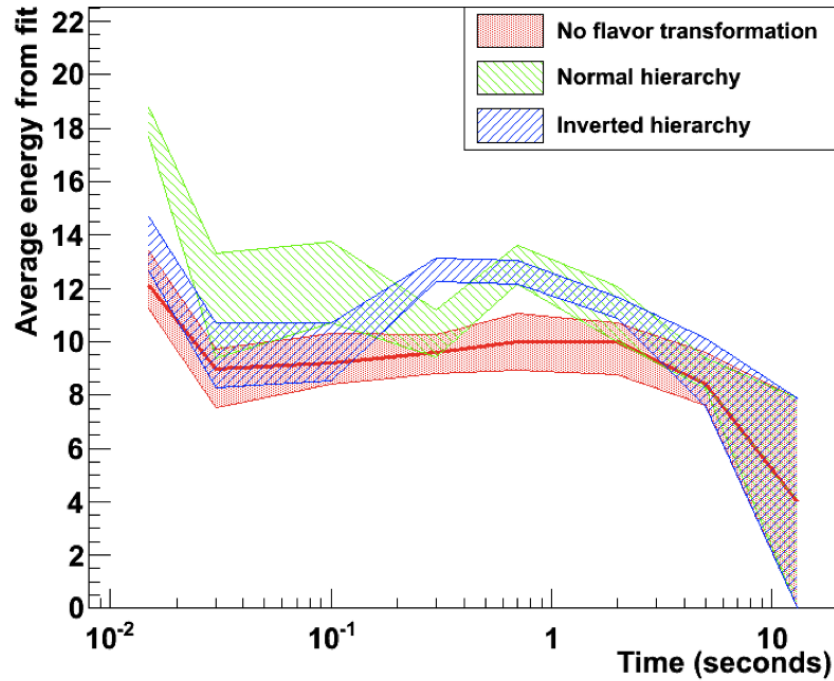


Figure 7-6: Average ν_e energy from fit to SNOwGLOBES-smearred pinched-thermal spectrum as a function of time, for a flux model based on [3] and including collective oscillations, for two different hierarchy assumptions (34 kton at 10 kpc). The bands represent 1σ error bars from the fit. The solid red line is the truth $\langle E_\nu \rangle$ for the unoscillated spectrum. This plot shows that there is meaningful information to be obtained by tracking ν_e spectra as a function of time. – *checking with AF, JJC, HD*

- 1 discussed earlier. Furthermore, the product of the average beta energy with this rate sets
- 2 the scale of the power being introduced into the detector at which we should be concerned
- 3 about controlling backgrounds. This radioactive power from ^{39}Ar is approximately:

$$P_{\text{Rad}} \sim 0.25 \text{ MeV} \times 10 \text{ MHz} = 2.5 \times 10^6 \text{ MeV/s.} \quad (7.2)$$

- 4 Because the backgrounds in this category can be not just in the bulk argon, but on the surface
- 5 of or embedded in any of the supporting materials (*e.g.* wire frames, signal wires, photon
- 6 collectors, readout electronics, cryostat lining/insulation, cavern walls, concrete cavern lining,
- 7 *etc.*), we must also be mindful of which type of radioactive decay is produced by each intrinsic
- 8 isotope and not just the total energy released. For instance, an alpha decay from an isotope in
- 9 the U or Th decay chain will deposit its full energy into the detector if it occurs in the active
- 10 region of the detector, but will deposit no energy if it occurs inside of some macroscopically
- 11 thick piece of support material because of the very short range ($\lesssim 1 \mu\text{m}$) in most solids.
- 12 We must therefore account for energy depositions from intrinsic contamination in different
- 13 locations (or groups of locations differently. This is clearly a tractable problem, but one
- 14 which must be handled with some level of care and forethought.

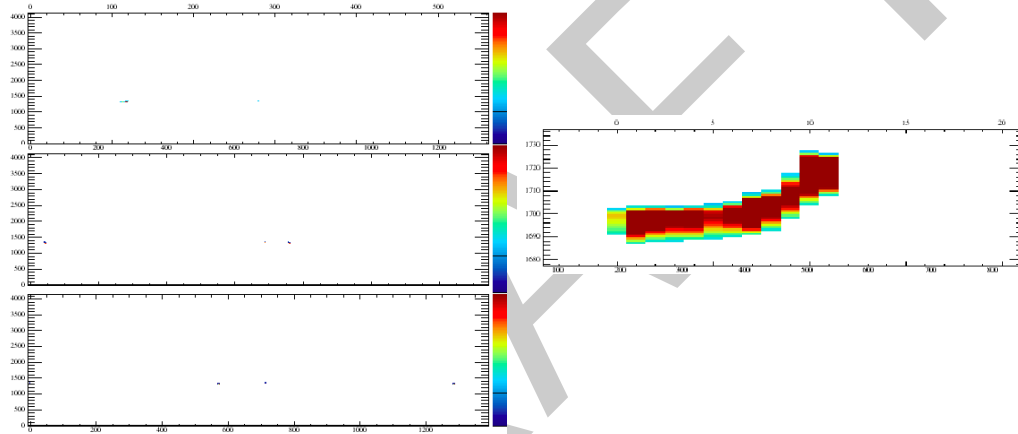


Figure 7-7: Left: raw event display of a typical 20-MeV event in the LBNE 10-kton geometry; the top panel shows the collection plane, and the lower two panels show the induction planes (with multiple images due to wire wrapping). Right: zoom of collection plane image.

1 There is clearly a large body of work on the control of radiological backgrounds in experiments
 2 like LBNE, so much of the work in this area will be cited from experiments like DARKSIDE,
 3 ICARUS, BOREXINO, KamLAND, and Super Kamiokande. Some work will remain however
 4 on understanding backgrounds particular to the SURF campus—either on the surface or at
 5 the 4850 level (radon levels and dust activity, for instance), and there remains a significant
 6 required effort to integrate existing and new work into the LBNE simulation, reconstruction,
 7 and analysis framework.

7.3.1.1 Cleanliness Database

Radioactive decays, including cosmogenic spallation products, tend to make <10 MeV signals, but may have impact on the detector performance due to the large number of charged particles and scintillation photons they produce in liquid argon. While backgrounds from radioactive decay lie below the main supernova signal range, they inhabit a potential region of interest for physics signatures. The decay events are mainly from radioactive isotope ^{39}Ar in natural argon, the ^{238}U and ^{232}Th decay chains through the airborne (dust) contamination in the detector, and radioactive elements in detector construction materials (which will also have a significant U/Th component). Measurements were made of the decay of ^{39}Ar in natural argon [71], purity in liquid argon due to outgassing from various materials [72]. The LBNE Collaboration also endeavors to build up a cleanliness database that includes material outgassing characteristics and radioactivity of detector construction materials. Systematic studies of the airborne contamination are also carried out at Homestake and South Dakota School of Mines and Technology (SDSMT) [73], which include, (1) the survey of the radioactivity data of rock samples and other substances in the Sanford Underground Research Facility (SURF), (2) simulation study of decay events in liquid argon, and (3) the characterization of dust particles on the surface at SURF and in the Davis Cavern at 4850 feet level. More efforts are planned by the LBNE Radiological and Cleanliness Control Group to make progress in the following aspects,

1. Developing more effective dust deposition monitoring method that can also be sensitive to smaller dust particles.
2. Determining the radioactivity of dust particles collected from underground site.
3. Implementing radioactive noise simulation in LBNE simulation tools and study the cleanliness requirements for various physics goals.
4. Tracing impact from decay events that may affect the performance of particular detector units, such as the HV units, TPC wires, etc.
5. Developing material purity model using material test data from the MTS.

The goal is to develop a reliable cleanliness control and monitoring procedure that can guarantee the contamination in the multi kiloton LBNE far detector at a level low enough so that we can extend the experiment threshold down to 5 MeV to 10 MeV in a detector that is also highly stable over 10 - 20 years of data taking.

7.3.2 Cosmogenic Backgrounds

As mentioned in 7.3, the cosmogenic backgrounds are where the depth of the far site will contribute to the signals seen in LBNE. We have compiled a list potential cosmogenic nuclides

1 (all either β^- or β^+ emitters) produced in argon, along with the nuclear data required to
2 calculate their decay spectra and the software infrastructure necessary to store and recall
3 them as needed. We are now in the process of compiling the activation cross sections, which
4 along with the decay lifetimes will determine the proportions with which we will sample
5 these spectra to simulate background events in LBNE. We will, of course, have different
6 proportions and overall numbers of these cosmogenic nuclides that will be added to LBNE
7 simulations for operation on the surface, and 4850 ft. (we will probably also look at 800
8 ft.) at SURF. These decays will be added to those from intrinsic radioactivity discussed in
9 Section 7.3.1, to build up the complete radioactive background model for LBNE.

DRAFT

8 Other Physics Opportunities with the LBNE Far Detector

In this chapter we summarize several physics topics that in principal could be addressed by the LBNE LAr-FD in a deep underground location, but which are particularly challenging for a LAr-TPC. Detection of low energy neutrinos such as geo-neutrinos and relic supernova neutrinos are challenging because of the intrinsic high detection thresholds ($> 1\text{MeV}$) of a LAr detector. Solar neutrino and dark matter searches require large detectors of order 100kton or more to be competitive, although the high energy and pointing resolutions of a LAr-TPC could be advantageous and offset some of the loss in performance due to the smaller masses of such detectors. Nevertheless, these topics are scientific opportunities that could be pursued by LBNE, in particular with the deployment of larger mass detectors at the far site. An aggressive R&D effort on radiopurity and cleanliness could potentially reduce the detection thresholds of a LAr detector and enhance the low energy scientific reach.

8.1 Solar Neutrinos

Even after the long standing mystery of missing solar neutrinos [?] was explained by data from the Super-Kamiokande and SNO [?] experiments as flavor transformation of solar neutrinos, there are still interesting open questions in solar neutrino physics. Some of these are astrophysical (like a measurement of the fraction of energy production via CNO cycle in the sun, or flux variations due to helio-seismological modes which reach the solar core, or long-term stability of the solar core temperature). But even particle physics questions remain. Can the MSW model explain the amount of flavor transformation as a function of energy, or are non-standard neutrino interactions required? Do solar neutrinos and reactor anti-neutrinos oscillate with the same parameters? Some of these questions will be answered by experimental data in the immediate future (like SNO+, KamLAND solar phase, further Borexino data, etc.), but high statistics measurements will be necessary to further constrain alternatives to the standard oscillation scenario.

The solar neutrino physics potential of a large liquid Argon TPC largely depends on the energy threshold and depth. The decay of the naturally occurring ^{39}Ar produces β 's with

a 567 keV endpoint and with an expected background of 10 MHz in a 10 kton LAr-TPC limits the fundamental reach of LAr detectors to ν with ≥ 1 MeV. The number of solar neutrinos expected in a 10 kton LAr-TPC is 9 events per day from Fermi transition and 26 events per day from Gamow-Teller transitions assuming a 4.5 MeV threshold and 31% ν_e . The ICARUS collaboration has reported a 10 MeV neutrino energy threshold (as reported by the ICARUS collaboration [?]). With such a high threshold the LBNE LArFD could still measure the CC/NC ratio of ^8B solar neutrinos with high statistical accuracy and thereby test the MSW flavor transformation curve (see Figure 8-1) with high precision if the detector itself has low radioactivity levels. To significantly improve on existing measurements of the MSW transition and limits on the day/night effect, a LAr detector of 34 kton or more is required. In addition, since the spallation of the ^{40}Ar (a rather complex nucleus compared to

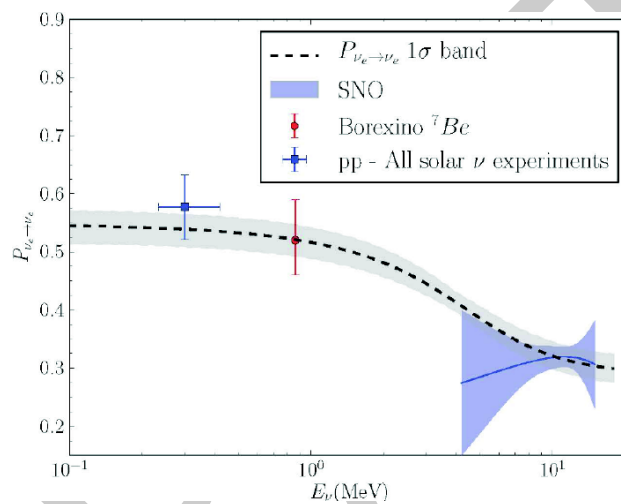


Figure 8-1: Measurements of the solar MSW transition

^{16}O) is likely to produce many long-lived spallation products which could limit the detection threshold for low energy neutrinos. Only a TPC at the deepest location has a reasonable chance of detecting solar neutrinos. Studies of the spallation background in the LAr-FD are underway. As an example, Figure 8-2 shows the ^{40}Cl production rate in a 10kton LAr-TPC as a function of depth. ^{40}Cl is a beta emitter with an endpoint of 7.48 MeV.

8.2 Geoneutrinos

Within the earth it is believed that radioactive decays of uranium and thorium are the most significant source of heat that causes mantle convection, the fundamental geological process that regulates the thermal evolution of the earth and shapes its surface. Until recently, estimates of the total uranium and thorium content of the earth were inferred from earth formation models. However, it has been known for a long time that the uranium and thorium decays produce electron anti-neutrinos, so-called geo-neutrinos, and the detection of these geo-neutrinos near the surface of the earth can directly inform us of the deep earth uranium

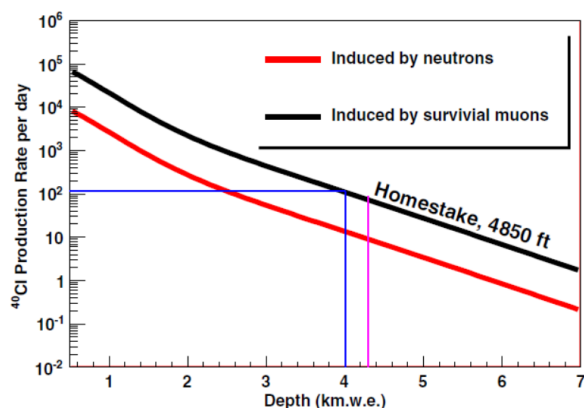


Figure 8-2: ^{40}Cl production rates in a 10 kton detector produced by (n,p) reaction as a function of depth.

and thorium content. The low flux of electron anti-neutrinos from reactors, so called reactor neutrinos, at SURF makes it a suitable site to probe geo-neutrinos.

In a liquid Ar detector electron anti-neutrinos can be detected by Ar inverse-beta-decay



The threshold for this reaction is approximately 8.5 MeV, which means that it cannot be used to detect either geo-neutrinos or reactor neutrinos. There are also elastic scattering reactions; however, these are sensitive to neutrinos as well as antineutrinos, so in order to eliminate backgrounds from solar neutrinos we need to be able to reject these by pointing at a level better than one in a thousand. Detecting geo-neutrinos with a massive LAr detector deep underground at SURF will be very difficult.

8.3 Indirect Searches for WIMP Dark Matter

If the true nature of DM does indeed involve a weakly-interacting particle with a mass in the 100's of GeV, one of the main search strategies involves looking for anomalous signals in astrophysical data from its annihilation (or decay) into SM particles, like neutrinos. Signals of DM via neutrinos can come from such distant objects as the galactic center, the center of the Sun or even the Earth. As our solar system moves through the DM halo, WIMPs interact with the nuclei of celestial bodies and become trapped in the body's gravitational well. Over time, the WIMPs accumulate near the core of the body, enhancing the possibility of annihilation. The high-energy neutrinos ($E \sim m_{\text{WIMP}}$) from these annihilations can free-stream through the astrophysical body and emerge roughly unaffected (although oscillation and matter effects can slightly alter the energy spectrum). For the Sun, the background

1 of neutrinos are produced at much lower energies via the nuclear fusion process. Thus,
2 the detection of high-energy neutrinos pointing to the Sun and detected in the LBNE far
3 detector would be clear evidence of DM annihilation (see [?]). Since the LBNE far detector
4 has relatively large mass of the order 10s of kt, it can act as a "neutrino telescope" and be used
5 to search for signals of DM annihilations coming from the Sun and/or the core of the Earth.
6 IceCube [?] and Super-Kamiokande have searched for DM through this method but have not
7 observed a signal of DM annihilation into neutrinos. Compared to these experiments which
8 are based on Cerenkov light detection using large PMT's, LBNE LAr TPC can provide
9 much better angular resolution that can help far more accurate pointing resolution. The
10 mass of the IceCube's 1 km^3 ice volume is of the order $\sim 2.6 \times 10^4$ that of the 34kt LBNE
11 far detector. This requires the LBNE far detector to perform better by $\sim 2.6 \times 10^4$ than
12 IceCube. While this factor seems quite daunting, if not out right impossible, more thorough
13 studies are needed to investigate possible improvements in various performance factors to
14 accomplish this level of enhancement.

9 Conclusion

In the previous chapters, we have presented the physics opportunities and capabilities of the LBNE program, so we conclude this document with a discussion of possible timeframes for the different stages for LBNE. With DOE CD-1 approval in hand the Collaboration and Project are working toward the technical design specifications, including detailed costs and schedule, in preparation for CD-2. With CD-2 the LBNE Phase-I project will be baselined. Currently, the timescale for CD-2 is projected to be 2016, although the DOE has indicated flexibility in this, specifically to allow for incorporation of scope changes enabled by additional funding sources identified before then. It is also expected that on the timescale of CD-2, that CD-3a approval will allow expenditures for long-leadtime components and construction activities. The CD-4 milestone (completion of the construction project and transition to experiment operations) is currently projected for 2023. By this time the NOvA experiment will have surpassed its nominal exposure (6 years of operation at 700 kW), and the Main Injector neutrino beam operations will have shifted from the NuMI beam line to that for LBNE.

Timeline Scenario: The exact timeframe for accessing LBNE science goals will depend on how a complex sequence of developments take place. However, here we provide an example of one plausible scenario that integrates evolution of LBNE detector mass with development of the Project X beam.

1. Begin operation in 2023 with 700-kW beam and a 10-kt detector.
2. Three years later, in 2026, Project X phase 1 is completed, increasing the beam power to 1.2 MW [?], and the LBNE far detector fiducial mass is increased to 20 kt.
3. Two years later, in 2028, the LBNE far detector mass is increased to 34 kt.
4. Four years later (6 years after the completion of Project X phase 1), Project X phase 3 is completed, increasing the beam power to 2.4 MW.
5. Operate for six years with “full” detector mass and “full” beam power.

The evolution of the LBNE sensitivity to CP-violation under this scenario is illustrated in Fig. 9–1. In this graph, the accumulated exposure is plotted as a function of calendar year,

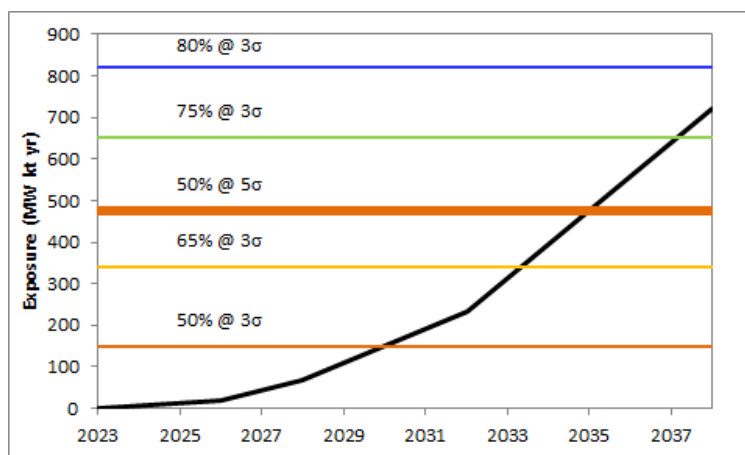


Figure 9–1: Evolution of exposure and sensitivity to non-zero or π value for δ_{CP} as a function of calendar year, under the scenario for rapid development of the later stages of LBNE and integration with Project X as described in the text.

beginning in 2023. Horizontal lines indicate exposure values that yield particular benchmarks in the sensitivity to leptonic CP violation. These benchmarks are specified in terms of the fraction of the range of δ_{CP} for which a non-zero (or π) value would be established at the stated level of statistical significance (3σ or 5σ) or better. In this scenario, LBNE would achieve 50% coverage of δ_{CP} at better than 5σ (and 70% coverage at better than 3σ) by 2035 (Note: no experiment will approach 100% in this metric). Also in this scenario the mass hierarchy will have been determined unambiguously within about 5 years.

We emphasize that the scenario described above is just one of a number of possibilities. An advantage of a staged approach to LBNE is the flexibility to coordinate with other major activities so that high points in the time profiles of costs do not overlap.

Alternatives: Considering the time it has taken to reach the current state of development of LBNE, it is unlikely that another program of similarly ambitious scope would be able to begin operation before 2025, particularly in light of the current constrained budget conditions in HEP. We note that similar-cost alternatives for the first phase of LBNE utilizing the existing NuMI beam were considered during the reconfiguration exercise in 2012. The conclusion of the panel was that none of these alternatives presented a path toward an experiment capable of a $5\text{--}\sigma$ CP violation signal. We also note that careful consideration of a large water Cherenkov option for LBNE was given prior to selection of the LArTPC technology for the far detector. This option did not present advantages in terms of cost or schedule.

Intensity Frontier Leadership: LBNE is an ambitious next stage in the series of world-leading long-baseline neutrino oscillation experiments in the U.S. that started with MINOS and continues with NOvA. By anchoring the U.S. Intensity Frontier program, LBNE provides a platform around which to grow and sustain core infrastructure for the community. This is especially the case for the development of Project X, which will accelerate progress towards

1 the science goals of LBNE while also greatly expanding the capability of Fermilab to host
2 compelling experimental programs that will explore other sectors of the Intensity Frontier.

3 Understanding the fundamental nature of fermion flavor, the existence of CP violation in the
4 lepton sector and how this relates to the baryon asymmetry of the universe; knowing whether
5 proton decay occurs and how; and elucidating the dynamics of supernova explosions all count
6 among the grand questions of our field. The bold approach adopted for LBNE provides the
7 most rapid and cost-effective means of addressing these questions. With the support of the
8 HEP community, the vision articulated in this document can be realized in a way that
9 maintains the level of excitement for Particle Physics and the inspirational impact it has in
10 the U.S and worldwide.

DRAFT

References

- [1] J. Gava, J. Kneller, C. Volpe, and G. C. McLaughlin, “A dynamical collective calculation of supernova neutrino signals,” *Phys. Rev. Lett.*, vol. 103, p. 071101, 2009.
- [2] S. Amoruso *et al.*, “Measurement of the mu decay spectrum with the ICARUS liquid argon TPC,” *Eur. Phys. J.*, vol. C33, pp. 233–241, 2004.
- [3] M. T. Keil, G. G. Raffelt, and H.-T. Janka, “Monte Carlo study of supernova neutrino spectra formation,” *Astrophys. J.*, vol. 590, pp. 971–991, 2003.
- [4] National Science and Technology Council Committee on Science, “The Physics of the Universe, a Strategic Plan for Federal Research at the Intersection of Physics and Astronomy,” 2004. <http://www.ostp.gov/html/physicsoftheuniverse2.pdf>.
- [5] Particle Physics Project Prioritization Panel, “U.S. Particle Physics: Scientific opportunities, a plan for the next ten years,” 2008. http://www.er.doe.gov/hep/files/pdfs/P5_Report06022008.pdf.
- [6] HEPAP Facilities Subpanel, “Input to the prioritization of proposed scientific user facilities for the Office of Science,” 2013.
- [7] DOE Office of High Energy Physics, “Mission Need Statement for a Long-Baseline Neutrino Experiment (LBNE),” tech. rep., DOE, 2009. LBNE-doc-6259.
- [8] A. S. Kronfeld, R. S. Tschirhart, U. Al-Binni, W. Altmannshofer, C. Ankenbrandt, *et al.*, “Project X: Physics Opportunities,” 2013.
- [9] “Neutrinos: Intensity Frontier Working Group Report, DPF Community Summer Study 2013,” 2013. <http://www.snowmass2013.org/tiki-index.php?page=Neutrinos>.
- [10] “LBNE Conceptual Design Report, volume 1: The LBNE Beamline at the Near Site.” LBNE Project Management Team - LBNE Doc 5235, 2012.
- [11] LBNE Project Office, “Key Assumptions: Physics Research Goals of the LBNE Project,” tech. rep., FNAL, 2010. LBNE Doc 3056v1.
- [12] LBNE Project Office, “Physics Research Goals before Reconfiguration,” tech. rep., FNAL, 2012. LBNE Doc 3056v5.

- [13] R. Mohapatra, S. Antusch, K. Babu, G. Barenboim, M.-C. Chen, *et al.*, “Theory of neutrinos: A White paper,” *Rept.Prog.Phys.*, vol. 70, pp. 1757–1867, 2007.
- [14] C. H. Albright and M.-C. Chen, “Model Predictions for Neutrino Oscillation Parameters,” *Phys.Rev.*, vol. D74, p. 113006, 2006.
- [15] G. Fogli, E. Lisi, A. Marrone, D. Montanino, A. Palazzo, *et al.*, “Global analysis of neutrino masses, mixings and phases: entering the era of leptonic CP violation searches,” *Phys.Rev.*, vol. D86, p. 013012, 2012.
- [16] J. Beringer *et al.*, “Review of Particle Physics (RPP),” *Phys.Rev.*, vol. D86, p. 010001, 2012.
- [17] C. Jarlskog, “A Basis Independent Formulation of the Connection Between Quark Mass Matrices, CP Violation and Experiment,” *Z.Phys.*, vol. C29, pp. 491–497, 1985.
- [18] W. Marciano and Z. Parsa, “Intense neutrino beams and leptonic CP violation,” *Nucl.Phys.Proc.Suppl.*, vol. 221, pp. 166–172, 2011.
- [19] K. Nakamura *et al.*, “Review of particle physics,” *J. Phys.*, vol. G37, p. 075021, 2010.
- [20] P. Adamson *et al.*, “Search for the disappearance of muon antineutrinos in the NuMI neutrino beam,” *Phys. Rev. D.*, vol. 84, p. 071103, 2011. arXiv:1108.1509 [hep-ex].
- [21] S. Mikheev and A. Y. Smirnov, “Resonance Amplification of Oscillations in Matter and Spectroscopy of Solar Neutrinos,” *Sov.J.Nucl.Phys.*, vol. 42, pp. 913–917, 1985.
- [22] L. Wolfenstein, “Neutrino Oscillations in Matter,” *Phys.Rev.*, vol. D17, pp. 2369–2374, 1978.
- [23] M. Freund, “Analytic approximations for three neutrino oscillation parameters and probabilities in matter,” *Phys.Rev.*, vol. D64, p. 053003, 2001.
- [24] J. Appel *et al.*, “Physics Working Group Report to the LBNE Reconfiguration Steering Committee,” 2012. http://www.fnal.gov/directorate/lbne_reconfiguration/files/LBNE-Reconfiguration-PhysicsWG-Report-August2012.pdf.
- [25] J. C. Pati and A. Salam, “Is Baryon Number Conserved?,” *Phys.Rev.Lett.*, vol. 31, pp. 661–664, 1973.
- [26] H. Georgi and S. Glashow, “Unity of All Elementary Particle Forces,” *Phys.Rev.Lett.*, vol. 32, pp. 438–441, 1974.
- [27] S. Dimopoulos, S. Raby, and F. Wilczek, “Proton Decay in Supersymmetric Models,” *Phys.Lett.*, vol. B112, p. 133, 1982.
- [28] P. Langacker, “Grand Unified Theories and Proton Decay,” *Phys.Rept.*, vol. 72, p. 185, 1981.

- [29] S. Raby, T. Walker, K. Babu, H. Baer, A. Balantekin, *et al.*, “DUSEL Theory White Paper,” 2008.
- [30] G. Senjanovic, “Proton decay and grand unification,” *AIP Conf.Proc.*, vol. 1200, pp. 131–141, 2010.
- [31] T. Li, D. V. Nanopoulos, and J. W. Walker, “Elements of F-ast Proton Decay,” *Nucl.Phys.*, vol. B846, pp. 43–99, 2011.
- [32] K. Scholberg, “Supernova neutrino detection,” 2007.
- [33] R. M. Bionta *et al.*, “Observation of a neutrino burst in coincidence with supernova SN1987A in the Large Magellanic Cloud,” *Phys. Rev. Lett.*, vol. 58, p. 1494, 1987.
- [34] K. Hirata *et al.*, “Observation of a neutrino burst from the supernova SN1987A,” *Phys. Rev. Lett.*, vol. 58, pp. 1490–1493, 1987.
- [35] A. Mirizzi, G. G. Raffelt, and P. D. Serpico, “Earth matter effects in supernova neutrinos: Optimal detector locations,” *JCAP*, vol. 0605, p. 012, 2006.
- [36] S. Choubey, B. Dasgupta, A. Dighe, and A. Mirizzi, “Signatures of collective and matter effects on supernova neutrinos at large detectors,” 2010.
- [37] P. Antonioli *et al.*, “Snews: The supernova early warning system,” *New J. Phys.*, vol. 6, p. 114, 2004.
- [38] NOvA Collaboration, “The NOvA Experiment Technical Design Report.” <http://lss.fnal.gov/archive/design/fermilab-design-2007-01.pdf>, 2007.
- [39] “Project X.” <http://projectx.fnal.gov>.
- [40] Y. K. Kim *et al.*, “LBNE Reconfiguration: Steering Committee Report,” 2012. http://www.fnal.gov/directorate/lbne_reconfiguration/index.shtml.
- [41] J. Allison *et al.*, “GEANT4 developments and applications,” *IEEE Trans. Nucl. Sci.*, vol. 53, no. 1, pp. 270–278, 2006.
- [42] The LArSoft Collaboration. <https://plone4.fnal.gov:4430/P1/Main/wiki/LArSoft/LArSoft>.
- [43]
- [44] F. An *et al.*, “Improved Measurement of Electron Antineutrino Disappearance at Daya Bay,” *Chin. Phys.*, vol. C37, p. 011001, 2013.
- [45] P. Adamson *et al.*, “Measurement of the neutrino mass splitting and flavor mixing by MINOS,” *Phys.Rev.Lett.*, vol. 106, p. 181801, 2011.

- [46] T. Fischer, S. C. Whitehouse, A. Mezzacappa, F. K. Thielemann, and M. Liebendorfer, “Protoneutron star evolution and the neutrino driven wind in general relativistic neutrino radiation hydrodynamics simulations,” *Astron. Astrophys.*, vol. 517, p. A80, 2010.
- [47] H. Minakata, H. Nunokawa, R. Tomas, and J. W. Valle, “Parameter Degeneracy in Flavor-Dependent Reconstruction of Supernova Neutrino Fluxes,” *JCAP*, vol. 0812, p. 006, 2008.
- [48] I. Tamborra, B. Muller, L. Hudepohl, H.-T. Janka, and G. Raffelt, “High-resolution supernova neutrino spectra represented by a simple fit,” *Phys.Rev.*, vol. D86, p. 125031, 2012.
- [49] H. Duan, G. M. Fuller, and Y.-Z. Qian, “Collective neutrino flavor transformation in supernovae,” *Phys.Rev.*, vol. D74, p. 123004, 2006.
- [50] G. L. Fogli, E. Lisi, A. Marrone, and A. Mirizzi, “Collective neutrino flavor transitions in supernovae and the role of trajectory averaging,” *JCAP*, vol. 0712, p. 010, 2007.
- [51] G. G. Raffelt and A. Y. Smirnov, “Self-induced spectral splits in supernova neutrino fluxes,” *Phys.Rev.*, vol. D76, p. 081301, 2007.
- [52] G. G. Raffelt and A. Y. Smirnov, “Adiabaticity and spectral splits in collective neutrino transformations,” *Phys.Rev.*, vol. D76, p. 125008, 2007.
- [53] A. Esteban-Pretel, A. Mirizzi, S. Pastor, R. Tomas, G. Raffelt, *et al.*, “Role of dense matter in collective supernova neutrino transformations,” *Phys.Rev.*, vol. D78, p. 085012, 2008.
- [54] H. Duan and J. P. Kneller, “Neutrino flavour transformation in supernovae,” *J.Phys.G*, vol. G36, p. 113201, 2009.
- [55] B. Dasgupta, A. Dighe, G. G. Raffelt, and A. Y. Smirnov, “Multiple Spectral Splits of Supernova Neutrinos,” *Phys.Rev.Lett.*, vol. 103, p. 051105, 2009.
- [56] H. Duan, G. M. Fuller, and Y.-Z. Qian, “Collective Neutrino Oscillations,” *Ann.Rev.Nucl.Part.Sci.*, vol. 60, pp. 569–594, 2010.
- [57] H. Duan and A. Friedland, “Self-induced suppression of collective neutrino oscillations in a supernova,” *Phys.Rev.Lett.*, vol. 106, p. 091101, 2011.
- [58] M. Wurm *et al.*, “The next-generation liquid-scintillator neutrino observatory LENA,” 2011.
- [59] T. Fischer, S. C. Whitehouse, A. Mezzacappa, F. K. Thielemann, and M. Liebendorfer, “The neutrino signal from protoneutron star accretion and black hole formation,” 2008.
- [60] R. C. Schirato and G. M. Fuller, “Connection between supernova shocks, flavor transformation, and the neutrino signal,” 2002.

- [61] F. Hanke, A. Marek, B. Muller, and H.-T. Janka, “Is Strong SASI Activity the Key to Successful Neutrino-Driven Supernova Explosions?,” *Astrophys.J.*, vol. 755, p. 138, 2012.
- [62] F. Hanke, B. Mueller, A. Wongwathanarat, A. Marek, and H.-T. Janka, “SASI Activity in Three-Dimensional Neutrino-Hydrodynamics Simulations of Supernova Cores,” *Astrophys.J.*, vol. 770, p. 66, 2013.
- [63] A. Friedland and A. Gruzinov, “Neutrino signatures of supernova turbulence,” 2006.
- [64] T. Lund and J. P. Kneller, “Combining collective, MSW, and turbulence effects in supernova neutrino flavor evolution,” 2013.
- [65] G. G. Raffelt, “Particle Physics from Stars,” *Ann. Rev. Nucl. Part. Sci.*, vol. 49, pp. 163–216, 1999.
- [66] K. Scholberg, “The SuperNova Early Warning System,” *Astron. Nachr.*, vol. 329, pp. 337–339, 2008.
- [67] A. Bueno, I. Gil Botella, and A. Rubbia, “Supernova neutrino detection in a liquid argon TPC,” 2003.
- [68] <http://www.phy.duke.edu/~schol/snowglobes>.
- [69] T. Totani, K. Sato, H. E. Dalhed, and J. R. Wilson, “Future detection of supernova neutrino burst and explosion mechanism,” *Astrophys. J.*, vol. 496, pp. 216–225, 1998.
- [70] D. Barker *et al.*, “Muon-induced background for beam neutrinos at the surface,” 2012. http://www.fnal.gov/directorate/lbne_reconfiguration/index.shtml.
- [71] P. Benetti *et al.*, “Measurement of the specific activity of ar-39 in natural argon,” *Nucl.Instrum.Meth.*, vol. A574, pp. 83–88, 2007.
- [72] “Material test data from the Fermilab Material Test Stand (MTS).” <http://lartptc-docdb.fnal.gov:80h80/cgi-bin/ShowDocument?docid=465>.
- [73] D. Tiedt, *Radioactive Background Simulation and Cleanliness Standards Analysis for Potential LBNE Detectors Located at SURF*. PhD thesis, South Dakota School of Mines and Technology, 2013.